Strong and weak interactions of organic molecules on oxide surfaces: Phenylphosphonic and boronic acids on rutile TiO_2(110) and tetraphenylporphyrins on MgO(100)

Starke und schwache Wechselwirkungen von organischen Molekülen auf Oxidoberflächen: Phenylphosphon- und Boronsäuren auf Rutil TiO_2(110) und Tetraphenylporphyrine auf MgO(100)

Der Naturwissenschaftlichen Fakultät der Friedrich-Alexander-Universität Erlangen-Nürnberg
zur Erlangung des Doktorgrades Dr. rer. nat.

vorgelegt von
Alexander Tobias Wolfram
aus Pegnitz

Als Dissertation genehmigt

von der Naturwissenschaftlichen Fakultät

der Friedrich-Alexander-Universität Erlangen-Nürnberg

Tag der mündlichen Prüfung: 13.09.2024

Gutachter: PD Dr. Ole Lytken
Prof. Dr. Federico J. Williams

Contents

1. Preface

I started my Ph.D. at the end of 2019 after finishing my master's thesis on electron-beam-induced deposition. I had little experience with ultra-high vacuum and its associated measurement techniques, such as X-ray photoelectron spectroscopy (XPS). In the last 4.5 years this has changed drastically as I have been working on the Scienta chamber. This is an older chamber, and as a result many things have broken. However, repairing this machine gave me a deep understanding of how ultra-high vacuum machines work. Of course, I measured on this machine as well, and this chamber proved to be a reliable workhorse for my TPD measurements.

In addition, I was fortunate to have the opportunity to make measurements at the Elettra synchrotron in Italy. Those beamtimes were always special: We worked in shifts to maximize our allocated beamtime, which is demanding, but at the same time I got really nice data and the time with the people there was fantastic. On my second beamtime we were joined by Prof. Federico Williams from Buenos Aires, and it was really educational and interesting to work with someone from a different university, giving new input and new ideas.

Although I spent a lot of time measuring data, I probably spent more time analyzing the data. The evaluations were challenging, and it was sometimes really annoying to try many different things - and none of them seemed to work. I often used programming to deal with these challenges, which did not bother me in the least. In the end, this enabled me to overcome challenges that I would not have been able to solve otherwise (I'm looking at you, random intensity spikes and second-order light features in NEXAFS).

Over the last 4.5 years I have been able to grow as a scientist and become very familiar with "my" techniques, X-ray photoelectron spectroscopy, Near-Edge X-ray Absorption Fine Structure, and temperature-programmed desorption. I have learned a lot about these techniques and their challenges, and in the following I will take the opportunity to include interesting experimental details alongside the results of my research.

2. Introduction

One of the most important and talked about elements today is carbon. There are public discussions about atmospheric carbon dioxide concentrations and great efforts are being made to minimize carbon emissions to achieve clean and sustainable energy. However, carbon is essential for life on Earth, as carbon atoms form the backbone of every living cell. What makes carbon so special is its chemical versatility, as it can form stable bonds with itself and other elements, especially hydrogen, oxygen, and nitrogen, allowing for the formation of large but stable molecules, such as porphyrins. Porphyrins are molecules consisting of a carbon macrocycle and a central cavity with four nitrogen atoms that allow for complexation of metal ions. This enables the synthesis of a wide variety of different molecules by adjusting the carbon macrocycle and the complexed metal ion, making porphyrins chemically very versatile molecules. This chemical versatility is demonstrated in biology, where porphyrins are part of the light-harvesting complex (chlorophyll) in photosynthesis, oxygen carriers in mammalian blood cells (hemoglobin), oxygen storage in muscle cells (myoglobin), or reaction centers in enzymatic reactions (cytochrome P450, cofactor F430), see Figure 1.

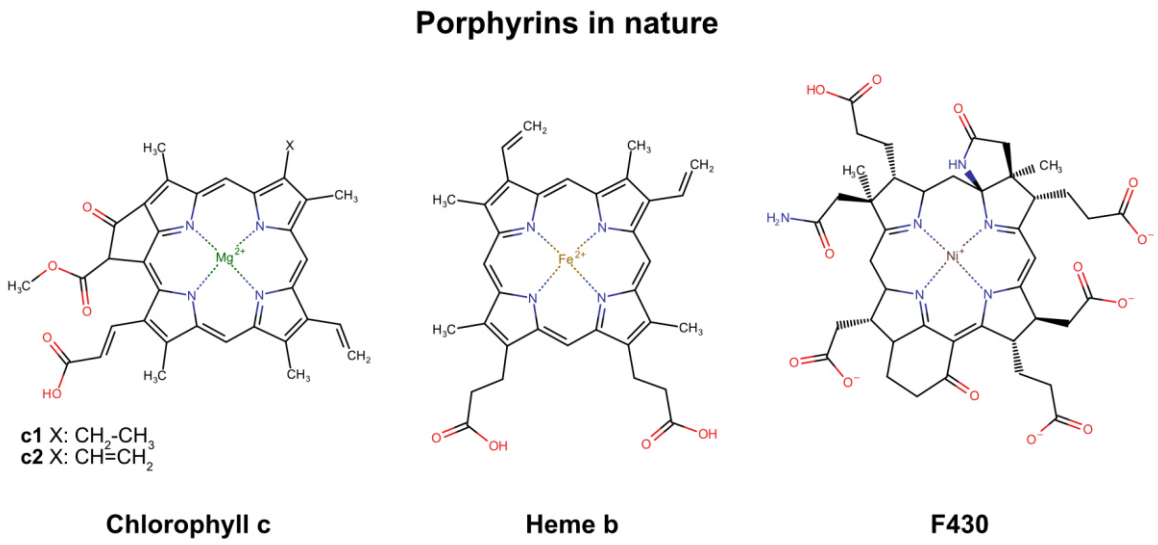

Figure 1: Chemical structures of naturally-occurring porphyrins. Chlorophyll c (left) is part of the light-harvesting complex in plants, heme b (center) is used in oxygen transport in the blood or in cytochrome P450 to catalyze oxidation reactions, and F430 (right) is a cofactor for an enzyme in the human body.

The versatility of these molecules has also been noticed by scientists who are using the ability of a porphyrin's metal center to coordinate with molecules to build sensors,[1] as materials for carbon dioxide capture[2] or use them as catalysts.[3] In addition, porphyrins are promising molecules for light absorption in dye-sensitized solar cells due to their optical properties and chemical stability.[4]

By combining the proven applicability of these molecules with the capabilities of organic chemists, it is possible to tailor the molecular properties to the desired application. In many applications, the molecules are often immobilized on an inorganic substrate; under ambient conditions, this is usually an oxide surface. A common strategy for immobilizing molecules on surfaces is the use of anchor groups, which are attached to the organic molecule and form strong bonds to the underlying substrate. This interaction can alter the physical properties of both the molecules and the substrate, and it is therefore crucial to understand the effects of molecular adsorption on both the molecule and the substrate, which in turn enables rational device design.

In this thesis, the adsorption of metallotetraphenylporphyrins on MgO(100) and of phenylphosphonic acid and phenylboronic acid derivatives on rutile TiO_2(110) has been studied. These systems were chosen to study the interaction of large organic molecules (porphyrins) and anchor groups (phosphonic acid and boronic acid) with oxides separately from each other.

2.1. Ultra-high vacuum

To understand the adsorption of a molecule on a surface, it is important to simplify the system as much as possible. If you were to try to adsorb a specific molecule onto an oxide surface under ambient conditions, the molecule would have to compete with all the molecules in the atmosphere to bind to the surface, and this makes it difficult to understand the bond to the surface at the molecular level. Atmospheric molecules include alcohols and carboxylic acids, and under ambient conditions their concentrations are high enough to form ordered layers on, for example, titanium dioxide within a few minutes.[5] This reaction is very fast, even though the atmospheric concentration of formic acid, the simplest carboxylic acid, is only about 2 ppbv in a semiurban environment.[6] The impingement rate Φ of a gas molecule onto a surface can be estimated as a function of pressure p according to[7]

$$\Phi = \mathrm{p} \cdot \sqrt{\frac{1}{2\pi \cdot \mathrm{k_B} \cdot \mathrm{m} \cdot \mathrm{T}}}$$

where k_B is the Boltzmann constant, m the mass of a gas molecule, and T the temperature of the gas. Thus, the impingement rate of formic acid at a pressure of 2×10^{-9} bar (corresponding to 2 ppbv) at room temperature is 5×10^{18} $s^{-1}m^{-2}$ and with the number of surface atoms being in the range of 10^{19} m^{-2}, it is not surprising that the surface is completely covered within minutes.

However, this equation also provides the solution to the problem: to decrease the flux of gas molecules onto the surface, the pressure must be lowered. In ultra-high vacuum (UHV), where pressures are around 1×10^{-10} mbar, the impingement rate of formic acid drops to 2×10^{14} $s^{-1}m^{-2}$, and even if every molecule would stick to the surface, it would take about 12 hours to completely cover the surface. Nevertheless, even under UHV conditions, molecules will adsorb slowly over time, but the adsorption rate is slow enough to perform experiments.

The most reactive sites on a surface are often defect sites, and in the case of rutile TiO_2(110) these are oxygen vacancies. These vacancies can bind molecules, such as carbon monoxide and water,[8, 9] often present in UHV chambers. STM measurements by Wendt et al. show that even at chamber pressures of around 10^{-10} mbar it only takes minutes until a significant amount of the oxygen vacancies has reacted with water[10] and forms surface OH groups. In the experiments in this

thesis, it is therefore to be expected that a significant amount of oxygen vacancies has reacted to surface OH groups.

2.2. Single crystals and their surfaces

Oxides are important industrial commodities. For example, titanium dioxide is used in the manufacture of paints, plastics, paper, corrosion-resistant coatings, antibacterial agents, water purification, and as an ultraviolet absorber in sunscreens.[11, 12] In many applications, titanium dioxide is used in the form of nanoparticles.[13] However, the properties of these nanoparticles are highly dependent on the synthesis method. This is due to the different polymorphs of TiO_2, which occurs mainly in three different crystal structures: rutile, anatase, and brookite. While the thermodynamically most stable rutile phase dominates for large nanoparticles (>35 nm) or after heat treatment, the brookite phase is the most stable between 11 and 35 nm particle size, while anatase is the most stable below 11 nm.[14] As a result, nanoparticle powders often contain several polymorphs, such as the well-known Degussa P25, which consists of 80% anatase and 20% rutile.[15]

TiO_2 nanoparticle samples are quite complicated, not only because they are mixtures of polymorphs, but the nanoparticles themselves have many different facets.[16] Molecules interact differently with different facets, and thus it would be very difficult to disentangle the effect of facets on the adsorption binding mode while still trying to understand how the molecule binds to the surface in the first place. To avoid these different effects, it is advantageous to use a model system with only one facet and an atomically well-defined surface: a single crystal.

In this thesis, the rutile TiO_2(110) single crystal surface is used, which is obtained by cutting the unit cell of the rutile crystal along the (110) plane, see Figure 2. The resulting crystal in Figure 3 (left) is colorless, which is due to the large band gap of about 3.0 eV. This makes the material an effective UV blocker, but at the same time it hinders photocatalytic efficiency by absorbing only a small fraction of the solar spectrum. For this reason, much attention has been focused on narrowing the band gap by doping.[17, 18] Another approach is used in dye-sensitized solar cells, where a dye molecule, such as a porphyrin molecule, with a smaller band gap is immobilized on the titania surface, and after light excitation, the excited electron in the unoccupied orbitals of the molecule can be transferred into the conduction band of titania.[4] Efficient electron transfer is crucial for good device performance, and therefore it is highly desirable to understand the electronic interactions between an organic molecule and the TiO_2 surface in detail. This includes

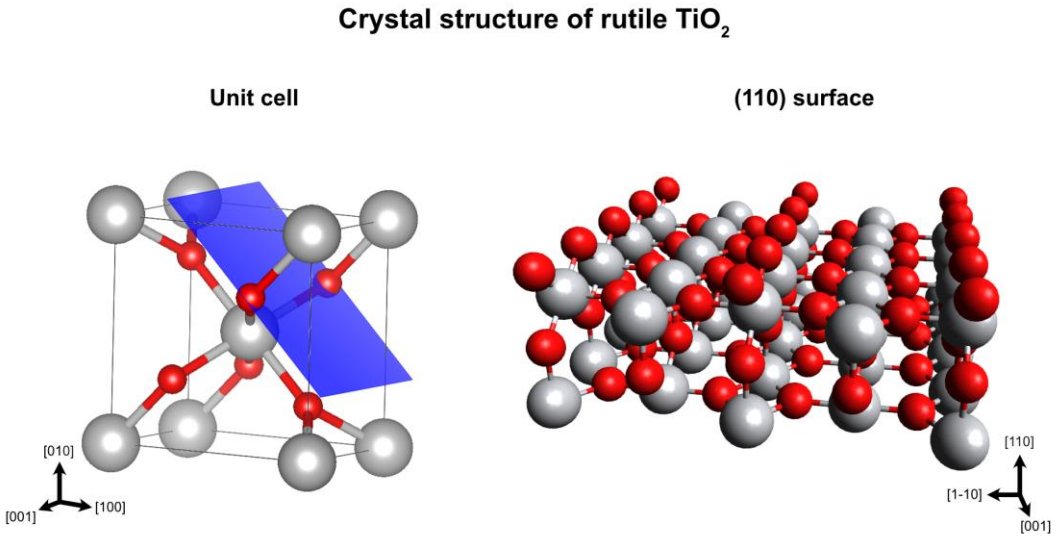

Figure 2: When the unit cell of a rutile TiO_2 crystal (left) is cut along the (110) plane (blue plane), the rutile TiO_2(110) single crystal surface is obtained (right). This surface consists of oxygen rows and five-fold coordinated titanium sites located in the depressions between the rows.

not only band alignment of the surface with the molecular levels, but also the tilt angle of the adsorbed molecule, which can critically influence device performance.[19]

Going back to rutile TiO_2(110), this surface has a very special surface structure with oxygen rows along the [001] direction, see Figure 2. Between the oxygen rows are in-plane titanium and oxygen atoms. While the in-plane oxygen atoms are threefold coordinated (as in the bulk), the in-plane titanium atoms are only five- instead of sixfold coordinated and are therefore also referred to as

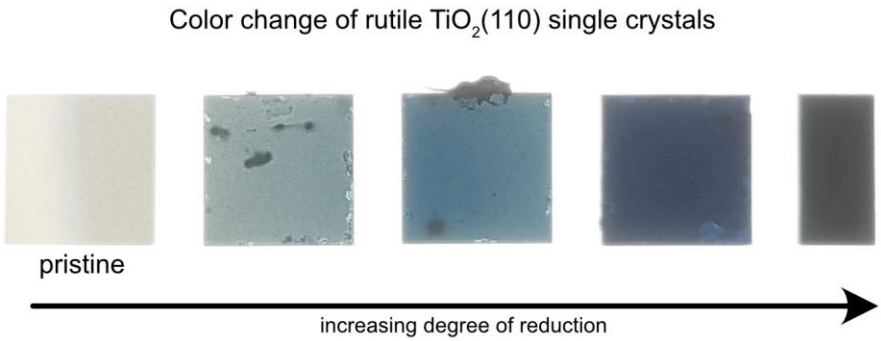

Figure 3: Rutile TiO_2(110) single crystals with different degrees of reduction. The color of the crystals changes from colorless over blue to black. The dark spots are contaminations on the backside of the crystal from the contact with the tantalum boat the crystals have been mounted in.

Ti 5c-sites. The adsorption of oxygen-containing acids is dictated by this surface structure: The Ti 5c-sites can bind to the oxygen of organic acids (such as carboxylic acids), while the proton of the acid can be transferred to the neighboring oxygen row. Additionally, steric limitations imposed by the oxygen rows strongly influence the molecular arrangement on the surface, forcing simple carboxylic acids to bind with both its oxygen atoms parallel to the oxygen rows.[20] This steric limitation can also critically influence the anchor group, as for the phosphonic acid anchor ($R\text{-}PO_3H_2$) only two of the oxygen atoms can bind to Ti 5c-sites, resulting in a bidentate adsorption mode on the intact rutile TiO_2(110) surface.[21-23][P2] As will be shown later in Chapter 5.4.1, a tridentate adsorption mode can be a stable configuration for phenylphosphonic acid on rutile TiO_2(110), but only in the presence of oxygen row vacancies. In fact, oxygen vacancies are a common defect of the rutile TiO_2(110) surface and for sputter-annealed samples the defect density is about 10% of the oxygen row atoms,[24, 25] but also higher values of 15% have been reported.[26]

Removing oxygen atoms from the surface results in a reduction of the oxide. This eventually reduces the bulk of the rutile TiO_2(110) crystal, and slowly changes its color from colorless to blue to black, see Figure 3. Under UHV conditions, the degree of reduction depends on annealing temperature and time. The bulk structure of reduced TiO_2 crystals is quite complex, including Ti^{3+} and Ti^{4+} interstitials and planar defects such as crystallographic shear planes. A more detailed description of this surface, including defects, can be found in the seminal review by Diebold.[25]

The reduction of the rutile TiO_2(110) surface also leads to the formation of small polarons, which are localized charge carriers that induce local lattice distortions. Their mobility is coupled to lattice vibrations and therefore shows a temperature dependence.[27] Polarons also directly affect the adsorption of small molecules such as CO,[28] O_2[24] or H_2O,[29] but vice versa, molecules can also influence the stability of polarons in the near-surface regions.[30] Therefore, it is not surprising that in many studies enhanced photocatalytic activity correlates with the presence of Ti^{3+}-ions, but the details of the underlying mechanism are still under investigation (see Ref. [31] and references therein).

The fact that the reduction of a rutile TiO_2(110) crystal is very easy makes this crystal a convenient substrate for experiments, as it makes the system conductive enough for a variety of experimental techniques.

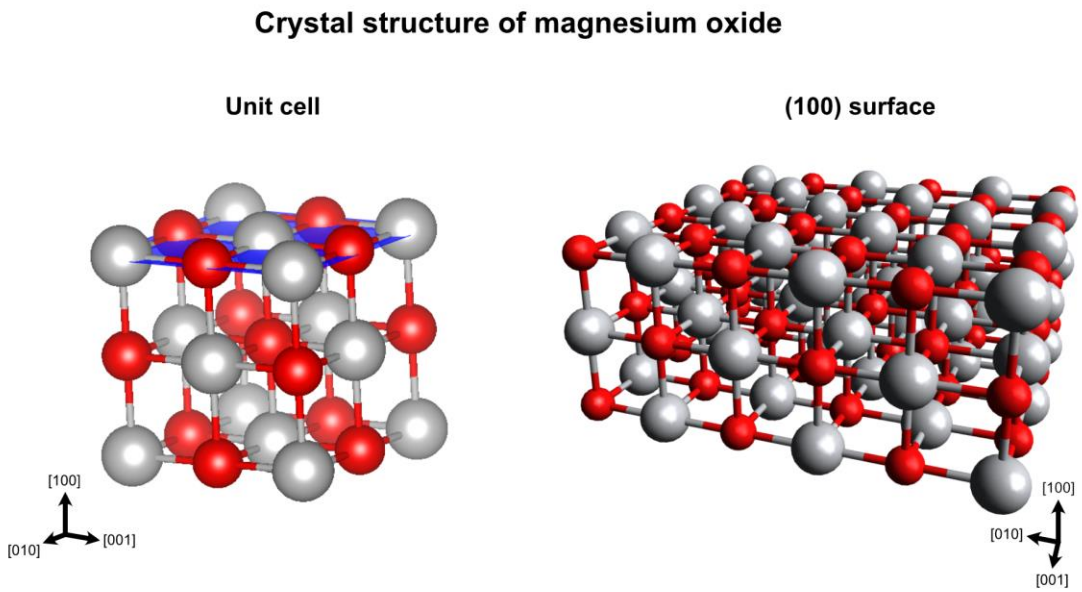

Figure 4: When the unit cell of a MgO crystal (left) is cut along the (100) plane (blue plane), the MgO(100) single crystal surface is obtained (right). This surface is very different to the already discussed rutile TiO_2(110) surface in Figure 3, as it is a flat surface with a checkerboard pattern of magnesium and oxygen anions.

In addition to the rutile TiO_2(110) surface, some experimental data was measured on the MgO(100) surface. The MgO(100) surface, see Figure 4, differs from the rutile TiO_2(110) surface in that it is a flat surface with a checkerboard pattern of oxygen anions and magnesium cations. Magnesium oxide single crystals can be used in UHV studies, but due to the low conductivity of the oxide, charging is a problem for some experimental techniques. While this is not a problem for atomic force microscopy,[32, 33] it is a problem for techniques relying on electrons, such as X-ray photoelectron spectroscopy.

Photoelectron studies of MgO single crystals are still possible,[34] but they require a special experimental setup to neutralize the charge during the measurement. I worked briefly with a PHI Quantera II XPS machine from Prof. Karl Mayrhofer's group, and this machine has a dual beam charge neutralization setup, making it suitable for measurements on insulating samples. However, this chamber does not have the necessary facilities for sample preparation like controlled evaporation and gas exposure, making it unsuitable for most of the experiments in this thesis. Unfortunately, not every UHV chamber is equipped with such a charge neutralization setup, and to make the MgO(100) surface accessible to such machines, the oxide layer can be grown as a thin

film on a conductive metal substrate.[35-39] This enables techniques such as scanning tunneling microscopy or X-ray photoelectron spectroscopy to be used on this surface.

When growing an oxide as a thin film, the substrate is of utmost importance because it acts as a template for the oxide to grow on. In this thesis, a silver (100) crystal was used to grow the MgO(100) thin film because the lattice mismatch of these two systems is less than 3% (408 pm for Ag,[40] 419 pm for MgO[41]), making silver a good template for growing MgO. However, silver is not the only possible substrate and other metals, for instance gold, chromium or molybdenum, can also be used.[39]

When the oxide film is grown as a thin film on a metal substrate, the metal can affect the reactivity of the oxide film on top. For a 2 monolayers thick MgO(100) thin film on Ag(100), NO_2 is oxidized only at high exposures to NO_3, but this reaction starts already at low exposures when the MgO film thickness exceeds 5 ML.[42] Therefore, it is very important to use a sufficiently thick oxide thin film on a metal substrate to prevent the interaction of the underlying metal with the adsorbents from affecting the experimental results.

2.3. Temperature measurements on oxide crystals

While it is easy to measure the temperature of a resistively-heated metal single crystal, it is much more difficult to obtain an accurate temperature reading for an oxide crystal. This is because it is not possible to spot-weld wires directly onto the poorly conducting crystal. This causes two problems: First, it is not possible to attach the resistively-heated wires directly to the crystal, and second, it is not possible to attach the thermocouple directly to the crystal.

By placing the crystal in a tantalum boat, see Scheme 1, the system can be resistively heated by tantalum wires spot-welded to the boat. It is also common to spot-weld the thermocouple to the supporting tantalum boat, but due to the poor thermal contact between the boat and the crystal, their temperatures can differ by hundreds of Kelvin from each other, see below.

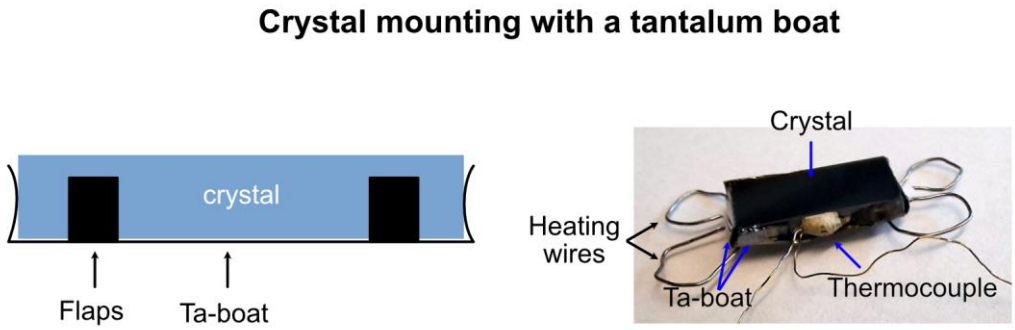

Scheme 1: Mounting a crystal in a tantalum boat allows the heating wires to be spot welded to the boat, which is in thermal contact with the crystal. The crystal is held in place by metal strips that press against the crystal on three sides, while only two flaps press against the crystal on the fourth side. This is necessary because the thermocouple is glued to the crystal in the gap between the flaps. The right side shows a mounted crystal with the two heating wires and the thermocouple glued to the side. The crystal appears to be black because the boat blocks all light passing through the backside of the crystal.

An accurate temperature reading can be obtained by gluing the thermocouple to the side of the crystal. In the beginning of this thesis, Ceramabond 571 ceramic glue (Kager GmbH) was used, but later on we noticed that Ceramabond 552 (Kager GmbH) is less prone to detachment from the crystal over time, which is due to a better match in the thermal expansion coefficients between the crystal and the glue, see Table 1.

Matching the thermal expansion coefficient of single-crystalline rutile TiO_2 is not trivial because this crystal has two different thermal expansion coefficients along the unit cell vectors of the crystal lattice. Considering the orientation of the crystal there are, from the perspective of the bulk,

Table 1: Thermal expansion coefficients of the two ceramic glues used to attach the thermocouple to the crystal and the thermal expansion coefficient of a rutile TiO_2(110) single crystal.

	Thermal expansion coefficient (10^{-6} K^{-1})
Ceramabond 552[43]	7.7
Ceramabond 571[22]	12.6
Rutile TiO_2 single crystal at 300 K[44]	7.1 (along [100] and [010] direction) 9.2 (along [001] direction)

two different planes to attach the thermocouple, see Scheme 2: The (1-10) and (001) plane. While the thermal expansion coefficient in the (001) plane is isotropic with 7.1×10^{-6} K^{-1}, the thermal expansion coefficient in the (1-10) plane is anisotropic, varying from 7.1×10^{-6} K^{-1} in the [110] direction to 9.2×10^{-6} K^{-1} in the [001] direction. The new glue has a thermal expansion coefficient of 7.7×10^{-6} K^{-1}, which falls between these two values, while the older glue, with a value of 12.6×10^{-6} K^{-1}, had a thermal expansion coefficient always larger than that of the crystal, explaining the better performance of Ceramabond 552.

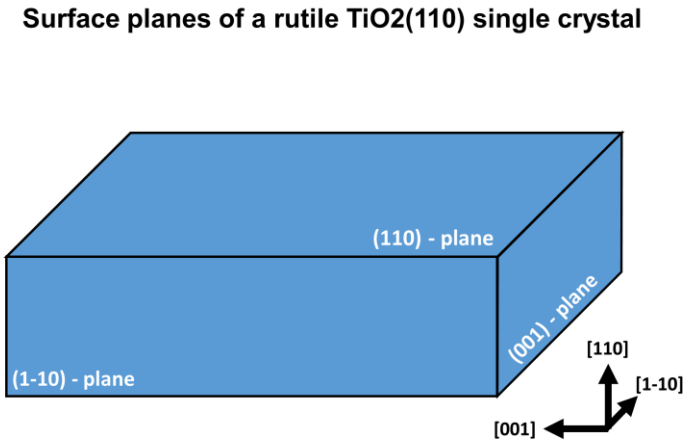

Scheme 2: Illustration of the different surface planes of a rutile TiO_2(110) single crystal. The planes indicate only the orientation of the crystal faces relative to the bulk orientation and do not necessarily indicate the facet present on the surface. For example, the (001) plane of rutile TiO_2(110) has a comparatively high surface energy[45, 46]and thus it will reconstruct.

In principle, it would be advantageous to always mount the thermocouple on the (001) facet, since the isotropic thermal expansion should result in a longer thermocouple life. However, with the current glue, the thermocouple lifetime on any side was found to be larger than the lifetime of a rutile TiO_2(110) crystal (due to reduction). Therefore, it is not worth the effort to characterize the crystal orientation prior to gluing.

During my Ph.D., we built a new sample holder that supported two thermocouples on the sample. This enabled us to measure the temperature of a thermocouple spot-welded to a tantalum boat and a thermocouple glued to the side of the crystal simultaneously, see Figure 5. The differences between the two temperature curves can be well explained by the poor thermal contact between the tantalum boat and the crystal, which causes a significant thermal lag between the two systems. As a result, the boat temperature is always about 300 – 350 K higher than the crystal temperature while heating.

There are ways to improve the thermal contact between the crystal and the tantalum boat, such as gluing the crystal directly to the tantalum.[47] However, a test with Ceramabond 571 resulted in a shattered crystal, presumably due to differences in the thermal expansion coefficients of the crystal, the glue, and the tantalum boat. With the new adhesive, Ceramabond 552, it may be possible to glue the crystal directly, but it was not necessary to investigate this further during my thesis.

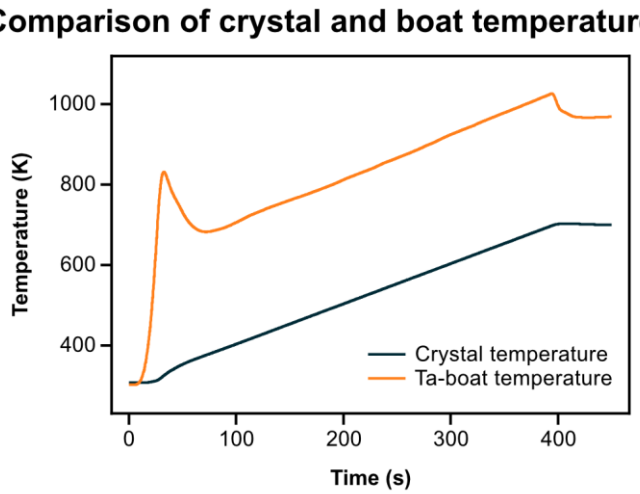

Figure 5: Simultaneous temperature measurement of a thermocouple glued to the side of a rutile TiO_2(110) crystal (crystal temperature) and the corresponding boat. The crystal is heated in UHV with a heating rate of 1 K/s from 300 to 600 K.

Figure 5 clearly shows that the temperature of the tantalum boat is significantly higher than the temperature of the crystal. Unfortunately, due to experimental limitations, we have already published data where only the tantalum boat temperature was measured[48] and the crystal temperature was estimated with the temperature of the boat based on a linear relationship. Now we were able to check this assumption by stepwise increasing the heater power while monitoring the temperature of the rutile TiO_2(110) crystal and the tantalum boat. At each heater power level, the system equilibrium temperature of the boat and crystal are measured, and the results are shown in Figure 6. Indeed, there is an almost linear relationship between boat and crystal temperatures, so it is very reasonable to use a linear correction scheme to determine the crystal temperature from the tantalum boat temperature.

Although this linear relationship can be used to calculate the temperature of the crystal from the temperature of the boat with good accuracy, the parameters of this curve are not universal because the thermal contact between the boat and the crystal differs for each boat-crystal combination.

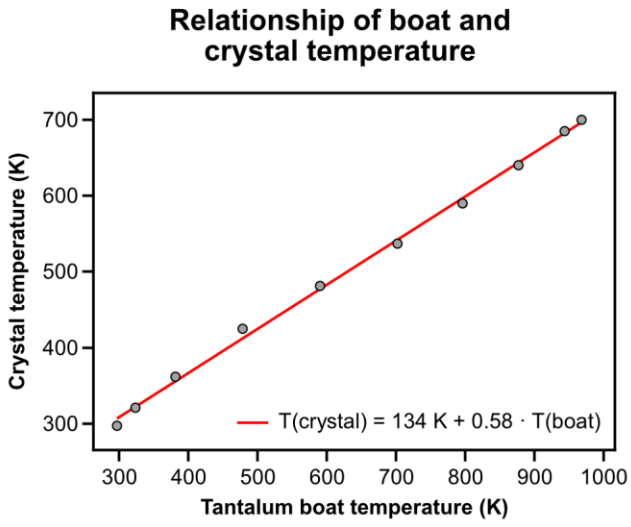

Figure 6: Plotting the temperature of the tantalum boat and the crystal (measured with a thermocouple glued to the side of the crystal) after allowing both temperatures to equilibrate shows an almost linear relationship.

3. Experimental Methods

In this thesis, mainly X-ray photoelectron spectroscopy (XPS), near-edge X-ray absorption fine structure spectroscopy (NEXAFS), and temperature-programmed desorption (TPD) were used to obtain information about organic molecules at oxide interfaces. These techniques are briefly introduced below.

3.1. X-ray photoelectron spectroscopy

When studying the adsorption of molecules on a surface, a major challenge is surface sensitivity: Based on the crystal structure,[41] a MgO cube of 1 cm^3 volume contains about 1×10^{23} atoms, while the 1 cm^2 MgO(100) face consists of only 2×10^{15} atoms, eight orders of magnitude less. It is therefore critical to have a measurement technique that is very sensitive to the atoms in the top layers, otherwise the atoms in the bulk will completely dominate.

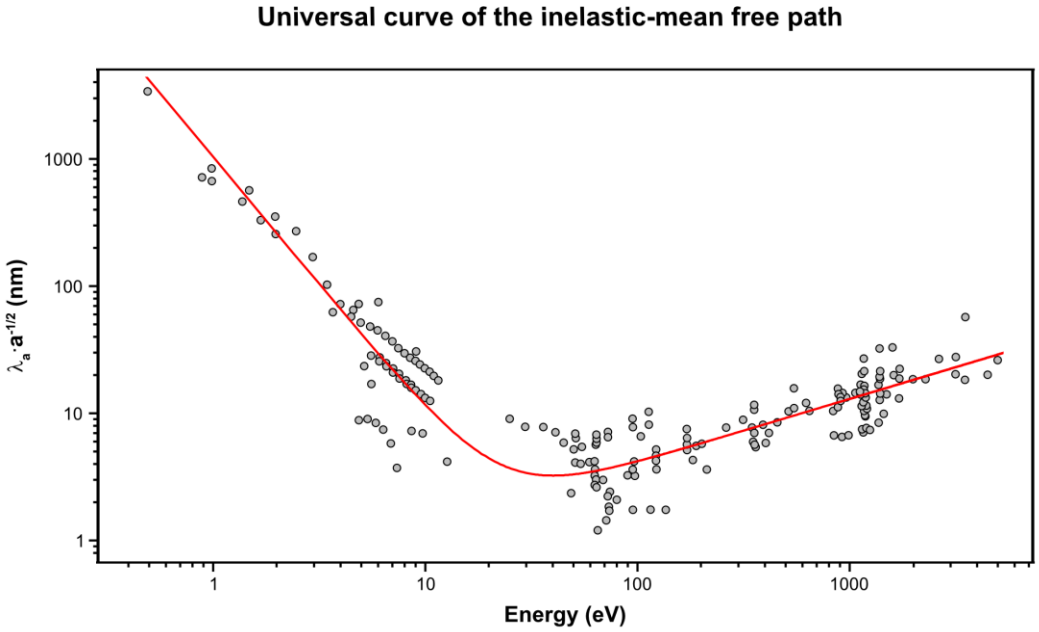

Figure 7: Universal curve for the inelastic mean free path (IMFP) obtained by Seah and Dench. The IMFP has a minimum at around 50 eV, but it increases both for smaller and larger kinetic energies. Adapted with permission from Ref. [49].

X-ray photoelectron spectroscopy (XPS) is a well-suited tool for surface characterization because it uses electrons to probe the surface. Electrons are subject to inelastic collisions as they travel through a solid, and the average distance an electron travels between inelastic collisions is called the inelastic mean-free path (IMFP). In general, the IMFP of an electron depends on its kinetic energy and the changes can be nicely illustrated with the so-called universal curve according to Seah and Dench[49] in Figure 7. The inelastic mean-free path has a minimum at about 50 eV and for both larger and smaller kinetic energies, the mean-free path increases significantly. In this thesis, kinetic energies between 40 and 1000 eV are used and thus according to Figure 7, the measured photoelectrons only provide information about the topmost few nanometers of the sample.

3.1.1. General concept

In X-ray photoelectron spectroscopy, a sample is illuminated with X-rays and the number of electrons released is measured as a function of their kinetic energy. A typical wide-range spectrum of a clean rutile TiO_2(110) surface is shown in Figure 8. This spectrum shows several peaks, and these peaks are characteristic of a sample containing titanium and oxygen atoms. The two peaks that stand out due to their larger width are assigned to Ti LMM and O KLL Auger peaks. They originate from Auger decays, while the other peaks originate from X-ray induced core-level excitations.

The signals from the different elements in the sample are clearly separated, and this elemental sensitivity arises from the photoelectric effect. This effect was discovered by Hertz in 1887[50] and explained by Einstein theoretically in 1905,[51] which earned him the Nobel Prize in 1921. While Hertz discovered this effect, other experimentalists such as William Hallwachs contributed significantly to our understanding.

The photoelectric effect gives a relationship between the energy of the incoming photon and the kinetic energy of the released photoelectron: If an electron absorbs a photon with an energy larger than its binding energy, the electron is emitted from the atom and the surplus of photon energy is converted into kinetic energy of the electron. Thus, the kinetic energy of an electron gives direct information about its binding energy. To calculate the binding energy E_B of a photoelectron one

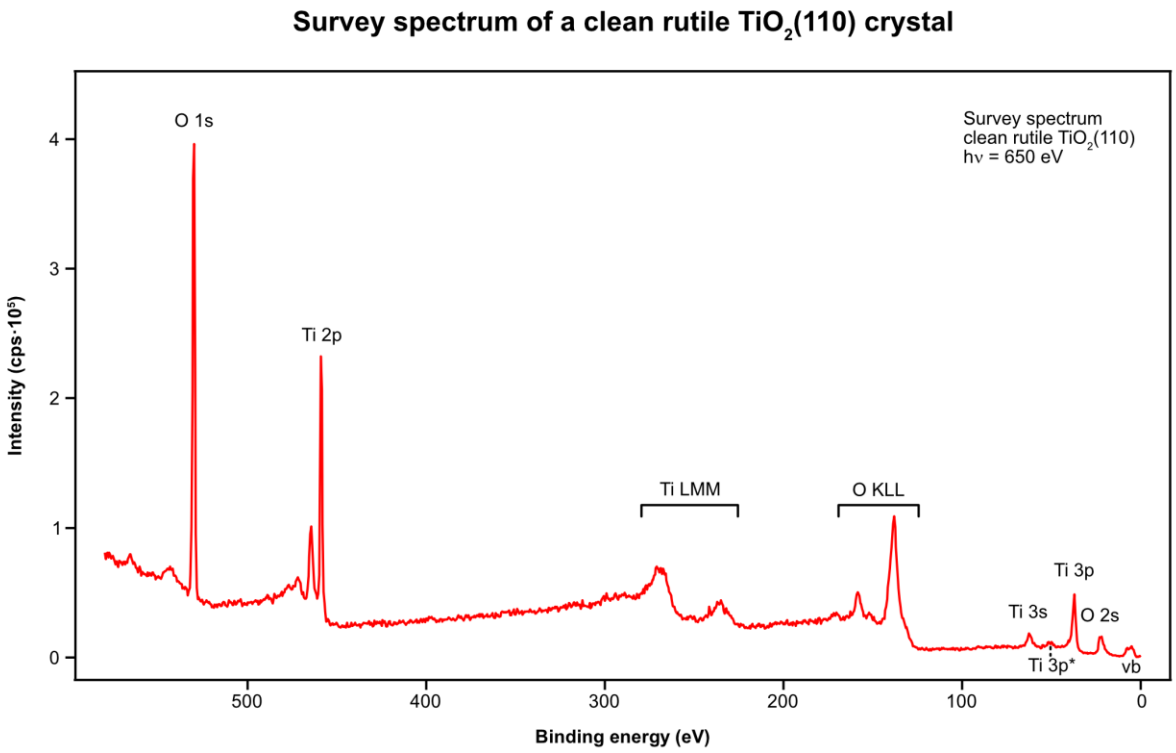

Figure 8: XPS survey spectrum of a clean rutile TiO_2(110) crystal containing sharp XPS peaks that can be assigned to their respective core levels based on their binding energies. There are also two Auger regions (Ti LMM and O KLL) with significantly broader peaks, which can be attributed to Auger decays. The increased background after each peak is the result of inelastically scattered electrons.

thus needs to know the energy of the incident photon hν, the kinetic energy E_{kin} of the corresponding photoelectron, and the work function of the electron analyzer $\phi_{analyzer}$.

$$E_B = h\nu - E_{kin} - \phi_{analyzer}$$

The work function of the analyzer is different for every UHV chamber and must be calibrated by measuring XPS on a reference sample, e.g. a gold sample, and aligning the binding energy axis with literature values.

It is theoretically possible to measure and identify every element in the periodic table using XPS. Unfortunately, this is almost impossible for hydrogen: Hydrogen possesses only one electron and thus it has no core electrons. As a result, the binding energy of its only valence electron varies significantly depending on the bonding partner, rendering it useless in elemental identification.

A closer look at any peak Figure 8 shows that the background after the peak towards larger binding energies is always higher than before the peak. While some photoelectrons from the few top layers are able to escape the surface without any inelastic collisions, more photoelectrons, especially from deeper layers, are subject to inelastic collisions as they try to escape from the material. This energy loss of an electron by inelastic scattering depends strongly on the material it travels through, and therefore the background contains information about the structure of the surface layers. Tougaard introduced an approach to extract information from the background more than 20 years ago,[52] and he recently published a practical guide to the use of backgrounds in quantitative XPS that illustrates his approach very well.[53] With such a background analysis one can gain information about the depth profile of a sample, such as the depth distribution of gold on nickel.[54]

In this thesis, molecules were deposited on an inorganic substrate, and although a detailed analysis of the background could be used to resolve the depth profile of carbon, such an analysis is unnecessarily complicated because the molecules always form a layer on top of the inorganic substrate. Therefore, it is much easier to calculate the thickness d of a smooth carbon overlayer by describing the attenuation of the substrate signal with a simple exponential function:

$$I^{sub} = I_0^{sub} \cdot \exp\left(-\frac{d}{\lambda^{sub}}\right)$$

where I_0^{sub} is the intensity of the unattenuated surface and λ^{sub} is the inelastic mean-free path of the substrate electrons through the overlayer. In principle, this equation is sufficient to determine the coverage, but this equation assumes that I_0^{sub} is known. While its value can be determined by measuring the clean surface intensity, this intensity depends on the beam intensity and sample position, both of which can vary from measurement to measurement. Much more reliable results can be obtained by including the overlayer intensity:

$$I^{over} = I_0^{over} \cdot \left(1 - \exp\left(-\frac{d}{\lambda^{over}}\right)\right)$$

The substrate and overlayer equations can be combined, and assuming that the inelastic mean-free paths for the substrate and overlayer electrons are identical, which is approximately fulfilled if the measured photoelectrons have similar kinetic energies, the equation simplifies to

$$\frac{I^{over}}{I^{sub}} = \frac{I_0^{over}}{I_0^{sub}} \cdot \left(\exp\left(\frac{d}{\lambda}\right) - 1\right)$$

Rearranging the equation allows for the calculation of the overlayer thickness d:

$$d = \lambda \cdot \ln\left(1 + \frac{I^{over}}{I^{sub}} \cdot \frac{I_0^{sub}}{I_0^{over}}\right)$$

This equation uses intensity ratios, so variations in total intensity do not matter as long as the overlayer and substrate intensities are measured under identical experimental conditions. This equation has been used to calculate the coverage of organic molecules on rutile TiO_2(110).

In my research, I also worked on porphyrin layers on a magnesium oxide thin film on a silver substrate. To calculate the coverage on such a system, it is necessary to extend this approach to three layers, meaning an organic layer (org) on top of a magnesium oxide (MgO) layer on top of a silver substrate (sub):

$$I^{org} = I_0^{org} \cdot \left(1 - \exp\left(-\frac{d^{org}}{\lambda}\right)\right)$$

$$I^{MgO} = I_0^{MgO} \cdot \left(1 - \exp\left(-\frac{d^{MgO}}{\lambda}\right)\right) \cdot \exp\left(-\frac{d^{org}}{\lambda}\right)$$

$$I^{sub} = I_0^{sub} \cdot \exp\left(-\frac{d^{MgO} + d^{org}}{\lambda}\right)$$

In these equations, it is assumed that the inelastic mean free path of the photoelectrons of all three core levels through the two overlayers is identical. Although the inelastic mean-free path varies with the material, this is a reasonable assumption as long as the kinetic energies of the photoelectrons are reasonably similar.

3.1.2. Chemical shift

The elemental sensitivity of XPS comes from measuring core electrons, which do not participate in the chemical bonds. While a change in electron density around an atom changes the binding energies of the core electrons slightly, the effect is not always significant enough to disentangle chemically different atoms. This is illustrated in Figure 9, where the C 1s core level of a monolayer

of 4-acetylphenylboronic acid on a rutile TiO_2(110) surface after deposition at 300 K shows a carbonyl signal at 287.4 eV that is clearly separated from the main carbon signal at 284.5 eV from the phenyl ring and the methyl group. While it is very simple to identify the clearly-separated signal of the carbonyl group, it is much harder to determine the binding-energy position of the methyl group. It could be on the high-binding energy side of the main carbon signal, but this could also be the carbon atom neighboring the boronic acid group. It may be possible to deconvolute the signal into its individual species, but in some cases there is significant uncertainty in the exact peak positions, as multiple deconvolutions may describe the observed signal similarly well.

This is the case for the C 1s signal of 4-acetylphenylboronic acid on rutile TiO_2(110) after annealing to 600 K in Figure 9. A reaction eliminating the carbonyl signal takes place, but there are two possible reaction products, tolylboronic acid and phenylboronic acid. The chemical sensitivity of XPS is not sufficient to separate the methyl signal from the phenyl ring signal and other techniques, such as infrared spectroscopy or mass spectrometry, are much better suited to determine which product has formed.

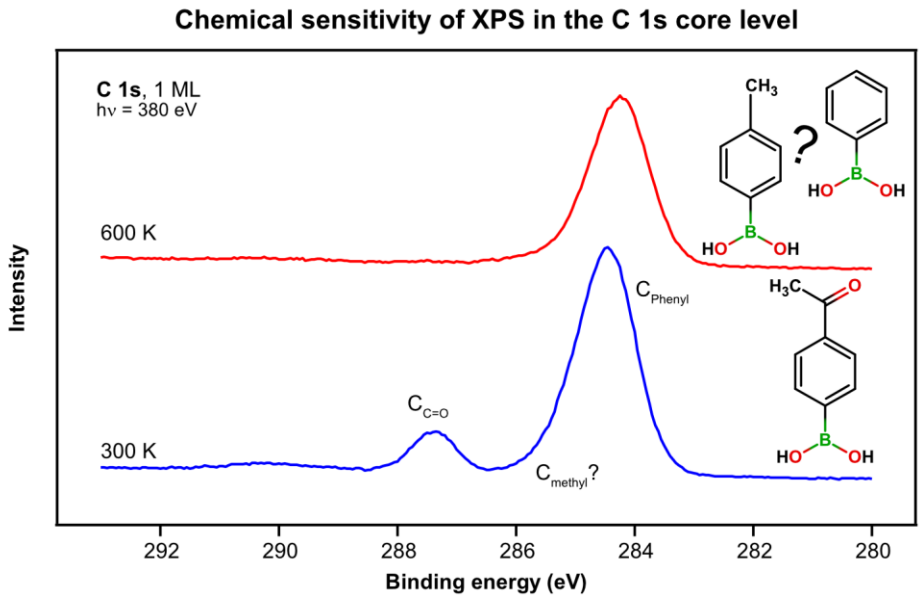

Figure 9: After deposition of 1 ML of 4-acetylphenylboronic acid on rutile TiO_2(110), the signal from the phenyl ring at 284.5 eV and the carbonyl carbon at 287.4 eV can be clearly distinguished. It is difficult to assign the position of the methyl carbon, but this signal is most likely in the high binding-energy shoulder of the phenyl ring signal. After annealing at 600 K for 1 min, we can clearly see the loss of the carbonyl carbon, indicating that an on-surface reaction has taken place. Two possible reaction products are shown (top right), but based on this core-level data alone, we cannot make a definitive assignment.

Although sometimes limited, chemical shifts are a very powerful tool to gain information about the investigated species. However, it is always important to keep in mind that chemical shifts are not the only cause for changes in peak shape or position. Effects such as spin-orbit splitting, shake-up and shake-off processes, and vibrational fine structures can also affect the spectrum. A discussion of the fundamentals of these initial and final state effects is beyond the scope of this thesis, and the interested reader can find additional information elsewhere.[55-58]

3.2. Mass spectrometry and temperature-programmed desorption

XPS can only identify products of on-surface reactions if they remain on the surface. With a mass spectrometer, however, it is possible to follow on-surface reactions by tracking desorbing fragments from a surface as a function of temperature. The chemical sensitivity of a mass spectrometer results from two factors: First, the mass of a desorbing fragment, and second, the fragmentation pattern. This is illustrated in Figure 10, where 2,4,6-triphenylboroxine was desorbed directly into a mass spectrometer. As expected, there are multiple peaks clustered around a mass of 312 amu, corresponding to the isotope pattern of the intact molecule. Measured with a better

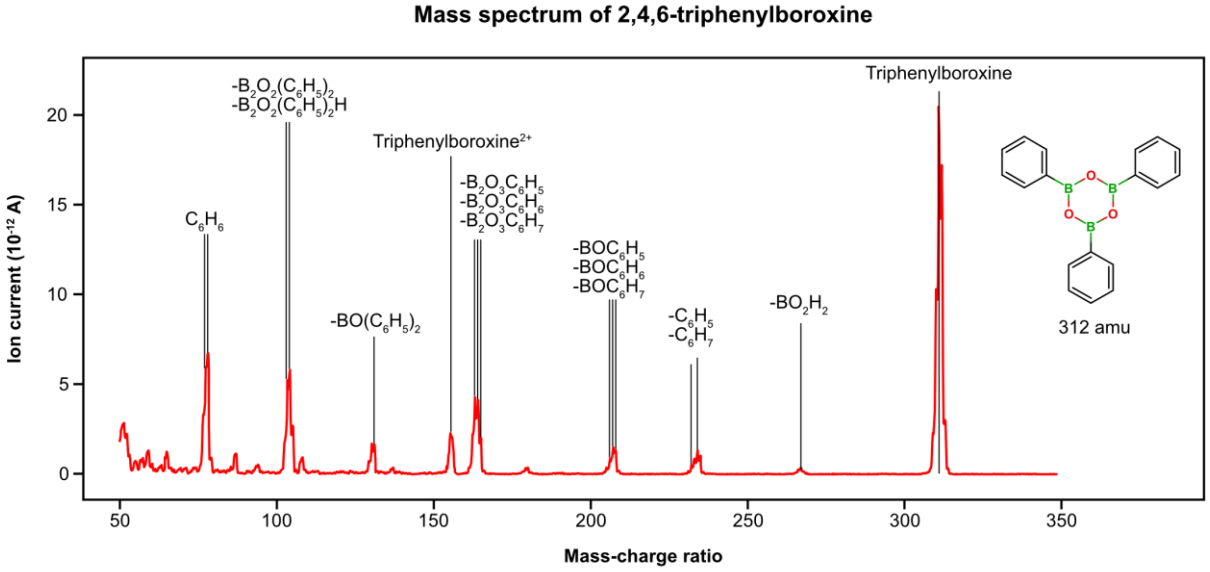

Figure 10: Mass spectrum of 2,4,6-triphenylboroxine. The intense signal from the intact molecule at 312 amu is accompanied by many other peaks of lower masses that can be attributed to cracking of the intact molecule after ionization. Each peak shows a splitting due to the statistical distribution of boron and carbon isotopes. Adapted from Ref. [P3].

resolution, where the individual peaks can be easily separated, the observed peak ratios match the pattern expected for a statistical distribution of ^{10}B:^{11}B of 20:80 and ^{12}C:^{13}C of 1:99. In addition to the molecular peaks at 312 amu, there are many peaks with lower masses due to the fragmentation of the original molecule into smaller fragments after ionization. Fragmentation depends on the structure of the parent fragment, making the fragmentation pattern unique to each molecule.

When monitoring on-surface reactions with temperature-programmed desorption (TPD), it is rare to measure a full mass spectrum; instead, it is much faster to track the intensity of selected mass-charge ratios as a function of temperature. Our group has used this before to follow on-surface reactions, such as different hydrogen evolution reactions of tetraphenylporphyrins on Cu(111), metalation of phthalocyanine at a metal-organic interface,[59] decomposition reactions of phthalic acid on Ag(100)[60] or layer-exchange reactions of different metallotetraphenylporphyrins on the rutile TiO_2(110) surface.[61]

3.2.1. Mass spectrometry for chemical identification

Thus, TPD would be the perfect tool to study the decomposition reaction of 4-acetylphenylboronic acid to either tolylboronic acid or phenylboronic acid, which we could not resolve with XPS, by following the desorption of carbon monoxide (tolylboronic acid) and acetaldehyde (phenylboronic acid). Unfortunately, there was not enough time to perform these experiments to answer this question.

Nevertheless, the chemical information obtained with a mass spectrometer was crucial for this thesis. This was especially true when validating the deposition of intact molecules from a Knudsen effusion cell, as organic molecules can decompose under evaporation conditions. For phenylphosphonic acid, we found that the saturation coverage of phenylphosphonic acid on rutile TiO_2(110) was lower compared to a previous published dataset.[48] In fact, this increased coverage was only observed for a single surface preparation, and we suspected that a decomposition reaction of the molecule in the evaporator might be responsible for the observed difference.

In Figure 11, the desorption spectra of about three monolayers of phenylphosphonic acid deposited using different evaporation temperatures are shown, while the intensity at the mass of the intact molecule (solid line, 158 amu) and a cyclic anhydride (dotted line, 420 amu) was followed. We

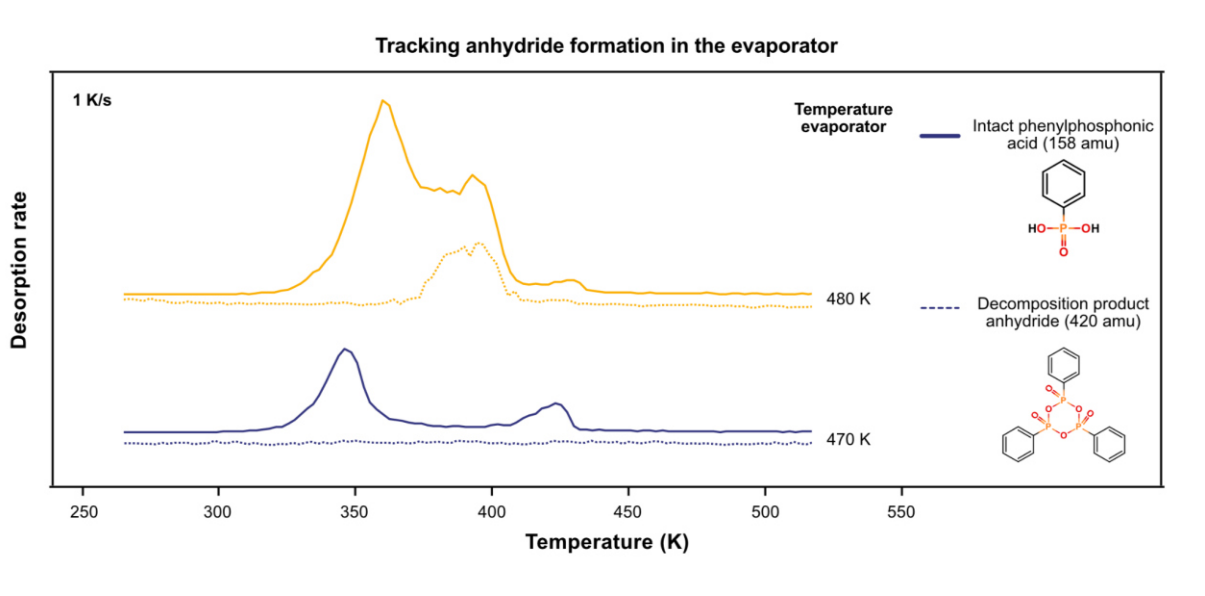

Figure 11: To test for anhydride formation during evaporation of phenylphosphonic acid, we measured temperature-programmed desorption spectra of several roughly 3 ML thick phenylphosphonic acid films from a rutile TiO_2(110) surface passivated by previous desorption experiments of phenylphosphonic acid. The data show a clear deposition of anhydrides for evaporator temperatures above 480 K.

observe no anhydride formation for evaporator temperatures below 470 K, but higher temperatures lead to a decomposition of phenylphosphonic acid into the anhydride. This suggests that the observed differences in coverage with an earlier data set are not due to the evaporation temperature, since the phenylphosphonic acid layers were prepared with evaporator temperatures of 400 K.

The same anhydride formation can take place for phenylboronic acids. In fact, these molecules are much more prone to anhydride formation, and it was crucial to validate that these molecules evaporated intact. This will be discussed in more detail in Chapter 5.3.

3.2.2. TPD to extract kinetic and thermodynamic parameters

Temperature-programmed desorption (TPD) can provide information beyond identifying the chemical species desorbing because it can be used to extract the kinetic and thermodynamic parameters of the desorption reaction. The extraction of these parameters is in principle also possible with XPS. However, the time required to measure TPD and XPS is very different; a desorption experiment can be done within minutes, whereas a temperature-programmed XPS (TP-XPS) experiment with our home setup would take days, if not weeks. TP-XPS has also advantages,

as it provides quantitative information about the species remaining on the surface. This information can be very valuable and at this chair it is used in the group of Dr. Maier to follow the reactions of ionic liquids,[62] or by Prof. Dr. Papp (now at the FU Berlin) to follow catalytic reactions at metal interfaces.[63-65] For my investigation of the desorption of metallotetraphenylporphyrins from MgO(100),[P1] however, TPD is clearly the faster technique to determine the adsorption energy of the desorbing molecules.

A desorption process with a desorption rate r can be described mathematically by the Polanyi-Wigner equation:

$$r = \nu \cdot \exp\left(-\frac{E}{RT}\right) \cdot \theta^n$$

with the prefactor for desorption ν, the adsorption energy E, the gas constant R, temperature T, surface coverage θ, and reaction order n. It is important to note that the prefactor and desorption energy can change as a function of coverage θ over the course of the desorption reaction.[66] This can make it difficult to accurately describe the complete desorption process. Exploring all the details of TPD is beyond the scope of this thesis and in the following, only the most important topics for this thesis are discussed and the interested reader is referred to Refs. [67-69].

3.2.3. Prefactor for desorption

The prefactor for desorption is often assumed to be 10^{13} s^{-1}. However, this is not generally true. The prefactor for desorption is sometimes also referred to as the attempt frequency, and in this simple picture it is the number of attempts an atom/molecule makes per unit time to overcome the activation energy barrier for desorption. So a prefactor of 10^{13} s^{-1} would fit, since this is the frequency range where molecular vibrations are often found. One would therefore expect the prefactor for desorption to increase slightly with molecular mass, as would be expected for a simple mass-spring system. However, Campbell and coworkers found experimentally that the prefactor for desorption increases by 6 orders of magnitude from 10^{13} s^{-1} for methane up to 10^{19} s^{-1} for n-decane,[70, 71] which exceeds the expected increase in prefactor solely based on changes to the vibrational frequency.

The authors explained the increase in the prefactor based on rotational entropy.[70] While rotational entropy seems unrelated to an attempt frequency, the relationship between entropy and the prefactor for desorption becomes apparent in transition-state theory, where the rate of the desorption reaction is expressed by the Eyring equation as:

$$r^{TST} = \frac{k_B T}{h} \cdot \exp\left(\frac{\Delta S^{\neq}}{R}\right) \cdot \exp\left(-\frac{\Delta H^{\neq}}{RT}\right)$$

where k_B and h are the Boltzmann and Planck constant, respectively, T is the temperature, and $\Delta S^{\neq}$ and $\Delta H^{\neq}$ are the entropy and enthalpy difference between the adsorbed state and the transition state, respectively. The prefactor for desorption is thus:

$$\nu^{TST} = \frac{k_B T}{h} \cdot \exp\left(\frac{\Delta S^{\neq}}{R}\right)$$

Assuming that there is no entropy difference between the adsorbed state and the transition state ($\Delta S^{\neq} = 0$), the prefactor for desorption at 300 K is $10^{12.8}$ s^{-1}, very close to the "standard" value of 10^{13} s^{-1}. However, if there is no activation energy barrier for adsorption, which is the case for many non-dissociative adsorption processes, the transition state for desorption becomes the molecule in the gas phase. Because the molecule in the gas phase has additional rotational degrees of freedom compared to the molecule on the surface, the prefactor for desorption increases. Viewing the prefactor for desorption purely as an attempt frequency therefore misses the influence of entropy on the observed prefactor for desorption. This became very important when analyzing the TPD spectra of tetraphenylporphyrins in Chapter 4, because the rotational entropy of these large organic molecules significantly influences the prefactor.

3.2.4. Compensation effect

There are several approaches to extract thermodynamic parameters from measured TPD spectra. Some approaches are simple, such as the Redhead analysis,[72] which uses only the temperature at maximum desorption rate, while other methods, such as the complete analysis by King,[73] analyze the entire spectral shape of multiple TPD spectra to extract even coverage-dependent effects on energy and prefactor simultaneously.

However, using the full spectral shape to extract kinetic and thermodynamic parameters can be dangerous because of the compensation effect. The compensation effect states that there is a linear relationship between activation energy and the logarithm of the pre-exponential factor.[74, 75] Such an effect can have a physico-chemical origin, but it can also arise from a coverage dependency of the activation energy[75, 76] or even just experimental noise.[74]

This is partially due to the strong correlation of the prefactor for desorption with the desorption energy, where a simultaneous change of both parameters compensates each others's error and leads to very similar desorption traces. This is illustrated in Figure 12 for a multilayer desorption TPD spectrum of Mg(II)-tetraphenylporphyrin on a rutile TiO_2(110) surface. This is a very simple system, where the desorption signal can be described by a simple Arrhenius equation. In the center, the desorption curve is fitted with the Arrhenius equation with both the prefactor and energy as free parameters. In a second step, the prefactor was fixed at a smaller (left) and larger (right) value,

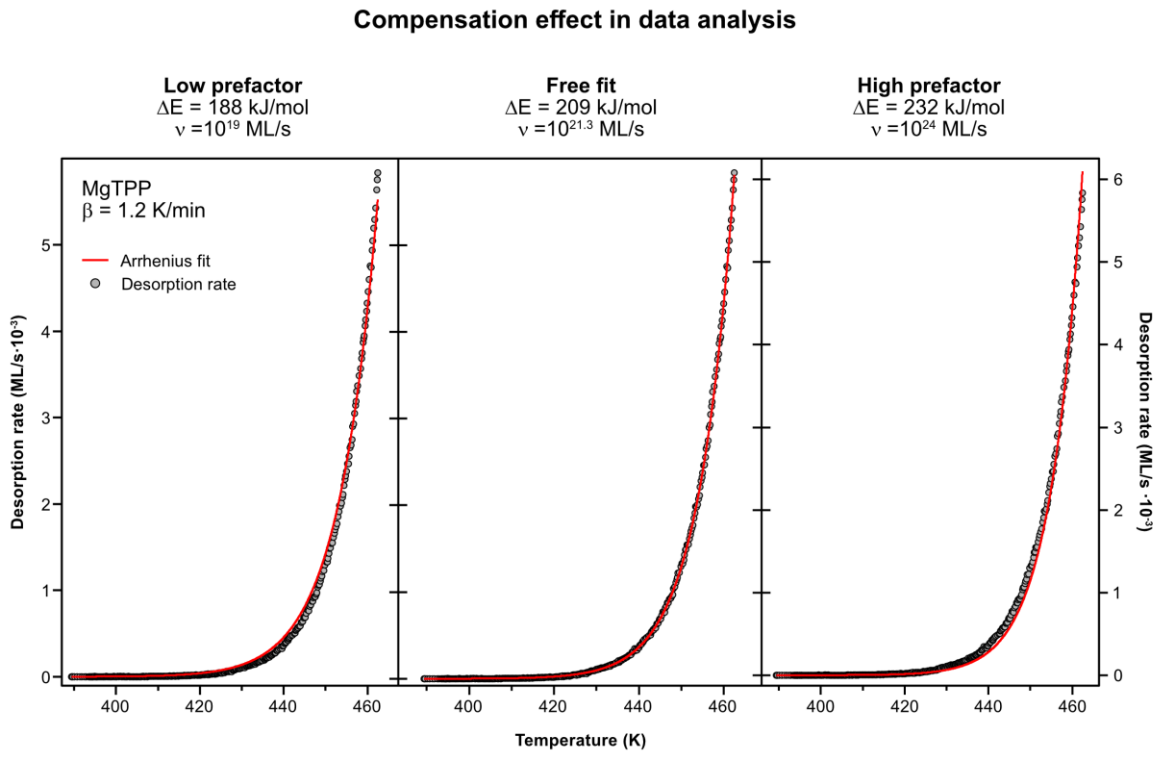

Figure 12: Multilayer desorption spectrum of MgTPP. The data are fitted to the Arrhenius equation in three different ways: With the prefactor and energy as free parameters (middle), and with the prefactor fixed to 10^{19} ML/s (left) and 10^{24} ML/s (right). Although the fit to the data in the middle is the best, the deviation of the other two fits from the data is very small, indicating that the massive changes in the prefactor are corrected by a corresponding increase or decrease in the Arrhenius desorption energy.

respectively, and the resulting fits still match the data reasonably well, because the energy compensated for the change in the prefactor.

Therefore, if an experimental effect even only slightly changes the shape of the TPD spectrum away from the ideal curve, the extracted prefactor and energy may be significantly off. Unfortunately, it is very easy to get a TPD spectrum that does not follow the ideal shape. The problem is that the mass spectrometer will detect any molecule with the correct mass, regardless of its origin. This means that if molecules were to adsorb, for example, on the back of the crystal or on the heating wires, desorption from these surfaces would contribute to the measured signal. Such effects can be minimized by using a sample holder specifically designed for TPD, minimizing desorption from the sample holder through efficient cooling, and using a small opening directly in front of the sample during deposition to adsorb molecules only on the sample, but it is difficult to eliminate such effects completely.

Figure 13 shows the sample holder at our lab, which was designed to be used for TPD measurements. This sample holder is made almost entirely of copper to provide efficient heat transfer away from the sample, minimizing desorption of molecules from the sample holder

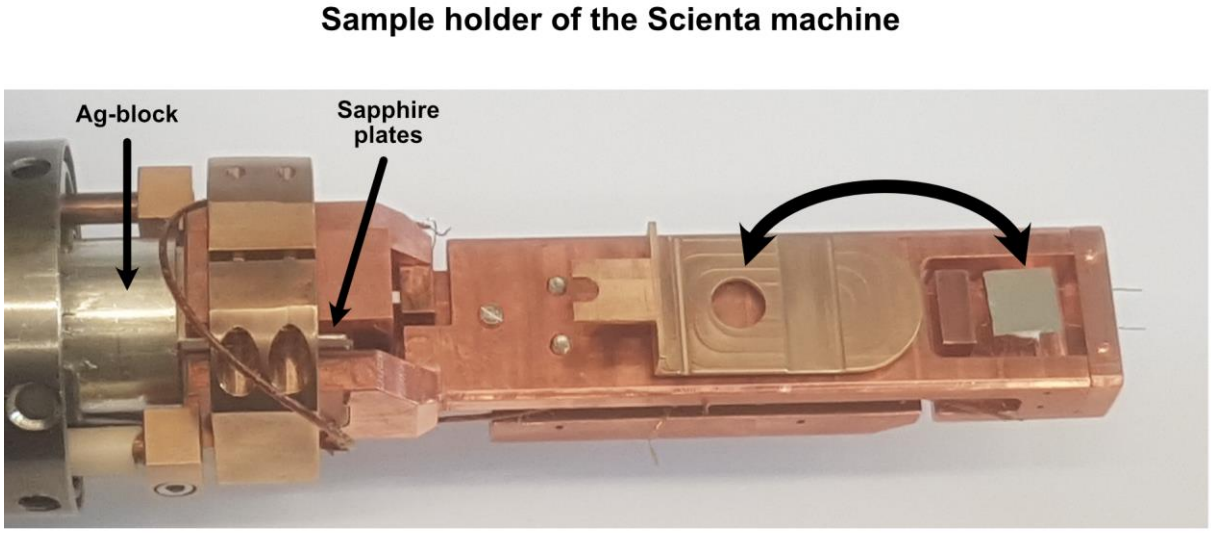

Figure 13: The sample holder used in the Scienta-lab. The colorless crystal in the boat with the thermocouple glued to its side is on the right side. The sample holder, assembled from three individual copper parts, is connected to a liquid nitrogen-cooled silver block on the left side via sapphire plates. This allows for efficient cooling and heat dissipation during a TPD measurement. In addition, the bronze-colored copper-beryllium shutter can be rotated in front of the crystal as indicated by the black arrow. In this configuration, the molecules can only be deposited on the quadratic 1 cm^2 crystal.

surfaces. In addition, this sample holder has a movable opening that can be rotated in front of the crystal prior to deposition to ensure that the molecules are deposited only on the crystal.

Unfortunately, this sample holder was built *after* most of the TPD data was measured. The previous sample holder also had a movable plate with an opening, but the design was otherwise not optimized for TPD. It was therefore impossible to exclude additional desorption from other surfaces during the experiments, and as described above, these very small deviations from the ideal curve can be enough to result in incorrect adsorption energies.

Importantly, this type of compensation effect only plays a role in analysis methods utilizing the full peak shape, like the complete analysis by King.[73] Thus, simpler analysis methods, such as Redhead's method, which rely only on the position of the peak maximum, do not suffer from this problem. For this reason, simple Redhead analysis was used to extract adsorption energies of metallotetraphenylporphyrins desorbing from MgO(100), which will be discussed in more detail in Chapter 4.

3.3. Near-edge X-ray absorption fine structure spectroscopy

The orientation of a molecule at an interface is an important piece of information when trying to understand the interaction of a molecule with a surface. One technique that can determine this orientation is near-edge X-ray absorption fine structure (NEXAFS), also called X-ray absorption near-edge spectroscopy (XANES). In this technique, the X-ray absorption cross section is measured as a function of photon energy by sweeping the photon energy across an absorption edge. A NEXAFS spectrum is shown in Scheme 3; in this spectrum, two different regions are visible: the π*-region (blue) with sharp peaks and the σ*-region (green) with broad peaks.

The different peak shapes and positions originate from the excitation process itself. When increasing the photon energy, the photon energy is initially too low to excite a core electron and no absorption is observed. Just before the absorption edge, the incoming photons provide enough

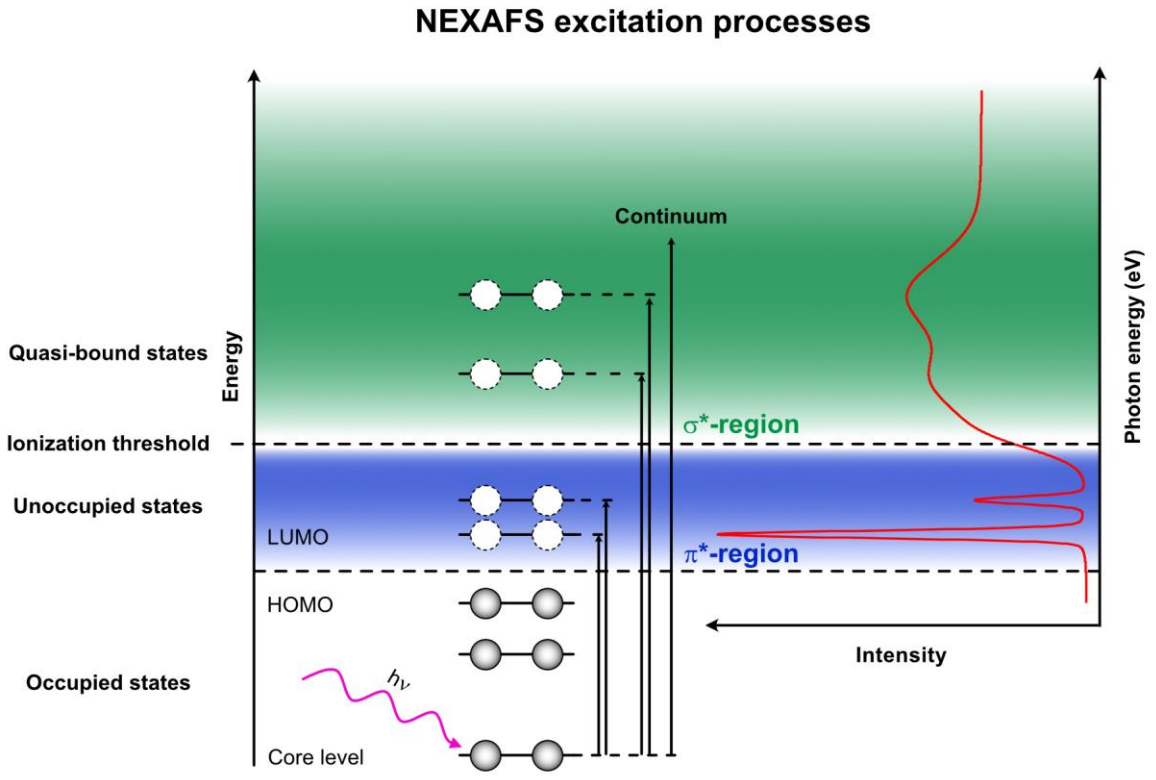

Scheme 3: Schematic representation of the NEXAFS excitation process. With sufficient photon energy, a core level electron can be resonantly excited into an unoccupied orbital below (π-resonances) or above (σ*-resonances) the ionization threshold. This results in sharp or broad signals, respectively. Additionally, core-electrons can be excited directly into the continuum.*

energy to excite a core electron to a bound, unoccupied state, see Scheme 3, but the electron does not gain enough energy to escape the potential well of the atom. This results in sharp peaks just before the edge jump. If the photon energy is further increased to overcome the binding energy of the core electrons, a core electron can be resonantly excited to an unbound σ* state. This excitation results in broad peaks because the lifetime of the σ* state is significantly shorter than that of the π* state, causing lifetime broadening.[77] It is also possible to remove a core electron without a resonant excitation, which is the same physical process as in XPS. This non-resonant absorption of X-rays does not result in a peak, but in an increased background intensity, the so-called edge jump.

The edge jump can be a useful feature in the analysis of NEXAFS spectra, but geometrical information is contained in the π*- and σ*-signals. In addition, the energetics of the unoccupied orbitals are closely related to the energetics of the binding orbitals, making NEXAFS chemically very sensitive. In this thesis, both the geometric and chemical sensitivity of NEXAFS have been used to extract information about small organic molecules at the rutile TiO_2(110) interface. The corresponding details are discussed in Chapter 6.

In NEXAFS, the absorption cross section is measured as a function of photon energy. A common way to do this is to follow the secondary electron signal produced by the X-ray absorption process. In general, there are three approaches to doing this: Total yield, Partial yield, and Auger yield. Total yield measures the current between the sample and ground, i.e. the signal from all emitted electrons. The obtained signal is dominated by slow secondary electrons from deeper layers. This makes total yield a good technique for bulk NEXAFS measurements, but due to the lack of surface sensitivity, the signal from the surface layer is only a small feature on a huge background, making it difficult to analyze the surface signal.

To make the technique more surface sensitive, the signal of the low-energy electrons can be suppressed by applying a retardation voltage to an electron detector placed in front of the sample. This technique is called partial-yield NEXAFS. It provides good signal intensity while being significantly more surface sensitive than total-yield NEXAFS.

To make NEXAFS even more surface sensitive, one can use Auger-yield NEXAFS. In this technique, the Auger signal corresponding to the studied absorption edge is followed using an electron analyzer. The energy of the Auger electrons is well defined because it follows a decay

process shown in Scheme 4. A core hole is created by the absorption of a photon and another electron subsequently fills this hole. The energy difference between the core hole and the second electron is transferred to another electron, allowing that electron to escape with a kinetic energy specific to the energy of the electrons involved. In Auger-yield NEXAFS, only Auger electrons with a certain energy are detected, i.e. if an Auger electron is subject to an inelastic collision, it will not be detected. As a result, the intensity in Auger-yield NEXAFS is lower than in partial-yield NEXAFS, requiring longer measurement times.

This can be a significant problem, as X-ray induced decomposition reactions can alter the sample during the measurement. Beam damage can become a significant problem, especially with the increasing brilliance of synchrotron light sources, and a nice overview of beam damage is given in a recent review by Bras.[78] In this thesis, no evidence of beam damage was found. Nevertheless, the position of the X-ray beam on the sample was changed for each Auger-yield NEXAFS measurement so that a fresh, unirradiated spot is measured at each angle of incidence (or temperature).

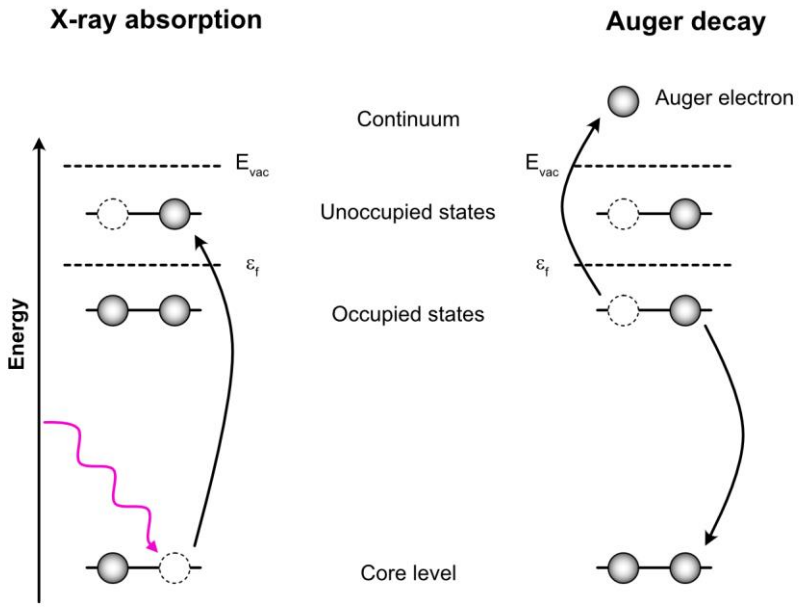

Scheme 4: X-ray absorption process (left) and the subsequent Auger decay process (right) for an electron excited into a π state.*

3.4. Scripting to enable efficient data processing

Over the past few decades, personal computers have become part of our everyday lives, giving scientists easy access to significant amounts of computing power. This enabled researchers to perform more complex experiments, generate more data, and analyze it with more computationally demanding algorithms. This enables scientists to track particle collisions at the Large Hadron Collider (LHC) at CERN, where approximately one petabyte (10^6 gigabytes) of data is generated every second.[79] That example is an extreme case, and in my research I had to deal with much smaller datasets; nevertheless, computers played an integral role in this thesis in measuring and analyzing data. Nowadays computers are really powerful and with all this computing power available, there is only one problem: How to tell the computer what to do with the data? For many problems there is prewritten software, for example *CasaXPS* as a processing software for XPS spectra (available under http://www.casaxps.com/). However, when very specific problems arise or new analysis methods need to be developed or tested, it is necessary to be able to write your own code.

In this thesis I mainly used a scripting language implemented in *Igor Pro* (Version 6.37). Additionally, for some specific problems I used Python. *Igor Pro* (available at https://www.wavemetrics.com/) is a software specifically designed for the analysis of scientific and engineering data with a graphical user interface, while still being incredibly flexible by including its own scripting language that allows direct access to the functions of the built-in library.

The capabilities of the scripting language are well-illustrated by a script written by my supervisor, PD Dr. Ole Lytken, called *EccentricXPS* (available for free at https://www.wavemetrics.com/project/EccentricXPS). This script provides a full graphical user interface to compare and fit XPS and NEXAFS spectra within Igor, enabling a fast and efficient workflow. This script also includes a photoemission clean-up algorithm for Auger-yield NEXAFS spectra, which will be discussed in more detail in Chapter 6.4.2. In this thesis, it turned out to be very helpful to be able to access the underlying data structure and functions from the command line, which, for example, simplified construction of XPS spectra consisting of up to 96 contributions (see Chapter 5.4.1) or dealing with second-order light (see Chapter 6.4.3) in C K-edge NEXAFS.

Although *EccentricXPS* is a powerful script, its functionality is specifically tailored to the analysis of XPS and Auger-NEXAFS data, and in my research, I encountered challenges that required very specific capabilities. One such challenge was high-intensity noise spikes in photoemission spectra measured at the Materials Science Beamline at the synchrotron in Trieste. Figure 14 illustrates the problem: Two spectra were measured in sequence under identical conditions and show clear deviations far beyond the experimental noise, especially at low binding energies.

The Specs Phoibos 150 1D-delay line detector has 100 channels that measure in parallel, and an analysis of these 100 channels reveals that these noise spikes are only present in a few of the channels, see Figure 15. The spikes we see in the spectrum are therefore caused by a small number of data points having very larger intensities. In the following, these noise spikes will be referred to as aberrant data points.

Unfortunately, these aberrations appear in an unpredictable manner and although there is some preference to some channels, they appeared in almost all 100 detector channels. Removing these

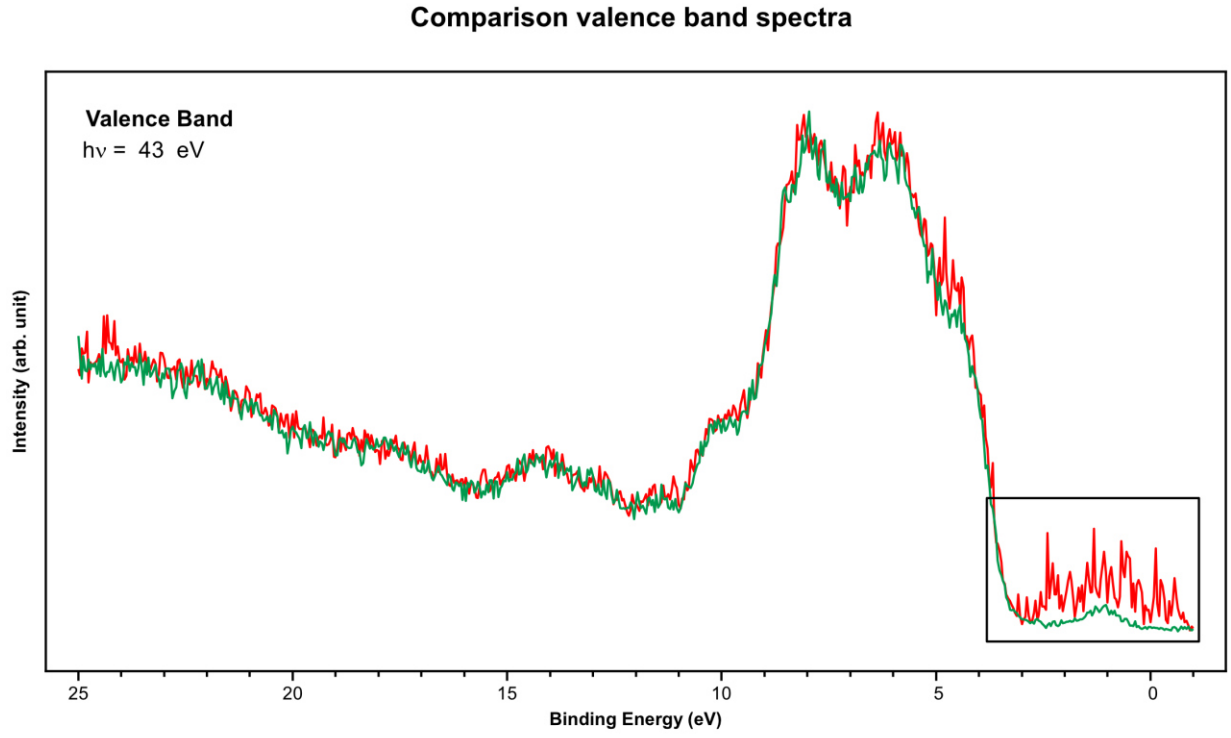

Figure 14: Valence band spectrum of 1 ML of phenylphosphonic acid on rutile TiO_2(110) after annealing to 750 K for 1 min measured consecutively under identical conditions. The black box highlights the area of strongest deviation, although there are also deviations at 4.5 eV and 24 eV.

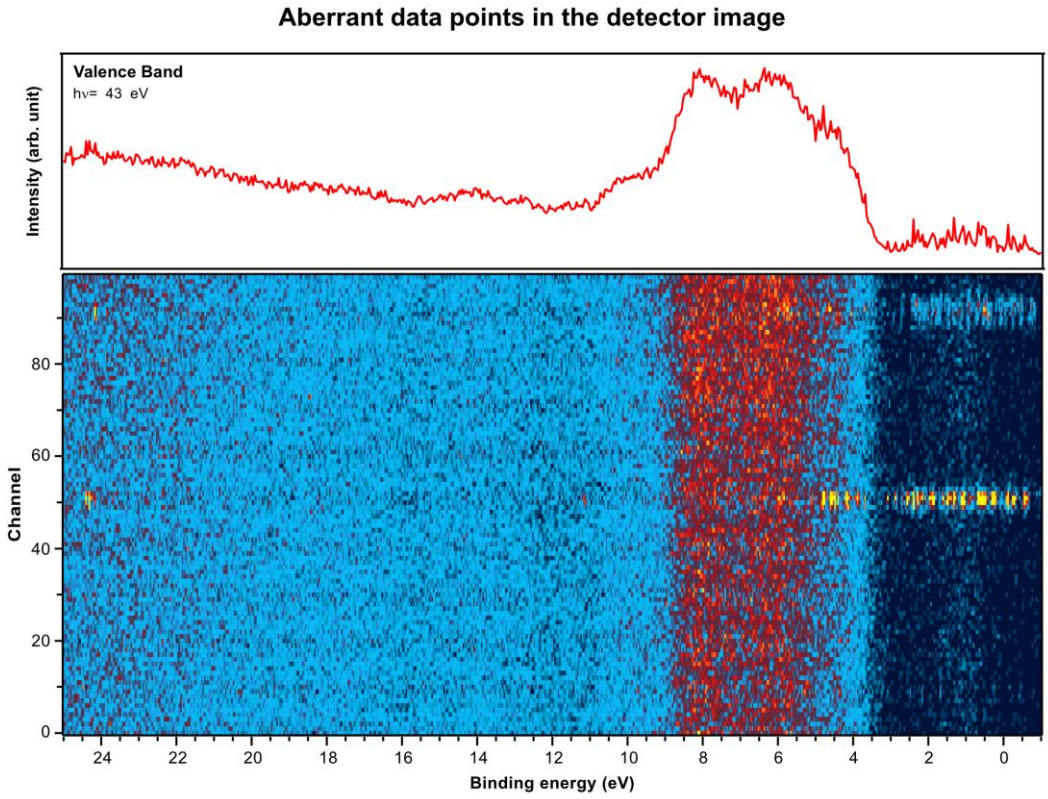

Figure 15: The two-dimensional image and one-dimensional spectrum of the valence band spectrum (same data as in Figure 14, red line). The high-intensity aberrant data points come from spikes in only a few channels. The color scheme of the image changes from dark blue, cyan, orange to yellow as the intensity increases. Vertical features correspond to the XPS peaks in the spectrum, and the presence of horizontal features corresponds to the aberrations observed in the spectrum. The image is interpolated to correct for the binding energy offset of the detector channels due to their physical location in the detector. The displayed image is an average of all four measured sweeps.

aberrations by hand would require analyzing over 5000 images by hand, and that is simply not feasible.

To automatically distinguish the aberrant data points on the noisy background of the experimental data, it is assumed that the experimental data follows a Poisson probability distribution. The Poisson distribution describes the probability of measuring a discrete number of events in a fixed interval of time, if these events occur with a constant mean rate and independently of the time since the last event – assumptions well met by a photoelectron measurement at a fixed binding energy.[80, 81]

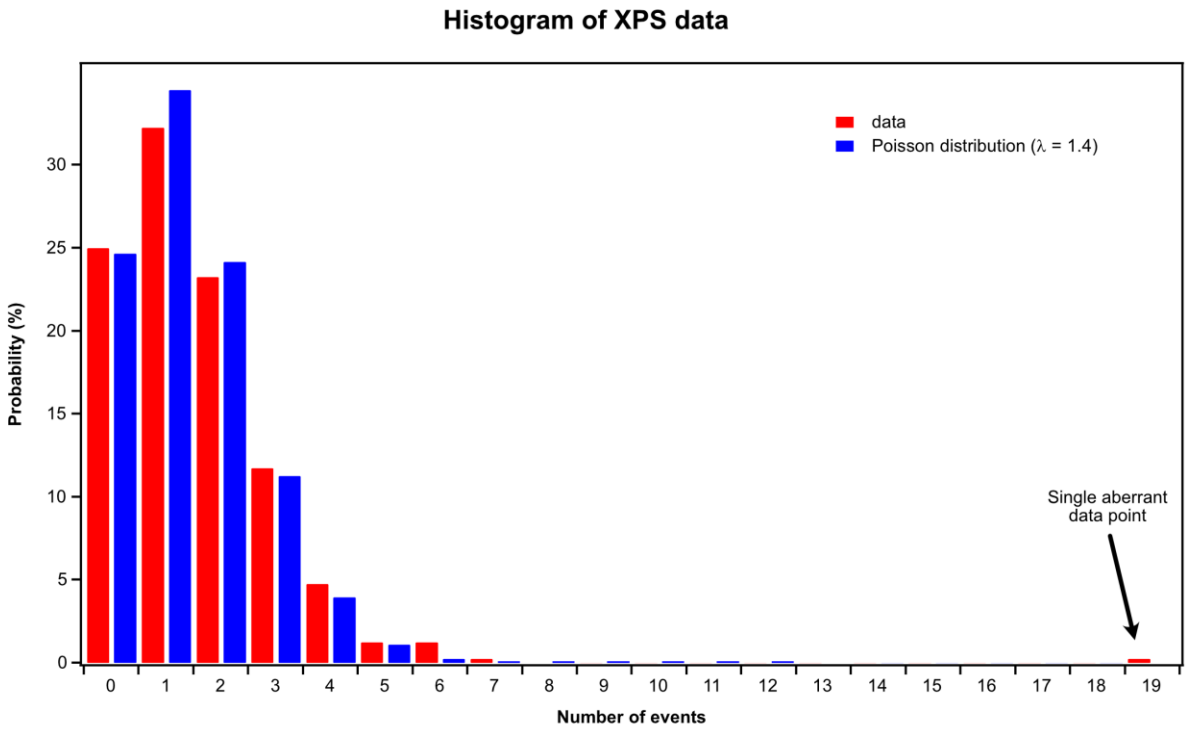

Figure 16: Histogram of the experimental data from the valence band image shown in Figure 15 at a binding energy of 5.8 eV (red). The ideal Poisson distribution for a mean value of 1.4 (blue) agrees well with the experimentally observed distribution. However, there is a high-intensity outlier in the experimental data, which is attributed to the aberrations discussed above.

This can be illustrated by creating a histogram at a selected binding energy for the valence band image shown in Figure 15, see Figure 16. Comparing it to an ideal Poisson distribution with a mean value of 1.4 results in a very good match, indicating the data is indeed Poisson-distributed. There is one outlier with 19 events, which is clearly an aberrant data point, as the probability for this intensity to occur is only 1×10^{-13} % if following an ideal Poisson distribution with a mean value of 1.4.

Based on the Poisson distribution, one can now define a criterion to identify aberrant data points. We define a confidence interval, which is defined here as the percentage of data points we want to keep if all data points were to follow an ideal Poisson distribution. For a given Poisson distribution, we can now calculate a threshold intensity below which the percentage of data points of the Poisson distribution is equal to the confidence interval. Above this intensity, all data points are removed. As a result, we remove some data points that follow the ideal Poisson distribution, but we also remove all the high-intensity aberrant data points.

To apply such a definition, we need to know the mean value λ of the ideal Poisson distribution. Unfortunately, the true mean value is unknown, but in an infinitely large, Poisson-distributed data set, it is the average value of all data points. Therefore, the mean value can be estimated using the average intensity of all data points at a given binding-energy position.

Such a definition of the mean value requires an iterative implementation because the initial calculation of the mean value takes into account all data points – including aberrant data points that skew the mean value to slightly larger values. If an aberrant data point is removed, the mean value of the remaining data points changes and all data points must be checked again against the new ideal Poisson distribution based on the updated mean value. This is repeated until no more data points are removed, which is usually the case after three to five iterations.

To correct for the observed aberrations, a confidence interval of 99.9937% was used, meaning that if all data points followed an ideal Poisson distribution, only 0.0063% of the data points would be

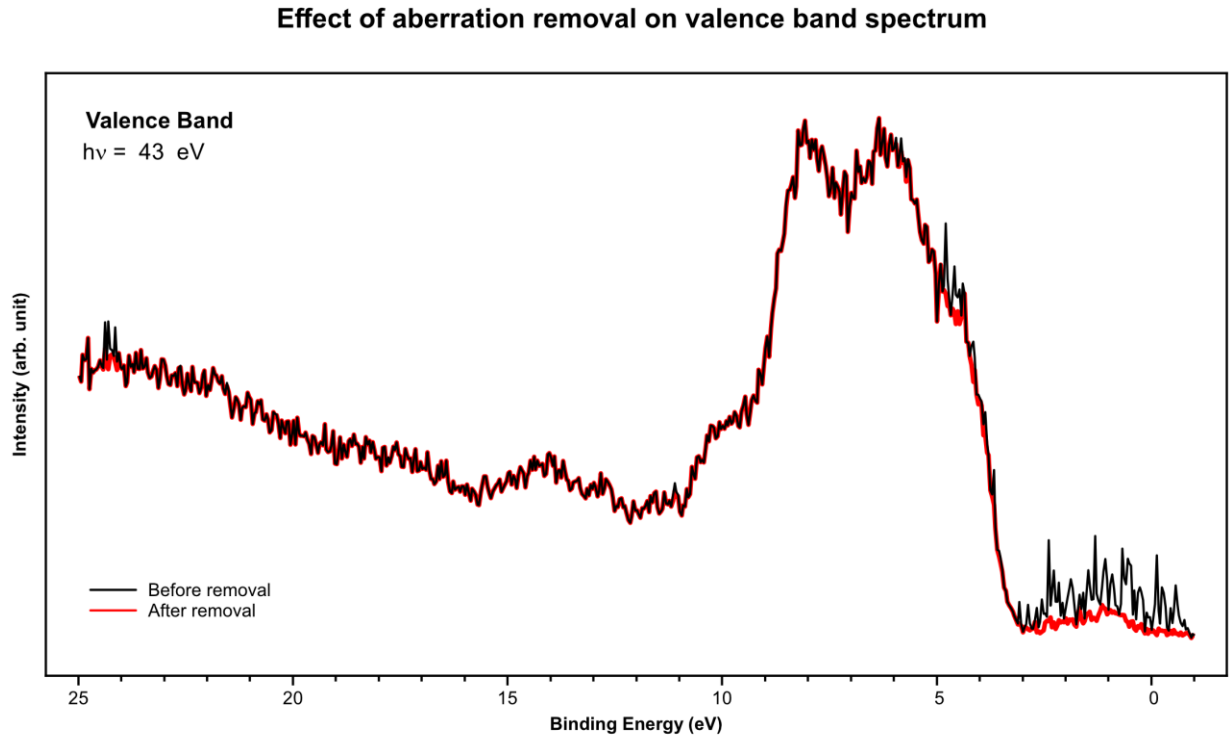

Figure 17: Valence band spectrum from Figure 15 before (red) and after (black) removal of data points as described in the text with a cutoff probability of 99.99366 %. The high intensity values are quite well removed, but in regions without the aberrations the traces are identical, indicating that this approach does not even change the experimental noise.

erroneously removed. This conservative confidence interval was sufficient to obtain very reasonable spectra, see Figure 17. In the regions with aberrant data points, the intensity is significantly lower and the resulting peak shape is close to what would be expected.

There is a great risk in changing the experimental data to what the user believes to be correct, and this is the reason we chose a very conservative confidence interval of 99.9937%. We clearly do not overcorrect data, as in regions without aberrant data points in Figure 17, we do not even change the experimental noise.

An important part of scripting is user feedback. Especially when removing data points, it is detrimental for the user to be able to assess the effect of the algorithm on the spectrum to judge if the resulting output is reasonable. Thus, the graphical user interface shown in Figure 18 was

Graphical user interface for the algorithm

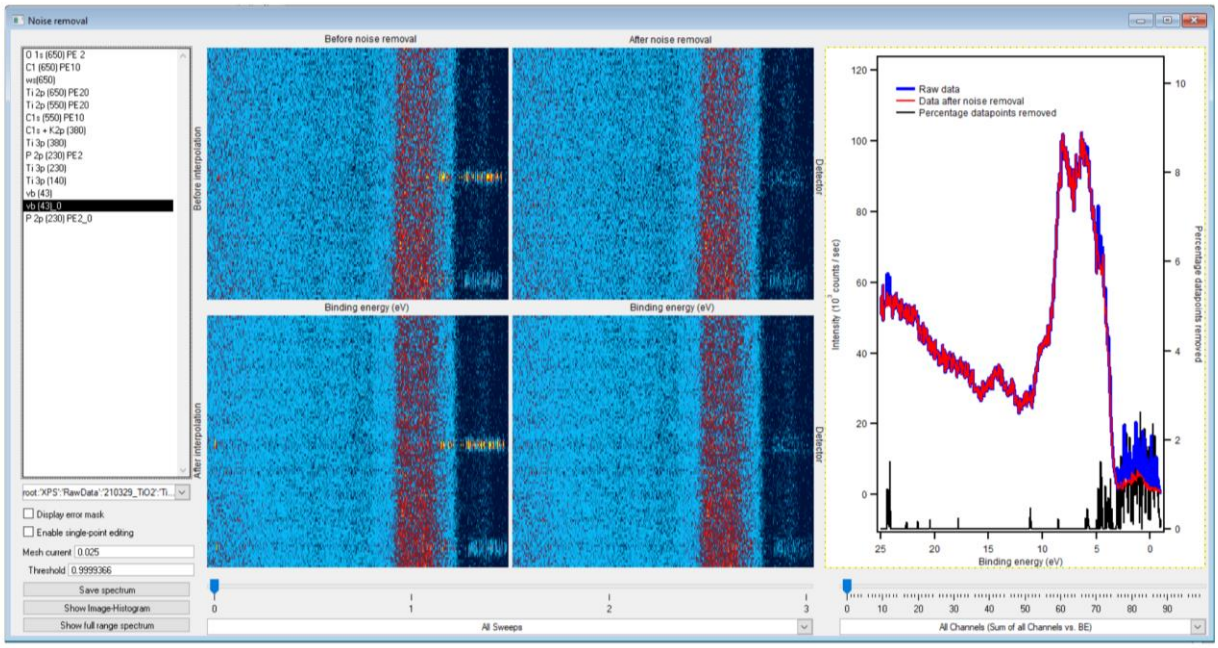

Figure 18: Screenshot of the graphical user interface of the aberration removal script. On the left, an input data browser is implemented, as well as some functionality to set or retrieve useful information (e.g. setting the confidence interval ("Threshold")). The four images in the middle show the data before/after interpolation (top/bottom) and before/after aberration removal (left/right). The spectra after interpolation are shown on the right, and the black line indicates how many data points were removed in the aberration removal process. The interface also allows quick selection of the sweep or individual channels (below images / spectra). The effect of interpolation is very small for this example because the data was measured at the lowest possible pass energy of only 2 eV.

implemented, which consists of a data browser and input parameter controls (left), an image area (middle), and a spectrum area (right). The left side is the user input area where the user can select the input data and parameters such as the confidence interval (called “Threshold” in the program). In the middle, two columns of images are shown before and after removal of aberrant data points (there are four images due to the underlying data structure and interpolations that are necessary steps in the calculation itself). The XPS spectra before and after correction are displayed on the right side of the interface, with the black line representing the percentage of data points removed. This gives a very quick overview of where the algorithm has removed data points and how this has affected the spectrum.

While we were able to deal with these aberrations efficiently, the origin of these aberrations remains unknown. They were observed mainly for very low intensity measurements, for example, when measuring with a pass energy of 2 eV and slit settings of 50/100 μm. At higher intensities, the aberrations were not a problem. These aberrations are also present in other measurements from the Materials Science Beamline, but they occur less often and with lower intensity, and since they have no obvious effect on the resulting XPS spectrum, they have gone unnoticed. It is most likely caused by a problem with the hemispherical energy analyzer, but since these problems are difficult to reproduce, finding the cause is almost impossible.

Although the idea of this algorithm is simple, implementing it involved many steps. This includes rewriting the data importer from scratch, implementing data transformations to convert the raw data to spectra, and implementing the algorithm itself, while at the same time optimizing all these steps to take only a few seconds instead of minutes.

Data correction and data analysis today require the use of computers, and especially in science, where flexibility is key, it is very helpful to be able to write scripts specifically tailored to the application. This is just one example of how I used programming to correct or analyze data, which has enabled me to create more complex correction or analysis schemes than what would have been possible without it.

The advent of large language models, such as Chat GPT or Microsoft Copilot, makes it possible for a layman with no programming experience to generate code from plain text. These programs are already changing the way we work, and it is exciting to see what is possible when these programs get even better. This thesis, for example, was proof-read with the help of the program

“DeepL Write”,(https://www.deepl.com/write) which is an AI-powered writing assistant that corrects grammar, spelling, and punctuation, as well as providing suggestions for alternative words and phrasing.

4. TPD of metallotetraphenylporphyrins on MgO(100) thin films

In this thesis, the adsorption of metallotetraphenylporphyrins, see Scheme 5, on MgO(100) thin films on Ag(100) is investigated. As already mentioned in the introduction, porphyrins can bind to metal ions and in this thesis, cobalt, magnesium, and zinc were used as metal centers.

It is well-known from scanning tunneling microscopy measurements that these molecules adopt a flat adsorption geometry on a surface,[82-84] as this maximizes the dispersive interactions between the large, flat macrocycle and the surface. Unfortunately, this relatively strong interaction between the molecule and the surface increases the desorption temperature of the molecule, which pushes the desorption temperature above the onset temperature of decomposition reactions, such as dehydrogenation reactions on a copper surface.[85] This also explains why there had been no publications extracting adsorption energies using temperature-programmed desorption, although the desorption spectra of monolayers and multilayers of these molecules have been reported.[86-88] However, knowing the adsorption energies of tetraphenylporphyrins would be a valuable benchmark for density-functional theory (DFT) calculations, as it is difficult to describe dispersive

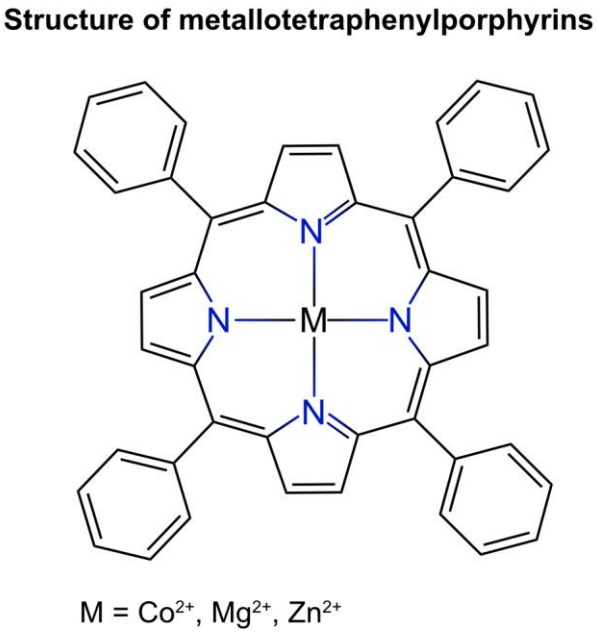

Scheme 5. General structure of a metallotetraphenylporphyrin. The metal center is coordinated by the nitrogen atoms of the four pyrrole rings. Investigated metal ions are Co^{2+}, Mg^{2+}, and Zn^{2+}.

interactions in this theoretical framework[89-92] and newly developed methods must first be validated against experimental values.

While tetraphenylporphyrins decompose before desorption in UHV, it is possible to remove them from the interface by replacing them. This was shown in a recent study from our group by Maximilian Muth, where we followed exchange reactions at a buried metallotetraphenylporphyrin interface on rutile TiO_2(110), which enabled us to determine relative adsorption energies.[61] Another option is to follow porphyrin desorption in solution,[93, 94] but the resulting adsorption energies are more complicated to interpret because they involve solvation energies of the porphyrin molecules and the exchange of adsorbed molecules with solvent molecules at the interface.

A completely different approach is to determine the adsorption energy of the adsorption process itself, which can be done by single crystal adsorption calorimetry.[95, 96] Although it is possible to obtain the adsorption energy in this way, it is far from simple and measuring monolayer adsorption energies requires a specialized experimental setup, which is only available to a few research groups.

In conclusion, it is very difficult to obtain monolayer adsorption energies of tetraphenylporphyrins. However, we were able to measure monolayer desorption TPD spectra of magnesium(II)-, cobalt(II)-, and zinc(II)-tetraphenylporphyrin (MgTPP, CoTPP, and ZnTPP, respectively) because the MgO(100) surface is so inert that monolayers of metallotetraphenylporphyrins desorb almost completely before decomposition, see Figure 19.

I did not measure these monolayer TPD spectra, as these spectra were part of an unpublished data set, but I did do all the analysis. I combined this data set with multilayer TPDs of porphyrins, and we received additional theoretical support from the group of Prof. Bernd Meyer, resulting in a combined experimental and theoretical study of the adsorption energies of tetraphenylporphyrins on MgO(110).[P1]

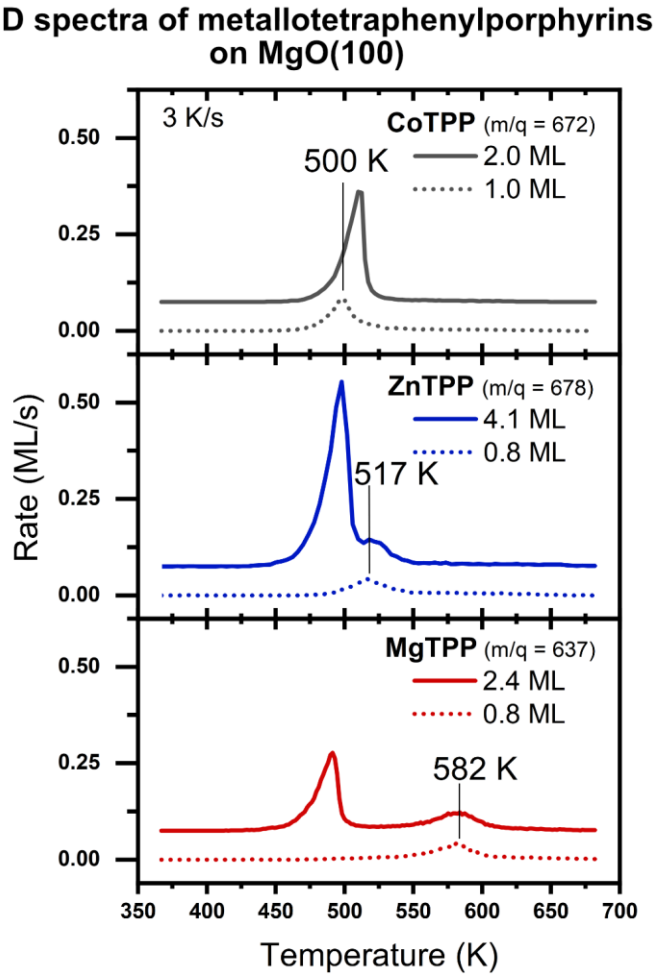

Figure 19: Temperature-programmed desorption spectra for Co(II)-, Zn(II)-, and Mg(II)-tetraphenylporphyrin desorbing from a MgO(100) surface. The full line spectra are desorption spectra for initial coverages beyond a fully saturated monolayer, causing a multilayer desorption peak at about 500 K. For ZnTPP and MgTPP, a separate peak is observed at higher temperatures due to monolayer desorption. For CoTPP, the monolayer desorption peak is at the same position as the multilayer desorption peak. Adapted from Ref. [P1].

4.1. Estimating the prefactor for desorption to extract adsorption energies

There are several approaches to extract the adsorption energies from TPD spectra, e.g. by a complete analysis.[73] Unfortunately, a complete analysis requires not only high-quality spectra to avoid compensation effects (see Chapter 3.2.4), but it also requires a large number of spectra. This is not feasible with the system at hand.

To avoid problems with the compensation effect, we thus decided to use a method that is insensitive to it, namely Redhead analysis.[72] This method is insensitive to the compensation effect, because it does not use the peak shape, but only the temperature of maximum desorption rate to extract the adsorption energy. Unfortunately, this trades one problem for another, because we now need the correct prefactor for desorption. In addition, the prefactor, desorption energy, and desorption order must remain constant throughout the desorption process. Before applying the analysis, it is therefore necessary to verify that these assumptions are reasonable for the system at hand.

Metallotetraphenylporphyrins do form an equilibrium of a 2D gas phase of highly mobile molecules with immobile islands at room temperature, as observed for CoTPP on Ag(111).[88] Such an equilibrium can lead to a desorption order of 0.5, if the diffusion of molecules from the 2D islands into the 2D gas phase is the rate limiting step.[97-99] This equilibrium is observed for tetraphenylporphyrins at room temperature, but at the desorption temperature of over 500 K, one expects the equilibrium to shift massively towards the entropically-favored 2D gas phase. The assumption of a 2D gas phase is further supported by DFT calculations by Ninova et al., where different adsorption sites of CoTPP on a MgO(100) terrace were found to have very similar adsorption energies.[82] Assuming the molecules desorb from a pure 2D gas phase, the desorption energy and the prefactor for desorption become independent of coverage and the desorption order becomes 1.

Thus, the assumptions of the Redhead analysis should be fulfilled, but to use it, one important piece of information is still missing: the value of the prefactor for desorption. As outlined in Chapter 3.2.3, the typical value of 10^{13} s^{-1} is not applicable to large molecules and values of around 10^{19} s^{-1} are much more realistic for this system. However, we have to determine the value for the prefactor for desorption from somewhere else.

4.1.1. Using multilayer desorption spectra to determine the prefactor for desorption

The initial plan was to use the multilayer prefactor for desorption in Redhead analysis. Thus, multilayer desorption spectra were measured for all three metalloporphyrins and an average prefactor for desorption of $10^{21.6}$ ML/s and multilayer heats of sublimation of 219, 213, and 209 kJ/mol were obtained for CoTPP, ZnTPP, and MgTPP, respectively (the corresponding spectra will be discussed in Chapter 4.3). Note that the prefactor for desorption is, as expected, significantly larger than 10^{13} s^{-1}. Unfortunately, the prefactor for multilayer desorption is not the prefactor for monolayer desorption and therefore cannot be used to extract the monolayer adsorption energies on MgO(100).

The reason for this is illustrated in Scheme 6: When a molecule desorbs from the top layer, there is always a molecule below it that immediately replaces the desorbed surface molecule. As a result, the surface has not changed, and only the number of molecules in the bulk changes. Since the prefactor for desorption is given by the entropy difference between the initial state and the transition state, as already outlined in Chapter 3.2.3, the entropy difference is given by the entropy of the molecule in the bulk and the entropy of a molecule in the transition state. This entropy difference is larger than the entropy difference of a molecule in top layer relative to the transition state, because the molecule in topmost layer has most likely more degrees of freedom, resulting in

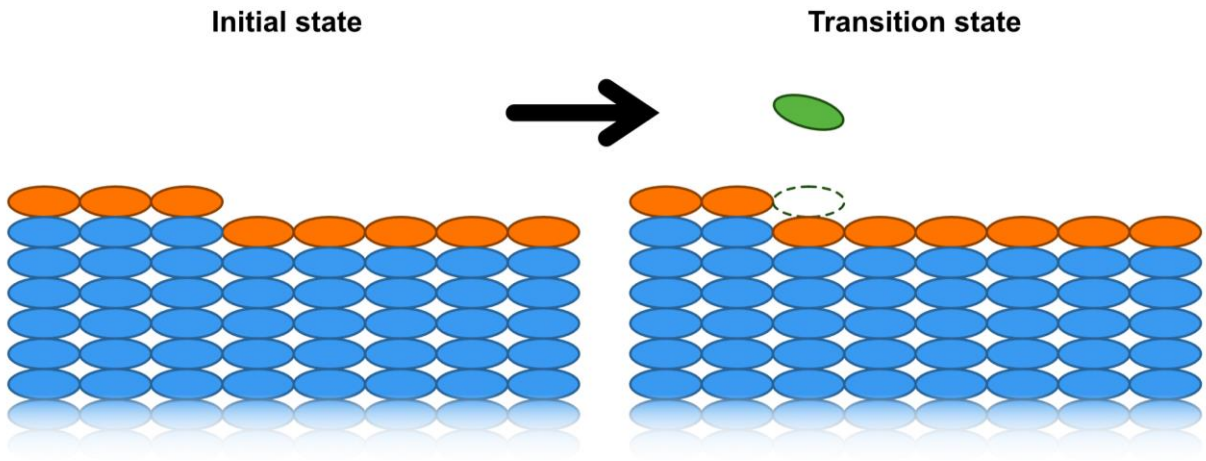

Scheme 6: Illustration of the desorption process of a molecule from a multilayer. As the molecule desorbs, the underlying molecules are exposed to the vacuum interface and immediately replenish the surface. Thus, the surface has not changed and a bulk molecule has effectively been removed.

a larger entropy. Thus, the multilayer prefactor for desorption represents only an upper bound on the monolayer prefactor for desorption.

4.1.2. Using transition-state theory to calculate a prefactor for desorption

Since multilayer desorption spectra cannot be used to access the value of the prefactor for desorption experimentally, classical transition-state theory was used to calculate the prefactor for desorption. This approach provides reasonable estimates of the desorption prefactor for the desorption of large organic molecules,[100-102] although the resulting prefactor may be too large.[100] All details of the calculation for this system can be found in Ref. [P1], but the idea is to describe the prefactor for desorption by the ratio of the molecular partition functions of the transition state $z^{\neq}$ and the adsorbed state z^{ads} according to:

$$\nu^{theory} = \frac{k_B T}{h} \cdot \frac{z^{\neq}}{z^{ads}}$$

where k_B and h denote the Boltzmann and Planck constants and T the temperature. Only the relevant parts of the partition function need to be considered, which are changes in translations, rotations, and vibrations:

$$\frac{z^{\neq}}{z^{ads}} = \frac{z^{\neq}_{trans}}{z^{ads}_{trans}} \cdot \frac{z^{\neq}_{rot}}{z^{ads}_{rot}} \cdot \frac{z^{\neq}_{vib}}{z^{ads}_{vib}}$$

These three partition functions must be evaluated for the system at hand. For simplicity, the transition state is assumed to be the gas phase molecule, which is correct if there is no free energy activation barrier to the adsorption process. The adsorbed state is, as outlined above, assumed to be a 2D surface gas, and thus the translational partition functions cancel out, since both the adsorbed and transition states have two translational degrees of freedom in the surface plane. The third degree of freedom perpendicular to the surface must not be included in the partition function of the transition state because it is along the reaction coordinate.

To obtain information about the vibrational partition functions, it would be necessary to compare the differences in vibrational frequencies of the adsorbed state and the transition state. We do not have the data for that, but for coronene, an organic molecule of comparable size to tetraphenylporphyrin, the frequencies of the molecule in the gas phase and the condensed phase

differ by less than 1%,[103] and thus both partition functions should approximately cancel each other out. This approximation will lead to a slight overestimation of the prefactor for desorption, because the frustrated rotations in the adsorbed state will lead to low-energy vibrations, which can contribute significantly to the entropy of the adsorbed state.[104]

Some rotations of the molecule are suppressed in the adsorbed state, but these rotations are possible in the transition state. Since these rotations have significant entropy, their contribution to the partition functions cannot be neglected. Using the DFT calculated gas-phase geometries of the three metalloporphyrins provided by Prof. Bernd Meyer, it is possible to calculate the partition functions of the rotations assuming the molecule behaves as a static rotator. For the adsorbed molecule, only a rotation in the surface plane is possible, while the molecule can rotate around all three axes in the transition state.

To sum up, in this approach the ratios of the translational and vibrational partition functions are set to unity and the prefactor is calculated based only on the rotational partition functions of the adsorbed and transition states. This results in an average prefactor for desorption of $10^{18.9}$ s^{-1} (more details can be found in Ref. [P1]).

Using this calculated prefactor, which, as expected, is smaller than the experimental prefactor from multilayer desorption, we were able to determine the monolayer adsorption energies using Redhead analysis, see Table 2.

Table 2: List of desorption temperature, moments of inertia calculated from DFT-optimized gas-phase geometries, the resulting calculated prefactor for desorption, the experimentally-determined multilayer prefactor for desorption, and the monolayer desorption energy obtained by Redhead analysis with a prefactor for desorption of $10^{18.9}$ s^{-1}. The moments for inertia are used to calculate the rotational partition functions assuming the molecule behaves as a static rotator. Adapted from Ref. [P1].

	T_{des} (K)	I_x (kg·m^2)	I_y (kg·m^2)	I_z (kg·m^2)	$\nu_{2D\,gas}^{theory}$ (s^{-1})	$\nu_{multilayer}^{exp}$ (s^{-1})	E_{des} (kJ/mol)
CoTPP	500	$1.43 \cdot 10^{-43}$	$1.42 \cdot 10^{-43}$	$2.70 \cdot 10^{-43}$	$10^{18.8}$	$10^{22.1}$	186
ZnTPP	517	$1.44 \cdot 10^{-43}$	$1.44 \cdot 10^{-43}$	$2.78 \cdot 10^{-43}$	$10^{18.9}$	$10^{21.4}$	193
MgTPP	582	$1.44 \cdot 10^{-43}$	$1.44 \cdot 10^{-43}$	$2.79 \cdot 10^{-43}$	$10^{19.0}$	$10^{21.3}$	217

4.2. Comparison with DFT-calculations

Prof. Bernd Meyer calculated the adsorption energies of the three metallotetraphenylporphyrins on the MgO(100) surface using density-functional theory. He used a newly developed dispersion correction, called D3^{surf}, which had previously only been validated against experimental results on metal surfaces.[101, 105] He found adsorption energies of 209, 171 and 174 kJ/mol for Mg(II)-, Zn(II)-, and Co(II)-tetraphenylporphyrin, respectively, which are in good agreement with the experimental values of 217, 193, and 186 kJ/mol. This good agreement between theory and experiment, especially after considering the size of the molecule, makes us confident that the theoretical description works well.

The DFT-optimized adsorption geometries in Figure 20 show that the metal centers of MgTPP and ZnTPP interact with surface oxygen atoms, causing the macrocycle to deform. In contrast, the cobalt center in CoTPP does not move closer to the surface and the molecule is almost exclusively van-der-Waals bound, completely in line with our observation that the monolayer and multilayer desorption signal of CoTPP is at the same temperature.

The difference in adsorption energy between MgTPP and ZnTPP can be well explained by the oxophilicity of the metal center. We calculated the adsorption energy of a water molecule to the gas-phase metallotetraphenylporphyrin and we observe that the magnesium-oxygen distance is

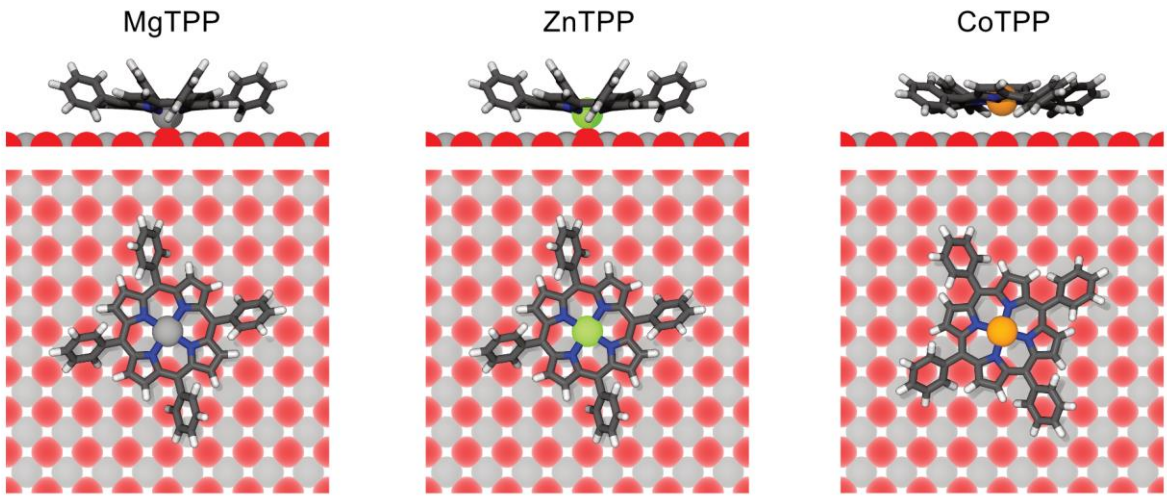

Figure 20: DFT-optimized structures for Mg(II)-, Zn(II)-, and Co(II)-tetraphenylporphyrin adsorbed ontop of an oxygen atom on MgO(100). While MgTPP and ZnTPP deform to decrease the metal to surface oxygen distance, this is not possible for CoTPP. Adapted from Ref. [P1].

significantly smaller than the zinc-oxygen distance, see Table 3, indicating a stronger attraction between oxygen and magnesium. Olsson et al. found MgTPP in solution to be significantly more oxophilic compared to ZnTPP[106], supporting our results. Thus the adsorption energy difference between MgTPP and ZnTPP arises from the oxophilicity of the metal center.

Based on these considerations, we would expect the oxophilicity of CoTPP to be even lower than for ZnTPP, but the results of our calculations in Table 3 show that the Co^{2+} center is more oxophilic than Zn^{2+}. The reason why the cobalt center in CoTPP does not move closer to the surface can be found in deformation energies. When the metal center moves close to the surface, the whole porphyrin macrocycle needs to deform, see Figure 20. The deformation of the macrocycle costs energy and this energy depends on the rigidity of the porphyrin core, which is strongly influenced by the directionality of the bonds of the metal center to the central four nitrogen atoms. In the case of the closed-shell Mg^{2+} and Zn^{2+} systems, there is little directionality, which leads to a rather flexible porphyrin core. In contrast, for the open-shell Co^{2+} ion ($3d^7$ configuration), the directionality of the bonds decreases the flexibility of the porphyrin core for out-of-plane deformations.[107] The reason why the cobalt center is not interacting with the surface is thus the increased rigidity of the porphyrin center, although the cobalt center has a oxophilicity comparable to the zinc center.

The results of this study have enabled a deeper understanding of how the interplay between the metal center's oxophilicity and the porphyrin core's rigidity affects the adsorption energy and geometry of metallotetraphenylporphyrins on MgO(100). Furthermore, these data serve as a valuable benchmark for validating theoretical descriptions of dispersive interactions.

Table 3: Calculated adsorption energy E_{ads}^{W} of a water molecule on the metal center of different metalloporphyrins and the corresponding metal-oxygen distance d_{M-O}. The lower the adsorption energy, the higher the oxophilicity of the metal center and the smaller the distance between the metal center and the water molecule. Adapted from Ref [P1].

Porphyrin	E_{ads}^{W} (kJ/mol)	d_{M-O} (Å)
MgTPP	–60.2	2.175
ZnTPP	–34.3	2.396
CoTPP	–37.8	2.350

4.3. Multilayer TPDs of metallotetraphenylporphyrins

Multilayer desorption spectra of metallotetraphenylporphyrins were not measured with a linear heating ramp, but inspired by multilayer desorption measurements of water by Speedy et al.,[108] the temperature was modulated with a triangle wave, see Figure 21.

The great advantage of this measurement is that one can measure the desorption rate during the heating and cooling cycle and directly check whether the measured desorption signal follows the assumptions of multilayer desorption, where the desorption rate is independent of the coverage. This means that the desorption signal on the rising edge of a heating/cooling cycle must be the same as that on the subsequent falling edge. If this is not the case and a hysteresis is observed, it is immediately clear that the desorption process is not following multilayer assumptions and the data should not be used to extract the multilayer prefactor for desorption. While it is hard to see

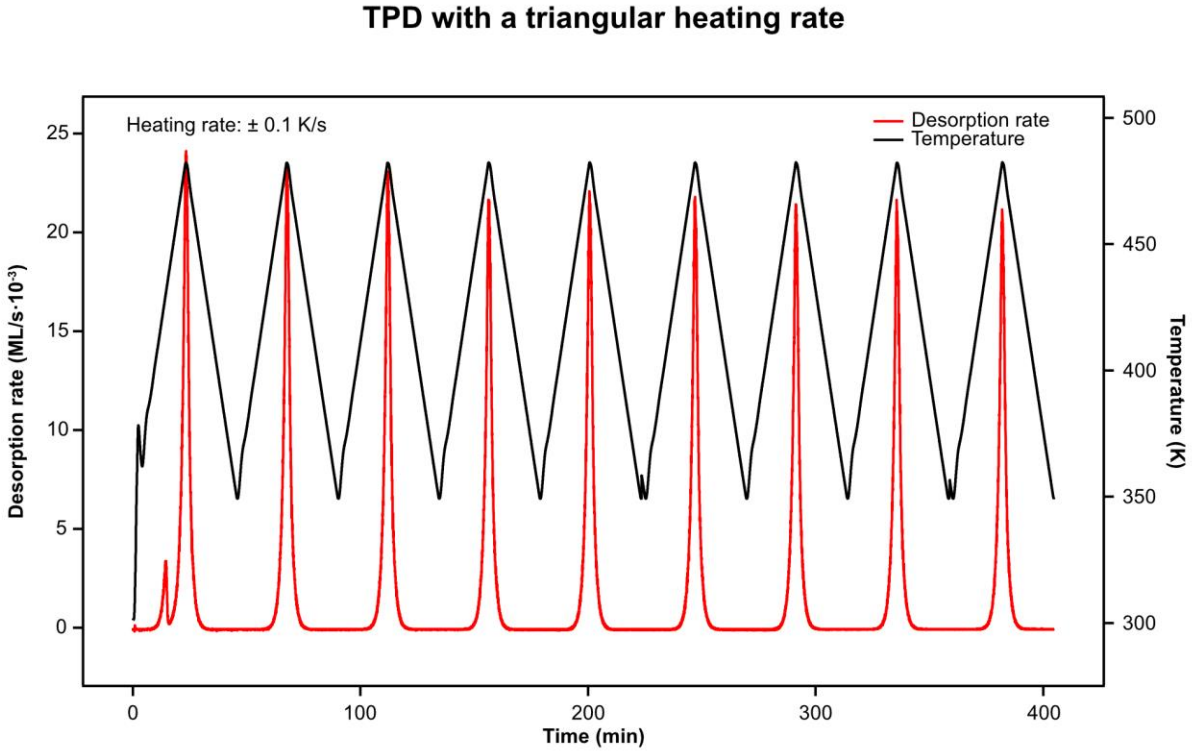

Figure 21: Multilayer TPD of ZnTPP using triangular temperature modulation. The maximum temperature and heating rate are chosen to desorb about 5 ML of molecules in each heating/cooling cycle. For clarity, only the first 9 heating/cooling cycles are shown, but in the experiment this was continued until all porphyrins were desorbed from the surface.

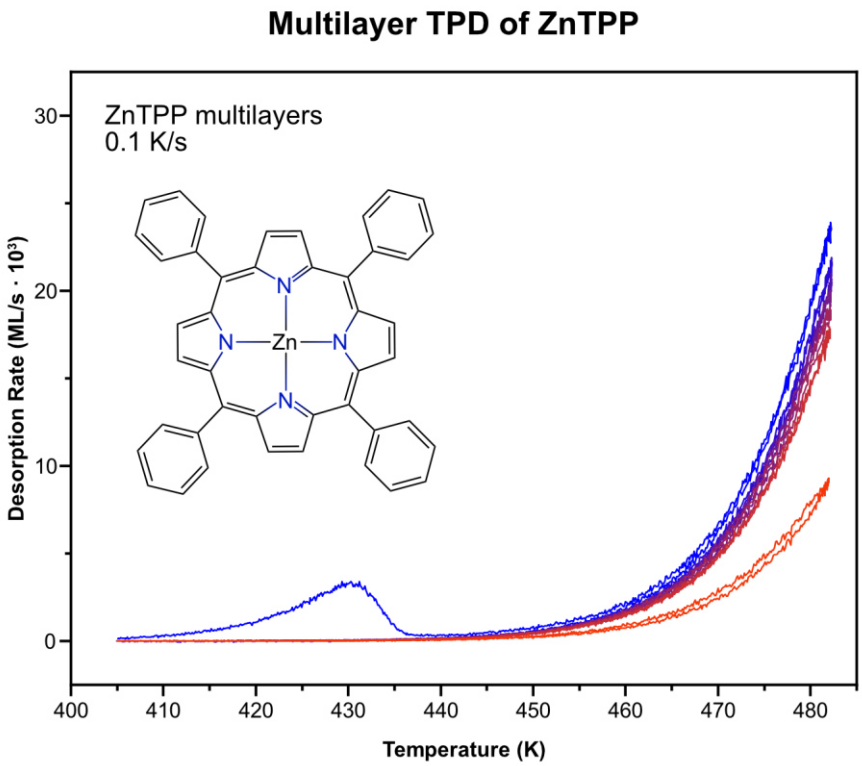

Figure 22: Desorption series consisting of 27 consecutive linear heating and cooling ramps (from blue to red) at a heating rate of 0.1 K/s, eventually resulting in complete desorption of the 103 ML thick ZnTPP film. For clarity, only every fourth heating/cooling curve is shown. This is the same data as shown in Figure 21. Adapted from Ref. [P1].

such deviations in Figure 21, it becomes very easy to identify deviations in Figure 22 when the same data are plotted against the temperature.

The first heating/cooling cycle in Figure 22 is very different from the others because there is an additional desorption peak at 430 K. From the second heating/cooling cycle on, there is only a small decrease in the desorption rate and the subsequent curves are almost on top of each other, fulfilling the assumptions of multilayer desorption. The last few curves show a relatively rapid decrease in desorption rate, indicating that the multilayers have desorbed and the surface is depleted of porphyrin molecules.

A small additional desorption peak during initial heating is not uncommon in TPD because desorption can occur from other surfaces, such as the heating wires. However, this is not the case in these measurements because great care was taken to avoid adsorption of these molecules on any

surface other than the crystal. Instead, we assign this peak to an amorphous-crystalline transition, which has been extensively studied for water[108, 109] and is also known for organic molecules such as benzene[110] and even tetraphenylporphyrin.[87]

Indeed, constructing an isothermal desorption spectrum by taking the desorption rate at 470 K from each heating/cooling cycle in Figure 22 gives a curve that agrees very well with the simulated isothermal desorption curves for an amorphous-crystalline transition by Zhdanov and Norton in Figure 23.[111] The isothermal desorption spectra can be divided into three steps: Initial crystallization, crystal growth, and surface depletion. The film is initially amorphous, and when it reaches a high enough temperature, the molecules start to desorb, causing the desorption peak at 430 K in Figure 22. At the same time, the molecules become mobile enough to rearrange and they start to form crystalline structures. These crystallites grow quickly and since desorption from them requires a larger desorption energy, the desorption temperature shifts to higher temperatures, explaining the drop in desorption rate at 430 K in Figure 22. After the initial crystallization, the small crystallites will then grow slowly in an Ostwald ripening process, merging into larger crystallites, which causes the slow decrease in desorption rate, see Figure 23. Before all crystallites can merge into a single crystal, the surface is depleted of molecules, causing a rapid decrease in desorption rate.

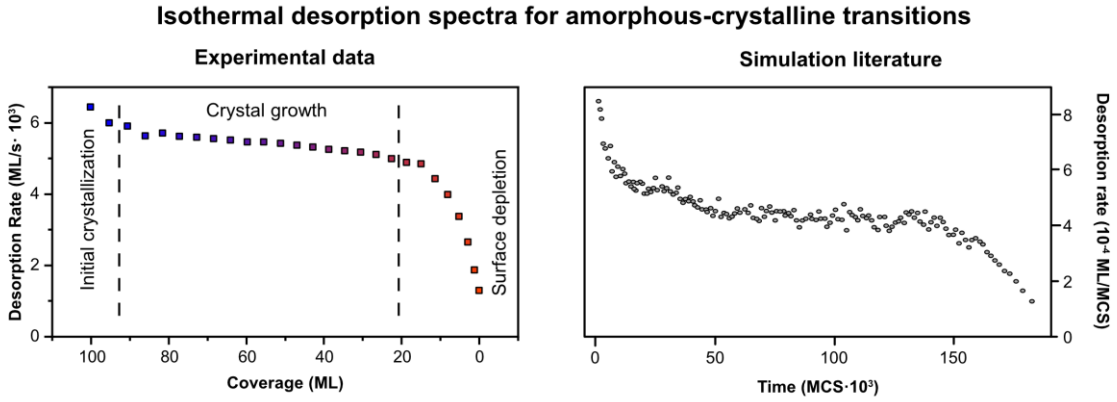

Figure 23: Isothermal desorption spectrum constructed from TPD data (left) in Figure 22 at a temperature of 470 K and a Monte Carlo simulation of isothermal desorption from an amorphous 2-dimensional lattice film of 80 ML (right). Figure adapted with permission from Ref [111] and [P1]. Both data sets have the same sigmoidal shape. The initial decrease of the desorption rate is much more pronounced in the simulation compared to the experimental data, because the first experimental data point is at 470 K, where the amorphous deposit is already almost completely crystalline. The experimental coverage axis can be converted to a time axis witch each heating/cooling cycle lasting 40 min.

To prevent this amorphous-crystalline transition from affecting our analysis in Figure 24, we decided to exclude the first few measured heating/cooling cycles, where we expect strong changes due to crystallization (more details can be found in the Supporting Information of Ref. [P1]). The selected multilayer spectra in Figure 24 follow a linear relationship in an Arrhenius plot and allow for the extraction of multilayer adsorption energies and multilayer prefactors for desorption.

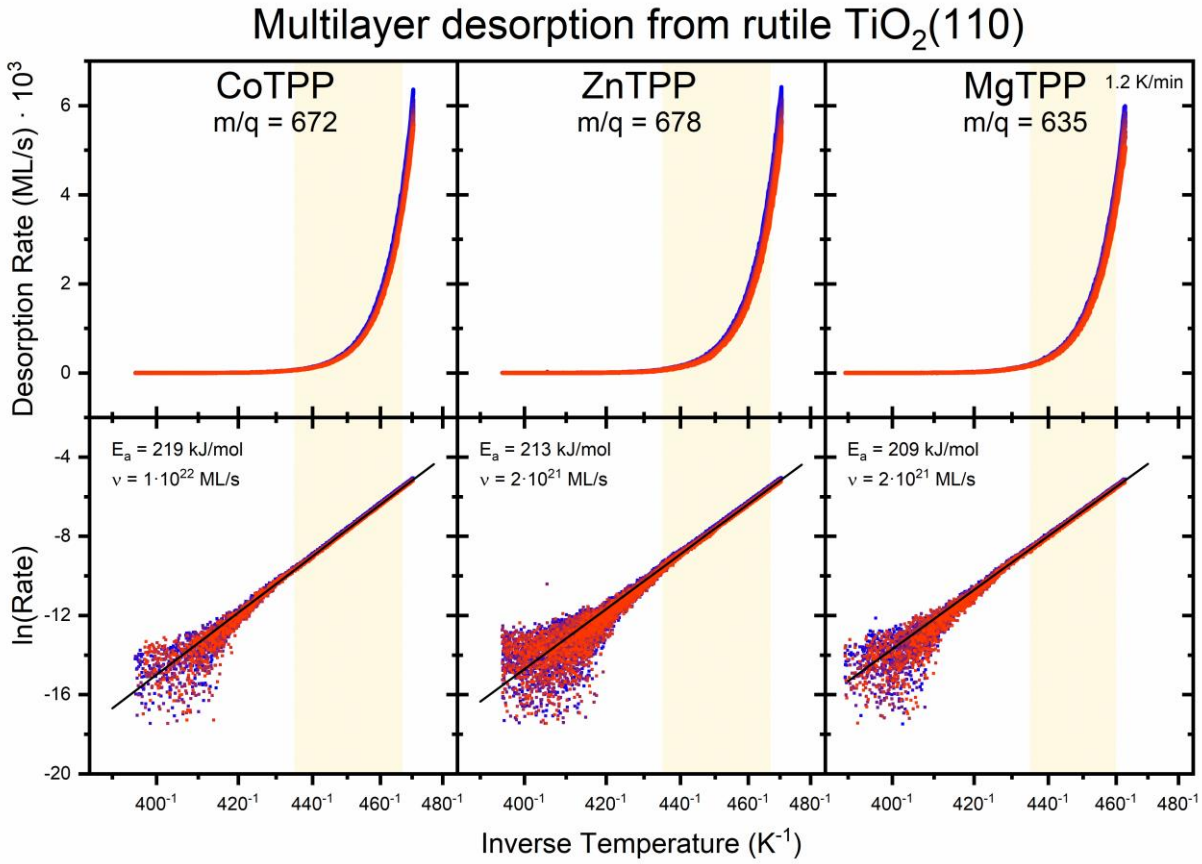

Figure 24: Multilayer desorption spectra for Co^{2+}-, Zn^{2+}-, and Mg^{2+}-tetraphenylporphyrin from a rutile TiO_2(110) surface with a heating rate of 1.2 K/min. The yellow areas indicate the data points fitted linearly in the Arrhenius plot, resulting in the shown averaged fit, adsorption energies, and prefactors. The trace color indicates the order in which the spectra where recorded, starting from blue (first) to red (last). Adapted from Ref. [P1].

5. Linker groups on rutile TiO_2(110)

5.1. Importance of linker groups

Combining organic and inorganic materials to create blends with new physical properties is an old idea. Maya Blue, a pigment used by the ancient Maya in pottery and sculpting, is a blend of the organic dye indigo with the inorganic clay palygorskite, and this colored material exhibits tremendous stability against acids, alkalis, organic reagents, and biodegradation.[112] Then as now, combing organic and inorganic materials proves to be crucial in the development of new materials in organic electronics,[113-115] corrosion inhibition,[116, 117] and anti-biofouling.[118] In all of the applications listed, the immobilization of an organic functional molecule on an inorganic substrate is critical. A common approach to achieve this is the use of linker groups that form covalent bonds to the surface. The archetypal system is thiols that bind to a gold surface, resulting in fairly well-defined self-assembled monolayers.[119, 120] Although thiols bind strongly to gold, they show only weak interactions with oxide surfaces.[121] Anchor groups that are much better suited for use on oxides include silanes, carboxylic acids, phosphonic acids or hydroxamic acids.[122-124]

The choice of anchor group also depends heavily on the intended application. For example, in dye-sensitized solar cells (DSSCs), it is critical to have good electrical contact between the light-absorbing dye and the substrate, while also having a strong bond to prevent slow dye desorption over time in the presence of even trace amounts of water. It is therefore necessary to have an intimate understanding of the chemistry of the anchor groups at the interface in order to design efficient devices with good long-term stability.

A very well studied anchor group for oxide surfaces is the carboxylic acid anchor group, which is a very common anchor group in DSSCs.[124, 125] However, dyes anchored with this group suffer from slow desorption in the presence of even trace amounts of water, which affects the long-term performance of these devices.[126, 127] In contrast, the phosphonic acid anchor group binds more strongly to the surface,[128-130] which improves long-term stability.

However, the phosphonic acid anchor group is much less studied and therefore we decided to investigate this anchor group on the rutile TiO_2(110) surface as a function of coverage and temperature, both parameters known to influence the adsorption mode of the anchor group.[48,

131, 132] We chose rutile TiO_2(110) as the model surface because TiO_2 nanoparticles are often used as the substrate in DSSCs.[124, 125]

We also studied the boronic acid anchor group on the rutile TiO_2(110) surface. This is a more exotic anchor group that has not received much attention in the surface science community. This anchor group can be used for sensing of sugars[133] or anchoring of glycoproteins on organic layers,[134] but also in perovskite solar cells to improve device performance.[135] Additionally, this anchor group has a Lewis-acidic boron atom, which could allow for unique surface chemistry at an oxide interface. We therefore wanted to understand this anchor group better.

5.2. Advantages of synchrotron measurements

Both phosphonic and boronic acids bind to the titania surface through their oxygen atoms. As a result, the O 1s core level contains crucial chemical information about the adsorption mode of the molecule. A measurement of such a system with an laboratory Al Kα X-ray source (1486.7 eV photon energy[136]) results in an O 1s core-level spectrum dominated by the signal of all oxygen substrate atoms in the near-surface region (about 5-7 nm). This makes it impossible to extract chemical information from the molecular contribution because it is too small to be deconvoluted from the substrate contribution. One way to decrease the contribution of deep-lying oxygen signals has already been outlined in Figure 7: Decreasing the inelastic mean free path by adjusting the kinetic energy of the photoelectrons.

With the Al Kα X-ray source, the kinetic energy of the O 1s photoelectrons is about 950 eV, and the surface sensitivity could be significantly increased by decreasing the kinetic energy to about 100 eV. This corresponds to a photon energy of 650 eV, but unfortunately, it is not possible to tune the photon energy of an Al Kα X-ray source while maintaining a high photon flux. This is due to the photon generation mechanism: In laboratory X-ray sources, accelerated electrons create core holes in an anode material, e.g. aluminum. When these core holes are filled by a higher-level electron, the energy difference can be released as a photon. Thus, this approach primarily produces photons with discrete energies corresponding to these specific transitions.

X-rays produced by a synchrotron light source do not suffer from this problem. Instead of an anode material with discrete transitions, in a synchrotron light source, electrons in a storage ring are deflected by magnets to produce X-rays. This enables these systems to generate a high photon flux over a wide range of photon energies, making them ideal for studying the O 1s core-level spectrum of linker groups on an oxide surface. At the Materials Science Beamline at Elettra, the photon flux is on the order of 10^{10} photons/second.[137] This high flux enables us to optimize the energy resolution of our measurements by using strict slit settings on the monochromator and a low pass energy of only 2 eV on the electron analyzer. The increased resolution comes at the expense of intensity, but even with these settings, it took less time to obtain spectra with noise levels comparable to our home-lab machine. This does not mean that our home-lab machine is unbearably slow; it just highlights the capabilities of a synchrotron light source.

At synchrotron light sources, this increased photon flux is focused onto a small surface area, as the beam size at the Materials Science Beamline is only about 0.5 mm^2. When working with intense and highly focused beams, it is therefore always important to consider beam-induced degradation.[78] To minimize potential beam damage, the illuminated spot was changed regularly, although no evidence of beam damage was found during the measurements.

Synchrotron radiation provides high photon flux over a wide range of photon energies, which is also essential for near-edge absorption fine structure (NEXAFS) measurements. In addition, synchrotron light generated by a bending magnet is typically elliptically polarized, and the polarization is useful to extract the orientation of the unoccupied orbitals of the adsorbed molecule.

5.3. Challenges in evaporating organic linker groups

Samples were prepared by deposition of model linker molecules using a Knudsen effusion cell. These model molecules all share the same structural motif: The anchor group is attached to a phenyl ring, see for example phenylphosphonic acid in Figure 25. Such a structure keeps the molecule simple and keeps it easy to evaporate, while the rather inert phenyl ring can be used to extract information about the orientation of an attached carbon moiety using C K-edge NEXAFS (see Chapter 6.1 for more details).

It is important to prevent decomposition reactions of the molecules in the evaporator, so only graphite crucibles were used. However, an inert crucible material can only prevent decomposition reactions between the molecules and crucible surface, but it cannot suppress inter- or intramolecular decomposition reactions of the molecules in the crucible. This posed a significant problem for the investigation of boronic acids due to their tendency to form anhydrides. A mass spectrum of phenylboronic acid (122 amu) evaporated into the mass spectrometer in Figure 26, shows a significant peak of 2,4,6-triphenylboroxine (312 amu), a cyclic anhydride formed by three phenylboronic acid monomers. This anhydride signal does not change over time (not shown), indicating that the phenylboronic acid molecule is constantly decomposing under evaporation

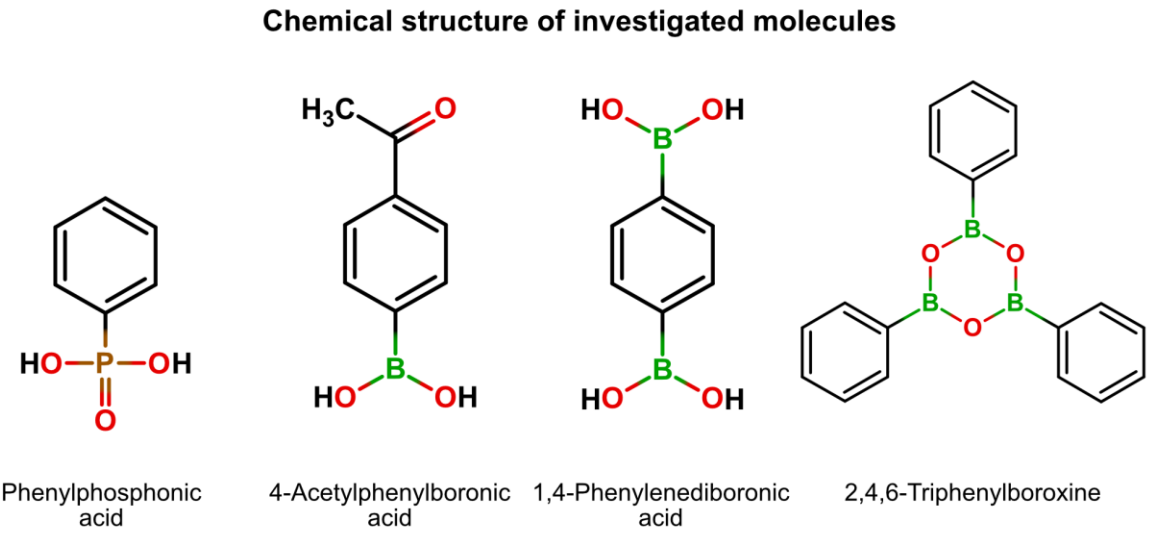

Figure 25: Small organic molecules studied on the surface of rutile TiO_2(110). They all share the same structural pattern: An acid linker group attached to a phenyl ring. With boronic acids, it was not possible to deposit pure phenylboronic acid because we always got 2,4,6-triphenylboroxine impurities. To avoid this, the molecule had to be chemically functionalized, and to study the effect of anhydride deposition, the anhydride was also investigated.

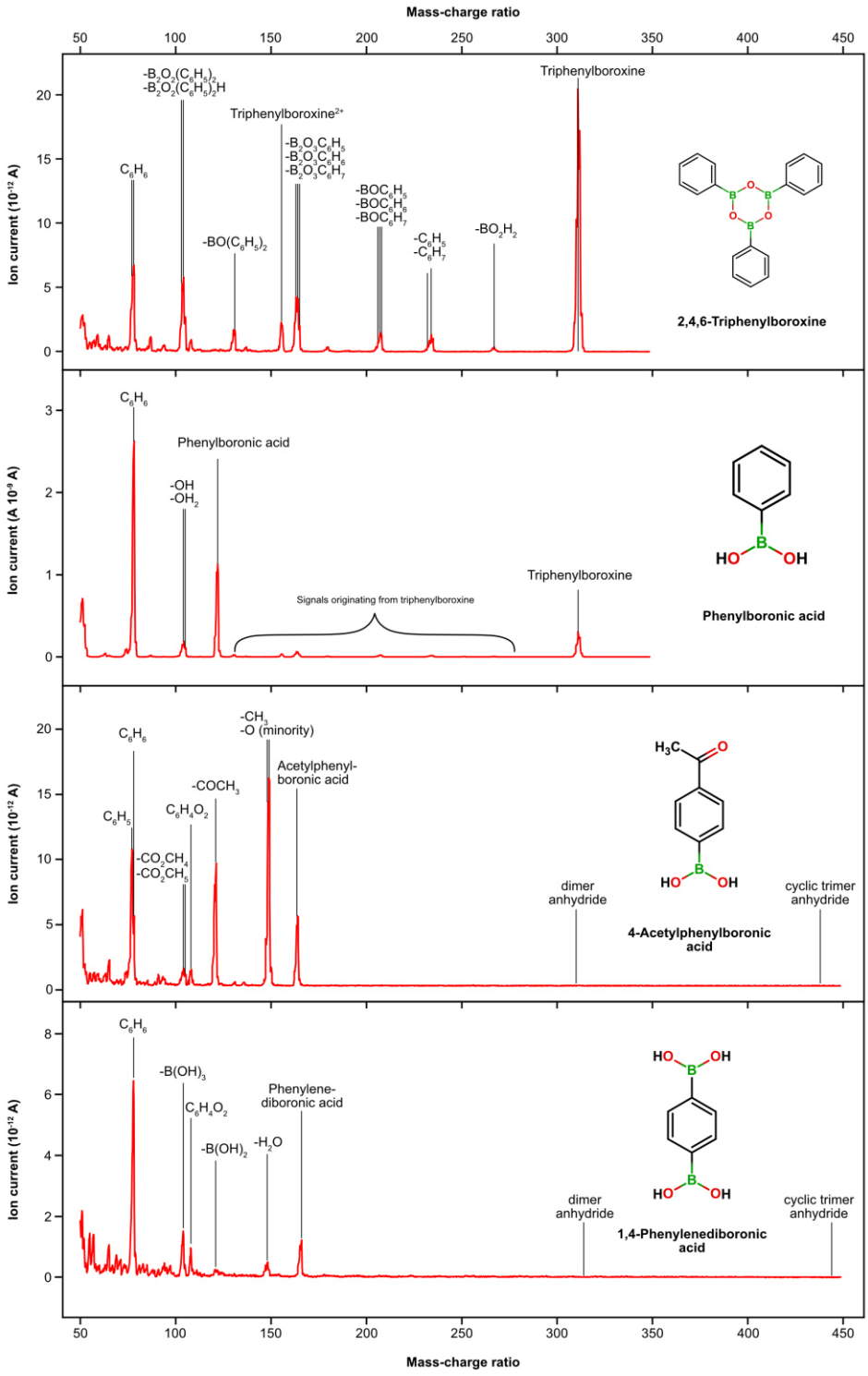

Figure 26: Mass spectra of phenylboronic acid and derivatives when evaporated directly into the mass spectrometer. While phenylboronic acid clearly shows sign of decomposition to 2,4,6-triphenylboroxine, we do not find any evidence for the formation of anhydrides for 4-acetylphenylboronic acid and 1,4-phenylenediboronic acid. Adapted from Ref. [P3].

conditions. Therefore, it is not possible to deposit phenylboronic acid without co-deposition of the anhydride.

Too-high evaporation temperatures can lead to such decomposition reactions, as was briefly discussed with phenylphosphonic acid in Figure 11 in Chapter 3.2.1: Below 470 K pure phenylphosphonic acid is deposited, but exceeding this temperature leads to deposition of the anhydride. Since we observed decomposition of phenylboronic acid, we first tried to obtain clean deposits by lowering the evaporator temperature. However, lowering the evaporator temperature causes a decrease in the deposition rate. As a crude rule of thumb, the deposition rate is halved when the evaporator temperature is lowered by 10 K.[138] Consequently, the deposition time must increase with decreasing evaporation temperatures to maintain the deposition rate at the surface, which gives a practical lower temperature limit.

Besides temperature, the deposition rate at the surface is strongly influenced by the geometry of the setup. The crucible-sample distance and the crucible area are two important parameters that can be adjusted. Therefore, we designed an evaporator with a very large carbon crucible that is placed only a few centimeters away from the sample, see Figure 27. This increased the crucible area from 0.3 cm^2 to 16 cm^2, while decreasing the evaporator-sample distance from about 25 cm to about 3 cm. Thus, these geometric changes should increase the evaporation rate by a factor of 3700, allowing the evaporation temperature to be lowered by very roughly 120 K, while maintaining the deposition rate at the surface. This is an immense increase in evaporation rate, and it clearly shows that evaporation geometry can have a huge impact on the evaporation temperature.

Figure 27: Picture of the evaporator used to evaporate boronic acids (left). Since the large surface area and close proximity to the sample enable comparatively low evaporation temperatures, it is sufficient to heat this evaporator with hot air. A direct comparison of the carbon crucibles of this evaporator and our standard evaporators (right) illustrates the massive difference in surface area of 16 cm^2 and 0.3 cm^2.

With this new evaporator, we were able to significantly lower the evaporation temperatures, but it was still not enough to prevent unwanted co-deposition of the anhydride with phenylboronic acid.

Another way to prevent chemical reactions is to change the reactivity of the molecule itself. We thus focused our attention on derivatives of phenylboronic acid, specifically 4-methoxyphenylboronic acid, 4-acetylphenylboronic acid, and 1,4-phenylenediboronic acid. We were able to evaporate the intact monomer without anhydride contamination for 4-acetylphenylboronic acid and 1,4-phenylenediboronic acid, see Figure 26, but we were unable to achieve this for 4-methoxyphenylboronic acid (not shown). Importantly, it was necessary to recrystallize 4-acetylphenylboronic acid in a 10:1 mixture of deionized water and isopropyl alcohol, which resulted in a material consisting of fine needles, see Figure 28. When only deionized water was used instead, a plate-like material was formed, resulting in the evaporation of the anhydride. We suspect that small amounts of undissolved anhydride molecules act as crystallization nuclei and pure anhydride crystals are formed. In the presence of small amounts of isopropyl alcohol, these crystallization nuclei are dissolved and crystals containing only the monomer are obtained.

It has been a time-consuming project to find out if it is possible to obtain clean deposits of phenylboronic acid and its derivatives. This is primarily due to the fact that it takes a lot of time to

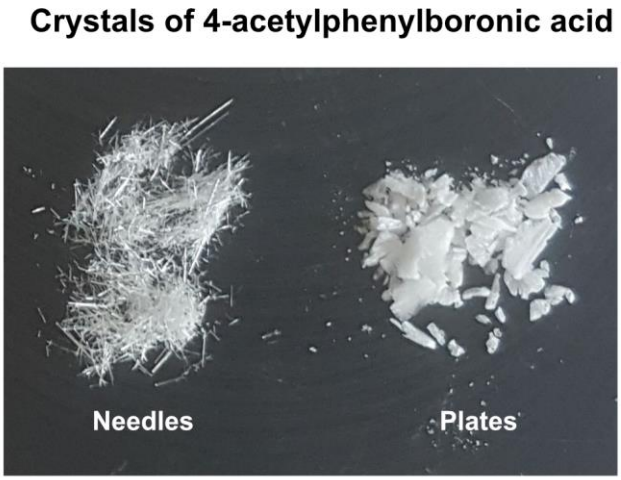

Figure 28: Image of the fine needles obtained for 4-acetylphenylboronic acid (left), which resulted in successful evaporation of the pure monomer. We also obtained plates after recrystallization (right), which resulted in evaporation of the corresponding anhydride. Adapted from Ref. [P3].

prepare and measure samples in UHV. I am grateful to Prof. Dr. Libuda and Dr. Olaf Brummel for allowing me to work on one of their Attenuated Total Reflection (ATR) infrared spectrometers. This enabled a quick evaluation of the powders after vacuum treatment, as ATR measurements under ambient conditions are quick and easy, while UHV testing is much more involved. The ATR-IR measurements confirm the previously outlined observations: A comparison of the spectrum of the fine needles with the spectrum of the as-supplied powder (which was identical to the spectrum of the plates) in Figure 29, shows clear differences between the two species. Most prominent, there are two intense feature for the recrystallized sample at 3470 and 3320 cm^{-1}, but there are also differences in the fingerprint region, for example, the recrystallized sample has an additional peak at 790 cm^{-1}. Thus, ATR-IR is a quick and sensitive tool for distinguishing between powders that contain primarily the anhydride or the intact acid once the spectrum of the pure compound is available.

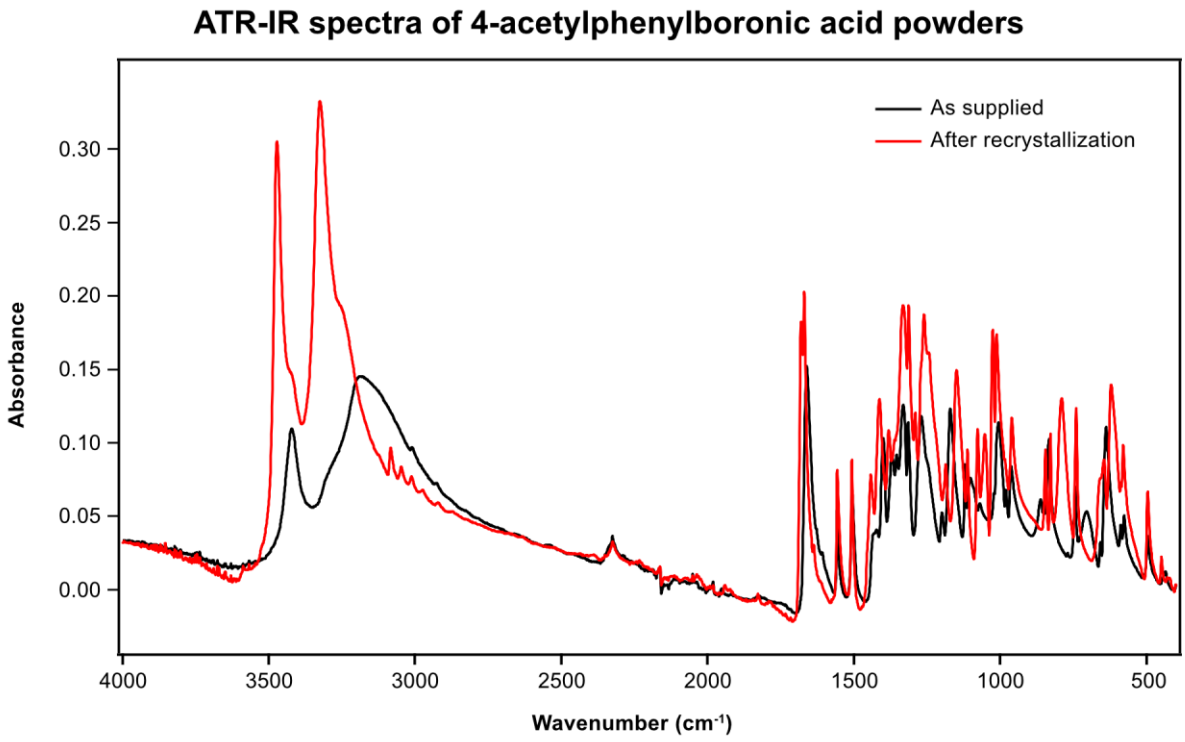

Figure 29: ATR-IR spectra of 4-acetylphenylboronic acid as supplied (black line) and after recrystallization into fine needles and a 24 h vacuum treatment (red line).

In summary, while the deposition of phenylphosphonic acid from a Knudsen effusion cell is comparatively simple, the deposition of boronic acids is much more challenging. Lowering the evaporation temperature is not sufficient to obtain pure boronic acids, and chemical functionalization is necessary to prevent the evaporation of anhydrides. However, this is still not sufficient for 4-acetylphenylboronic acid, which must be recrystallized into fine needles before evaporation.

5.4. Interpreting XPS data of monolayer coverages of organic linker groups

As mentioned above, the O 1s core level contains important chemical information about the bond between the linker group and the surface, but this signal overlaps with the intense substrate contributions. Even when measuring the O 1s core level at the synchrotron, where the surface sensitivity is significantly enhanced, the molecular signal remains only a high binding-energy shoulder on the intense substrate signal at 530.2 eV, see Figure 30.

To analyze the molecular signal, it is therefore necessary to separate the substrate contribution from the molecular contribution. A common approach is to describe the substrate contribution by the shape of the clean-surface O 1s spectrum. This approach can work well, but in the case of phenylphosphonic acid on rutile TiO_2(110), the shape of the substrate peak contribution changes upon adsorption of the molecules, see for example the low binding energy shoulder of the substrate in Figure 30. Using an incorrect description for the substrate contribution leads to a large uncertainty in the less intense molecular contributions, making interpretation of the data very challenging.

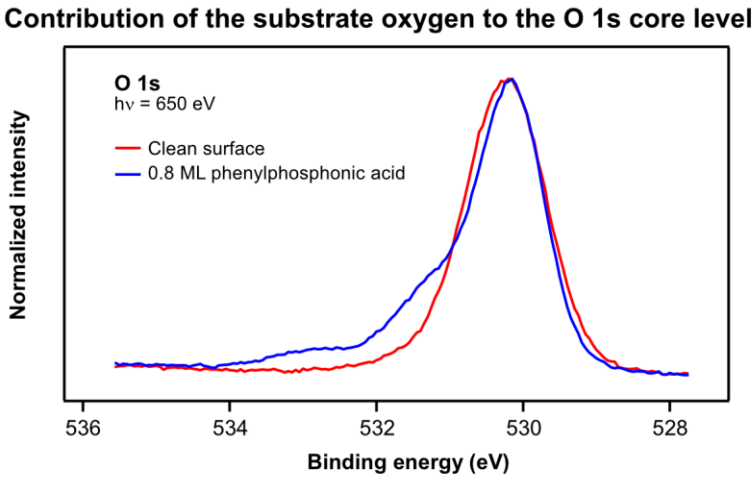

Figure 30: Normalized O 1s spectra of the clean surface and 0.8 monolayers of phenylphosphonic acid on rutile TiO_2(110) measured at a photon energy of 650 eV at 300 K. Although the covered surface has additional peaks at higher binding energies due to contributions from the anchoring group, the shape of the substrate contribution changes (best seen on the low binding energy shoulder of the substrate peak). Adapted from Ref. [P2].

This effect is quite pronounced for phenylphosphonic acid and since it is not possible to determine the new shape of the substrate contribution experimentally, we asked Prof. Dr. Bernd Meyer to tackle this challenge using density-functional theory calculations.

5.4.1. Interpreting experimental XPS spectra with DFT-calculations: Phenylphosphonic acid on rutile TiO_2(110)

In order to interpret our experimental XPS data with density-function theory (DFT) calculations, we need a way to directly compare them to each other. Unfortunately, DFT cannot be used to directly predict a full XPS spectrum; instead, it can be used to calculate the relative XPS binding-energy shifts of the atoms involved. It is common to use DFT-calculated XPS binding-energy shifts to follow chemical changes or to fit a spectrum with components at these positions to the experimental data,[139-142] which is typically limited to only a few different binding energy species. In this thesis, however, it was necessary to consider the contributions of up to 96 different oxygen atoms, and instead of fitting the theoretically-predicted components to the experimental spectrum, we want to predicted the full shape of the O 1s core-level spectrum.

To predict a complete XPS spectrum, it is necessary to know the absolute binding-energy positions, intensity, and peak shape of each individual contribution. The DFT calculation can only provide relative XPS binding-energy shifts of each oxygen atom, and we have to determine the other parameters from somewhere else. We calculated the relative intensities of each atom using the DFT-optimized geometry by calculating the expected attenuation based on the depth relative to the height of the oxygen row. This was done using an inelastic mean-free path of 5.8 Å, calculated for photoelectrons with 120 eV kinetic energy passing through TiO_2 using the TPP2M algorithm developed by Tanuma, Powell, and Penn[143] implemented in the program QUASES-IMFP-TPP2M Ver.3.0 (available for free under http://www.quases.com/products/quases-imfp-tpp2m/). To obtain the peak shape and absolute binding-energy position, we used the clean surface as our reference system. There are 11 different oxygen atoms within the first three trilayers, see Figure 31, and thus we fitted the experimentally-measured O 1s core-level spectrum of the clean surface with 11 peaks, where all relative binding-energy positions were fixed according to the calculated shifts and relative intensities were fixed based on the calculated attenuation. In addition, all 11 components were forced to have the same peak shape. Thus, the clean surface spectrum is

fitted with only three free parameters: Peak width (1.04 eV), Gaussian-to-Lorentzian ratio (0.45:0.55), and the total binding-energy shift (530.21 eV).

The fit to the experimental data is very good, see Figure 31, but there is a small deviation at the high binding energy shoulder at 531.6 eV (marked by an arrow). In fact, a deviation at this binding energy is to be expected, because at this binding-energy position surface OH groups are found on the clean rutile TiO_2(110) surface.[144, 145] These hydroxyl groups are formed by the reaction of water with oxygen vacancies, which are a common defect on vacuum-prepared rutile TiO_2(110) and which cannot be completely avoided experimentally.

With the absolute binding-energy position and the peak shape, we know all parameters that are necessary to predict the full O 1s core-level spectra from DFT-calculated relative binding-energy shifts. The last piece of information is the intensity of each component, but the intensities will differ due to the attenuation caused by the adsorbed molecules. Instead of predicting the intensities, we decided to simply scale the area of the calculated spectra to the area of the experimental spectra.

In our experiment, we investigated overall three (sub)monolayer coverages of phenylphosphonic acid on rutile TiO_2(110), which were annealed from 300 to 750 K for 1 min in steps of 50 K. The experimental O 1s core-level spectra in Figure 32 show an intense substrate peak at 530.1 eV with the molecular contributions on the high-binding energy shoulder. At temperatures below 450 K, two different molecular peaks are visible for all three coverages at 531.5 and 533 eV. Upon annealing to 500 K, the signal at 533 eV disappears while the shape of the high binding energy shoulder at 531.5 eV changes. We observe these trends for all three coverages, indicating no coverage dependence of the adsorption binding mode. The only significant difference is observed for 1.7 ML below 400 K, but this is caused by molecules desorbing from the second layer and not by a change in the adsorption binding mode. Therefore, we find only two different adsorption binding modes: A low temperature species below 450 K and a high temperature species above 500 K.

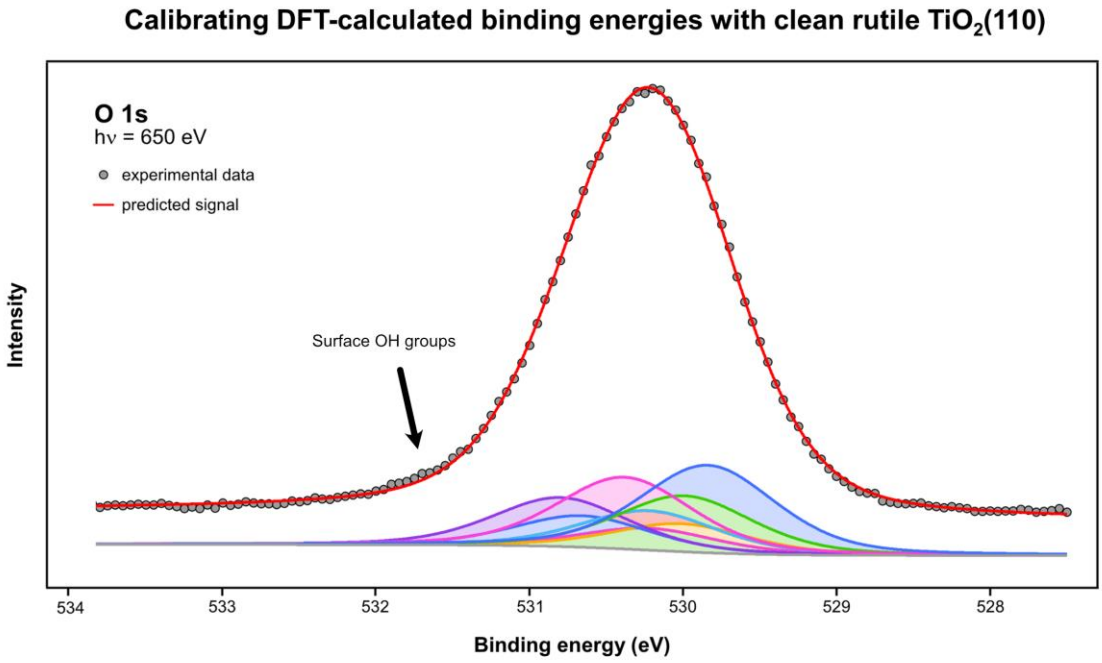

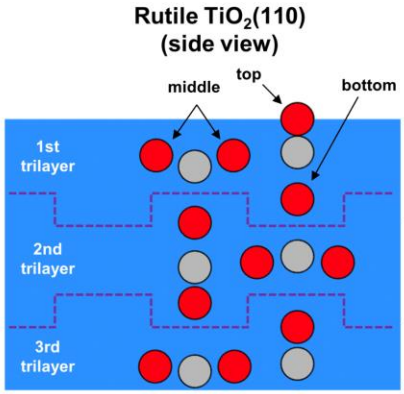

		Depth (Å)	Relative intensity	Relative shift (eV)	Absolute position (eV)
1st trilayer	top	0.00	1.00	-0.37	529.84
	middle	1.17	2× 0.82	+0.17	530.38
	bottom	2.58	0.64	-0.22	529.99
2nd trilayer	top	3.33	0.56	+0.59	530.80
	middle	4.61	2× 0.45	+0.01	530.22
	bottom	5.91	0.36	+0.45	530.66
3rd trilayer	top	6.68	0.32	-0.20	530.01
	middle	7.96	2× 0.25	+0.01	530.22

Figure 31: Calibrating the calculated clean-surface O 1s core-level shifts to the clean surface. The calculation yields the relative binding energy as well as the depth in the crystal. Using a very simplistic model, the expected XPS intensity of each oxygen atom within the first three trilayers is calculated assuming an inelastic mean-free path of 5.8 Å. The clean surface spectrum is subsequently fitted, while the relative binding energies and the relative intensities are fixed. The obtained information about the absolute peak position at 530.21 eV and peak shape parameters (width: 1.04 eV; Gaussian-to-Lorentzian of 0.45:0.55) were subsequently used to predict the O 1s core-level spectra of the other DFT structures. Adapted from Ref. [P2].

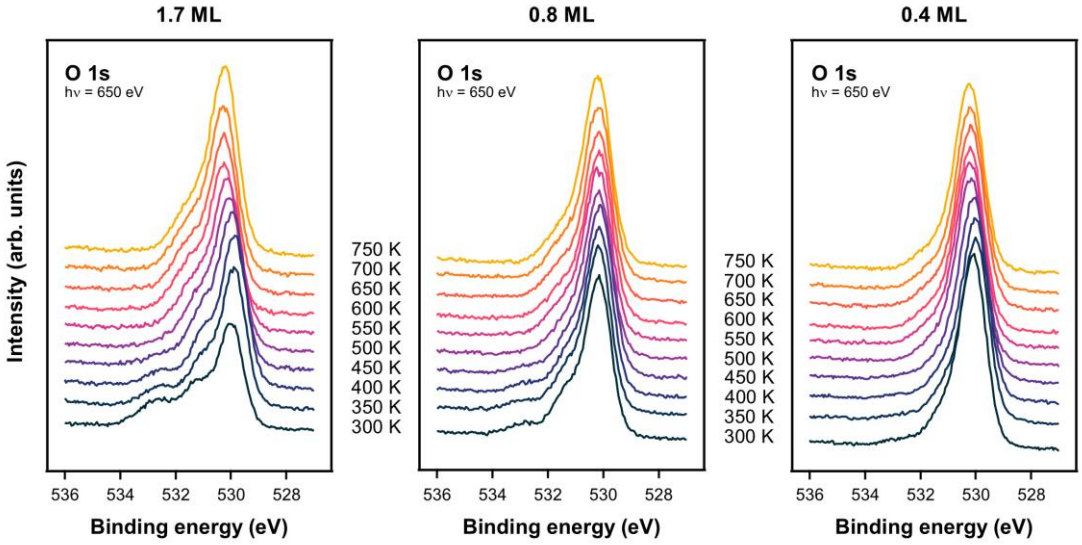

Figure 32: Experimental O 1s spectra for three different coverages of phenylphosphonic acid on rutile TiO_2(110), annealed at the indicated temperatures for 1 min. The spectra are dominated by the intense substrate peak located at 530.1 eV, while the high binding-energy shoulder is caused by the adsorbed molecules. For 1.7 ML, the changes between 300 and 400 K are the result of molecules desorbing from the second layer. Adapted from Ref. [P2].

Starting with the low-temperature species, the energetically most promising DFT structures suggest a bidentate adsorption mode, where two oxygen atoms of the molecule bind to two Ti 5c sites, while the third oxygen atom interacts with the oxygen row via hydrogen bonding, see Figure 33. There are two ways in which the protons can be distributed: The bidentate one-fold deprotonated adsorption mode (PPA 1) is singly deprotonated and still has a P-OH group, whereas in the two-fold deprotonated adsorption mode (PPA 2) the proton of the P-OH group is transferred to the oxygen row. Although this results in a very small change in adsorption geometry and energy, the resulting predicted XPS spectra are very different, see Figure 33. While we find a poor agreement between a primitive PPA 2 monolayer and the experimental data, the spectrum of the primitive PPA 1 monolayer agrees exceptionally well. Although the absolute binding-energy position is slightly off, the shape of the overall spectrum is reproduced, including changes to the substrate peak shape.

Comparing the calculated binding-energy shifts of the clean surface in Figure 31 with the shifts of the primitive PPA 1 structure in Figure 34 reveals the reasons for the change in the substrate peak shape: First, the binding-energy position of the oxygen row atoms shifts from the low binding

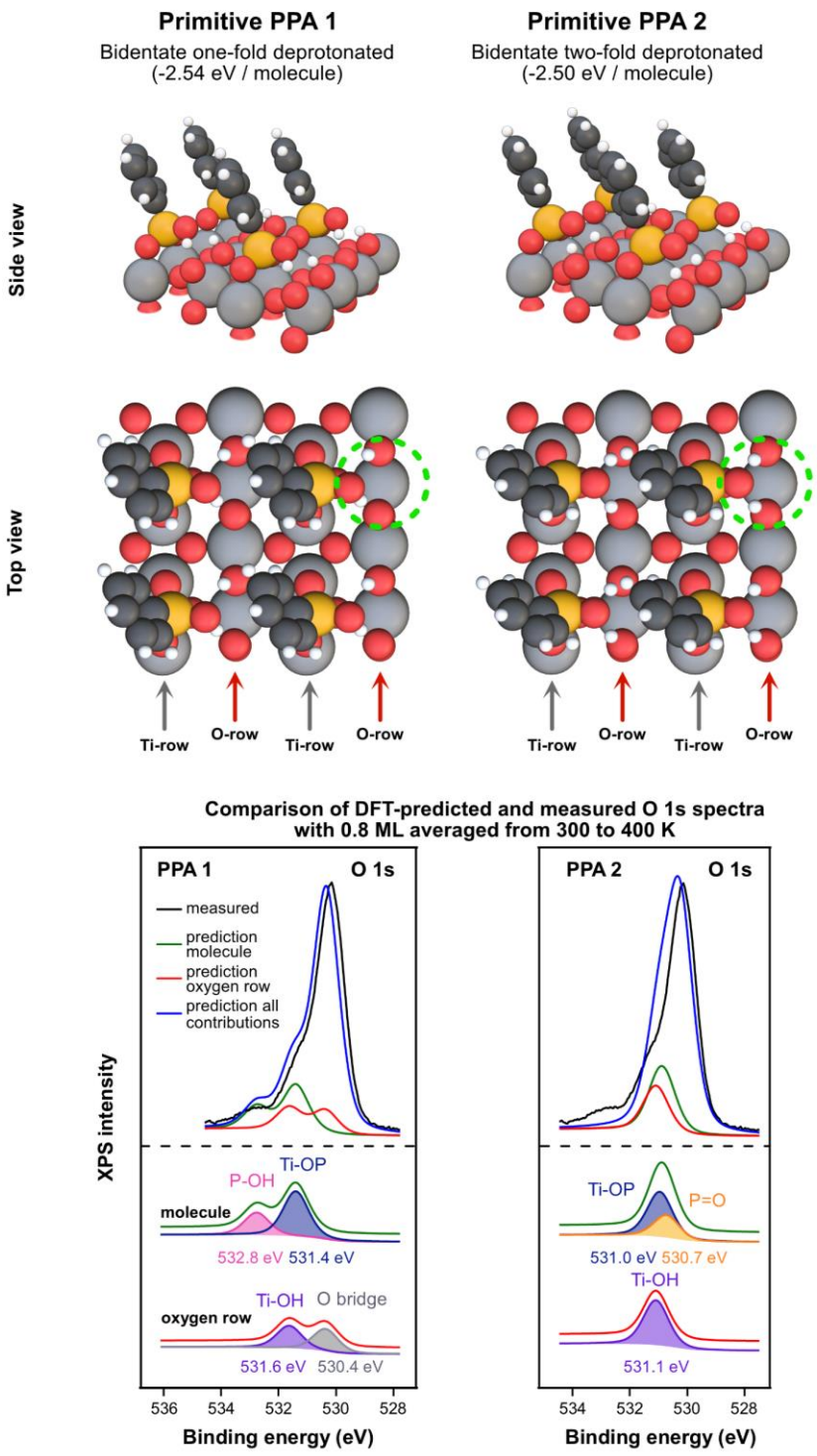

Figure 33: DFT-predicted O 1s core-level spectra of the bidentate one- and twofold deprotonated adsorption binding modes with experimental O 1s core-level spectra with a coverage of 0.8 ML averaged from 300 to 400 K. Calculations were performed on a unit cell containing only a single molecule, but for the presentation the unit cell was accordingly multiplied. Adapted from Ref. [P2].

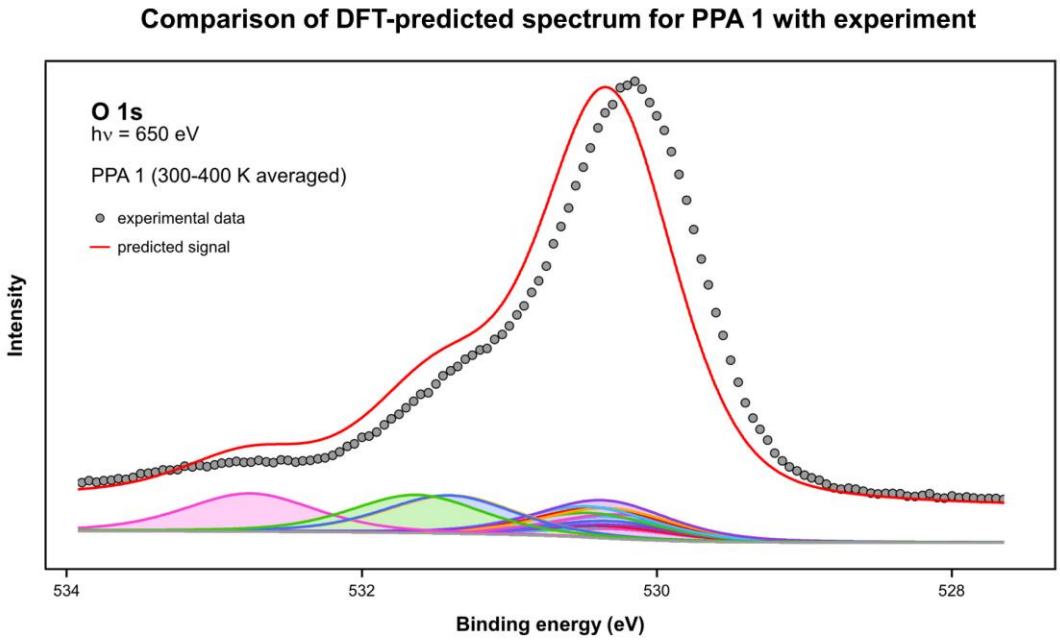

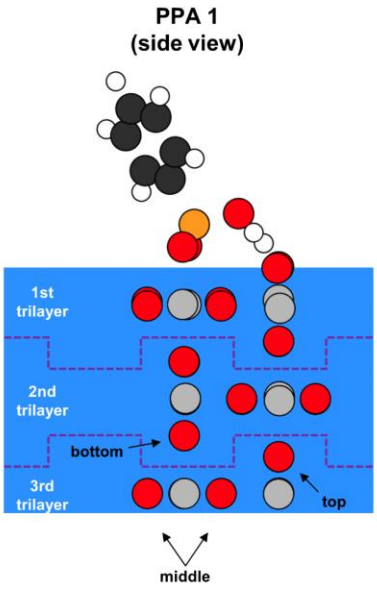

		Relative intensity	Relative shift (eV)	Absolute binding energy (eV)
Contribution from molecule	P-OH	1.00	+2.55	532.76
	Ti-O-P	1.00	+1.20 / +1.18	531.41 / 531.39
1st trilayer	top	1.00	+1.43 / +0.15	531.64 / 530.36
	middle	0.81 / 0.79	+0.24 / +0.16	530.45 / 530.37
		0.81 / 0.79	+0.25 / +0.11	530.46 / 530.32
	bottom	0.64	+0.04 / +0.24	530.25 / 530.45
2nd trilayer	top	0.57	2×+0.11	2×530.32
	middle	0.45 / 0.46	+0.10 / +0.08	530.31 / 530.29
		0.45 / 0.46	+0.09 / +0.07	530.30 / 530.28
	bottom	0.36	+0.08 / +0.07	530.29 / 530.28
3rd trilayer	top	0.32	-0.02 / +0.11	530.19 / 530.32
	middle	0.26 / 0.26	2×+0.06	2×530.27
		0.26 / 0.26	+0.06 / +0.05	530.27 / 530.26

Figure 34: Details on the calculation of the XPS spectrum of PPA 1. The table shows the relative intensities extracted from the DFT-optimized geometry are given in combination with the relative binding-energy shifts. These calculated parameters are then used in combination with the peak shape parameters and the absolute binding energy extracted for the clean surface in Figure 31 to predict the full XPS spectrum. Adapted from Ref. [P2].

energy side to the high binding-energy side of the substrate signal due to the presence of protons. Second, the spread of the XPS binding-energy shifts of all the substrate oxygen atoms is much smaller in the PPA 1 structure than for the clean surface. The spread in the XPS binding-energy shifts of the clean surface is caused by well-known relaxations of the oxygen atoms,[146-148] see Figure 31. After adsorption of a molecule, the oxygen atoms re-relax back, closer to their expected bulk positions, see Figure 34, aligning their O 1s binding energies in the process. Such an effect is not unique to phosphonic acid, as re-relaxations have already been reported for formic acid using photoelectron diffraction[149] and low-energy electron diffraction[150].

At about 500 K we observe an on-surface reaction, which is a technologically very relevant reaction, as annealing monolayers of phosphonic acids on oxides increases their adhesion strength significantly.[132, 151, 152] The observed temperature range is consistent with the water desorption temperature observed on the clean rutile TiO_2(110) surface by the recombination of surface OH groups,[153-156] although this temperature can change in the presence of adsorbed molecules.[157] In this reaction, two surface OH groups form water and an oxygen vacancy. Since each adsorbed molecule provides two protons, one oxygen vacancy can be formed for each molecule. The adsorbed phenylphosphonic acid molecule will most likely react to this new oxygen vacancy by dropping its third, unbound oxygen atom into the oxygen vacancy, forming a tridentate adsorption mode (PPA 3). However, the calculated O 1s core-level spectrum of a primitive PPA 3 monolayer does not match the experimental O 1s spectrum, see Figure 35 (left).

In PPA 3, the oxygen vacancies are evenly distributed, i.e., each molecule is adjacent to one oxygen vacancy. However, it is also possible to distribute the oxygen vacancies unevenly, with half of the molecules being adjacent to two vacancies and the other half being adjacent to no oxygen vacancies, see Figure 36. This results in two very different adsorption binding modes. If there are no oxygen vacancies next to the molecule, the molecule can only bind in a bidentate adsorption mode (PPA 4), where two oxygen atoms bind to Ti 5c sites and the third oxygen atom faces away from the surface, resulting in a strongly tilted phenyl ring. In the case of two adjacent oxygen vacancies, the molecule binds in a rotated tridentate adsorption mode (PPA 5), with two molecular oxygen atoms filling the two vacancies and the third oxygen atom binding to a Ti 5c site. Note that the bidentate adsorption mode PPA 4 is very different from the previously discussed bidentate PPA 1 and PPA 2 due to the lack of protons.

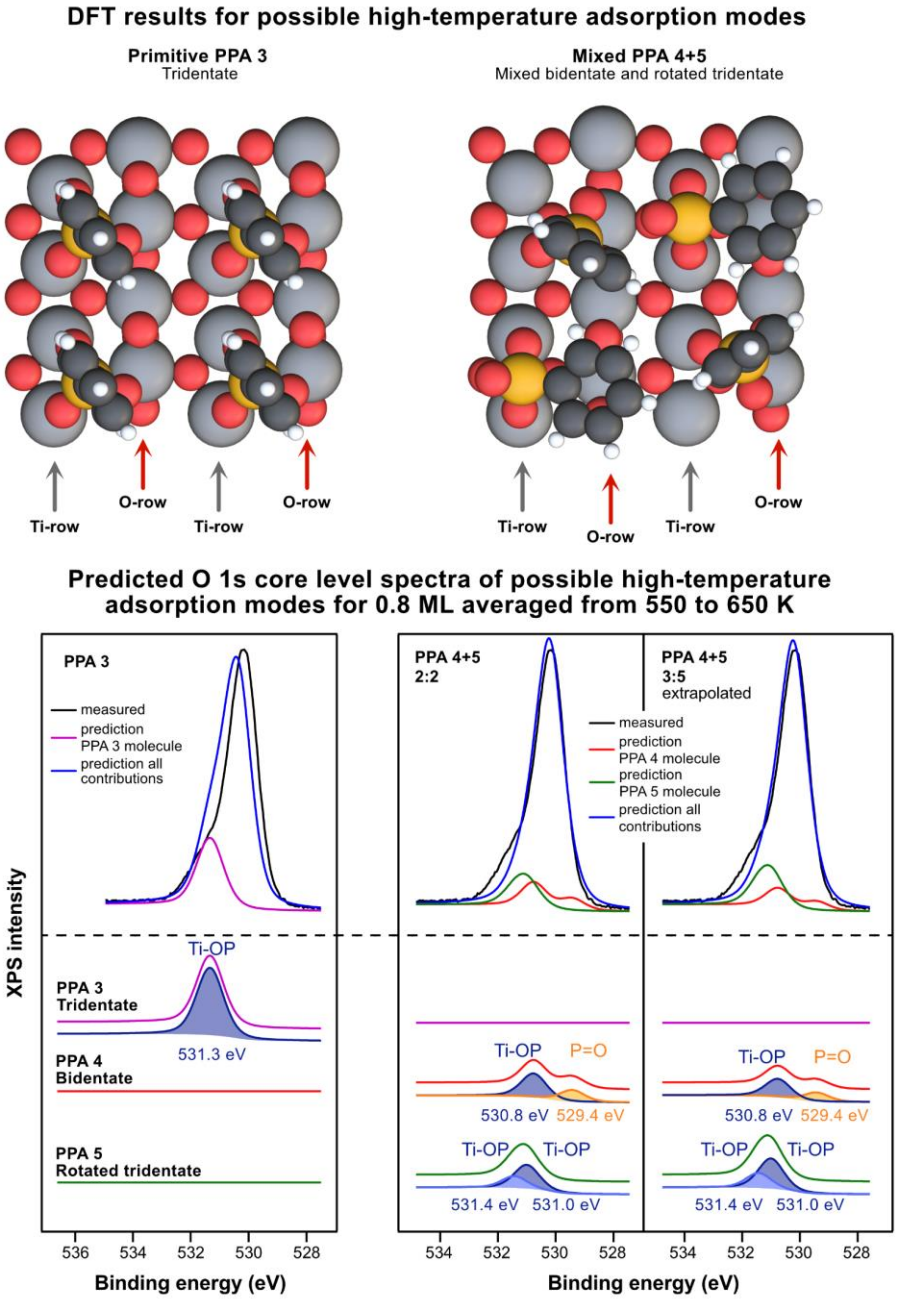

Figure 35: DFT-optimized structure and corresponding predicted O 1s core-level spectra for the tridentate (PPA 3) and mixed bidentate-tridentate (PPA 4+5) structures. The O 1s signal of the mixed PPA 4+5 structure was extrapolated to account for a potential 3:5 ratio between PPA 4 and PPA 5 caused by naturally-occurring oxygen vacancies. This was done by dividing the structure into four quadrants and multiplying the signal from each quadrant to obtain a 3:5 ratio. Adapted from Ref. [P2].

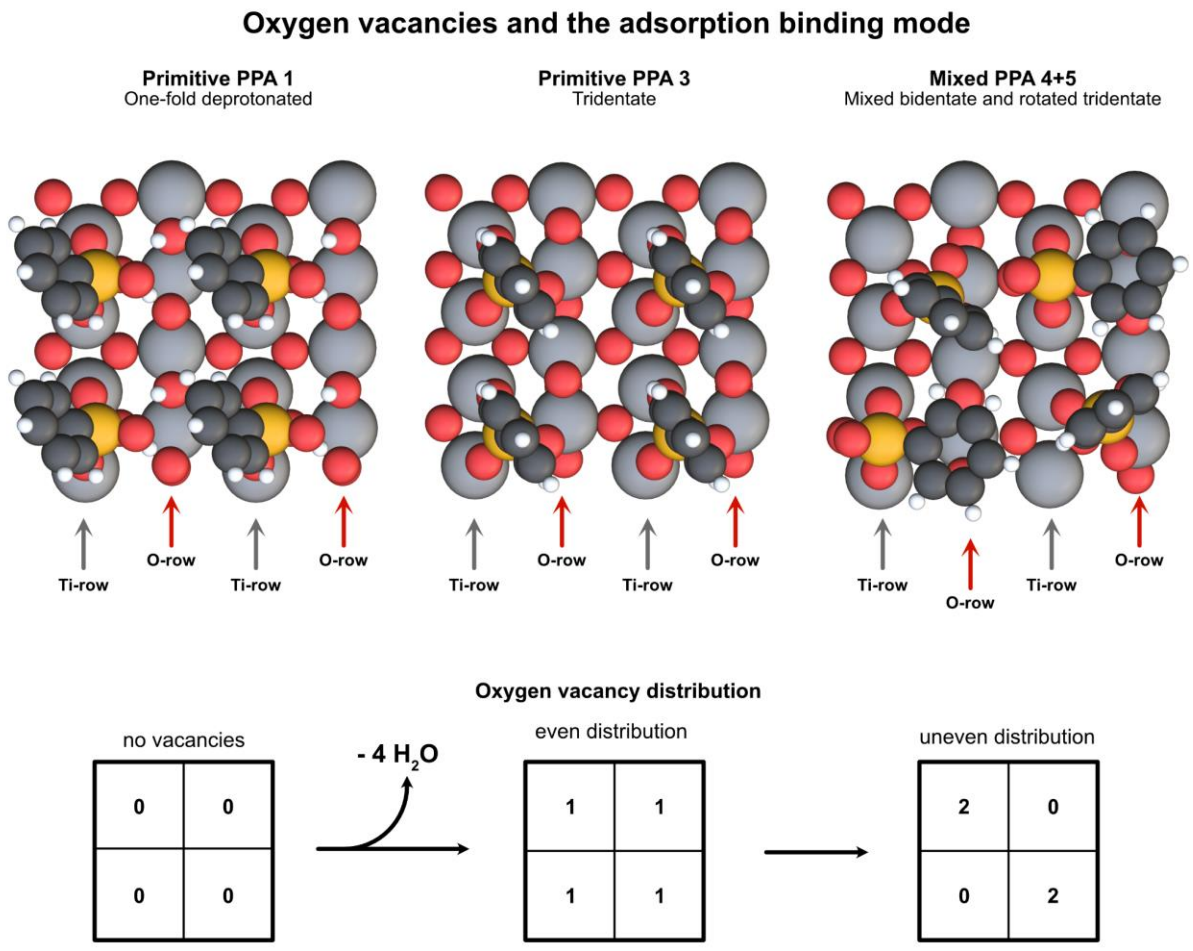

Figure 36: Illustration of the on-surface reaction of phenylphosphonic acid after annealing. The primitive PPA 1 structure found at temperatures below 450 K releases four water molecules, forming four oxygen vacancies. If these oxygen vacancies were evenly distributed, i.e. one molecule per vacancy, a primitive PPA 3 monolayer would be formed. However, it is also possible to distribute these vacancies unevenly, resulting in two different molecular species on the surface: Molecules can be adjacent to two vacancies (PPA 5) or to no vacancy (PPA 4), resulting in very different phenyl-ring orientations. Adapted from Ref. [P2].

The O 1s spectrum of the mixed PPA 4+5 structure is an improvement over the PPA 3 spectrum, see Figure 35, but it is still not as good of a match as PPA 1 for the low temperature data.

The P 2p core level can also provide valuable information about the adsorption binding mode, and experimentally we observe a single doublet at 133.6 / 134.5 eV after deposition of the molecules at room temperature, see Figure 37. Upon annealing the deposits above 450 K, the signal broadens and the resulting spectra can be described by adding a second doublet shifted by 0.5 eV to higher

binding energies. Thus, at low temperatures there is only one phosphorus species, but after annealing there are at least two different phosphorus species on the surface.

DFT can also help to interpret these experimental data. However, it is not possible to predict the P 2p XPS spectra from the calculation because it is not possible to obtain absolute XPS binding energies from DFT calculations, and even the binding-energy shifts from different structures are not comparable. We avoided this for the O 1s core level by using the oxygen atoms in the fourth trilayer as a bulklike reference, but there is no bulklike reference in the P 2p core level. Instead,

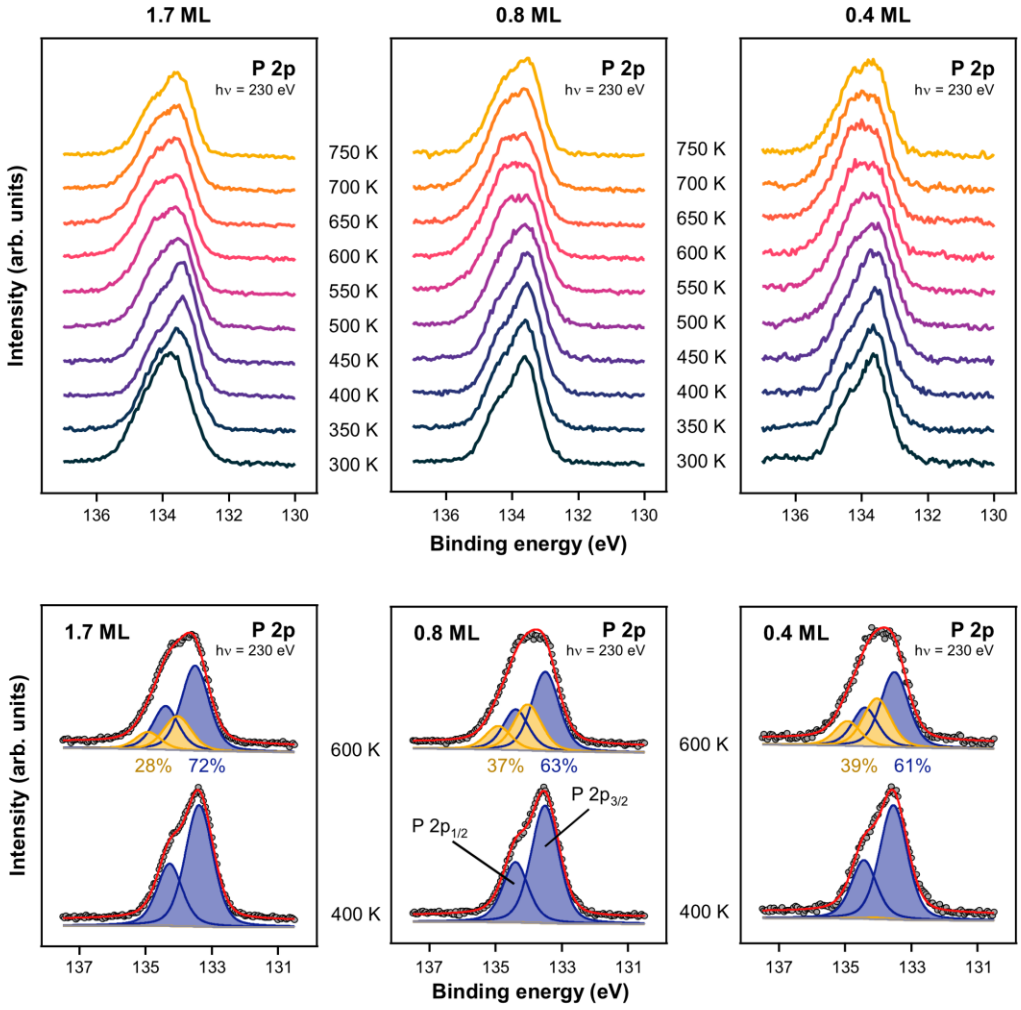

Figure 37: Experimental P 2p spectra for three different coverages of phenylphosphonic acid on rutile TiO_2(110) annealed for 1 min at the indicated temperatures. Below 450 K, the data can be described by a single P 2p doublet, indicating a single phosphorus species. We observe a peak broadening above 500 K and at least two doublets are required to describe the data. For 1.7 ML, the changes in the signal between 300 and 400 K are due to the desorption of molecules in the second layer. Adapted from Ref. [P2].

we created new adsorption structures containing mixtures of the different adsorption modes, for example, one PPA 4, one PPA 5, and two PPA 1. We now use the PPA 5 phosphorus atom as an internal reference and thus we are able to compare the relative binding-energy shifts of the different adsorption binding modes, see Table 4. We find that the P 2p binding-energy position of the bidentate one-fold deprotonated PPA 1 and the rotated tridentate PPA 5 to be almost the same, and only PPA 4 is shifted by about 0.9-1.0 eV to higher binding energies, see Table 4.

These results are in qualitative agreement with our experimental observation in Figure 37: The main peak remains at the same binding-energy position after heating (conversion of PPA 1 to PPA 5), while a new species is formed at higher binding energies (PPA 4). However, the experimentally observed shift is only about 0.5 eV, significantly smaller than the calculated binding-energy shift of 0.9-1.0 eV. This discrepancy could be due to the lower accuracy of the P 2p calculations compared to the O 1s calculations (see Ref. [P2] for more details).

Based on the calculations, we would expect a 1:1 ratio between the two phosphorus species, but we observe experimentally a 4:6 ratio. This discrepancy can be explained by the influence of naturally-occurring oxygen vacancies, which are formed during surface preparation by sputter-annealing cycles. The concentration of the oxygen vacancies is reported to be between 5 – 15% of the oxygen row atoms.[24-26] If we assume to have two oxygen vacancies per eight adsorbed molecules (corresponding to 12.5% oxygen vacancies) and consider that vacancies prefer to distribute unevenly, the two oxygen vacancies convert one molecule from bidentate (PPA 4) to rotated tridentate (PPA 5), resulting in a 3:5 ratio between PPA 4 and PPA 5. This ratio is in very good agreement with the experimentally-observed ratio of 4:6 in the P 2p core level, supporting a mixed PPA 4+5 structure. Naturally-occurring oxygen vacancies will also change the O 1s core-

Table 4: DFT-calculated relative binding-energy positions in eV for two different structures containing molecules with the identified adsorption binding modes. The binding energies are relative to the phosphorus in the PPA 5 molecule. Adapted from Ref. [P2].

	Structure 1	Structure 2
PPA 1	-0.11 / +0.13	Not present
PPA 3	Not present	+0.15 / +0.21
PPA 4	1.00	0.94
PPA 5	0.0	0.0

level spectrum. Unfortunately, it is not feasible to run a DFT calculation on a unit cell containing eight molecules, because the calculation of the O 1s core-level shifts is rather involved. Therefore, we extrapolate the spectrum by dividing the PPA 4+5 structure into four quadrants (2×PPA 4 and 2×PPA 5) and multiplying the signal from each quadrant to obtain a 3:5 ratio. Overall, we obtain a decent fit in Figure 35 for the high-temperature species that reproduces the general features in the O 1s core level, including changes in the substrate-related contributions, but it fails to capture the high binding-energy shoulder. Although a mixed PPA 4+5 adsorption mode agrees very well with the P 2p core level, the imperfect fit to the O 1s core-level data suggests that our description of the surface is still incomplete. More details on the DFT calculations, including all the DFT-calculated binding-energy shifts, can be found in Ref. [P2].

There is one piece of experimental observation that was not addressed in these calculations: Polarons. As previously discussed in Chapter 2.2, polarons are localized excess charge carriers, which are typical for the rutile TiO_2(110) surface. The presence of polarons can be observed both in the Ti 2p core level and in the valence band. As expected, we observe polaron-related signals for the clean surface, see Figure 38. In the Ti 2p core level we observe a shoulder at lower binding energies, indicating the presence of Ti^{3+}, and in the valence band we observe the bandgap state at about 1 eV. However, upon adsorption of molecules, the polaron-related signals lose intensity beyond what would be expected based on attenuation alone. When the covered surface is annealed above 500 K, the polaron-related signals return with intensities comparable to the clean surface. However, these signals are still attenuated by the carbon overlayer, and therefore the polaron-related signals at 600 K are significantly more intense than for the clean surface.

There are two possible explanations for the increased polaron signal at high temperatures: First, the molecules in the mixed PPA 4+5 adsorption mode increase the overall polaron concentration. Second, the molecules stabilize the polarons in the first surface layer instead of the second layer, which is the most stable position for the clean surface.[79, 158-160] Polarons in the first surface layer are attenuated less and the experimental data would be in line with having the same polaron concentration as for the clean surface in the first surface layer.

Explaining all the observations of the polarons requires in-depth DFT calculations including polarons. Nonetheless, our calculations suggest that surface re-relaxations could be the cause for our observations. When the molecules adsorb, the oxygen atoms of the surface-near layers re-relax

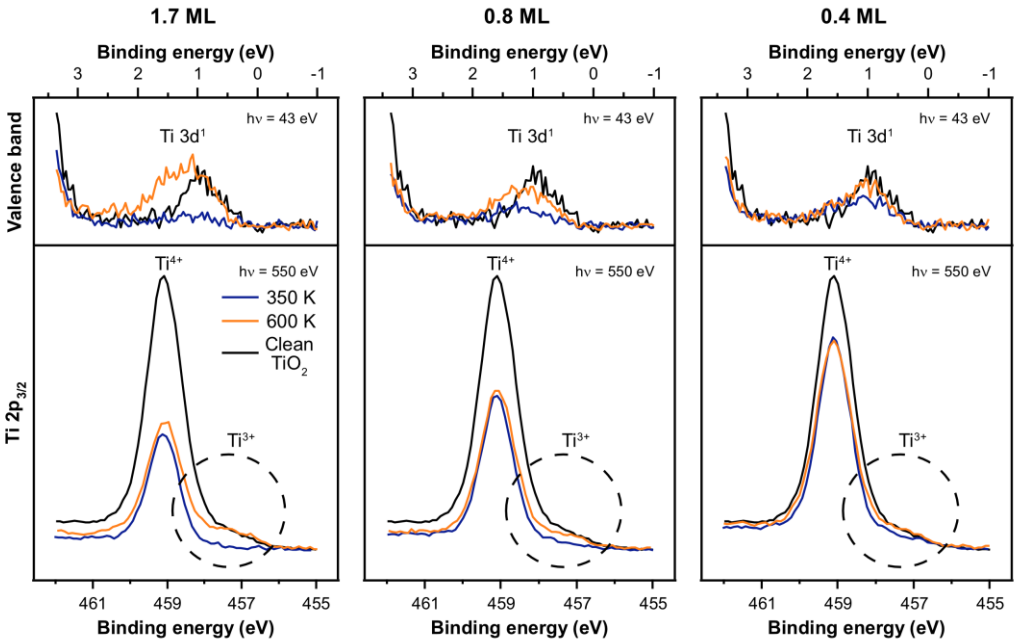

Figure 38: Valence band and Ti 2p spectra for three different inital phenylphosphonic acid coverages on rutile TiO_2(110), annealed at 350 and 600 K for 1 min. Small near-surface polarons are visible as the Ti $3d^1$ bandgap state in the valence band and the Ti^{3+} shoulder in the Ti 2p region. The small polarons of the clean surface are suppressed upon adsorption of phenylphosphonic acid, but they return upon annealing at 600 K. Correcting for the attenuation of the substrate signal caused by the phenylphosphonic acid overlayer (10, 50 and 65% for 0.5, 0.8, and 1.7 ML, respectively), the small polaron intensity at 600 K is about twice as high as that of the clean surface. Adapted from Ref. [P2].

back towards the bulk position. As polarons distort the lattice around them, the re-relaxations could remove the stabilization of polarons in the surface-near layers compared to the bulk, resulting in a decreased polaron concentration in the surface-near regions. When the adsorption mode changes from PPA 1 to PPA 4+5, the massive loss of oxygen row atoms introduces distortions, especially around the oxygen vacancies, which could stabilize polarons in the first surface layer.

It is the exception, not the norm, to have such detailed DFT calculations to aid in data interpretation. If no calculations of the O 1s core-level binding energies are available, one is forced to assign the observed binding-energy positions based on literature values and/or multilayer reference data. However, for phenylphosphonic acid on rutile TiO_2(110), we can compare multilayer spectra to DFT-calculated binding energies.

The multilayer spectrum of phenylphosphonic acid in Figure 39 has two peaks in a 2:1 ratio at 534 and 532.5 eV, which can be assigned to the P-OH and P=O species, respectively. Assuming the

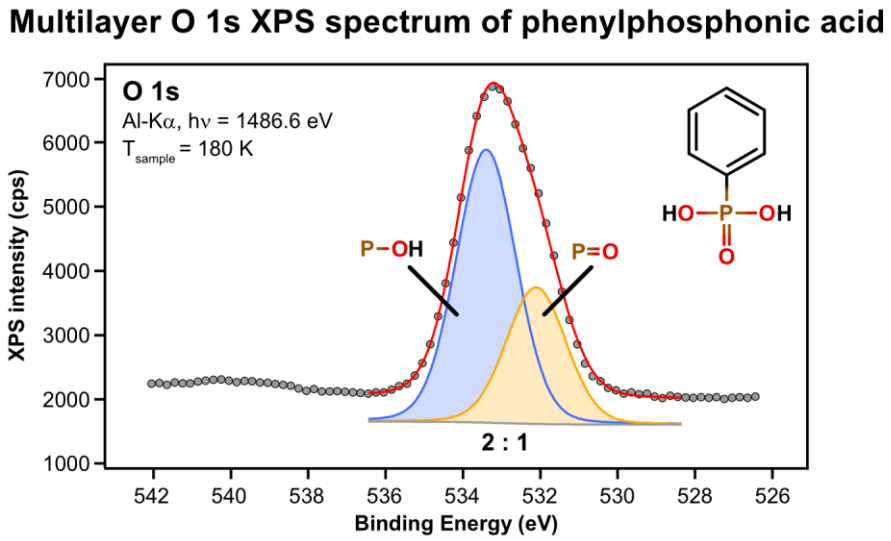

Figure 39: Phenylphosphonic acid multilayer spectrum on a rutile TiO_2(110) surface, where the substrate oxygen signal is not observable due to attenuation. The spectrum is aligned to the C 1s signal at 285.0 eV. Adapted from Ref. [P2].

binding-energy position of the P-OH and P=O species does not change upon adsorption, it is possible to predict the XPS peak positions of the potential adsorption binding modes. This also requires the binding-energy position of the Ti-O-P and Ti-OH group, but these can be found in the literature at about 531.5 eV, on the shoulder of the substrate oxygen signal.[48, 131, 161]

For the adsorption of phenylphosphonic acid on rutile TiO_2(110), we can compare the predictions based on these simple considerations with our DFT-predicted O 1s spectra, see Figure 40. A direct comparison with DFT calculations shows that while the Ti-OH and Ti-OP binding-energy positions agree well, the molecular contributions of the P-OH and especially the P=O contribution deviate significantly. This is probably caused by differences in the hydrogen bonding network for molecules bound in a multilayer and the adsorbed molecules in the monolayer.

If the experimental data had been interpreted according to the scheme outlined in Figure 40, one would have assigned the low-temperature species to a two-fold deprotonated adsorption mode instead of a one-fold deprotonated adsorption mode. One would come to such a different conclusion because the DFT-predicted binding-energy position of the P-OH group unfortunately matches quite well with the multilayer binding-energy position of the P=O group.

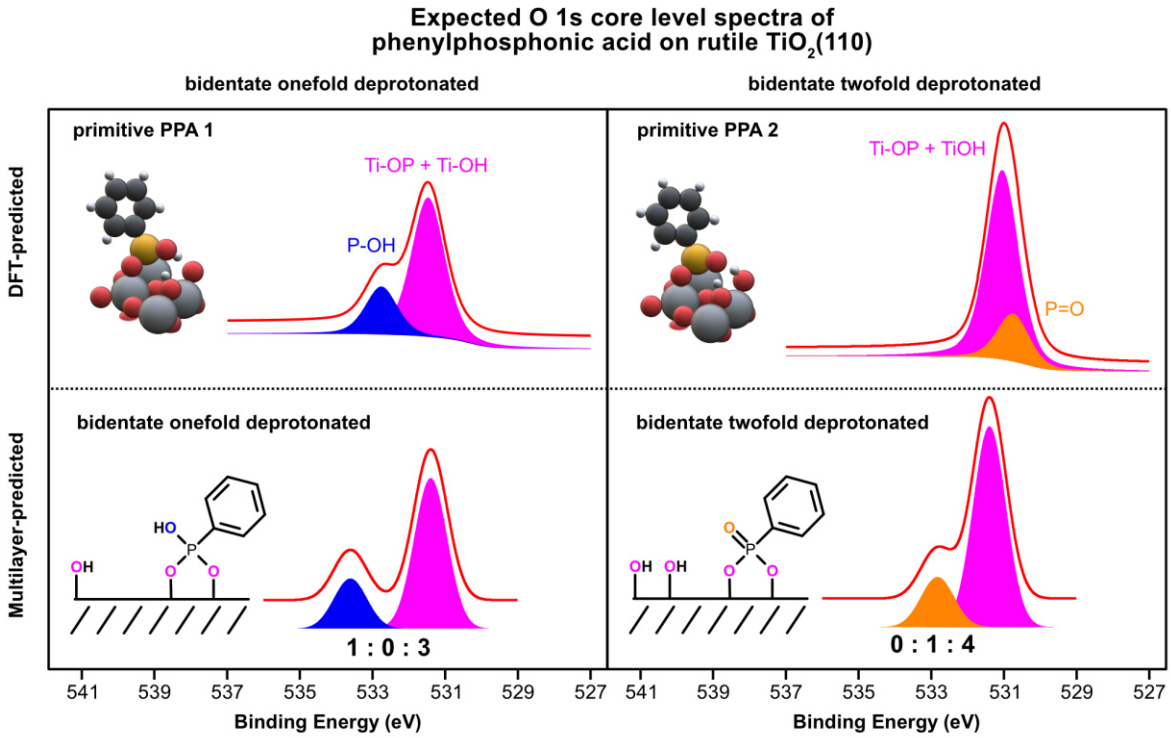

Figure 40: Comparison of the DFT-predicted O 1s core levels (top) with spectra fingerprints predicted based on multilayer data and literature references. Critically, the binding-energy positions of the P-OH and P=O groups in the DFT calculations differ significantly from their respective multilayer-predicted fingerprints.

In addition, our calculations clearly show that the P=O species can have very different binding-energy positions in a primitive PPA 2 monolayer (530.7 eV) and in the high-temperature PPA 4+5 monolayer (529.4 eV). Therefore, it is not possible to assign a single binding-energy position to P=O for this system. Our results therefore strongly suggest that multilayer references are not suitable for interpreting the O 1s signal for phenylphosphonic acid because the binding-energy positions of the different species are very different from a multilayer reference and change depending on the adsorption binding motif.

When interpreting O 1s core-level data without in-depth DFT-calculations, it is therefore very important to keep the limitation of multilayer references in mind.

5.4.2. Determining the adsorption binding mode without DFT calculations: Boronic acid derivatives on rutile TiO_2(110)

In general, acids bind to the rutile TiO_2(110) surface by deprotonation of the OH group and subsequent formation of a Ti-O bond. Such a behavior is expected for Brønsted acids, like phosphonic acid, but boronic acids behave primarily like Lewis acids. In aqueous solution, for example, they do not deprotonate at their B-OH group, but they react with water to form a tetrahedral R-$B(OH)_3^-$ anion and release a proton.[162] On the rutile TiO_2(110) surface, the boron atom could therefore react with an oxygen-row atom and as a result, the bond between boronic acid and the surface could be mediated primarily by the boron atom. However, these acids can also exhibit Brønsted acidity in solution if the formation of a tetrahedral anion is suppressed.[163] It is therefore also reasonable that boronic acids could act as a Brønsted acid, especially because alcohols like ethanol or catechol, which should possess similar Brønsted acidity as a B-OH group, are known to deprotonate on the rutile TiO_2(110) surface.[43, 164]

Fortunately, we are able to distinguish a tetrahedral from a trigonal boron geometry with B K-edge NEXAFS. While a tetrahedral boron center, like for boric acid at pH 13[165] or in the mineral danburite ($CaB_2Si_2O_8$)[166], has only a broad σ*-resonance at 198 eV, trigonal planar boron, like for boric acid (crystalline[166, 167] or in water at pH 5[165]) or in the mineral ludwigite ($Mg_2Fe^{3+}BO_5$)[166], has both π*- and σ*-resonances at about 195 and 210 eV, respectively. We followed the B K-edge NEXAFS signals for all three investigated phenylboronic acid derivatives, namely 4-acetylphenylboronic acid, 1,4-phenylenediboronic acid, and 2,4,6-triphenylboroxine, and we always observed a clear π*-resonance, see Figure 41. This indicates a trigonal planar boron geometry and based on that we can exclude strong interactions between the boron atom of the acid group with surface oxygen atoms.

The signal in Figure 41 also shows that all three molecules remain on the surface even after annealing, which indicates a strong interaction with the rutile TiO_2(110) surface. Since there is no bond between the boron atom and the surface, we must have a strong interaction between the oxygen atoms of the boronic acid group and the titanium atoms of the surface. Depending on the degree of deprotonation, we can have either a monodentate adsorption mode, where only one proton is transferred from the acid group to the oxygen rows, or a bidentate adsorption mode, where both protons are transferred. O'Rourke *et al.* performed DFT-calculations on boronic acid

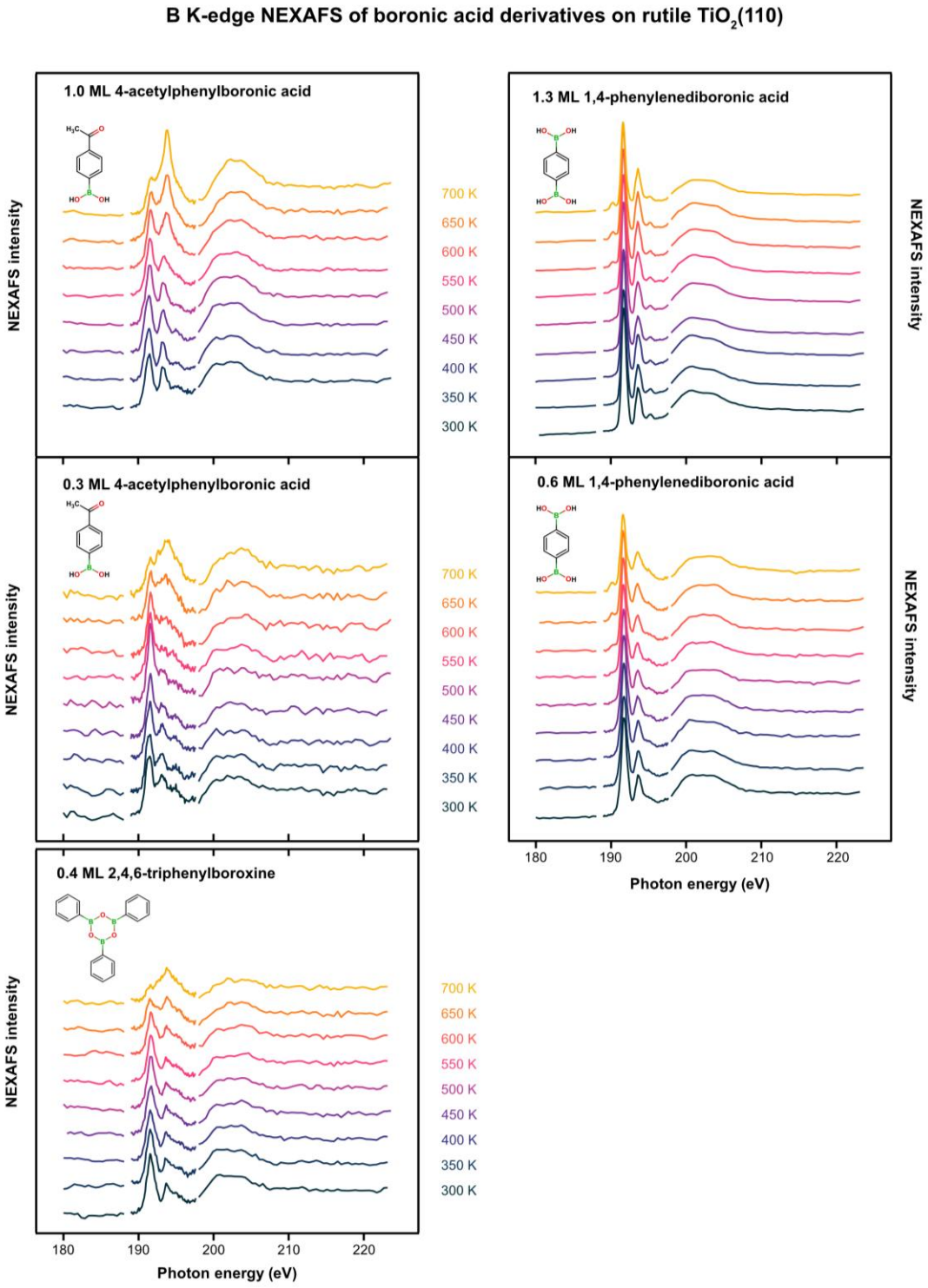

*Figure 41: B K-edge NEXAFS spectra three phenylboronic acid derivatives on rutile TiO2(110) measured at an orbital and azimuthal **E**-field vector of 40° and 45°, respectively. With this **E**-field vector orientation, the observed NEXAFS signal becomes almost independent of the molecular orientation, making these measurements chemically sensitive (see Chapter 6.3.1 for more details). We always observe clear π*-resonances, indicating that the local boron geometry is always primarily trigonal planar.*

($HB(OH)_2$) and found for non-interacting molecules both a monodentate and bidentate adsorption mode to be stable, although the bidentate adsorption mode is energetically slightly more favored by 0.12 eV.[22] However, the relative stability between these two species could change when increasing the coverage and therefore both adsorption binding modes are reasonable.

The O 1s core level is very sensitive towards the adsorption binding mode, but the signal of the molecule overlaps with the signal of the oxide substrate. Since we do not have in-depth DFT-calculations, we are forced to subtract the substrate contribution from our experimental spectra to perform a quantitative analysis. As outlined above, the substrate peak shape can change upon adsorption of molecules, which can make subtraction of the clean surface peak shape problematic. Fortunately, while we observe a slight decrease in substrate peak width (<0.1 eV) upon adsorption of the three phenylboronic acid derivatives, this change is significantly weaker than observed for the adsorption of phenylphosphonic acid. This enables us to subtract the shape of the clean surface spectrum from the experimental data, while allowing a small changes to the peak width. Nonetheless, subtracting the clean surface peak shape introduces some uncertainty, as the molecular signal can be a very small shoulder on the substrate contribution, see Figure 42.

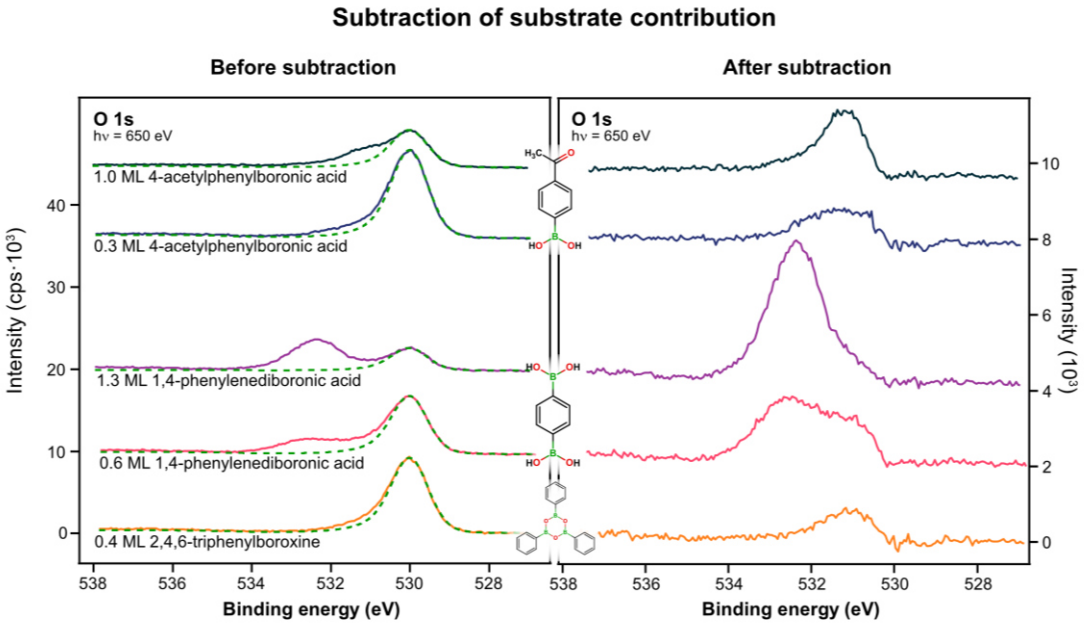

Figure 42: Spectra of 4-acetylphenylboronic acid, 1,4,-phenylenediboronic acid, and 2,4,6-triphenyl-boroxine on rutile TiO_2(110) at 300 K before (left) and after (right) subtraction of the substrate contribution. The clean surface peak shape used for subtraction is indicated as the green dashed line. The spectra are aligned to a substrate peak position of 530.0 eV.

As we do not have any DFT-calculations and there are no literature XPS references of boronic acid adsorbed on TiO_2, we can only use multilayer references to determine the binding-energy positions of the individual components. As outlined in the previous subchapter, these references can be misleading and we therefore constructed our fit models based on spectra of adsorbed molecules, where we were able to determine the binding-energy position of individual components.

A spectrum well-suited as a starting point is that of 2,4,6-triphenylboroxine, but first we have to discuss the on-surface species formed upon adsorption of the molecule. Initially, we were expecting the large cyclic anhydride to adsorb via relatively weak van-der-Waals interactions. Such a bond would result in molecular desorption after mild annealing, but we do observe significant amounts of carbon remaining on the surface up to 600 K. This clearly indicates that we have a strong interaction between the molecule and the surface and since we do not observe any tetrahedral boron in B K-edge NEXAFS in Figure 41, the boroxine ring most likely undergoes an on-surface ring-opening reaction upon adsorption of the molecule into three phenylboronic acid monomers. These monomers correspond to the monomers formed upon adsorption of phenylboronic acid and subsequent annealing to about 500 K, where all surface OH groups have desorbed as water and leave oxygen vacancies behind. These vacancies can be distributed evenly, with one molecule next to one vacancy. In that case, the oxygen atoms of the boronic acid group will bind with one oxygen atom in the vacancy and the other oxygen atom to a titanium-row atom, resulting in an orientation perpendicular to the oxygen rows. The oxygen vacancies could also distribute unevenly. In such a case, half the molecules are next to no oxygen vacancy and the other half is next to two vacancies. Molecules next to two vacancies will most likely bind with both oxygen atoms in the vacancy and molecules next to no vacancies bind to two titania-row atoms.

In principle, C K-edge NEXAFS would be the perfect tool to distinguish between an even and uneven oxygen vacancy distribution, as the phenyl ring is conjugated to the boronic acid group and therefore will have the same azimuthal orientation. Although we measured C K-edge NEXAFS, we are unable to say anything about the azimuthal orientation of these molecules, because we measured at an electric-field azimuthal angle of 45°, where we lose all information about the azimuthal orientation of the molecule (see Chapter 6.2 for more details). Irrespective of the exact orientation of the on-surface species, it will always form two Ti-O-B bonds and since

this is the only molecular species in the O 1s spectrum, we can determine the position of the Ti-O-B species to be at 531.07 eV, see Figure 43, and the full-width of a purely Gaussian peak of 1.15 eV.

Using the position and shape of the Ti-O-B species, we can describe the spectrum of 0.6 ML of 1,4-phenylenediboronic acid at 550 K. Again, we should have a bidentate adsorption mode without any protons, but we also have a second boronic acid group, which points towards the vacuum. This group can be subject to a condensation reaction with other boronic acids group, which we also observe the for multilayers of 1,4-phenylenediboronic acid in Figure 44. For 0.6 ML the polymerization is, based on the B : O ratio, incomplete (see Ref. [P3] for more details) and thus we have to add one peak for the B-O-B species and the B-OH species each. Forcing a peak ratio matching the polymerization degree of 71%, we arrive at the fit shown in Figure 43. With the same model, we can fit the spectrum of 1.3 ML 1,4-phenylenediboronic acid at 550 K, again considering the incomplete polymerization based on the B : O ratio of now 31%. We observe a much lower degree of polymerization for the larger coverage, which we attribute to an increased molecular flexibility at lower coverages, allowing the molecules to accommodate a geometry more susceptible to condensation.

To sum up, we find 1,4-phenylenediboronic acid to form a bidentate adsorption mode after annealing above 500 K, which is the same adsorption binding mode we find after the ring-opening reaction for 2,4,6-triphenylboroxine already at room temperature. 1,4-phenylenediboronic acid shows partial polymerization of the second boronic acid group pointing towards the vacuum interface, but the degree of polymerization is larger for the lower coverage.

At 300 K, all protons are still present at the surface and, as discussed above, both a monodentate and bidentate adsorption mode are plausible. However, for 1.0 ML of 4-acetylphenylboronic acid and 1.3 ML of 1,4-phenylenediboronic acid, a monodentate adsorption mode must dominate due to coverage. For the boronic acid derivatives, we define a monolayer based on the Ti 2p : C 1s peak area ratio of a saturated layer of 4-acetylphenylboronic acid. Comparing this to the ratio of a monolayer of phenylphosphonic acid, we arrive at a coverage of 1.5 4-acetylphenylboronic acid molecules per two titania row atoms. In a bidentate adsorption mode, we can adsorb at most one molecule per two titania row atoms and therefore a monodentate adsorption binding mode must dominate at monolayer saturation coverage.

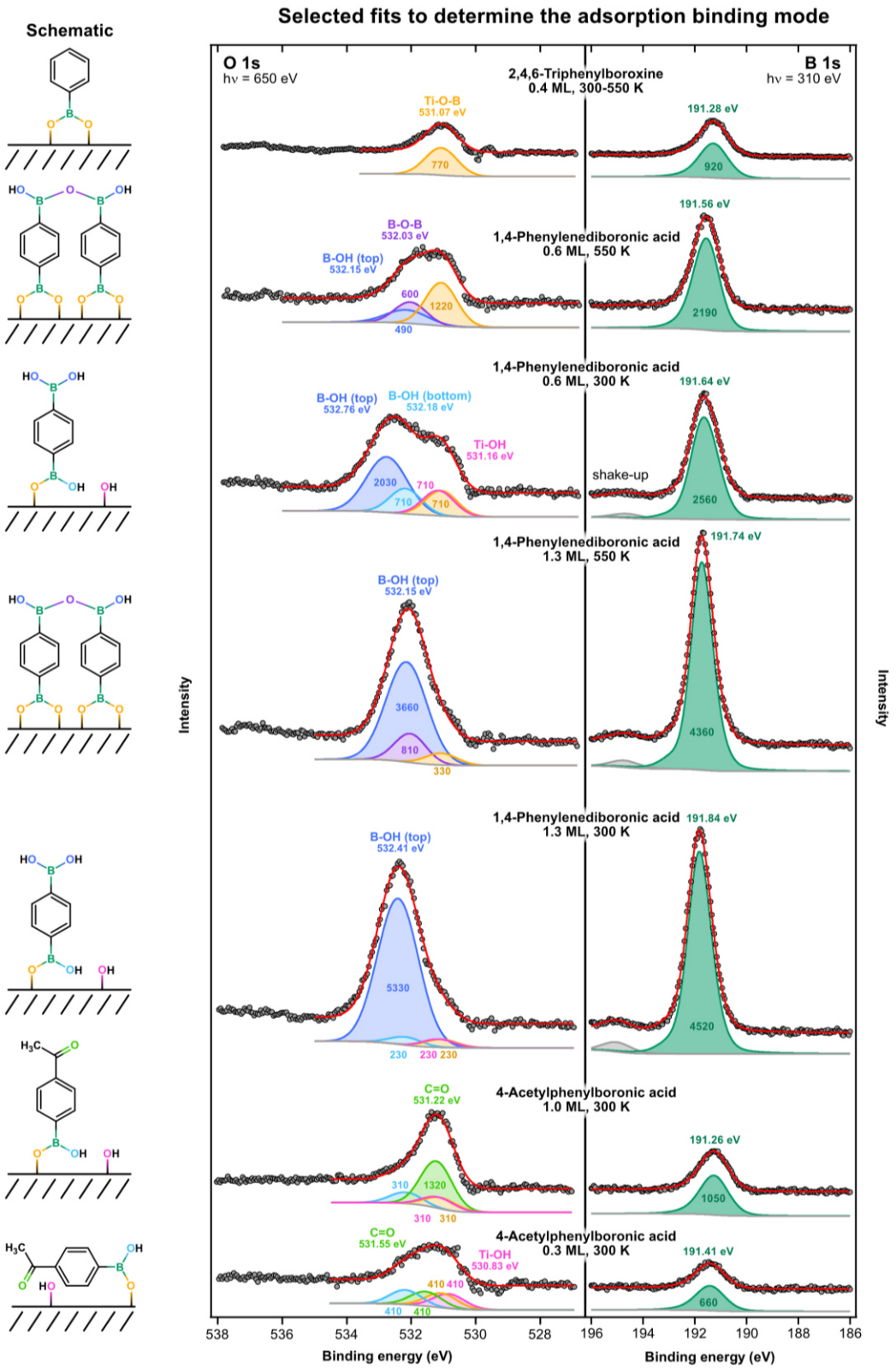

Figure 43: Selected B 1s and substrate-subtracted O 1s spectra of three phenylboronic acid derivatives deposited on rutile TiO_2(110) and annealed at the indicated temperatures for 1 min. At these temperatures, stable species are formed, which are illustrated schematically in the left column. The colors for the various oxygen atoms match the colors of the fitted peaks. Adapted from Ref. [P3].

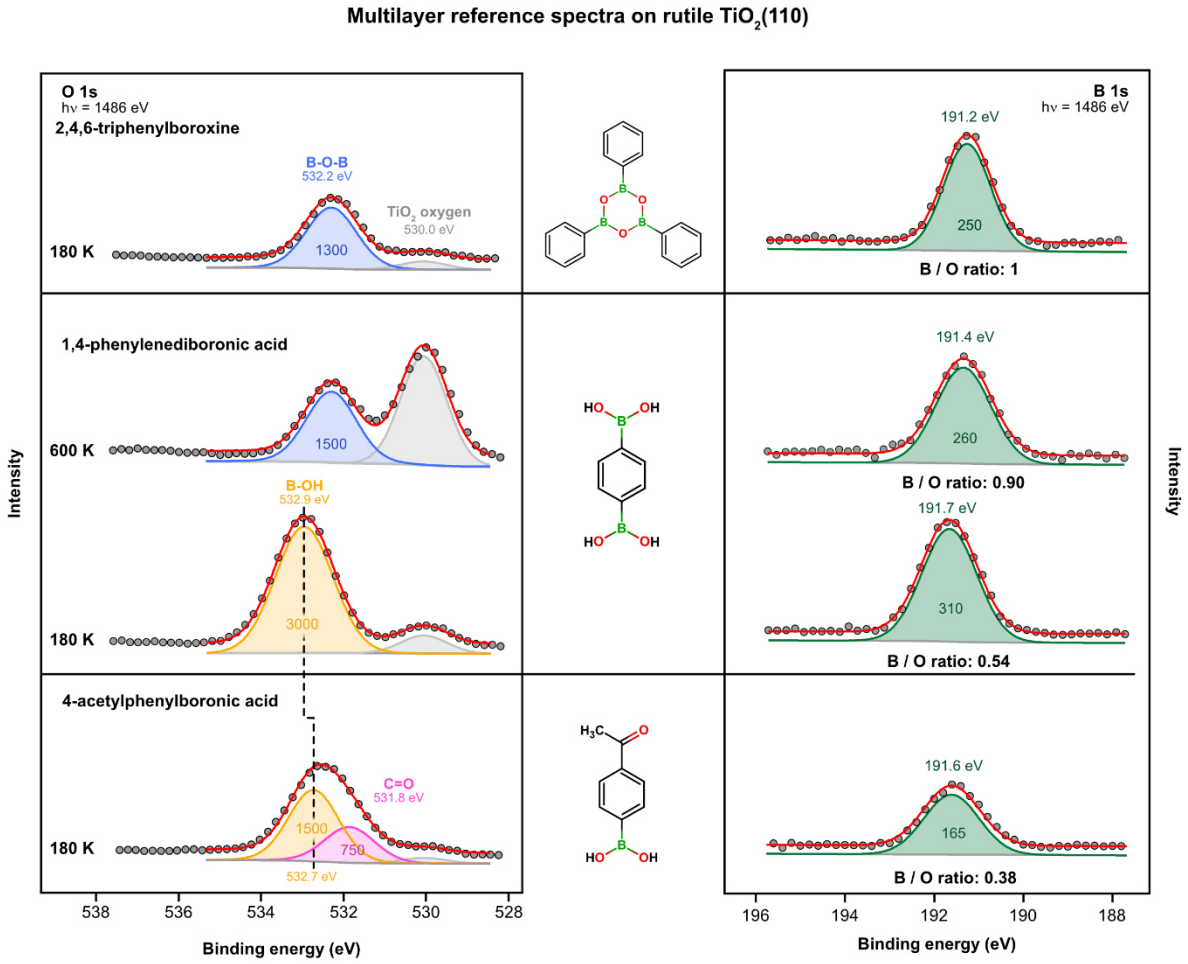

Figure 44: Laboratory-source Al K-α O 1s and B 1s spectra of multilayers of 1,4-phenylenediboronic acid, 2,4,6-triphenylboroxine, and 4-acetylphenylboronic acid deposited on rutile TiO_2(110) at 180 K to avoid coadsorption of water. When annealing multilayers of 1,4-phenylenediboronic acid at 600 K for 1 min, we observe roughly half the molecules desorbing and the other half polymerizing. This is also reflected in the B : O ratio, which changes from 0.52 (expected for the intact molecule) to 0.88 (close to full polymerization). The B : O ratio is normalized to the B : O ratio of 2,4,6-triphenylboroxine, which is assumed to be 1. Spectra are aligned to the substrate oxygen position at 530.0 eV. Adapted from Ref. [P3].

It would be relatively straightforward to fit the O 1s spectra for a monodentate adsorption mode, if we would have to consider the Ti-OH, B-OH, and Ti-O-B group only. However, the investigated molecules possess additional functional groups containing oxygen atoms. Starting with 1.0 ML of 4-acetylphenylboronic acid, we have to add an additional peak for the carbonyl group. We find the signal of the carbonyl group to be significantly more intense than the signal of the on-surface species, which indicates that the molecule is rather upright standing and the carbonyl group is pointing towards the vacuum interface. This also explains the discrepancy in the carbonyl peak

position in the monolayer (531.2 eV) and the multilayer spectrum (531.8 eV) in Figure 44 and Figure 45 due to differences in the hydrogen bonding at the carbonyl group. We can use the binding-energy positions of the Ti-OH (531.16 eV) and B-OH (532.18 eV) extracted for 1.0 ML of 4-acetylphenylboronic acid to fit the spectrum of 1.3 ML 1,4-phenylenediboronic acid, resulting in a good match. This spectrum is dominated by a new species called B-OH (top), which describes the B-OH groups pointing towards the vacuum interface and all B-OH groups of the molecules in the 2nd layer. Since this peak incorporates multiple species, it is allowed to be slightly broader than the peaks of the on-surface species. Again, the binding-energy position of the B-OH oxygen atoms at the vacuum interface (532.41 eV) is different from that of the multilayer (532.9 eV) in Figure 44, which is most likely due to differences in the hydrogen bonding network.

For 0.6 ML 1,4-phenylenediboronic acid, we can use a very similar fit model of a monodentate adsorption mode as for the high coverage, only allowing the signal from the B-OH groups at the vacuum interface to shift to higher binding energies. For 0.3 ML 4-acetylphenylboronic acid, it is immediately obvious that the carbonyl signal is no longer more intense than the signal of the boronic acid group at the oxide interface. We attribute this to a change in the molecular orientation,

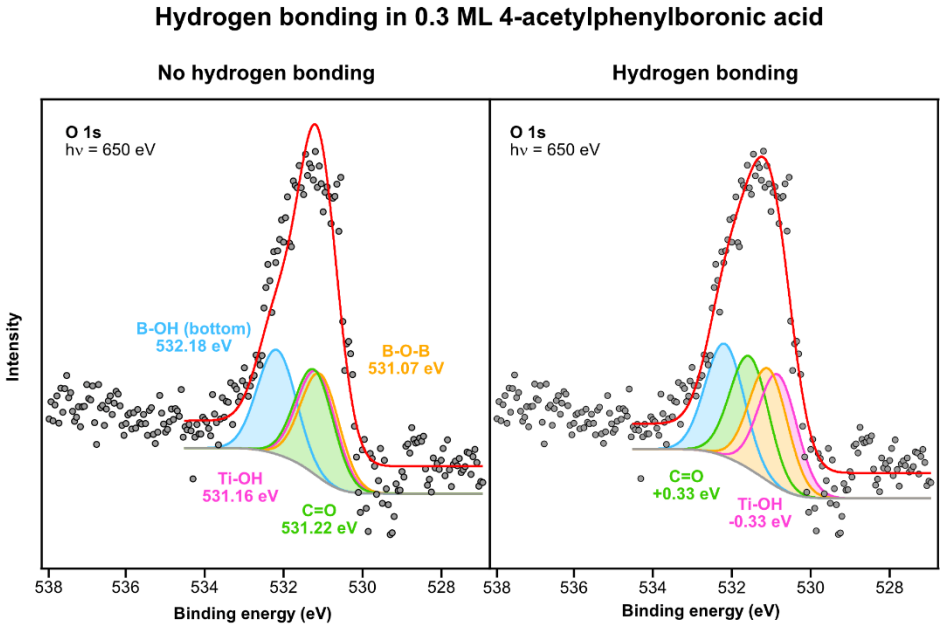

Figure 45: Hydrogen bonding within the 0.3 ML of 4-acetylphenylboronic acid layer at 300 K. Shifting the carbonyl (C=O) peak to higher binding energies and the surface hydroxyl (Ti-OH) peak to lower binding energies, consistent with hydrogen bonding between the two groups, significantly improves the quality of the fit. Adapted from Ref. [P3].

where a more flat-lying molecule leads to similar attenuation of the different oxygen species. This could be due to hydrogen bonding between the carbonyl group and a surface OH group, most likely a Ti-OH group. This also influences the binding-energy position of the two species and we find indeed a better fit to the experimental data when we allow the carbonyl group to shift to higher binding energies (+0.33 eV) and the Ti-OH group to lower binding energies (-0.33 eV), see Figure 45. Such an interpretation is also in line with our observations in the C 1s core level in Figure 46, where the carbonyl group position is clearly different for the two coverages. This indicates a considerable different chemical environment of the carbonyl group, in line with a significantly different hydrogen-bonding environment.

We can describe the O 1s spectra of 0.3 ML 4-acetylphenylboronic acid and 0.6 ML 1,4-phenylenediboronic acid with a fit model corresponding to a monodentate adsorption mode. In principle, there are enough titanium atoms available to form a bidentate adsorption mode and we could also fit the experimental data with such a model, see Figure 47. However, this would require the Ti-OH binding-energy position to be at 531.91 eV, which is very high for this group usually found at 531.3 – 531.6 eV.[48, 161, 168] A lower a binding-energy position is also

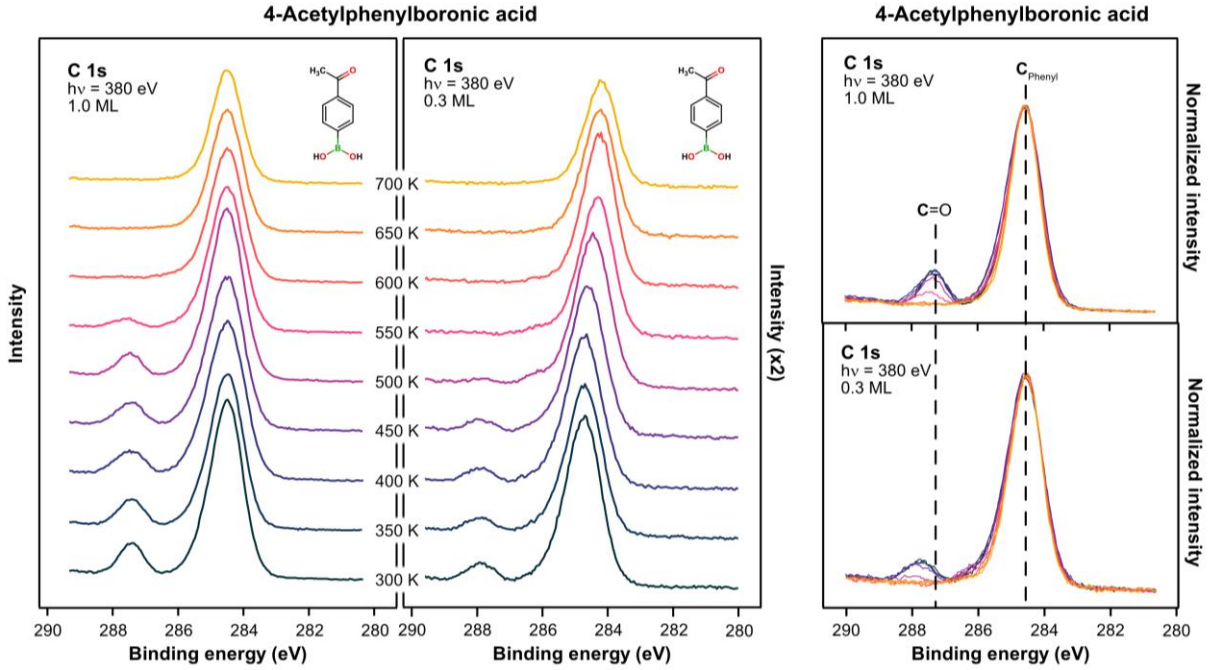

Figure 46: C 1s core-level spectra of 4-acetylphenylboronic acid on rutile TiO_2(110) annealed at the indicated temperatures for 1 min. Scaling and aligning the C 1s data (left), it becomes apparent that the carbonyl signal (C=O) is very different for the two coverages, indicating a different chemical environment of the carbonyl group. Adapted from Ref. [P3].

supported by our DFT-calculations for phenylphosphonic acid on rutile TiO_2(110), where the Ti-OH groups are found at 531.1 eV for PPA 2 or 531.6 eV for PPA 1.[P2] Considering a lower binding-energy position agrees better with literature and is consistent with the other fit models, a bidentate adsorption mode is unlikely and the molecules bind most likely in a monodentate adsorption mode.

To sum up, our data is consistent with a monodentate adsorption binding mode for 4-acetylphenylboronic acid and 1,4-phenylenediboronic acid at full monolayer coverage and submonolayer coverage. We see a clear coverage dependency in the O 1s core level for 4-acetylphenylboronic acid, where for a coverage of 0.3 ML the molecule is strongly tilted and the

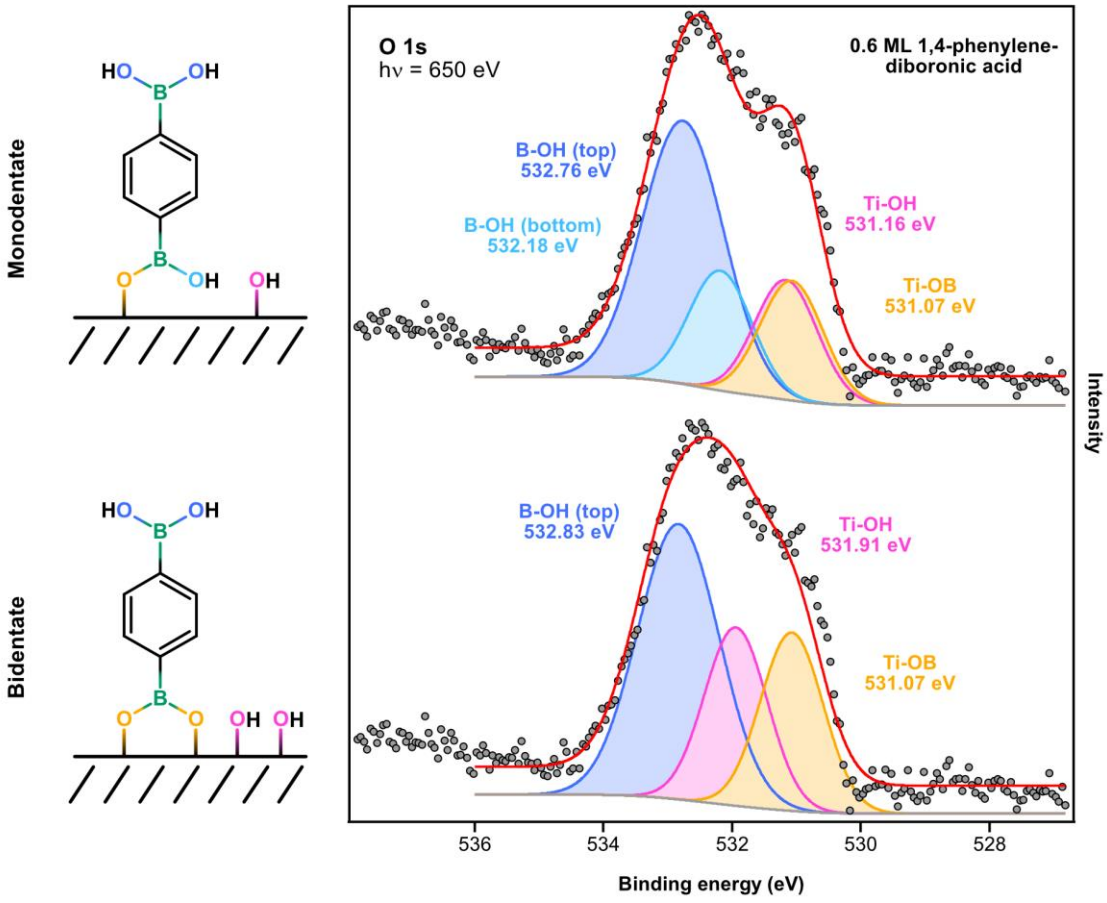

Figure 47: Comparison of a monodentate (top) and bidentate (bottom) fit model to the experimental O 1s spectrum of 1,4-phenylenediboronic acid on rutile TiO_2(110) aligned to the subtracted substrate contribution at 530.00 eV. Both models give good fits, but the model for the bidentate adsorption mode requires the Ti-OH groups to be at 531.9 eV, which is unusually high. Adapted from Ref. [P3].

carbonyl group hydrogen bonds to the surface, but at saturation coverage the carbonyl groups point towards the vacuum interface.

It is very important to keep in mind that the outlined analysis is associated with uncertainties. Without DFT calculations, we are forced to subtract the substrate contribution and even small errors in the substrate peak shape will have a significant influence on signal remaining after subtraction. This is especially the case for our low-coverage measurements. For 2,4,6-triphenylboroxine, we assumed in Figure 43 a bidentate adsorption mode, but with a single peak we are unable to describe the high-binding energy shoulder of the asymmetric signal after subtraction properly. We could add a second peak at 532.03 eV to improve the fit, which corresponds to the B-O-B species and would indicate an incomplete ring-opening reaction. However, the origin of this asymmetric peak shape could also come from an imperfect subtraction of the substrate contribution, making the remaining signal only appear asymmetric. Considering the relative intensity of the substrate and the molecule contribution for 2,4,6-triphenylboroxine in Figure 42, we are very hesitant to consider this shoulder to be significant. In fact, if we had only the O 1s spectrum of 2,4,6-triphenylboroxine, it would have been almost impossible to assign the adsorption binding mode. However, we can compare the O 1s spectra of three different phenylboronic acid derivatives, and we find the binding-energy position of the Ti-O-B species matching all of our other spectra. Additionally, we do not assign the adsorption binding mode based solely on the O 1s core level. The ring opening reaction is also in line with the surprisingly high desorption temperature and a quite upright standing phenyl ring in C K-edge NEXAFS (discussed below).

In summary, we are unable to gain the same atomistic understanding of the interaction of phenylboronic acid derivatives as for phenylphosphonic acid, where we had in-depth DFT calculations. Nonetheless, after careful analysis of the high-resolution synchrotron-radiation O 1s core level, we are able to determine the most-likely adsorption binding modes at room temperature and after desorption of surface OH groups at around 500 K. However, it is not trivial to arrive at these conclusions, as this analysis requires the subtraction of the substrate peak shape. We are only able to do this, because the shape of the substrate signal does, in contrast to phenylphosphonic acid, not change strongly upon adsorption of phenylboronic acid derivatives.

6. Auger-yield NEXAFS

To understand the behavior of molecules at a surface, NEXAFS spectroscopy can provide valuable information about the molecular orientation relative to the surface and chemical information. The details on the basic working principles of NEXAFS have already been discussed in Chapter 3.3 and this chapter deals with how the information was extracted from an Auger-yield measurement and what challenges can arise when using this method.

6.1. Using C K-edge NEXAFS to extract information about the molecular orientation

NEXAFS allows the extraction of geometrical information of the unoccupied orbitals relative to the surface. We chose to investigate small organic molecules with a phenyl ring attached to the anchor group because the lowest energy unoccupied orbital on a phenyl ring is a π* orbital with a nodal plane in the plane of all six phenyl ring carbon atoms. Thus, the orientation of this unoccupied orbital is correlated with the orientation of the phenyl ring, and as a result, C K-edge NEXAFS provides direct information about the orientation of the carbon moiety attached to the anchoring group.

6.1.1. General theory

The observed NEXAFS intensity is, according to Fermi's Golden Rule, proportional to the transition dipole moment for an electron changing from the initial state $|\Psi_i\rangle$ to the final state $|\Psi_f\rangle$:[77]

$$I \propto \left(\langle\Psi_f|\vec{\mathbf{E}}\cdot\vec{\mathbf{p}}|\Psi_i\rangle\right)^2 = \left(\vec{\mathbf{E}}\langle\Psi_f|\vec{\mathbf{p}}|\Psi_i\rangle\right)^2$$

In this thesis, only the boron and carbon K-edges were measured, so the initial state was always a 1s electron. For the 1s initial state, the intensity depends only on the symmetry of the final state orbital vector $\vec{\mathbf{O}}$ and the electric-field vector $\vec{\mathbf{E}}$:

$$I \propto \left(\vec{\mathbf{E}}(\omega t)\cdot\vec{\mathbf{O}}\right)^2 = \left(E_x\cdot O_x + E_y\cdot O_y + E_z\cdot O_z\right)^2$$

At the Material Science Beamline with a bending magnet, the incident light is elliptically polarized, so the electric-field vector changes orientation as a function of time t, which is illustrated in Scheme 7. In the experiment, all possible electric-field vector orientations will contribute to the signal because we are averaging over many excitation processes. Mathematically, this is equivalent to an integral:

$$I \propto \frac{1}{2\pi}\int_0^{2\pi} \left(\vec{\mathbf{E}}(\omega t)\cdot\vec{\mathbf{O}}\right)^2 d(\omega t) \propto \left(\vec{\mathbf{E}}_1\cdot\vec{\mathbf{O}}\right)^2 + \left(\vec{\mathbf{E}}_2\cdot\vec{\mathbf{O}}\right)^2$$

The resulting intensity is proportional to the major $\vec{\boldsymbol{E}}_1$ and minor $\vec{\boldsymbol{E}}_2$ component of the elliptically polarized light. For a bending magnet light source, the major component $\vec{\boldsymbol{E}}_1$ is parallel to the storage ring plane, and this component is often referred to as the parallel component (analogously, the minority component is referred to as the perpendicular component).

Often the electric-field vectors of the major and minor components are expressed as unit vectors, and to account for the differences in magnitude, the polarization factor P is introduced:

$$I \propto P\cdot\left(\vec{\mathbf{E}}^{\parallel}\cdot\vec{\mathbf{O}}\right)^2 + (1-P)\cdot\left(\vec{\mathbf{E}}^{\perp}\cdot\vec{\mathbf{O}}\right)^2$$

where $\vec{\mathbf{E}}^{\parallel}$ and $\vec{\mathbf{E}}^{\perp}$ are the unit electric-field vectors along the orientation of the major and minor components, respectively. At the Materials Science Beamline, the polarization factor P is reported to be 0.8.[137]

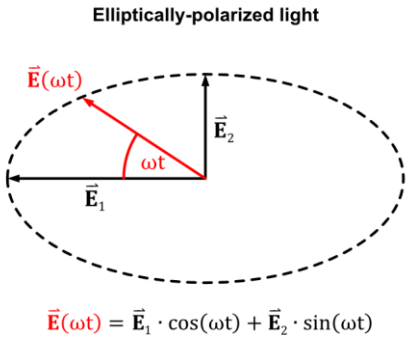

Scheme 7: Schematic of elliptically-polarized light when the observer is looking directly in the direction of light propagation. The electric-field vector of the light changes as a function of time, following an ellipsoid. This resulting trajectory can be described by two vectors along the major axis $\vec{\boldsymbol{E}}_1$ and minor $\vec{\boldsymbol{E}}_2$ axis of the ellipse. For a bending magnet light source, the major component is parallel to the plane of the storage ring and is therefore often referred to as the parallel component. Analogously, the minor component is often called the orthogonal component.

It is convenient to define the electric-field vector and the orbital vector in spherical coordinates relative to the surface. The polar angle θ is given relative to the surface normal and the azimuthal angle ϕ is the angle between the y-axis and the orthogonal projection of the vector onto the surface plane, see Scheme 8. In this coordinate system, the y-axis is defined to be parallel to a high-symmetry direction of the substrate (which will become important later).

In spherical coordinates, the normalized orbital vector $\vec{\mathbf{O}}$ and electric-field vector $\vec{\mathbf{E}}$ are defined as:

$$\vec{\mathbf{O}}(\theta_O, \phi_O) = \begin{pmatrix} \sin(\theta_O) \cdot \cos(\phi_O) \\ \sin(\theta_O) \cdot \sin(\phi_O) \\ \cos(\theta_O) \end{pmatrix}, \vec{\mathbf{E}}(\theta_E, \phi_E) = \begin{pmatrix} \sin(\theta_E) \cdot \cos(\phi_E) \\ \sin(\theta_E) \cdot \sin(\phi_E) \\ \cos(\theta_E) \end{pmatrix}$$

It is possible to express the orientation of the electric field minority component as a rotation of the electric field majority component. Considering that the sample rotates around an axis perpendicular to the storage ring plane, the polar angle of the minority electric-field vector will

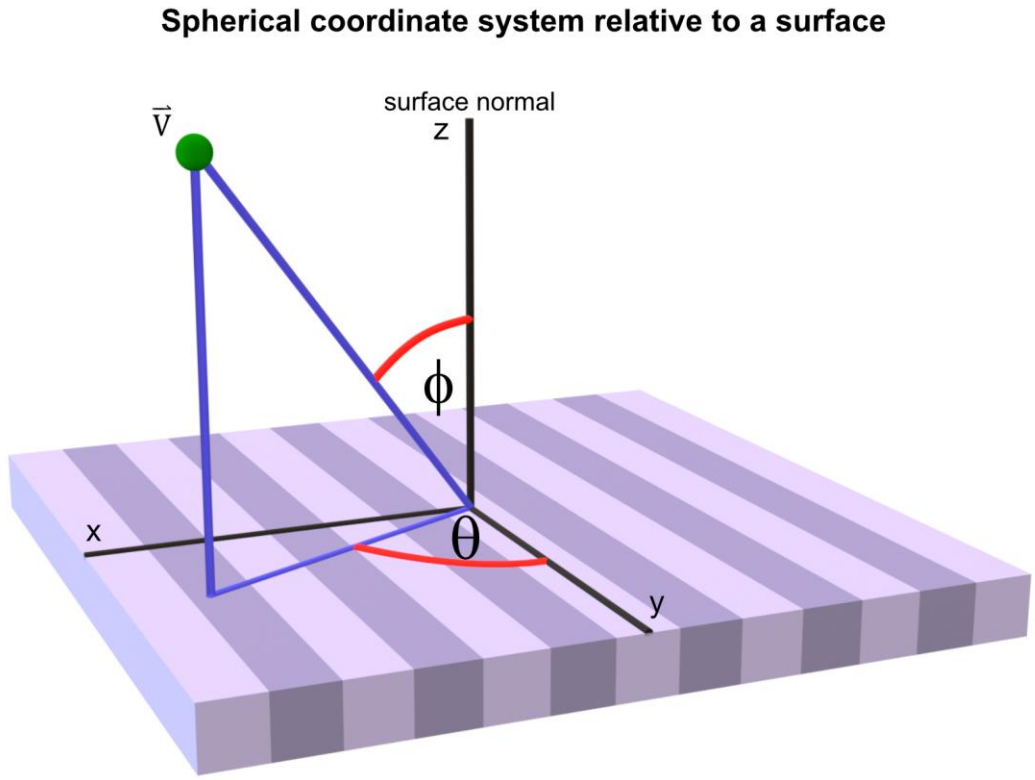

Scheme 8: The coordinate system is defined with the z-axis parallel to the surface normal and the xy-plane being parallel to the crystal surface. Any vector of unit length can be expressed by two angles: the polar angle ϕ and the azimuthal angle θ. The y-axis for this sketch is along the direction of a high-symmetry axis of the substrate, which will become important later.

always be in the surface plane ($\theta_E^{\perp} = 90°$). The azimuthal angle ϕ_E changes as the sample is rotated, but this angle is always perpendicular to the azimuthal angle of the majority component. Thus, the minority electric-field vector $\vec{\mathbf{E}}^{\perp}$ can be expressed as a function of the majority electric-field vector, where $\vec{\mathbf{E}}(\theta_E, \phi_E)$ is the electric-field vector of the majority component.

$$\vec{\mathbf{E}}^{\perp}(\phi_E^{\perp}) = \vec{\mathbf{E}}(\theta_E = 90°, \phi_E + 90°) = \begin{pmatrix} \sin(90°) \cdot \cos(\phi_E + 90°) \\ \sin(90°) \cdot \sin(\phi_E + 90°) \\ \cos(90°) \end{pmatrix} = \begin{pmatrix} -\sin(\phi_E) \\ \cos(\phi_E) \\ 0 \end{pmatrix}$$

Thus, the measured intensity can be expressed as:

$$I \propto P \cdot \left(\vec{\mathbf{E}}(\theta_E, \phi_E) \cdot \vec{\mathbf{O}}\right)^2 + (1 - P) \cdot \left(\vec{\mathbf{E}}(90°, \phi_E + 90°) \cdot \vec{\mathbf{O}}\right)^2$$

This equation describes the NEXAFS signal of a single molecular orbital orientation when excited with elliptically polarized light. However, depending on the investigated sample, several different molecular orientations may be present. For organic monolayers, it is very important to consider the symmetry of the surface because there can be multiple, isoenergetic adsorption orientations. In the case of the twofold rotational symmetry of the rutile TiO_2(110) surface, there are for a single molecular orientation three additional symmetry-equivalent orientations, as illustrated in Figure 48. Assuming the domain size is significantly smaller than the illuminated area, the measured NEXAFS signal is the average signal from all four mirror domains (for clarity θ_E and ϕ_E are omitted):

$$f_{4D}(\theta_O, \phi_O) = \frac{1}{4} \cdot I(\theta_O, \phi_O) + \frac{1}{4} \cdot I(-\theta_O, \phi_O) + \frac{1}{4} \cdot I(\theta_O, -\phi_O) + \frac{1}{4} \cdot I(-\theta_O, -\phi_O)$$

With this equation we can finally describe the angular dependency of the π* peak area and this enables us to determine the orbital polar angle of the phenyl ring attached to an anchor group. We did this for the three boronic acid derivatives, see Figure 49, and this gives us information about the orientation of the phenyl ring. The results show that the small orbital polar angle of 37° for 0.3 ML of 4-acetylphenylboronic acid is in line with the carbonyl group interacting with the surface, while the surprisingly large orbital polar angle of 50° found for 0.4 ML of 2,4,6-triphenylboroxine supports our hypothesis of a ring-opening reaction of this molecule into phenylboronic acid monomers.

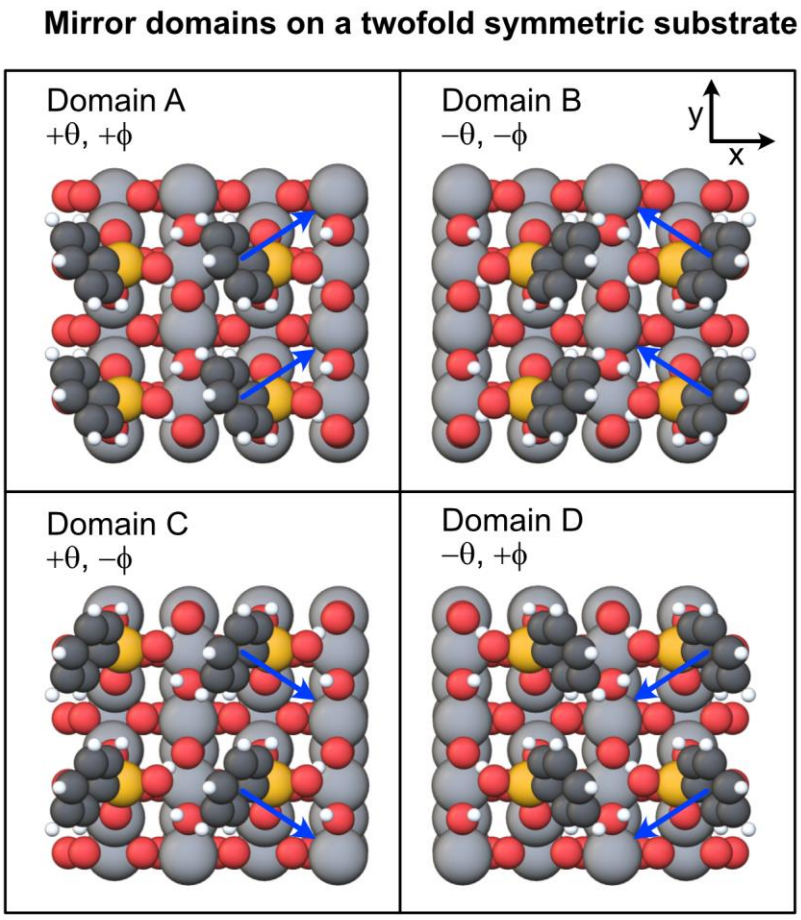

Figure 48: On the twofold symmetric surface of rutile TiO_2(110) molecules can adsorb in four symmetrically equivalent domains, here shown for phenylphosphonic acid. The blue arrows indicate the orientation of the molecular orbital vector.

This outlined equation is specific for a twofold symmetric substrate with four mirror domains. When deriving an equation for another system, it is very important to consider the substrate symmetry and the size of the domains, since the derived equation is only applicable to a system that satisfies the underlying assumptions. If this is not the case, the appropriate equation must be derived following the steps outlined above. For some systems, suitable equations can be found in the literature, e.g. in the book by Stöhr.[77] However, it is important to understand the assumptions behind these equations, and their applicability to the system at hand must be carefully verified.

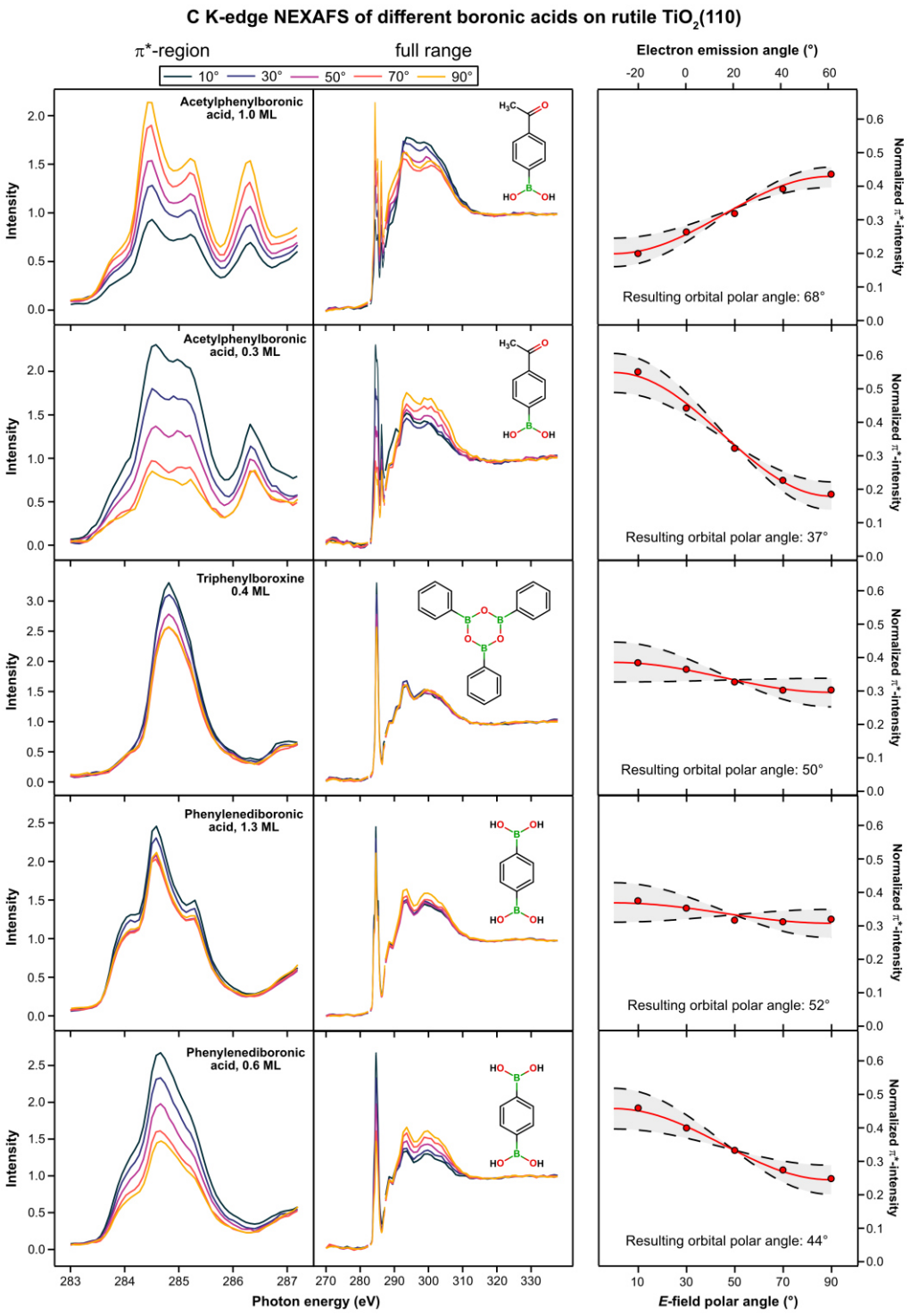

*Figure 49: Angular-dependent C K-edge NEXAFS spectra for an **E**-field azimuthal angle of 45° of three boronic acid derivatives on rutile TiO_2(110) after annealing at 400 K for 1 min. The full NEXAFS spectrum (middle) has breaks at 283 and 287 eV, indicating the transition from the fine energy resolution in the π*-region to the coarse resolution used everywhere else (see Chapter 6.2). The area of π*-peaks (left) changes as a function of the **E**-field polar angle and this change was used to extract the orbital polar angle (right). The red line indicates the best fit and the dashed black lines indicate the calculated angular dependency if the orbital polar angle would vary by ±5°. Adapted from Ref. [P3].*

6.1.2. DFT-predicted angular dependencies in C K-edge NEXAFS for phenylphosphonic acid on rutile TiO_2(110)

Comparing the orientation of phenyl rings in DFT-calculated structures with experimentally determined angles is trivial at first glance. However, this does not work for a system with multiple

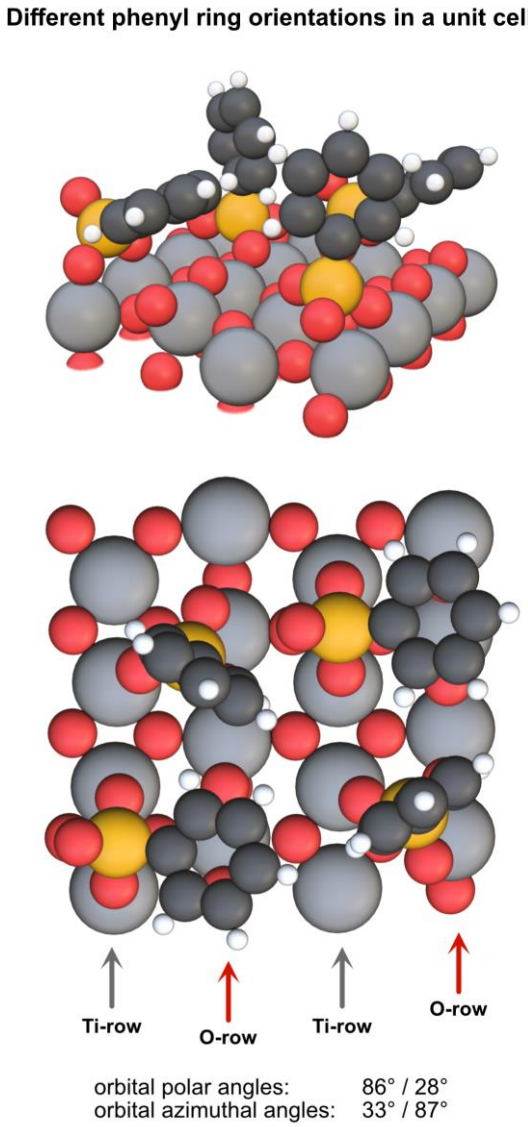

Figure 50: DFT-optimized adsorption structure of phenylphosphonic acid on rutile TiO_2(110) with two different adsorption modes within the unit cell, resulting in a total of two different molecular orientations. To compare experimental C K-edge NEXAFS data with this structure, it is necessary to calculate the expected angular dependency of the π-peak area as the sum of the four individual contributions. Adapted from Ref. [P2].*

different molecular orientations within the DFT-calculated unit cell, such as the PPA 4+5 structure of phenylphosphonic acid on rutile TiO_2(110), see Figure 50.

It is virtually impossible to extract multiple different orientations from the experimental data without any further assumptions, and due to the non-linearity of the NEXAFS signal, the experimentally-extracted polar and azimuthal angles do not even correspond to the average angle of the different orientations. Therefore, to compare the experimental results with the theoretical calculations, it is more reasonable to calculate the angular dependency of the π* peak area as a function of the electric-field polar angle and compare these results directly with the experiment.

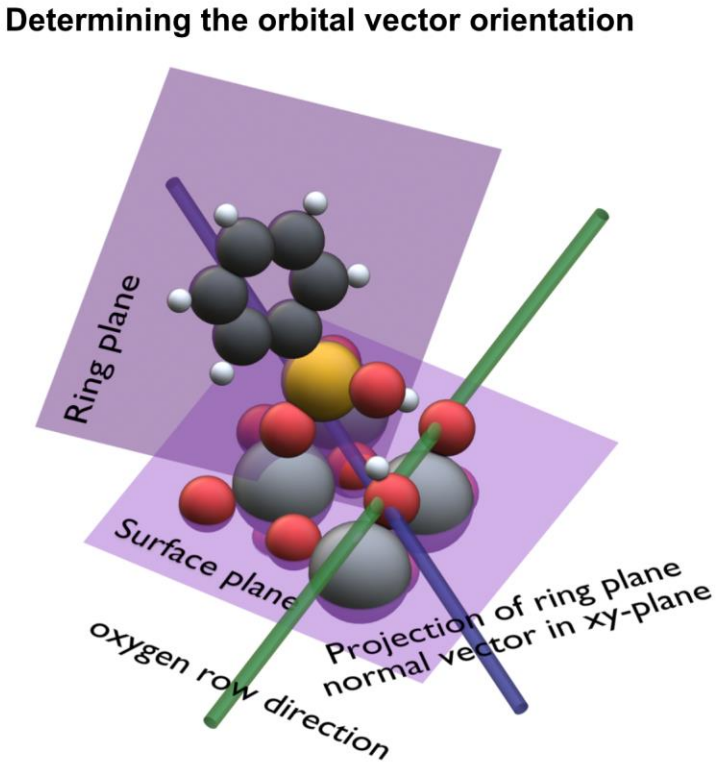

Figure 51: The orbital polar and orbital azimuthal angles of the LUMO located on the phenyl ring were determined by finding the best-fit plane through the six carbon atoms and the best-fit plane through the titania atoms in the first layer. The orbital polar angle is the angle between the ring plane normal vector and the surface plane normal vector, while the azimuthal angle is given by the angle between the orthogonal projection of the ring plane normal vector onto the xy-plane and the unit vector in the y-direction.

Extracting the polar and azimuthal orientation from DFT-optimized structures is trivial, see Figure 51. It is important, however, to consider that the orbital vector for excitations into the π*-orbital is the normal vector of the phenyl ring plane. With the orientation of the molecule, the absolute NEXAFS intensities were then calculated according to the equation for a twofold symmetric substrate with four mirror domains described in the previous subchapter. If the structure contained more than one molecule, the angular dependency was calculated as the average intensity of all orientations.

Before we can compare our calculated intensities with experiment, we have to consider that there is an unknown scaling constant between the calculated absolute intensities and the experimental π* peak areas. We can determine this value by a least-square fit of the experimental data to the theoretically-predicted spectrum, but as a result, the normalization factor is different for each fit, leading to differently scaled experimental data points in the corresponding figures.

With the normalization factor, we can directly compare the experimentally determined angular dependencies of the π* peak area with the theoretically predicted ones. The results support the assignment of a mixed PPA 4+5 monolayer to the high-temperature species of phenylphosphonic acid discussed in Chapter 5.4.1, see Figure 52, as the fit of the PPA 4+5 monolayer in a 3:5 ratio due to naturally occurring oxygen vacancies is in excellent agreement with the experimental data. For a 2:2 ratio, we still obtain a very good agreement, but our experimental data do not fit at all with the predicted angular dependence of the primitive PPA 3 monolayer.

We also applied this procedure to the low-temperature adsorption mode and the primitive PPA 1 monolayer, which gave an excellent fit to the experimental O 1s core level. Surprisingly, this results in a poor fit to the experimental angular dependency, see Figure 53. We therefore explored different phenyl ring stacking patterns with four molecules and found that a T-stacked structure has a very similar adsorption energy, and the corresponding angular dependency matches the experimental data significantly better. This indicates that the low-temperature adsorption structure is a singly-deprotonated monodentate adsorption, where most likely a T-stacked structure with more than one phenyl-ring orientation is present at the surface.

Although changes in the adsorption geometry can alter the O 1s core-level spectrum, the differences between the T-stacked and primitive PPA 1 monolayers are limited to the phenyl ring

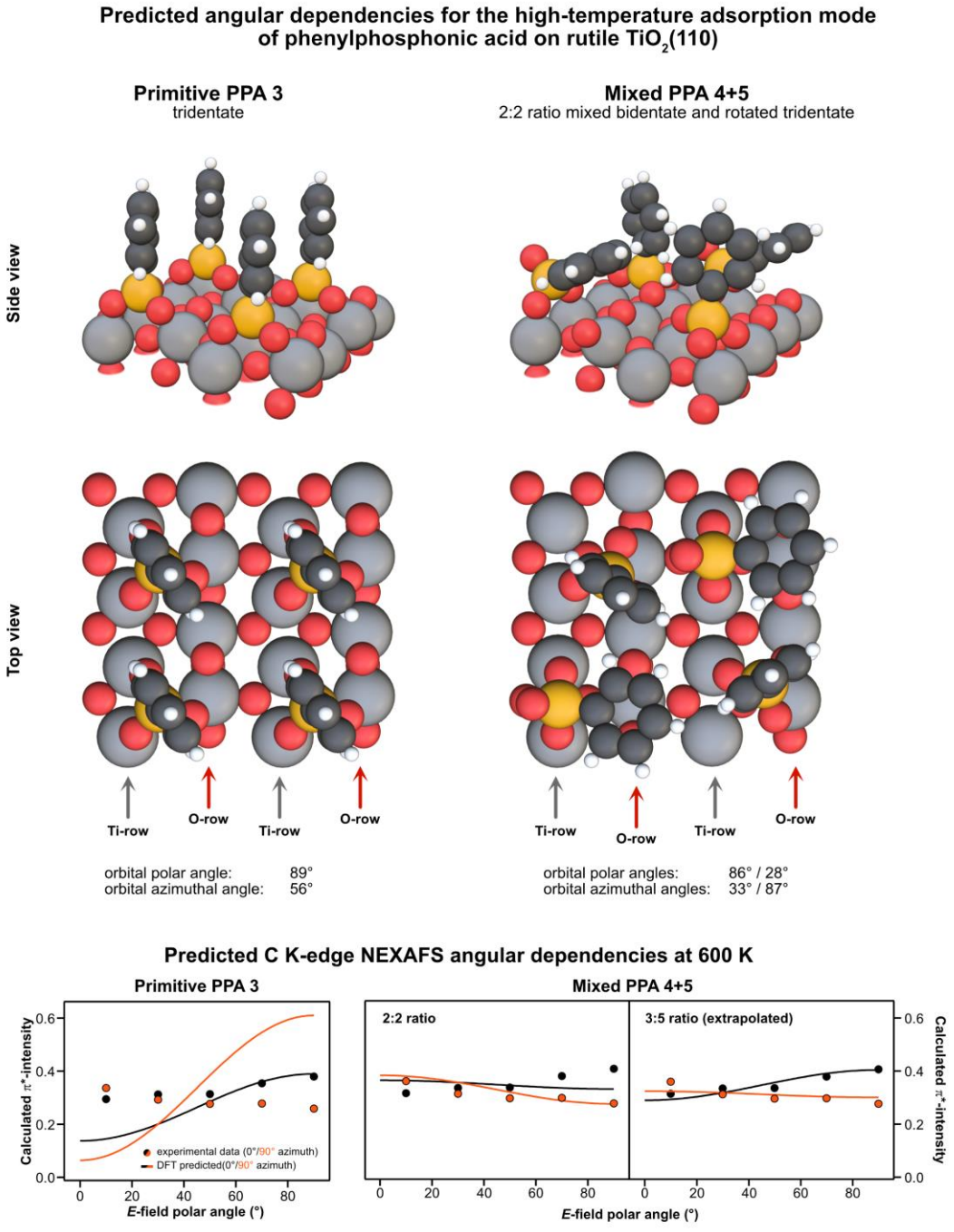

Figure 52: Predicted angular dependency of the π-peak area in Auger-yield C K-edge NEXAFS for the primitive PPA 3 structure and the mixed PPA 4+5 structure assuming a two-fold symmetric substrate with four mirror domains. In addition to the absolute intensities of the predictions, the experimental angular dependency for 0.45 ML of phenylphosphonic acid on rutile TiO_2(110) is added. Experimental intensities are scaled according to their best least-square fit to the theoretical curves to make them comparable to the corresponding predicted curve. Adapted from Ref. [P2].*

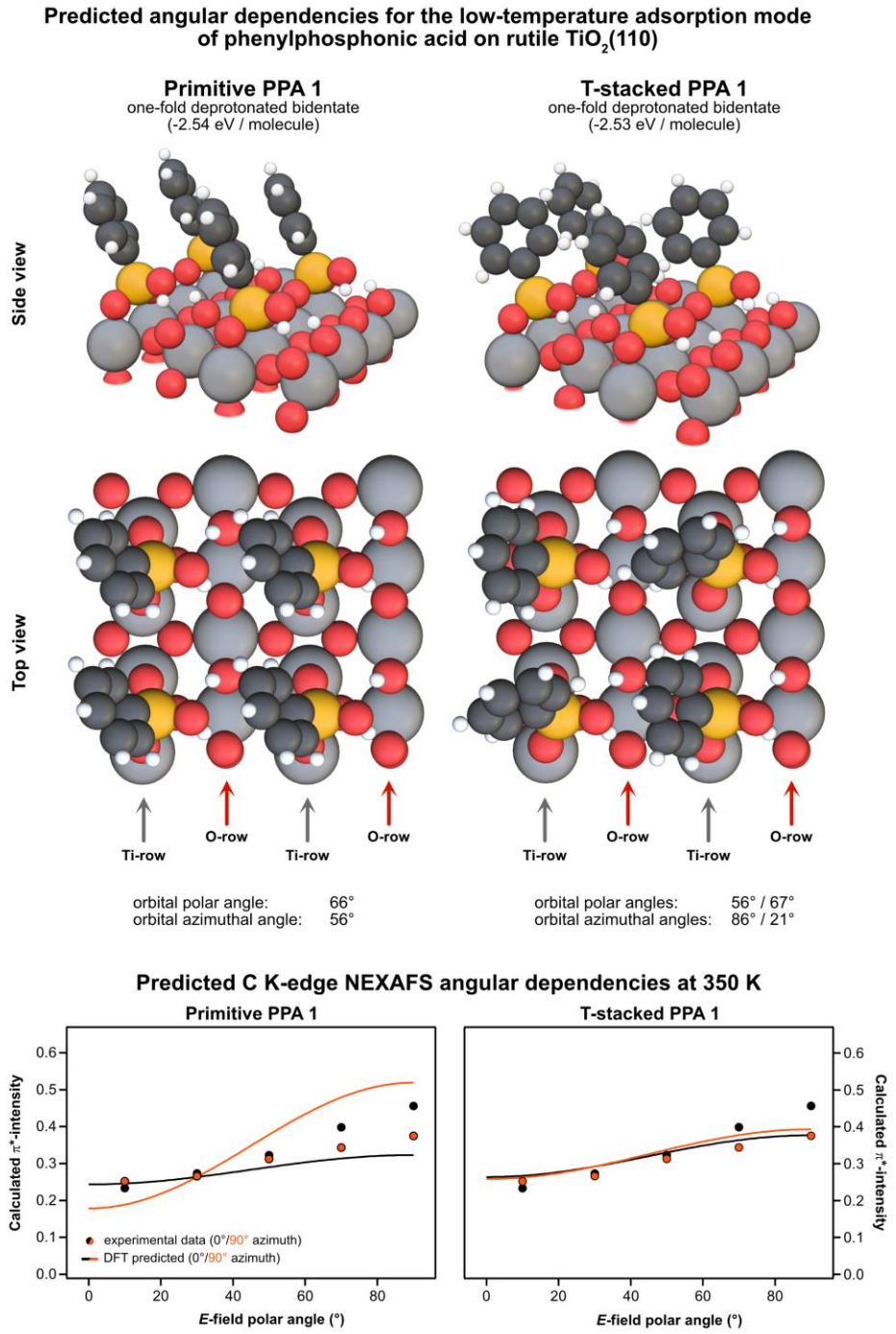

Figure 53: Predicted angular dependency of the π-peak area in Auger-yield C K-edge NEXAFS for the primitive PPA 1 structure and the T-stacked PPA 1 structure assuming a two-fold symmetric substrate with four mirror domains. In addition to the absolute intensities of the predictions, the experimental dependency for 0.45 ML of phenylphosphonic acid on rutile TiO_2(110) is added. The experimental intensities are scaled according to their best least-square fit to the theoretical curves to make them comparable to the corresponding predicted curve. Adapted from Ref. [P2].*

orientation, and therefore the predicted O 1s core-level spectrum of the T-stacked monolayer is virtually identical to that of the primitive PPA 1 monolayer (not shown).

6.2. Optimizing NEXAFS measurements

NEXAFS measurements are time-consuming, but synchrotron time is a limited and valuable commodity. It was therefore desirable to minimize the time required for NEXAFS measurements while still obtaining high quality data.

In C K-edge NEXAFS, two spectral features are important: First, the area of the π* peaks to extract information about the angular dependency, and second, the edge jump, which is needed to scale the spectrum, see Figure 54 (left). While the π* region requires a fine photon-energy step size, the edge jump requires a wide photon energy window. This results in long measurement times, which is undesirable at the synchrotron. A possible solution is to measure only the π* region with a fine photon-energy step size of 0.1 eV and the entire photon-energy window with a coarse step size of

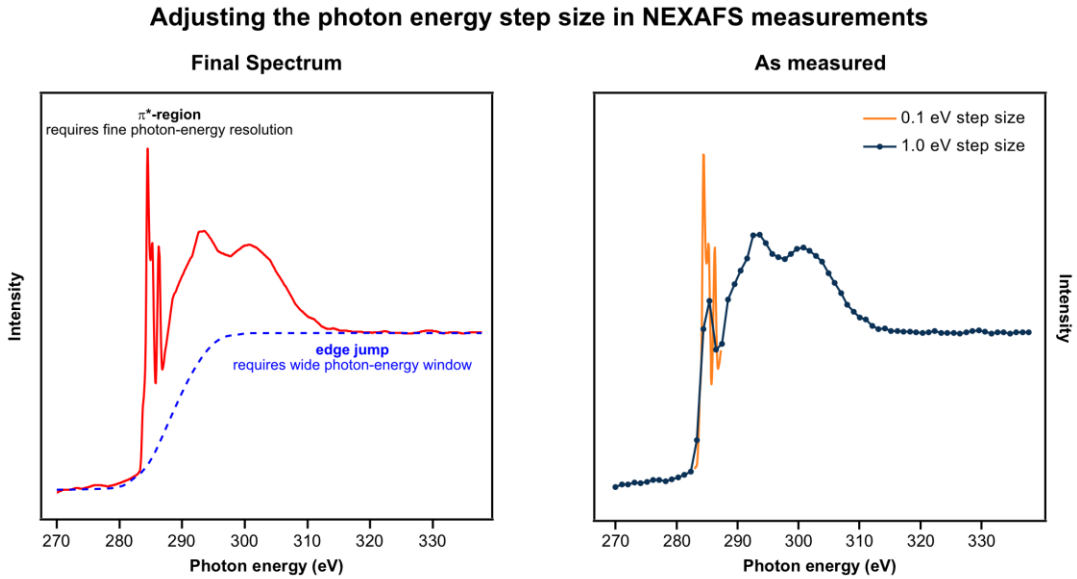

Figure 54: To extract information about the orientation of the phenyl ring, it is important to accurately determine the edge jump (requires a wide photon energy window) and the area of the π-peaks (requires a fine photon energy resolution). To meet both requirements, we decided to measure two independent NEXAFS spectra (right): One with a fine photon energy step size in a small window and another one with a coarse photon energy step size over a wide photon energy window. This allows us to accurately determine angular dependencies while minimizing measurement time.*

1.0 eV, resulting in the two spectra shown in Figure 54 (right). It should be noted that the π* peak shape of the coarse resolution measurement differs significantly from that of the fine resolution measurement. This is because the photon energy step size for the coarse resolution is so large that it cannot capture the peak shape of the narrow π* peaks.

A second reason why the C K-edge NEXAFS measurements take a lot of time is due to the system we are investigating: The rutile TiO_2(110) surface is twofold symmetric, and to determine the full orientation of the orbital vector, both the electric-field polar and azimuthal angle must be varied. While it is simple to vary the electric-field polar angle, the sample holder at the Materials Science Beamline does not allow for rotations around the azimuthal angle. The only way to change the electric-field azimuthal angle is to rotate the crystal outside of the chamber. After rotation, the crystal has to be cleaned and the surface has to be prepared again, which takes a lot of time.

One way to circumvent this, is to rotate the crystal so that the electric-field azimuthal angle is 45°, because for a twofold symmetric substrate with four mirror domains, the π*-intensity becomes independent of the orbital azimuthal angle at this electric-field azimuthal angle. This allows for the determination of the orbital polar angle simply by varying the electric-field polar angle. This saves a lot of time, but at the expense of information about the orbital azimuthal angle. For phenylphosphonic acid, we determined the full orientation of the phenyl ring, but for the measurements on phenylboronic acid derivatives, we decided to perform all measurements at an electric-field azimuthal angle of 45°. Thus we do not have any information about the azimuthal orientation of the phenyl ring for these molecules. In retrospect, it would have been very nice to have this information, because since the boronic acid group and the phenyl ring are part of the same π system, the orientation of the phenyl ring would give us direct information about the orientation of the boronic acid group. We would have been able to gain additional information about the adsorption binding mode at room temperature (monodentate is perpendicular to the oxygen rows and bidentate is parallel) and at 550 K (an even oxygen vacancy distribution leads to a perpendicular orientation to the oxygen rows, an uneven distribution to a parallel orientation). However, if we would have made these additional NEXAFS measurements and rotated the crystal, we would have been unable to measure three different molecules on overall five different surface preparations. In the future, it might be interesting to revisit the adsorption of phenylboronic acid

derivatives with NEXAFS to follow the changes in the phenyl-ring orientation as a function of temperature.

6.3. Using NEXAFS to gain chemical information

NEXAFS contains not only information about the orientation of the unoccupied orbitals, but also chemical information. In fact, NEXAFS is very sensitive to any chemical changes because the unoccupied orbitals are directly correlated to the binding orbitals.

6.3.1. Chemical sensitive NEXAFS: B K-edge NEXAFS of boronic acids on rutile TiO_2(110)

The observed NEXAFS intensity is dependent on the orientation of the electric-field vector. While this is crucial for determining the orientation of a molecule, it is highly undesirable when attempting to follow chemical changes.

Fortunately, it is possible to obtain a signal independent of changes in molecular orientation by selecting a specific orientation of the electric-field vector. As discussed in the previous subchapter, the measured NEXAFS intensity becomes independent of the orbital azimuthal angle when measured with an electric-field azimuthal angle of 45°. Therefore, an electric-field polar angle must be found for which the measured signal intensity becomes independent of the orbital polar angle. In Figure 55 the calculated dependency of the signal on the orbital polar angle is plotted for different electric-field polar angles. As expected, the NEXAFS intensity changes as a function of the molecular polar angle. However, for an electric-field polar angle of 50°, there is no angular dependency of the measured signal on the orbital polar angle. Thus, for an electric-field polar and azimuthal angle of 50° and 45°, respectively, the signal becomes independent of the molecular orientation for a twofold symmetric substrate with four mirror domains, enabling purely chemically sensitive measurements.

It is also possible calculate this special electric-field polar angle θ_E^* for a twofold symmetric substrate with four mirror domains according to

$$\theta_E^* = \operatorname{acos}\left(\sqrt{\frac{1}{3 \cdot P}}\right)$$

With the polarization factor P of the Materials Science Beamline of 0.8,[137] this special electric-field polar angle is 49.8°. The equation to calculate this angle is not unique to a twofold symmetric

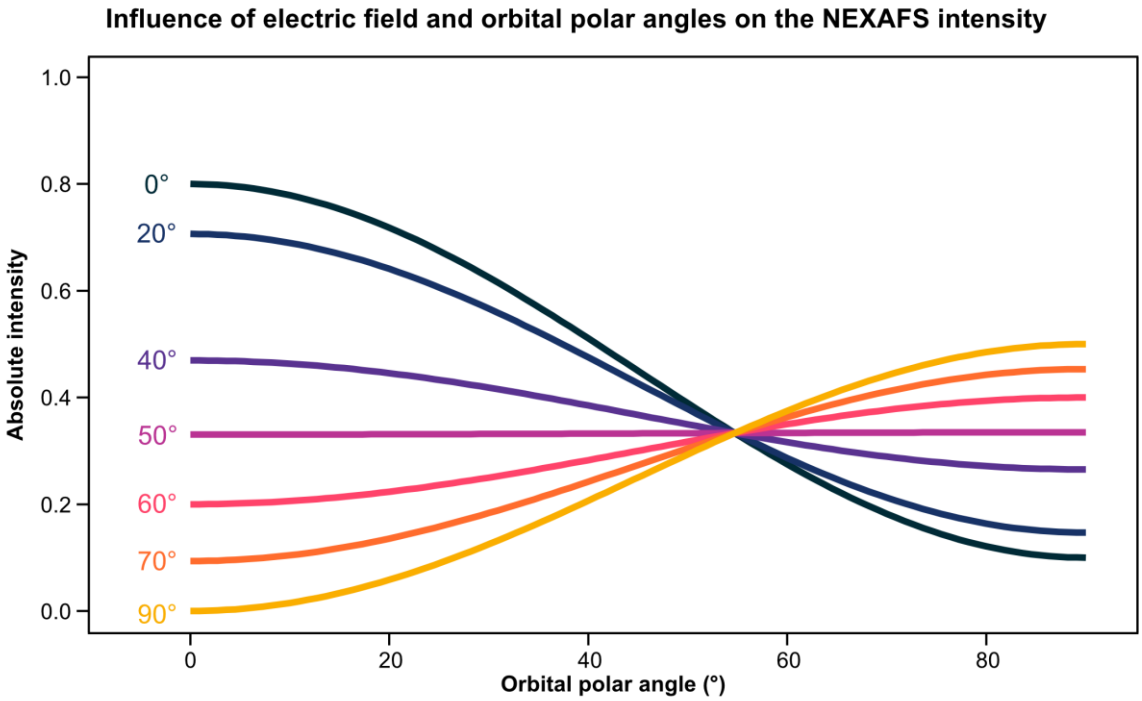

*Figure 55: Plot of the absolute NEXAFS intensity against the molecular polar angle at an azimuthal light incidence angle of 45°, calculated for a twofold symmetric substrate with four mirror domains and a light polarization of 0.8. We wanted to measure at an **E**-field polar angle of 50°, where the intensity is independent of the molecular orientation, but we accidentally measured at an **E**-field polar angle of 40° (light incidence angle of 50°). Adapted from Ref. [P3].*

substrate with four mirror domains, and according to Stöhr the same equation is obtained for a substrate with threefold or higher symmetry.[77]

We wanted to measure B K-edge NEXAFS at an electric-field polar and azimuthal angle of 50° and 45°, respectively. This would have allowed us to follow the changes in the B K-edge NEXAFS spectrum, and any changes would be due to chemical changes at the boron atom or the unoccupied orbitals. Unfortunately, I made a mistake: Instead of measuring at an electric-field polar angle of 50°, I measured instead at a *light incidence* angle of 50°, corresponding to an electric-field polar angle of 40°. The absolute NEXAFS intensity as a function of the molecular polar angle changes by a factor of up to 1.8 at an electric-field polar angle of 40°, see Figure 55. Therefore, we cannot exclude that changes in the NEXAFS signal at the B K-edge are caused by changes in the molecular orientation.

Nevertheless, the measured intensity is mostly chemically sensitive, which is supported by the experimental data in Figure 56, as changes in B K-edge NEXAFS are correlated with changes in

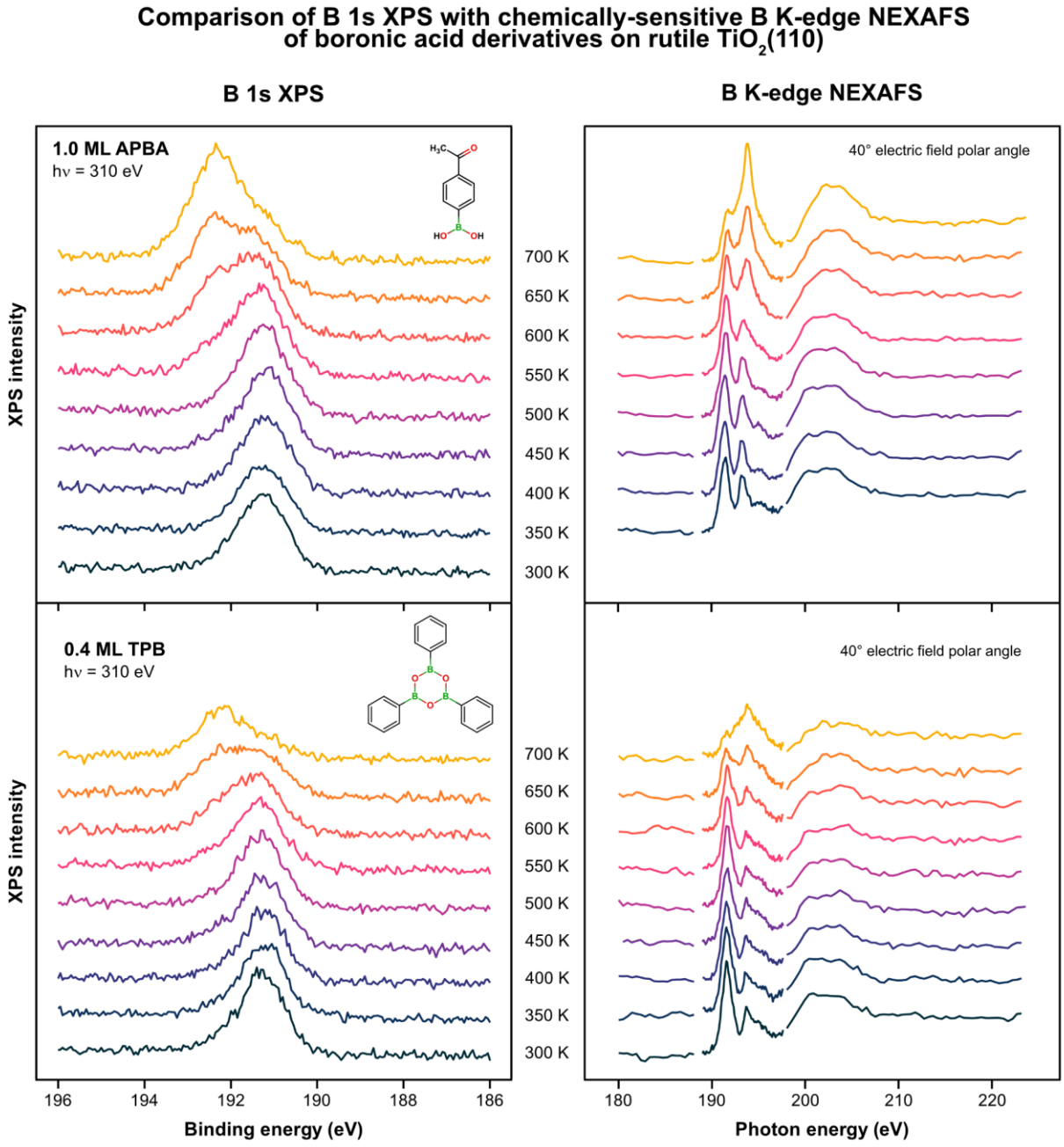

Figure 56: B 1s XPS (left) and B K-edge NEXAFS (right) of a saturation layer of 4-acetylphenylboronic acid and 0.4 ML of 2,4,6-triphenylboroxine on rutile TiO_2(110) as a function of temperature. The sample was annealed in steps of 50 K for 1 min before measurements at room temperature. B K-edge NEXAFS was measured at a polar angle of 40° and an azimuthal angle of 45°, so changes in the intensity of the individual signals are primarily caused by chemical changes. Adapted from Ref. [P3].

the B 1s XPS data. The B K-edge NEXAFS spectrum of 4-acetylphenylboronic acid in Figure 56 after annealing at 350 K shows two clear π* resonances and a third resonance at slightly higher photon energies. Although several resonances are present in B K-edge NEXAFS, only a single peak is observed in the corresponding B 1s XPS (the origin of these resonances will be discussed in more detail below). At 550 K, a high-binding energy shoulder appears in the B 1s XPS spectra and increases with increasing temperature. At the same time, the second π* resonance in B K-edge NEXAFS increases in intensity and shifts from 193.3 eV to a slightly higher photon energy of 193.8 eV, while the first and third π* resonance vanish.

Overall, we observe changes in B K-edge NEXAFS when our B 1s XPS data indicate a chemical change, but NEXAFS can provide us with additional information that would be inaccessible with B 1s XPS, which will be discussed in the following subchapter.

One interesting result of our mostly chemical sensitive NEXAFS is the behavior or 2,4,6-triphenylboroxine compared to 4-acetylphenylboronic acid in Figure 56, because the trends between these two molecules are identical, indicating the on-surface species formed by the adsorption of 2,4,6-triphenylboroxine is very similar to that formed by 4-acetylphenylboronic acid, supporting a ring-opening reaction of the boroxine upon adsorption.

6.3.2. Understanding NEXAFS resonances of phenylboronic acids using simple DFT-calculations

When we first saw multiple resonances in the B K-edge NEXAFS spectrum of 4-acetylphenylboronic acid, we were unsure whether these resonances indicated different boron species at the surface with identical B 1s XPS binding energies, see Figure 56. Especially considering the challenges of making clean deposits of these molecules, we wanted to verify that the observed number of resonances was reasonable.

To tackle this challenge, I collaborated with Prof. Federico Williams, who calculated the gas-phase X-ray absorption spectra of the studied molecules using a TD-DFT approach implemented in the free software package ORCA.[169] Although this theoretical approach is unable to describe the exact peak splitting and exact peak intensities,[170] we perform these calculations on a massively simplified system: The molecule in the gas phase. As a result, a significant discrepancy between theory and experiment is to be expected. Nevertheless, these calculations can give us information

about the number of resonances, which was already a very important piece of information for our system.

Comparison of the TD-DFT calculated B K-edge and C K-edge NEXAFS spectra with experiment shows a reasonably good agreement, see Figure 57. This verifies that the three different resonances in the π* region of 4-acetylphenylboronic acid do indeed originate from the intact molecule by

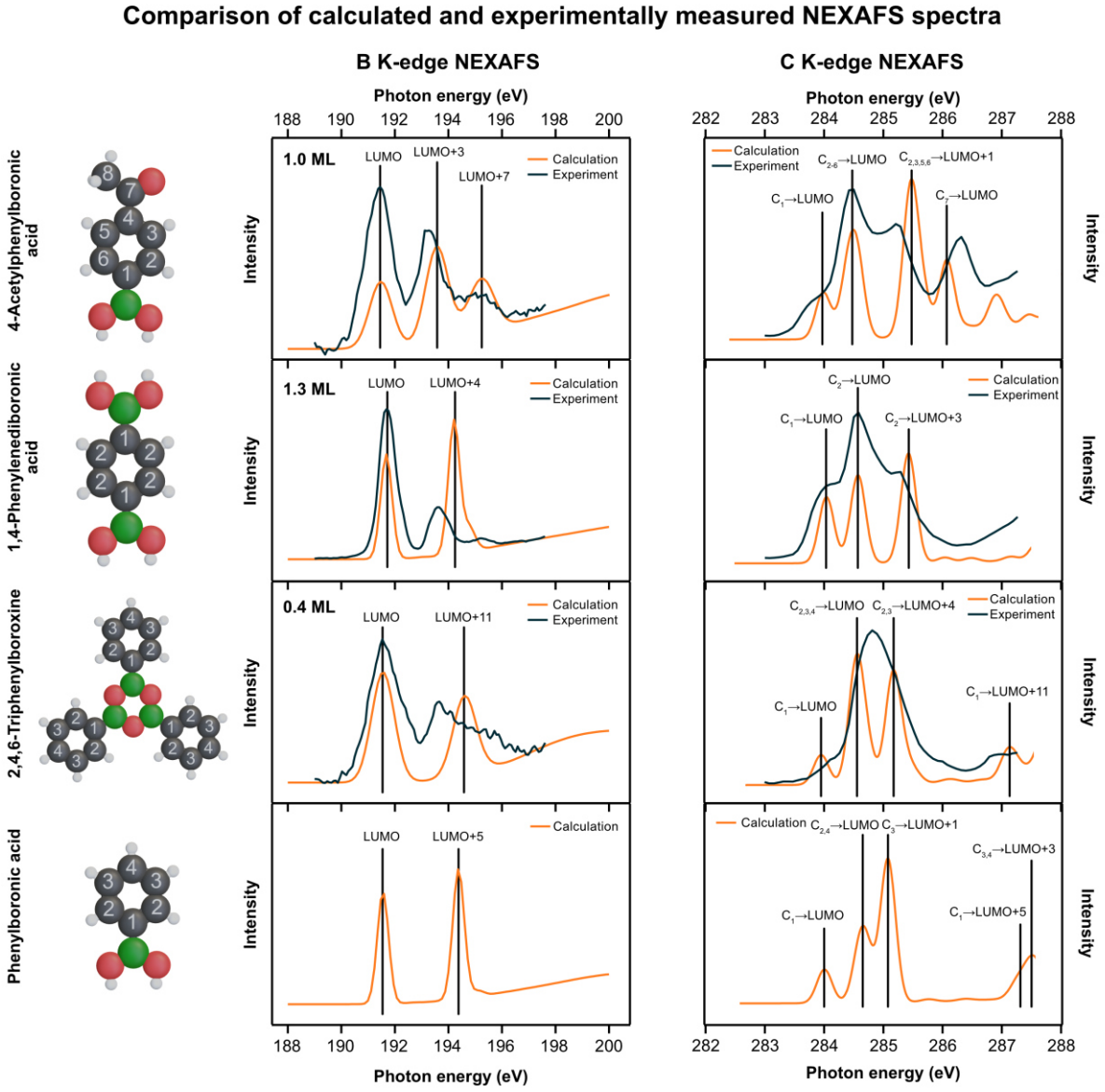

*Figure 57: TD-DFT Calculated gas-phase B K-edge and C K-edge NEXAFS spectra for four boronic acid derivatives, compared with the experimentally-measured spectra on rutile TiO_2(110) after annealing at 400 K for 1 min, using **E**-field polar angles of 40° and 50° for the B and C K-edges, respectively, and an **E**-field azimuthal angle of 45°. Adapted from Ref. [P3].*

excitations to different unoccupied orbitals. This is true for both B K-edge NEXAFS, where multiple resonances originate from the excitation of a core electron into different unoccupied states, and C K-edge NEXAFS, where a combination of excitations from different carbon atoms into different unoccupied orbitals causes the complex peak pattern.

In addition, these calculations enable us to look at other effects, such as how the π* resonances in the B K-edge NEXAFS change when the phenyl ring is rotated around the B-C bond. The results are shown in Figure 58, and for phenylboronic acid, the number of π* excitations decreases from two to one when the plane of the phenyl ring is perpendicular to the plane of the boron-oxygen atoms. In a simplified picture, this is caused by a hybridization between the π-system located on the phenyl ring and the π-system located on the boron and oxygen atoms. If the two π-systems are perpendicular to each other, no electronic interaction is possible and B 1s electrons can only be excited into the π* orbital located on the boron and oxygen atoms, resulting in a single peak. However, if the angle between the two π-systems is less than 90°, they can hybridize and excitation into two different unoccupied orbitals becomes possible. The separation of these two peaks

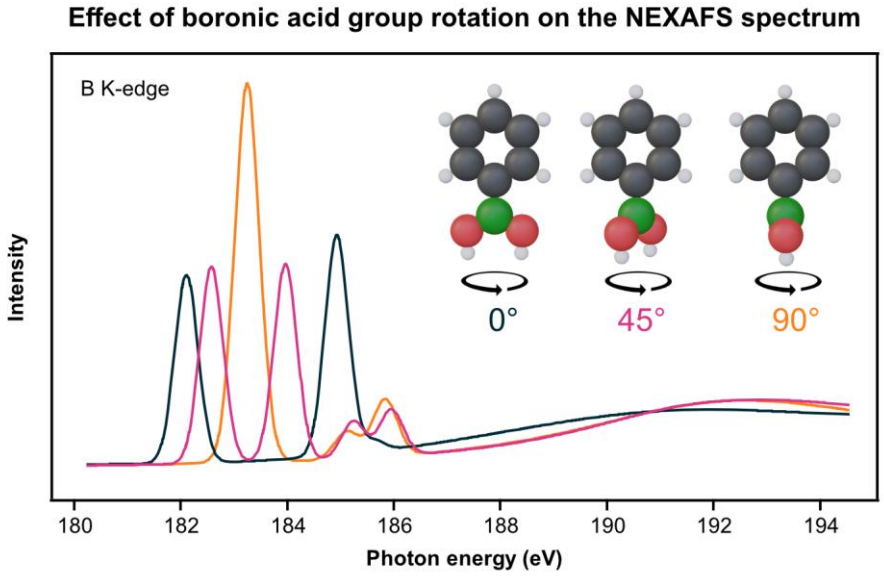

Figure 58: TD-DFT calculated B K-edge NEXAFS spectrum of phenylboronic acid for three different angles between the phenyl ring plane and the boron-oxygen plane. For the most stable structure at 0° rotation, two distinct π excitations are observed. As the angle between the acid group and the phenyl ring increases, the separation between these two signals decreases until only one signal is observed at 90°.*

depends on the angle between the boron-oxygen plane and the phenyl ring plane and is the strongest for 0°, where the overlap between the two π-systems is at its maximum.

Another important question we can address with our primarily chemical sensitive NEXAFS is the local geometry of the boron atom. As already discussed, boron has a trigonal-planar geometry in the boronic acid group, but it is well-known from solution chemistry that when boron reacts with water as a Lewis acid, a tetrahedral R-B$(OH)_3^-$ group forms.[162, 165] We tested the effect of the local boron geometry on the NEXAFS spectrum by performing calculations on phenylboronic acid and the corresponding phenylboronate anion, see Figure 59. While the intact acid shows intense π* resonances, the NEXAFS spectrum of the tetrahedrally coordinated boron atom shows no significant π* resonances. This result is also well documented in the literature, where π* resonances are only present for a trigonal planar geometry, and for a tetrahedral geometry there is only a broad σ* resonance at about 198 eV.[165-167]

In summary, these calculations are clearly not able to reproduce the experimental spectrum. This would require more complex calculations on the molecule adsorbed on the rutile TiO_2(110) surface. Nonetheless, these calculations are a valuable tool to get a better understanding of the

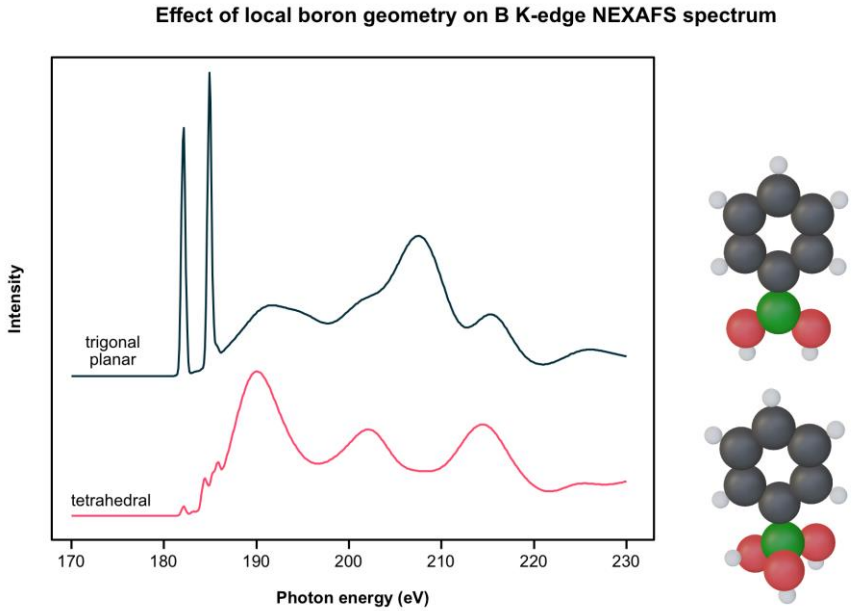

Figure 59: TD-DFT calculated B K-edge NEXAFS spectra of phenylboronic acid and the phenylboronate anion. The boronate anion has almost no π resonances, in agreement with experimental NEXAFS spectra from the literature.*

system. In this case, it was very helpful to confirm that the number of observed resonances is in line with what would be expected for these molecules. Additionally, it enabled us to test general trends, like rotating the boronic acid group out of the phenyl ring plane and checking the effect of a tetrahedral boron geometry on the π*-region. Because these calculations are so simple, they can be performed on a laptop in a reasonable amount of time, opening up the possibility to do them wherever and whenever needed.

6.4. How to get from an Auger-yield NEXAFS measurement to the final spectrum

Several Auger-yield NEXAFS spectra have been presented so far. However, the measured data were subjected to several correction steps before these spectra were obtained. These steps are correction for photon flux, removal of photoemission features, and, if necessary, removal of second-order light features.

How one gets from the raw data to the final NEXAFS spectrum is crucial for assessing the reliability of the results. Since this topic is often only briefly discussed in publications, the how and why of corrections to Auger-yield NEXAFS spectra will be discussed below.

6.4.1. Correct for photon flux

The first and obvious step is to correct for variations in the intensity of the incident light, the photon flux. When talking about photon flux corrections, it is important to distinguish between two possible sources of flux variations: Time and photon energy. The photon flux will vary over time because the beam intensity is directly related to the number of electrons in the storage ring. Over time, the number of electrons decreases, and when they are refilled, the sudden increase in photon flux can cause artefacts in the spectrum. The time-dependent photon flux variation is not a problem at the Materials Science Beamline at Elettra because the storage ring is operated in the so-called top-up injection mode, where the storage ring current deviates by less than 1% from the nominal current. As a result, the changes in beam intensity are smaller than the experimental noise and therefore irrelevant.

In contrast, flux variations as a function of photon energy can have a major effect. These variations originate from the interplay of the light emitted by the bending magnet and the light loss on the optical elements of the beam line. The photon flux of the Materials Science Beamline in Figure 60 shows strong variations with photon energy with a pronounced maximum at 150 eV and characteristic dips at 285, 530, and 575 eV. These characteristic dips can be attributed to absorption at the C K-edge, O K-edge, and Cr $L_{2,3}$ edges, respectively, as these elements are present on the optical elements of the beamline. While carbon and oxygen contaminate optical elements over time from the UHV-atmosphere, chromium is used as an adhesion layer for the gold coating on the optical elements and segregates to the surface over time.

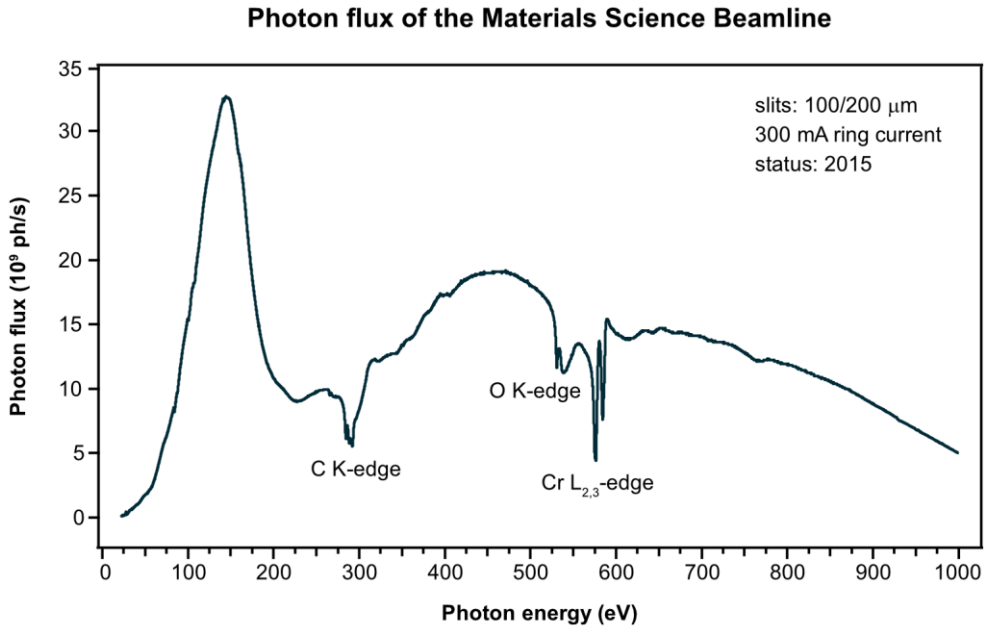

Figure 60: Photon flux at the Materials Science beamline measured with a photodiode. There are two distinct dips just below 300 eV and 560 eV and a small dip at 530 eV. These are due to the presence of carbon and chromium on the optical elements of the beamline. Carbon and oxygen accumulate on the optical elements over time, while chromium is used as an adhesion layer between the silicon and gold on the mirrors. The data for this figure is taken from Ref. [137].

A common and simple way to correct for photon flux is to divide the measured spectrum by the mesh current. The mesh current is the current measured between ground and a gold mesh placed in the path of the incoming X-ray beam. In principle, one measures total-yield NEXAFS of the gold mesh and since gold has a smooth quantum yield,[77] this gives good results. Unfortunately, this fails at the C K-edge because carbon also accumulates on the gold mesh over time. Thus, the measured mesh current is a total-yield C K-edge NEXAFS spectrum of the carbon impurities, see Figure 61 (top right).

To measure photon flux, it is instead possible to follow the intensity of a low binding-energy XPS peak as a function of photon energy. In this thesis, the Ti 3p peak of the rutile TiO_2(110) surface or the Au 4f peak of a polycrystalline gold foil were used. The photon flux is extracted from the measurement by fitting the XPS peak at each photon energy with an area and a y-offset. The resulting fit area gives the photon flux, and at the C K-edge, this photon flux is clearly different from the mesh current, see Figure 61 (right side).

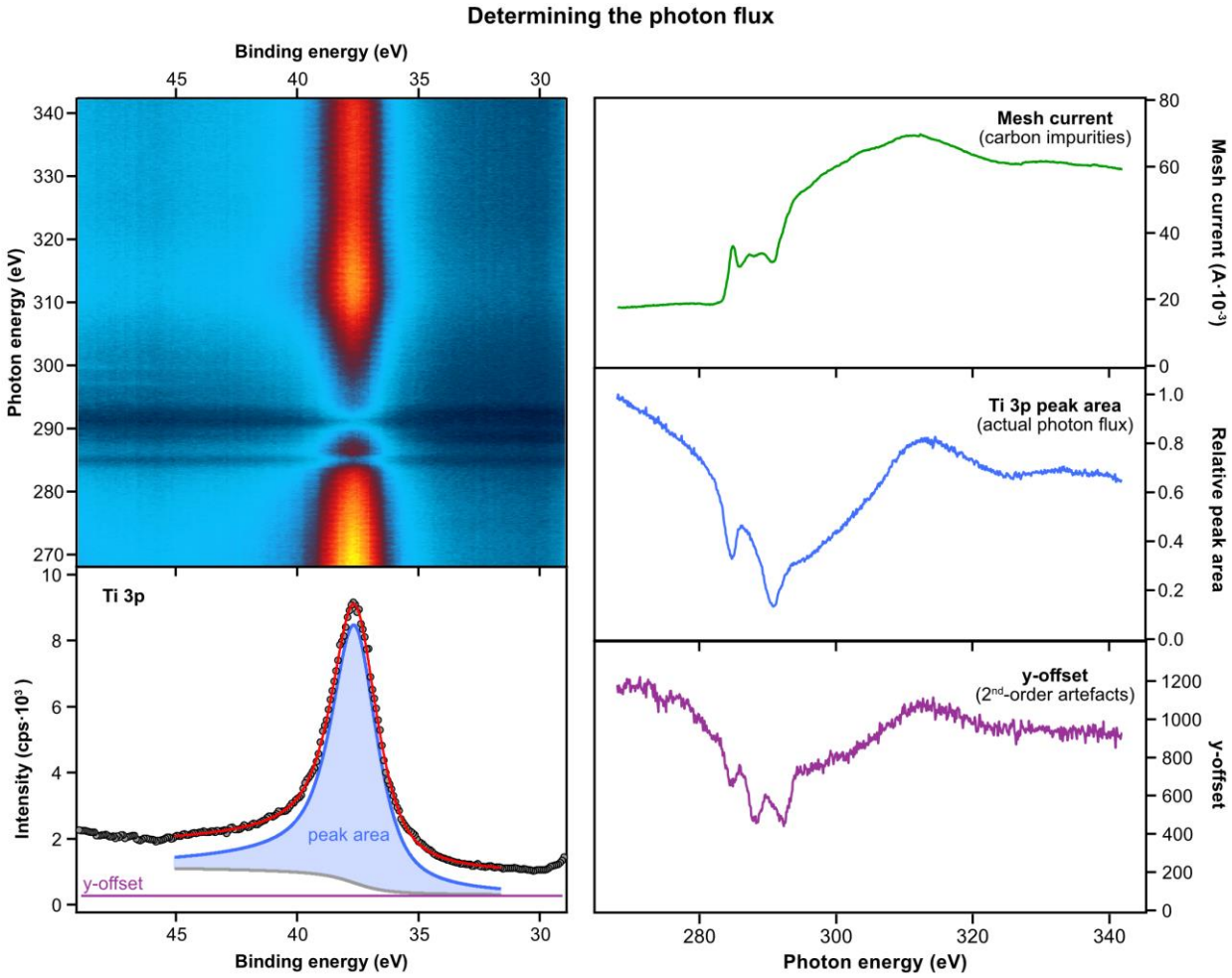

Figure 61: Extraction of the photon flux as the Ti 3p area from the measured image (top left). For each photon energy, the Ti 3p peak (bottom left) is fitted with only two free parameters: the area and the y-offset. The corresponding Ti 3p peak area and the y-offset (middle and bottom right) do not follow exactly the same shape in the photon energy range of 285 to 305 eV, which is the result of contributions of second-order light at the Cr $L_{2,3}$ absorption edge to the y-offset. It would be much easier to simply use the mesh current (top right) for photon flux correction, but the signal of the gold mesh deviates massively from the peak area (=photon flux) due to carbon contaminations.

It is critical to include a y-offset in the fit because the y-offset also changes with photon energy. One would expect the y-offset to follow the intensity of the peak area, since it should correspond to the number of inelastically-scattered electrons, and their intensity depends on the photon flux. However, a comparison in Figure 61 (bottom right) shows that this is not the case for photon energies between 285 eV and 305 eV, as the shape of the peak area and the y-offset are clearly different. In fact, the y-offset shows a new dip at 288 eV, which can be assigned to the Cr $L_{2,3}$

absorption edge excited with second-order light (second-order light will be discussed in more detail in Chapter 6.4.3).

Since the y-offset does not scale with the peak area, it is critical to fit the signal with a peak shape and y-offset when extracting the photon flux. This is especially true when following the intensity of the Ti 3p peak, as this peak has relatively low intensities and therefore the y-intercept can contribute significantly to the overall area. When following a much more intense XPS signal, such as the Au 4f peak of a clean polycrystalline gold foil, the contribution of the intercept is small and the total area of the signal gives a good approximation for the photon flux.

Using a XPS peak to extract the photon flux is not a perfect method, as it can suffer from photoelectron diffraction effects or from changes in the absorption cross section with photon energy. However, the errors introduced by this approach are much smaller than the errors introduced by ignoring the changes in photon flux or by using the mesh current with contamination at the investigated absorption edge. Photon flux corrections are critical at the C K-edge, but may be less important at other absorption edges, such as the B K-edge at about 190 eV, where the overall change in photon flux is smaller and smoother. Nevertheless, each NEXAFS spectrum in this work has been corrected with a photon flux measured on a low-energy XPS peak.

6.4.2. Correct for photoemission features

When measuring a NEXAFS spectrum, the incoming X-rays do not only interact with electrons at the desired absorption edge, but they can also create photoelectrons from core levels with binding energies smaller than the photon energy. For Auger NEXAFS, one can identify the signal of the unwanted photoemission processes in the Auger-yield image as diagonal features, see Figure 62, while the desired Auger intensity can be identified as vertical lines. The main problem with these photoemission features arises when they enter or leave the kinetic energy window, because this causes intensity changes in the NEXAFS spectrum.

The example in Figure 62 has only moderate photoemission features, but photoemission features can be much more pronounced, see the B K-edge NEXAFS in Figure 63. The top left image is completely dominated by the diagonal photoemission signals and the vertical line at 192 eV is barely visible. The corresponding spectrum below is dominated by photoemission features

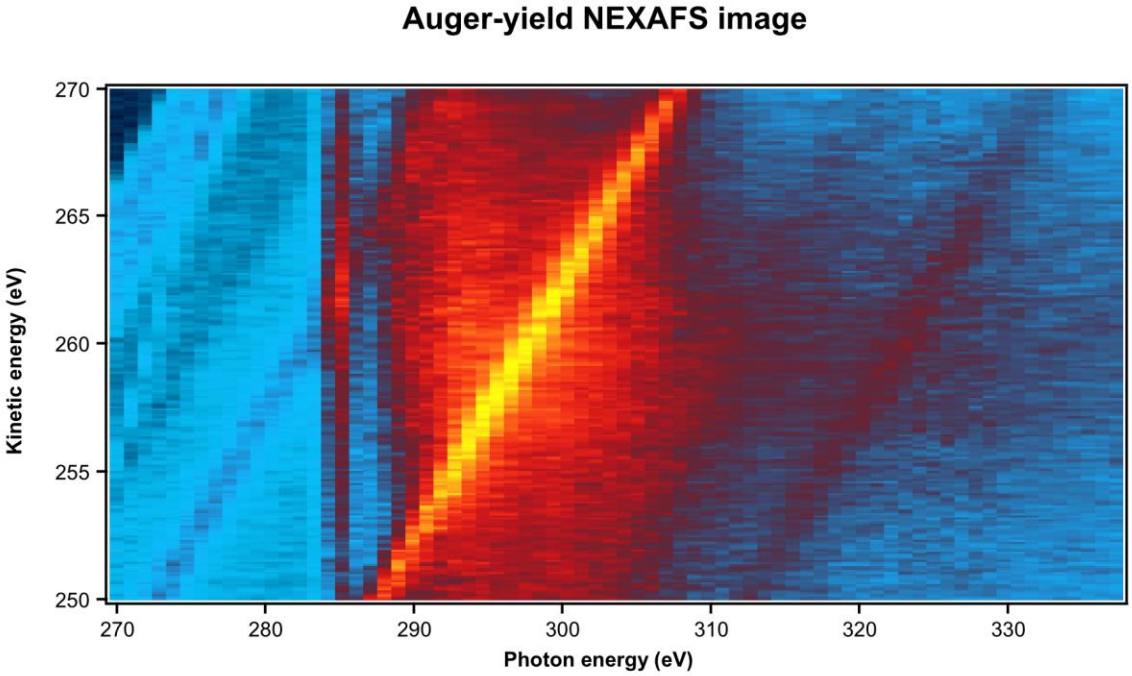

Figure 62: A coarse-resolution C K-edge NEXAFS image with diagonal (XPS-related) and vertical (NEXAFS) features after photon flux correction. It was recorded for 1 ML of 4-acetylphenylboronic acid on rutile TiO_2(110) after annealing at 400 K for 1 min at an electric-field polar and azimuthal angle of 40° and 45°, respectively.

entering and leaving the kinetic energy window, and in this state it is not possible to extract any information from the NEXAFS spectrum.

Fortunately, it is possible to remove photoemission features from Auger-yield NEXAFS, which has been addressed by our group previously.[171] The idea is to describe the measured image by three independent one-dimensional spectra: A XPS spectrum, a NEXAFS spectrum, and an Auger spectrum. It is possible to extract these three independent spectra using an iterative algorithm; the details of this approach are described in Ref.[171].

The capability of this approach is nicely illustrated in Figure 63. It was possible to remove the photoemission signals almost completely, so that the vertical components in Figure 63 (middle, top) are clearly visible. The clean-up is not perfect, as the intense Ti 3p line is still visible as a faint diagonal line, but it is at such low levels that it does not affect the obtained NEXAFS spectrum. The reason for the imperfect removal is found in the assumption that the photoemission intensity does not change with photon energy, but changes are possible due to changes in the absorption

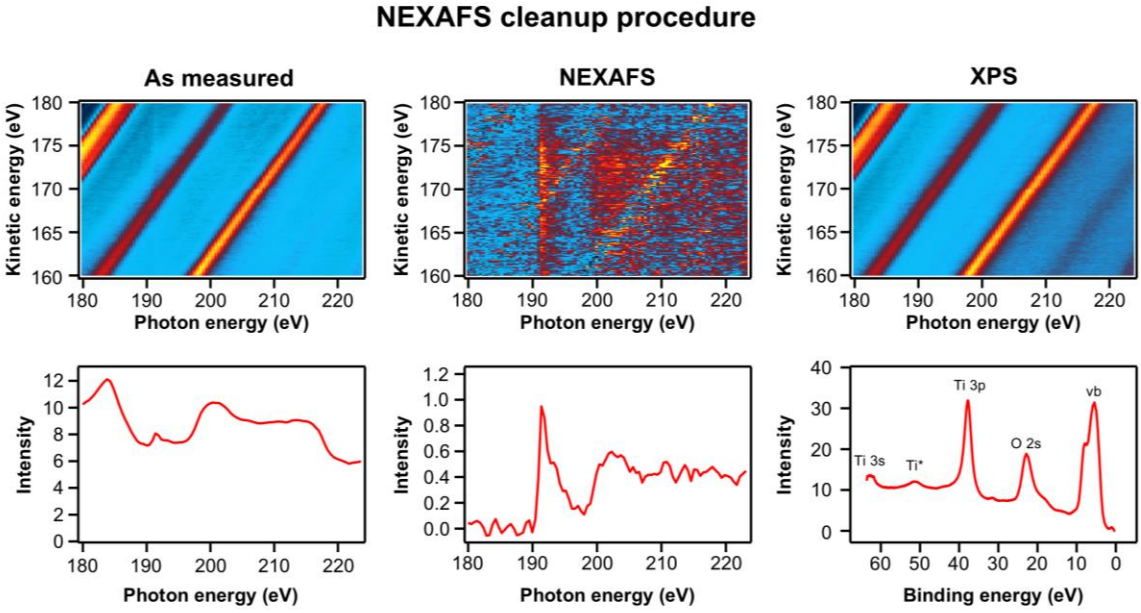

Figure 63: B K-edge NEXAFS spectrum dominated by XPS features (top left). The vertical features are only visible as a very faint line and the corresponding NEXAFS spectrum (bottom left) cannot be evaluated as it is. Separating the measured image into its NEXAFS (middle) and photoemission contributions (right), gives us access to both the NEXAFS spectrum and a XPS spectrum. Data was measured for 0.3 ML of 4-acetylphenylboronic acid on rutile TiO_2(110) after annealing at 450 K for 1 min with an electric-field polar and azimuthal angle of 40° and 45°, respectively. For visualization, a linear background is subtracted from the NEXAFS spectrum and 2D image. Adapted from Ref. [P3].

cross section as a function of photon energy, photoelectron diffraction effects, or errors in the photon flux. Overall, as this example clearly illustrates, removing photoemission features in Auger-yield NEXAFS is an important step in data analysis and gives access to systems that were previously inaccessible.

With this approach, one can obtain a NEXAFS spectrum without contributions from the photoemission feature, but also gain access to the XPS spectrum without NEXAFS contributions. In fact, the extracted XPS spectrum in Figure 63 (right, bottom) contains all the elemental and chemical information of a normal XPS spectrum. Although this is a very time consuming and complicated way to measure XPS, the additional information can be very helpful in analyzing the NEXAFS data. For example, the intensity of the Ti 3p substrate signal was used to scale the C K-edge NEXAFS data of phenylphosphonic acid, as this proved to be more reliable than scaling to the edge jump (details are given in Ref [P2]).

This algorithm for handling photoemission features is only applicable to Auger-yield NEXAFS. In partial-yield NEXAFS, photoemission features cannot be removed in the analysis, but the experimental conditions can be chosen in such a way that they are not relevant by adjusting the retardation voltage so that no photoemission signal enters the measured kinetic energy range in during the measurement.[77]

6.4.3. Correct for second-order light features

In the C K-edge NEXAFS spectrum of 0.5 ML of phenylphosphonic acid on rutile TiO_2(110), we noticed an intense additional feature at 290.8 eV compared to an older measurement, see Figure 64.

The additional feature is caused by second-order light. In this thesis, second-order light comes from the interplay of the bending-magnet light source and the monochromator. A bending magnet light source produces a broadband spectrum similar to a wiggler, and for experiments the desired wavelength is selected with a monochromator. The Materials Science Beamline uses a grating

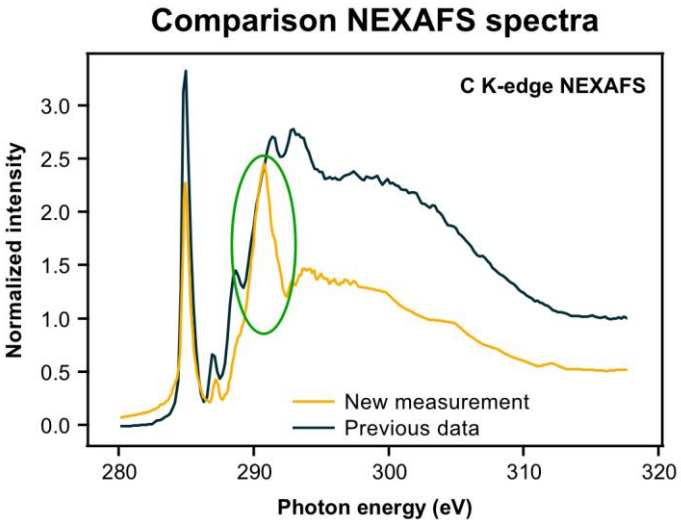

Figure 64: Comparison of C K-edge NEXAFS spectra of phenylphosphonic acid on rutile TiO_2(110) measured at two different beamtimes at an electric-field polar angle of 10° and an azimuthal angle of 0°. The previous measurement was performed on a full monolayer after annealing to 380 K for 1 min (see Ref. [48] for details), while the new measurement was performed on half a monolayer after annealing at 350 K for 1 min. For the new measurement, a new and intense feature at 290.8 eV is present. The new measurement is a combination of two separate measurements with high- and low-resolution regions, causing the sudden change to the noise level around 297 eV.

monochromator. For such a monochromator, the desired wavelength can be selected by adjusting the geometry according to the grating equation:

$$m \cdot \lambda = \Lambda \cdot (\sin(\theta_m) - \sin(\theta))$$

where Λ is the distance between two gratings, λ the wavelength of the passing light, θ_m and θ are the light emission and light incidence angle, respectively, and m is the diffraction order. Choosing a geometry to select the light of the first diffraction order with the desired wavelength λ allows light of the second diffraction order with half the wavelength also to pass. In principle, even higher-order light can pass, but since the intensity of light decreases with increasing diffraction order, only first- and second-order light are significant for the experiments in this thesis.

The presence of second-order light in the synchrotron measurements can be seen very clearly in Figure 65, where two wide-range XPS spectra of a layer of 4-acetylphenylboronic acid on rutile TiO_2(110) were measured at two different photon energies. For the lower photon energy of 340 eV, two additional peaks can be identified at 190 eV and 120 eV, corresponding to the expected positions of the intense substrate peaks when excited with the doubled photon energy of second-order light.

For XPS measurements, second-order light is not a problem because the excitation energy can be adjusted to prevent XPS second-order light peaks from overlapping with the core-level regions of interest. However, this is not possible for NEXAFS. It is possible to suppress higher-order light by selecting appropriate transmission filters,[172, 173] using several pairs of total reflection mirrors[174] or by using designated gratings.[175] Unfortunately, this is not available at the Materials Science Beamline, so it is necessary to correct the recorded data for second-order light contributions.

Mathematically, the measured Auger intensity in NEXAFS I_M is the sum of the first- and second-order contributions I_{1st} and I_{2nd}, respectively, as the sample is illuminated by first- and second-order light at the same time:

$$I_M = I_{1st}(\nu) \cdot F_{1st}(\nu) + I_{2nd}(\nu) \cdot F_{2nd}(\nu)$$

F_{1st} and F_{2nd} are the first- and second-order photon fluxes, as their intensity changes as a function of photon energy.

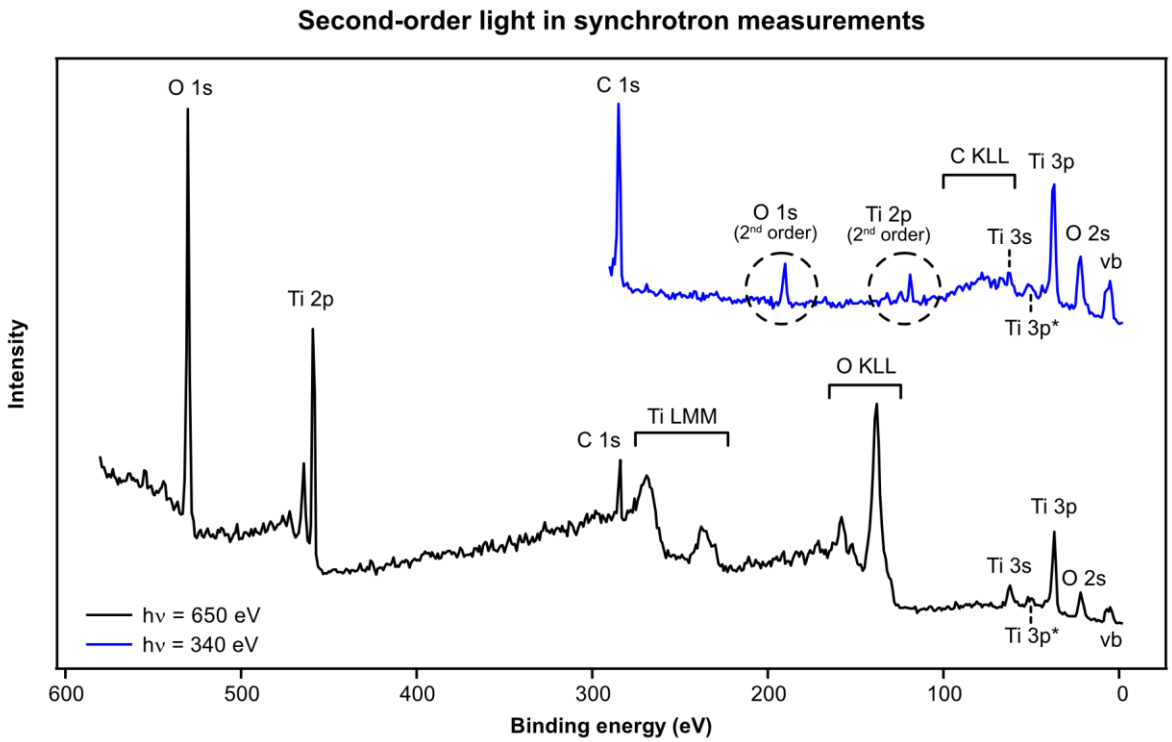

Figure 65: Wide-range synchrotron XPS spectra of 0.3 MLs of 4-acetylphenylboronic acid on rutile TiO_2(110) taken at two different excitation energies. The XPS peaks are at the same binding-energy positions for both measurements, while the Auger peaks are shifted. However, there are two sharp peaks in the low-excitation energy XPS spectrum at 190 eV and 120 eV that are not found in the high-excitation energy XPS spectrum. These additional peaks match the expected binding-energy position of the intense O 1s and Ti 2p substrate signals when excited with second-order light.

In many cases, the second-order photon flux is sufficiently low compared to F_{1st}, so that the contributions from second-order light can be safely ignored. However, this is not the case at the C K absorption edge at the Materials Science Beamline, where the first-order photon flux decreases by up to 85%, see Figure 66 (top left, purple graph).

An important step in the analysis of C K-edge NEXAFS data is the correction for the photon flux, which is done by dividing the measured intensity I_M with the first-order photon flux F_{1st}. To further simplify the equation, we assume that the intensity contribution of the second-order light I_{2nd} is a constant c, because there are no absorption edges in the second-order light range.

$$S_M = I_{1st}(\nu) + c \cdot \frac{F_{2nd}(\nu)}{F_{1st}(\nu)}$$

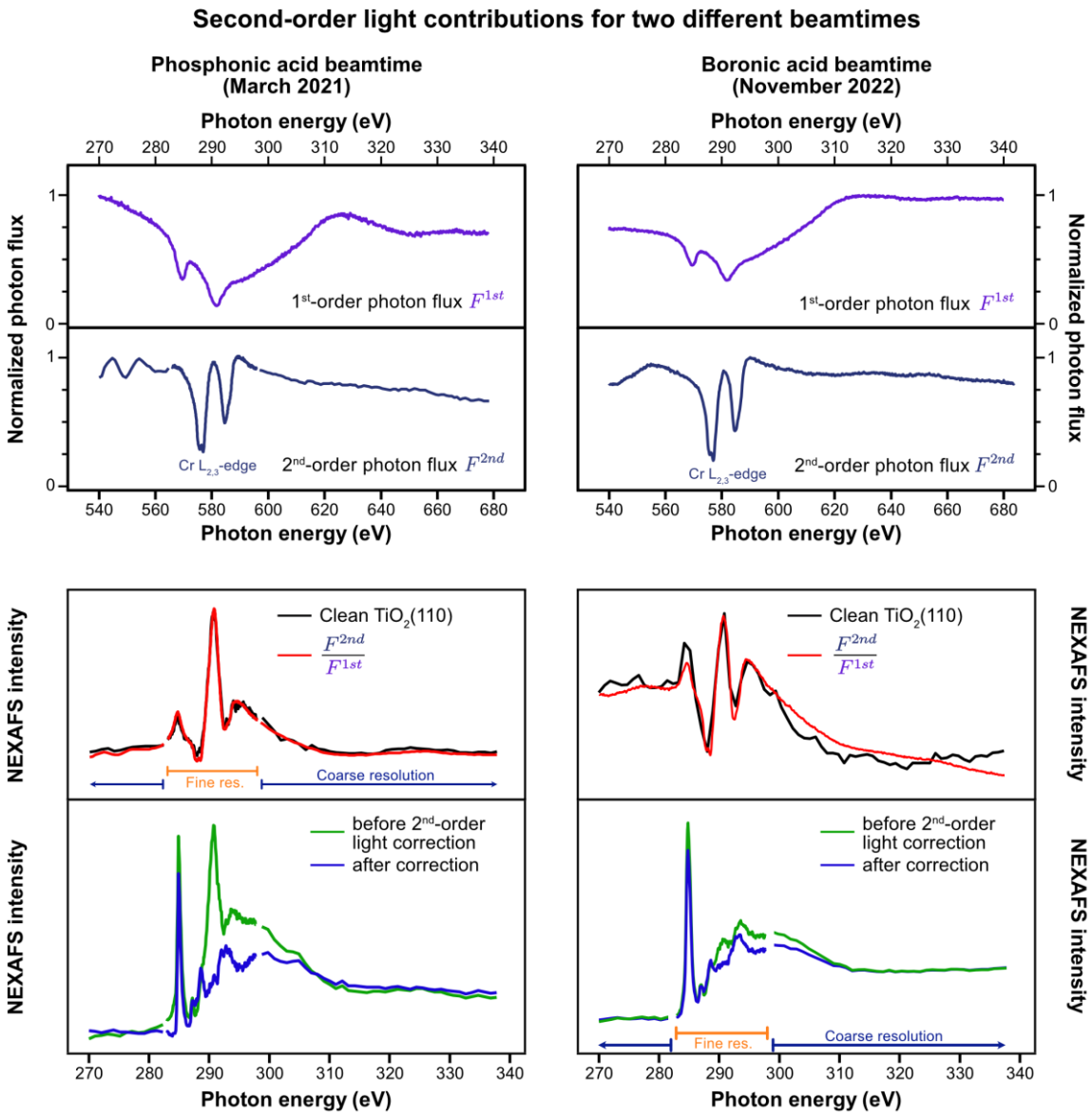

Figure 66: Photon fluxes for the first- and second-order C K-edge NEXAFS photon-energy window from two different beamtimes (measured by following the Ti 3p or Au 4f peak intensity). Massive dips are observed in both the first- and second-order photon fluxes, which are attributed to carbon and chromium contaminations on the optical elements, respectively. Based on the two photon fluxes, we are able to predict the shape of the second-order contribution, which can be fitted with a linear background and a scaling factor to match the experimental clean surface C K-edge NEXAFS spectrum (middle). The experimental spectra on the left are corrected for second-order light using a peak just before the onset of the π peak at 283 eV. For the right side, we scale with the average intensity between -2 and -7.5 eV binding energy obtained from separate XPS measurements. The resulting C K-edge NEXAFS spectra after correction (bottom) show that the second-order light contribution was significantly stronger in our earlier beamtime (left). Experimentally, we measured our C K-edge NEXAFS spectra with two photon energy resolutions, as discussed in the text. Adapted from Refs. [P2] and [P3].*

In case of the clean-surface NEXAFS spectrum, I_{1st} is also flat and featureless, so it is assumed to be a constant d, resulting in the equation

$$S_M^{clean} = c \cdot \frac{F_{2nd}(\nu)}{F_{1st}(\nu)} + d$$

This suggests that the clean surface spectrum can be simply described by the ratio of the two photon fluxes F_{2nd} and F_{1st}. Fitting this equation in combination with a linear background to the NEXAFS spectrum of the clean surface yields an almost perfect match, see Figure 66 (middle). This convincingly shows that second-order light causes the clean-surface features, as the interplay of the two strongly changing photon fluxes in Figure 66 (top) can reproduce the experimental spectrum very well.

It is also possible to use a clean surface NEXAFS spectrum recorded in the second-order light region instead of the second-order photon flux. Using a measured NEXAFS spectrum instead of the second-order light photon flux has the advantage that it does not assume the second-order intensity to be flat and featureless. The signal from the rutile TiO_2(110) surface is almost flat and featureless, with only a few small features from the O K edge falling into the second-order light region, see Figure 67, and as a result, both a photon flux (middle right) and a NEXAFS spectrum (middle left) result in reasonable estimates of the second-order light peak shape in Figure 66. In summary, it is possible to describe the shape of second-order light features if the first- and second-order photon fluxes are available or, instead of the second-order photon flux, a clean surface NEXAFS spectrum in the second-order light region.

To correct C K-edge NEXAFS spectra from second-order light features requires thus only the scaling factor c, which is a measure of the number of secondary electrons being generated by second-order light. These electrons originate primarily from substrate-related core levels, such as the Ti 3p and O 2s XPS peaks, but also the O KLL (503 eV kinetic energy) and Ti LMM (418 eV kinetic energy) Auger peaks.[176] In addition, there may be contributions from the overlayer, such as the C 1s, B 1s, or P 2p core levels. Unfortunately, the number of detected second-order light secondary electrons changes when the coverage or the angle of electron emission changes. This makes predicting the scaling factor very difficult, as it would require predicting the intensity contributions of the overlayer and an attenuated substrate, and it is much simpler to extract it from the experimental data instead.

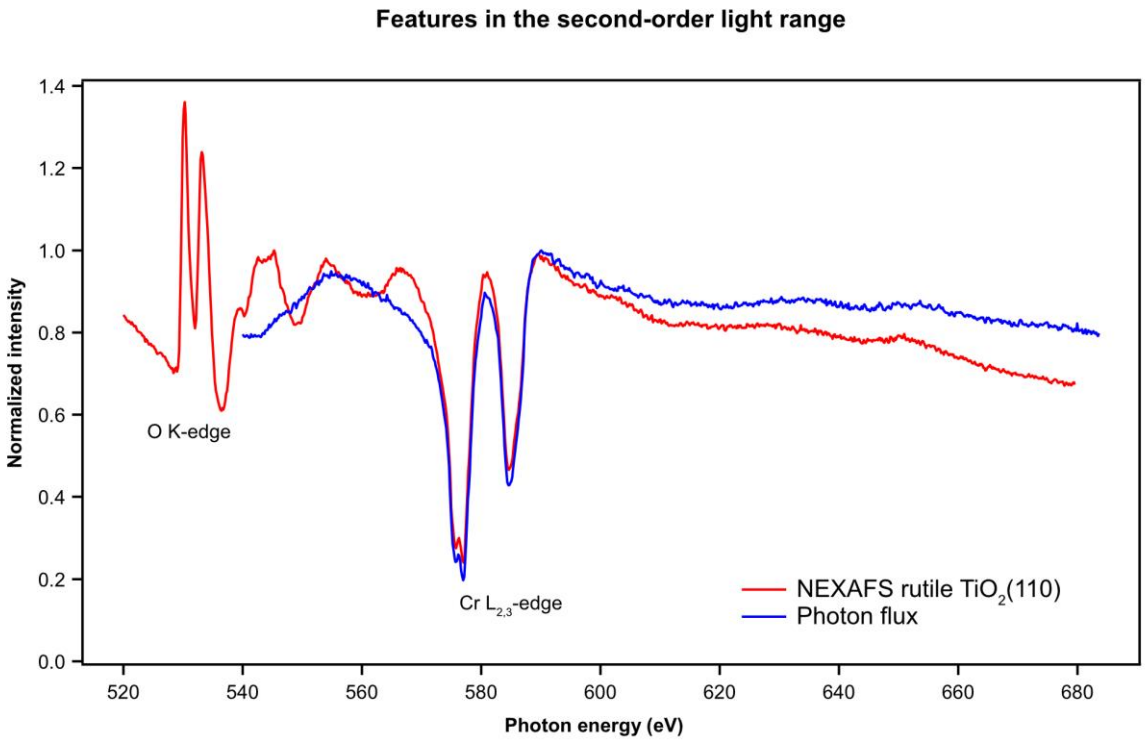

Figure 67: Comparison of a C K-edge NEXAFS spectrum of the clean rutile TiO_2(110) surface in the second-order light region with the second-order light photon flux. The deviations below 575 eV originate from the O K absorption edge, where some of the features also extend into the energy range relevant for second-order light contributions in C K-edge NEXAFS starting at about 540 eV.

This can be done using the first peak in the second-order light contribution at 284.7 eV, see Figure 68. We are forced to use the small peak instead of the intense second-order light feature at 292 eV because the intense feature overlaps with signals from the adsorbed molecule. Although the small peak overlaps with the first molecule-related π* resonance at 284.9 eV, the low photon energy shoulder extends far enough to no longer overlap with the π* resonance of the spectrum. Thus, a peak was fitted only to the small onset around 283 eV, see Figure 68 (left), and the second-order contribution was subtracted after scaling the calculated second-order spectrum according to this intensity. This works reasonably well, as it removes all second-order light features, see Figure 66 (bottom left). Unfortunately, the initial shoulder used for scaling is a small feature, see Figure 68 (left), and any scaling based on it will have some uncertainty associated with it, which is especially relevant around 292 eV, where the intense second-order light feature was present.

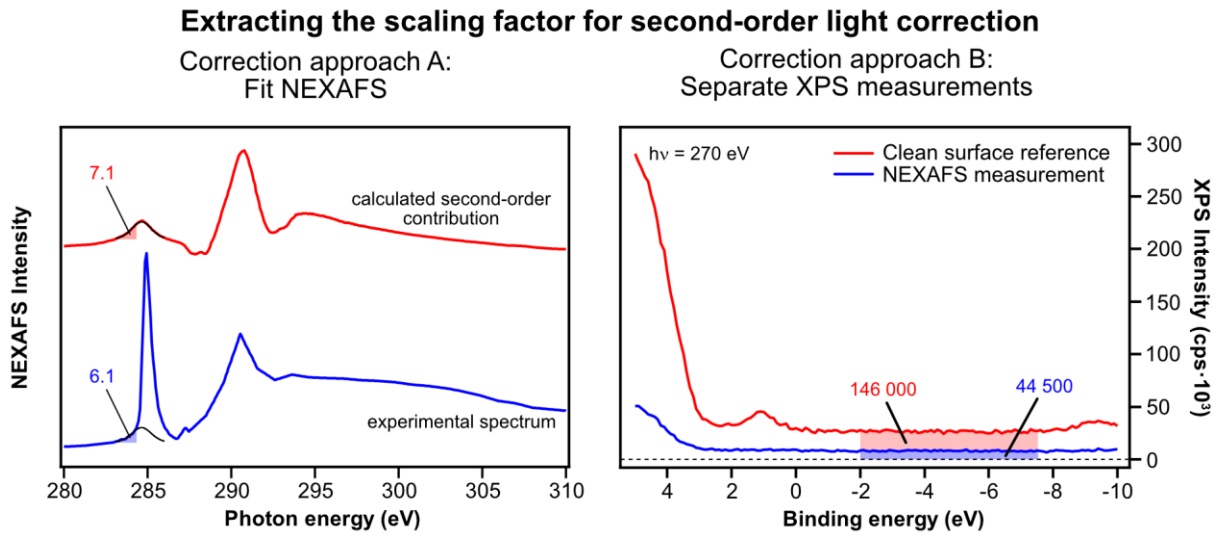

Figure 68: Comparison of the two correction approaches for second-order light: For phenylphosphonic acid NEXAFS spectra, the scaling factor applied before subtracting the calculated second-order light contribution was determined by fitting a small feature just at the onset of the π peak. Since it is a small feature in front of an intense peak, there is a significant uncertainty associated with its area. To avoid this uncertainty, a second approach was used: XPS spectra were measured at a photon energy of 270 eV below 0 eV binding energy. The intensity below 0 eV originates from second-order light, and extracting the area of this signal should give a more accurate scaling factor.*

Although this approach worked for the C K-edge NEXAFS data of phenylphosphonic acid on rutile TiO_2(110), it is only applicable to systems with no π* resonances overlapping with the signal at 283 eV. However, this is the best correction procedure we were able to use with the data available.

Of course, it is not desirable to fit a small feature directly in front of the π* resonances. Fortunately, there is a way around this by adding a quick additional measurement: For each measured NEXAFS spectrum, an additional XPS spectrum with binding energies between 5 and -10 eV was measured. For negative binding energies, all photoelectrons must come from second-order light, and we can use the area of this signal to scale the calculated second-order contribution before subtraction, see Figure 68 (right). This approach was applied to the C K-edge NEXAFS data of the boronic acid derivatives, and it worked similarly well, see Figure 66 (right side).

Unfortunately, it is hard to say whether the second approach works better, because the second-order light features were significantly less pronounced in the measurements with the boronic acid derivatives, see Figure 66 (bottom). This is surprising, as one would expect carbon to slowly

accumulate on the optical elements of the beamline over time, and thus the problems with second-order light should get worse, not better. We do not have a definitive answer to this observation, but we suspect that the beam parameters may be the reason. We measured phenylphosphonic acid in March 2021 with a storage ring energy and current of 2.4 GeV and 140 mA, respectively (large second-order light features), and the boronic acid derivatives in November 2022 with storage ring parameters of 2.0 GeV and 300 mA (small second-order light features). Changing the storage ring parameters will likely change the position of the beam on the optical elements, and depending on these positions, there may be slightly more or less carbon in the beam path.

The procedure shown enables the correction of second-order light, but this is not always necessary. At the B K edge, for example, the ratio of second- to first-order photon flux remains small and thus it is not necessary to correct for second-order light.

6.4.4. Conclusions

All these corrections outlined in the previous subchapters are necessary steps to obtain NEXAFS spectra, which can then be further evaluated to determine, for example, the adsorption geometry of a molecule. Over the last decade, we understood Auger-yield NEXAFS in our group better and better, starting with a proper photon flux correction, developing an algorithm for photoemission-feature removal,[171] and during my thesis, dealing with second-order light. Therefore, a quick summary of the most important lessons learned is given in Figure 69.

1. Photon flux correction

Why?

The photon flux varies as a function of photon energy and time. These changes have to be eliminated, especially when trying to remove photoemission features.

How?

It is possible to follow the photon flux by measuring the current of a gold mesh in the beam path. This is sufficient to correct for changes in photon flux with time and gives good results for changes with photon energy. However, this does not work at the C K-edge due to carbon contaminations on the mesh. Another option is to follow the intensity of a low-binding energy XPS peak. Although this method can suffer from photodiffraction effects, it usually gives a much better description of the photon flux in comparison to the gold mesh current.
In our experience, a polycrystalline gold foil is a very good sample for these measurements, but it can be more convenient to use a low-binding energy XPS peak of the sample already mounted (e.g. Ti 3p for rutile TiO_2(110)).

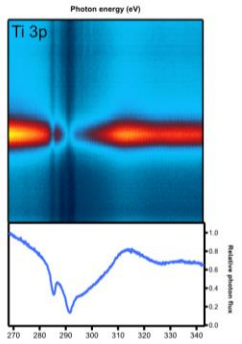

2. Removing photoemission features

Why?

In Auger-yield NEXAFS, photoemission features appear as diagonal lines in the 2D NEXAFS image. If they enter or leave the measured kinetic energy window, the intensity in the NEXAFS spectrum changes. These features can be very intense and they can potentially change the edge jump or peak areas and must therefore be eliminated.

How?

It is possible to separate the measured image into three independent spectra: NEXAFS, Auger, and XPS. An algorithm developed by our group[1] gives access to these three fundamental spectra, which can then be used for further evaluation. This algorithm assumes that the XPS features do not change intensity while travelling through the image. It is therefore very important to properly correct for the photon flux first.

[1]Lytken *et al.*, *J. Electron Spectros. Relat. Phenomena*, 218 (**2017**) 35-39

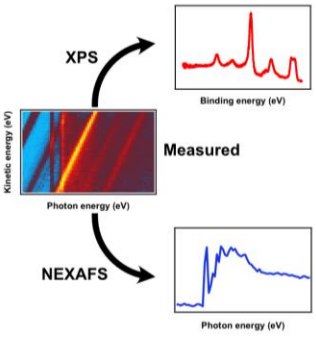

3. Removing 2nd-order light artefacts

Why?

Second-order light features arise when the ratio between the first- and second-order photon flux becomes large. This can be the case at the C K-edge, where the first-order photon flux decreases by up to 80% due to carbon contaminations of the optical elements. The most intense second-order light feature arises at a photon energy of 291 eV, but a smaller feature also contributes to the π^* peak area. Since these features can be very intense compared to the NEXAFS signal, it is necessary to remove them.

How?

The shape of second-order light features can be described by the ratio of the first- and second-order photon flux and the second-order light features can be removed by subtracting a scaled ratio of these two photon fluxes. However, the intensity of these features must be extracted separately. This can either be done by fitting the onset of the first second-order light feature (if there is no overlap with the π^*-resonances) or by performing additional XPS measurements for each NEXAFS measurement and using the intensity at negative binding energies.

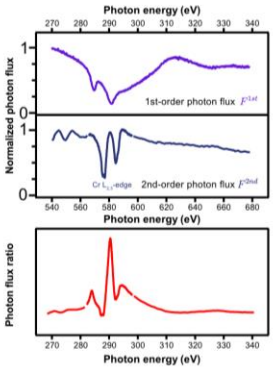

Figure 69: Overview over data treatment before analysis of the NEXAFS spectrum itself.

7. Conclusion and outlook

My research focused on the fundamental aspects of molecules binding to oxide surfaces. I studied large, mainly van-der-Waals-bound, metallotetraphenylporphyrin molecules on a thin MgO(100) film and the adsorption of the anchoring groups phosphonic acid and boronic acid on the rutile TiO_2(110) surface.

It is very difficult to determine the adsorption energy of metallotetraphenylporphyrins because monolayers of these molecules decompose before desorbing. However, on the inert MgO(100) surface, it was possible to desorb the monolayer and determine the adsorption energy. This is a useful benchmark for dispersion correction schemes in DFT and Prof. Bernd Meyer was able to reproduce the experimental adsorption energies with good accuracy, showing that his newly developed correction scheme works well. In addition, these calculations enabled an in-depth analysis of the adsorption geometry, which is determined by the oxophilicity of the metal center in combination with the rigidity of the porphyrin core (for details see Ref. [P1]).

The investigation of oxygen-containing anchor groups on the rutile TiO_2(110) surface by XPS is challenging because the O 1s signal of the anchor group overlaps with the signal of the substrate oxygen atoms. Although the molecular contributions of the phosphonic acid anchor group are clearly observed in the O 1s core-level spectrum, it is challenging to separate them from the substrate signal because the shape of the substrate signal contribution changes upon adsorption of the molecule. In a second collaboration with Prof. Bernd Meyer (Ref. [P2]), we used calculated O 1s core-level binding-energy shifts to predict the full O 1s core-level spectrum, including up to 96 oxygen atoms of the molecule and the first three trilayers of the substrate. We found excellent agreement for a bidentate one-fold deprotonated adsorption mode for temperatures below 450 K, as even the changes in substrate peak shape were reproduced. Comparing the predicted angular dependency of the π^* peak area with the experimental results, we suggest that the phenyl rings adopt a T-stacking pattern in the bidentate one-fold deprotonated adsorption mode. For the high-temperature species above 500 K, we were not able to obtain such a good agreement, but our data suggest a mixed bidentate and rotated tridentate adsorption mode in a ratio of 3:5. This pattern requires 1.25 oxygen vacancies per molecule, which originate primarily from the recombination and subsequent desorption of surface OH groups as water (1 vacancy per molecule) and from

naturally-occuring oxygen vacancies (which are about 12.5% of the oxygen row atoms, corresponding to 25% per molecule).

This direct comparison of the predicted O 1s core-level spectra and the predicted angular dependency of the π* peak area allowed us to validate our DFT calculations against the experiment. This gave us a detailed insight into the temperature dependency of the adsorption binding mode of the phosphonic acid group and revealed the effect of the adsorption of phosphonic acid groups on the substrate. We suggested that the changes to substrate relaxations might cause the observed change in near-surface polaron concentrations, and we hope to investigate this further with DFT calculations in the future.

Overall, the collaboration with Prof. Bernd Meyer enabled a detailed understanding of the investigated systems. Unfortunately, such in-depth calculations were not available for the study of phenylboronic acid derivatives on rutile TiO_2(110) (Ref. [P3]). Nevertheless, we were able to identify general patterns in the adsorption chemistry. Using B K-edge NEXAFS in an almost exclusively chemically sensitive mode, we found that the boron atom of this anchor group always remains in a trigonal planar geometry and does not form a fourth bond to a surface oxygen atom, indicating the strong bond must come from the oxygen atoms of the acid group. At room temperature, both 4-acetylphenylboronic acid and 1,4-phenylenediboronic acid adsorb in a monodentate adsorption mode. Upon annealing to 550 K, surface OH groups desorb as water and a bidentate adsorption mode forms. This bidentate adsorption mode can already be formed by 2,4,6-triphenylboroxine upon adsorption at room temperature by the formation of phenylboronic acid monomers via an on-surface ring-opening reaction. The functionalization of these molecules also influences their on-surface reactivity: We observe a coverage dependency on the decomposition temperature and orientation of the carbonyl group of 4-acetylphenylboronic acid, which interacts with the surface at low coverage and thus starts to decompose already at lower temperatures. For 1,4-phenylenediboronic acid, we observe the second boronic acid group to point always to the vacuum interface, which enables the formation of boronic acid networks by water elimination. These phenylboronic acid derivatives are an interesting system and the investigation in my thesis only scratched the surface. It would be very interesting to perform additional temperature-programmed desorption experiments to identify the desorption products and possible surface reactions.

In this thesis, I did not only focus on the details of the scientific knowledge gained about these systems, but also on the experimental techniques. This is especially true for Auger-yield NEXAFS, because the path from the measured image to the final spectrum involves several corrections. In my research, correction schemes for second-order light contributions were developed that allow the removal of unwanted second-order light features overlapping with the C K-edge NEXAFS signal.

8. Zusammenfassung und Ausblick

Meine Forschung konzentrierte sich auf grundlegende Aspekte der Bindung von Molekülen an Oxidoberflächen. Ich untersuchte große, hauptsächlich van-der-Waals-gebundene Metallotetraphenylporphyrinmoleküle auf einem dünnen MgO(100)-Film und die Adsorption von Phosphonsäure- und Boronsäure-Ankergruppen auf der Rutil TiO_2(110)-Oberfläche.

Aufgrund von Zersetzungsreaktionen ist es in der Regel schwierig, die Adsorptionsenergie der Monolagen von Metallotetraphenylporphyrinen zu bestimmen. Auf der inerten MgO(100)-Oberfläche war es jedoch möglich, die Monolage zu desorbieren und so die Adsorptionsenergie dieser Moleküle zu bestimmen. Dies ist eine nützliche Referenz für Dispersionskorrekturen in dichtefunktionaltheoretischen Rechnungen, und Prof. Bernd Meyer konnte mit einem neuen Korrekturschema die experimentellen Adsorptionsenergien mit guter Genauigkeit reproduzieren. Darüber hinaus ermöglichten diese Berechnungen eine detaillierte Analyse der Adsorptionsgeometrie, die durch die Oxophilie des Metallzentrums in Kombination mit der Steifigkeit des Porphyringerüstes bestimmt wird (für Details siehe Ref. [P1]).

Die Untersuchung von sauerstoffhaltigen Ankergruppen auf der Rutil-TiO_2(110)-Oberfläche mittels XPS ist herausfordernd, da sich das O 1s-Signal der Ankergruppe mit dem Signal der Substratsauerstoffatome überlagert. Obwohl die Signale der Ankergruppe im O 1s XPS Spektrum deutlich sichtbar sind, ist es sehr schwierig, diese Signale vom Substratsignal zu trennen, da die Adsorption des Moleküls das Substratsignal verändert. In einer zweiten Zusammenarbeit mit Prof. Bernd Meyer (Ref. [P2]) wurden die berechneten relativen Bindungsenergien von bis zu 96 verschiedenen Sauerstoffatomen des Moleküls und der ersten drei Oberflächenschichten verwendet, um das vollständige O 1s XPS Spektrum zu berechnen. Die experimentellen Daten für Temperaturen unter 450 K stimmen sehr gut mit dem berechneten Spektrum eines Moleküls im bidentaten einfach deprotonierten Adsorptionsmodus überein. Durch den Vergleich der theoretisch vorhergesagten und der experimentell bestimmten Winkelabhängigkeit der π^*-Peakfläche mittels NEXAFS konnte ermittelt werden, dass die Phenylringe wahrscheinlich in einer T-Konfiguration angeordnet sind. Leider ist die Übereinstimmung bei höheren Temperaturen (> 500 K) nicht so gut wie bei niedrigen Temperaturen, aber unsere Daten deuten auf einen gemischten bidentaten und rotierten tridentaten Adsorptionsmodus in einem Verhältnis von 3:5 hin. Dieser Adsorptionsmodus erfordert 1.25 Sauerstofffehlstellen pro adsorbiertem Molekül. Diese Sauerstofffehlstellen ergeben

sich aus der Rekombinationsreaktion der Hydroxylgruppen der Oberfläche zu Wasser (generiert eine Fehlstelle pro Molekül) und der Anzahl der natürlich vorkommenden Sauerstofffehlstellen (12.5 % in der Sauerstoffreihe, entspricht 25 % pro adsorbiertem Molekül).

Durch den direkten Vergleich der berechneten O 1s XPS Spektren und der berechneten Winkelabhängigkeiten der π* Peakflächen konnten die berechneten Strukturen experimentell bestätigt werden. Dies ermöglichte uns einen detaillierten Einblick in die Temperaturabhängigkeit des Adsorptionsmodus von Phenylphosphonsäure und dessen Einfluss auf die Oberfläche. Wir vermuten, dass die Änderungen der Substrat-Relaxationen die beobachteten Änderungen der oberflächennahen Polaronenkonzentrationen verursachen könnten, und wir hoffen, dies in Zukunft mit weiteren DFT-Rechnungen zu überprüfen.

Insgesamt haben die Kollaborationen mit Prof. Bernd Meyer zu einem tieferen Verständnis von Molekülen auf Oxidoberflächen geführt. Leider war es nicht möglich die Adsorption von Phenylboronsäurederivate in Ref. [P3] mithilfe ähnlich detaillierter Berechnungen zu analysieren. Nichtsdestotrotz konnten wir generelle Trends in der Adsorptionschemie identifizieren, zum Beispiel durch den Einsatz von B K-Kanten NEXAFS in einer nahezu vollständig chemisch sensitiven Messgeometrie. Es wurde herausgefunden, dass das Boratom dieser Ankergruppe immer in einer trigonal-planaren Geometrie verbleibt und keine vierte Bindung zu einem Oberflächen-Sauerstoffatom eingeht, was darauf hindeutet, dass die starke Bindung zu Oberfläche von den Sauerstoffatomen der Säuregruppe ausgehen muss. Bei Raumtemperatur adsorbieren sowohl 4-Acetylphenylboronsäure als auch 1,4-Phenylendiboronsäure in einem monodentaten Adsorptionsmodus. Nach dem Erhitzen auf 550 K desorbieren die OH-Gruppen der Oberfläche als Wasser und es bildet sich ein bidentater Adsorptionsmodus aus. Dieser bidentate Adsorptionsmodus kann von 2,4,6-Triphenylboroxin bereits bei der Adsorption bei Raumtemperatur durch die Bildung von Phenylboronsäuremonomeren über eine Ringöffnungsreaktion an der Oberfläche gebildet werden. Die Funktionalisierung dieser Moleküle beeinflusst auch ihre Reaktivität an der Oberfläche: Wir beobachten eine Bedeckungsabhängigkeit bei der Zersetzungsreaktionstemperatur und Ausrichtung der Carbonylgruppe in 4-Acetylphenylboronsäure, die bei geringer Bedeckung mit der Oberfläche wechselwirkt und dadurch bereits bei niedrigeren Temperaturen zersetzt wird. Bei 1,4-Phenylendiboronsäure beobachten wir, dass die zweite Borsäuregruppe immer zur Vakuumgrenzfläche zeigt, was die

Bildung von Borsäurenetzwerken durch Wassereliminierung ermöglicht. Insgesamt zeigen die untersuchten Phenylboronsäurederivate interessante chemische Eigenschaften und weitere Experimente sind notwendig um ein vollständigeres Bild der Reaktivität dieser Moleküle zu erhalten. Es wäre zum Beispiel sehr interessant mithilfe von TPD die Desorptionsprodukte als Funktion der Temperatur zu identifizieren um damit Rückschlüsse auf die Oberflächenreaktionen ziehen zu können.

In dieser Doktorarbeit habe ich mich nicht nur auf die Details meiner Resultate fokussiert, sondern auch den experimentellen Methoden große Aufmerksamkeit gewidmet. Dies ist besonders für Auger-yield NEXAFS der Fall, da bei dieser Methode das gemessene NEXAFS-Bild für verschiedene Effekte korrigiert werden muss. Während meiner Forschung wurde ein Korrekturschema entwickelt, mit dem es möglich ist, die von Licht zweiter Ordnung verursachten Signale, die sich mit dem C K-Kanten NEXAFS Signal überlagern, zu eliminieren.

9. Acknowledgements

The data for a Ph.D. thesis can be measured in ultra-high vacuum, but the thesis cannot be created in a vacuum – many people are involved and supported me in my scientific journey:

PD Dr. Ole Lytken, who spend a lot of time with me going through the data, giving me new ideas on how to proceed when I was stuck, giving me freedom to follow my own little (programming) projects, giving me unconventional ideas for my talks, and sharing your experience as a scientist and as an Igor-programmer with me. Not having your EccentricXPS procedure for XPS fitting and NEXAFS analysis would have made this thesis impossible. You shaped me as scientists, and I am very grateful for that.

Prof. Dr. Hans-Peter Steinrück, who gave me the opportunity to work at his chair and for creating a great and very pleasant working environment starting with my master's thesis until the end of my Ph.D. thesis.

My former and current colleagues, Dr. Daniel Wechsler, Dr. Elmar Kataev, Dr. Julia Köbl, and Maximilian Muth. It was a pleasure working with you.

Prof. Dr. Bernd Meyer for the fruitful collaborations and the great DFT results provided. They took some time, but they were totally worth it.

Prof. Dr. Federico Williams for joining us on our boronic acid beamtime and introducing me to simple DFT calculations using ORCA.

The beamline staff from the Materials Science Beamline at Elettra, especially Dr. Natalyia Tsud and Dr. Sascha Mehl. I am grateful for their support at day and (deep into) night and their willingness to let us come earlier and (sometimes) measure a bit longer.

Bernd Kreß and Hans-Peter Bäumler, for their quick and competent support whenever anything broke on the chamber. I would have done so many dumb mistakes without you and your expertise.

Friedhold Wölfel and all the members of the workshop, who did a lot of work in manufacturing UHV-equipment needed for my research. The quality has always been great.

All the other members of the chair of Physical Chemistry II: Although we never worked closely, it was always a pleasure to have you around.

Finally, I want to thank my family and friends, who gave me much-needed distraction from my work and helped to cheer me up when I was frustrated.

10. References

[1] Rakow, N. A.; Suslick, K. S., *A colorimetric sensor array for odour visualization*. Nature **406** (2000) 710-713. https://doi.org/10.1038/35021028.

[2] Kumar, S.; Wani, M. Y.; Arranja, C. T.; e Silva, J. d. A.; Avula, B.; Sobral, A. J. F. N., *Porphyrins as nanoreactors in the carbon dioxide capture and conversion: a review*. J. Mater. Chem. A **3** (2015) 19615-19637. https://doi.org/10.1039/C5TA05082K.

[3] Barona-Castaño, J. C.; Carmona-Vargas, C. C.; Brocksom, T. J.; De Oliveira, K. T., *Porphyrins as Catalysts in Scalable Organic Reactions*. Molecules **21** (2016) 310. https://doi.org/10.3390/molecules21030310.

[4] Higashino, T.; Imahori, H., *Porphyrins as excellent dyes for dye-sensitized solar cells: recent developments and insights*. Dalton Trans. **44** (2015) 448-463. https://doi.org/10.1039/C4DT02756F.

[5] Balajka, J.; Hines, M. A.; DeBenedetti, W. J. I.; Komora, M.; Pavelec, J.; Schmid, M.; Diebold, U., *High-affinity adsorption leads to molecularly ordered interfaces on TiO_2 in air and solution*. Science **361** (2018) 786-789. https://doi.org/10.1126/science.aat6752.

[6] Khwaja, H. A., *Atmospheric concentrations of carboxylic acids and related compounds at a semiurban site*. Atmos. Environ. **29** (1995) 127-139. https://doi.org/10.1016/1352-2310(94)00211-3.

[7] Jousten, K., Handbuch Vakuumtechnik, Springer-Verlag, 2018.

[8] Linsebigler, A.; Lu, G.; Yates, J. T., Jr., *CO chemisorption on TiO_2 (110): Oxygen vacancy site influence on CO adsorption*. J. Chem. Phys. **103** (1995) 9438-9443. https://doi.org/10.1063/1.470005.

[9] Schaub, R.; Thostrup, P.; Lopez, N.; Lægsgaard, E.; Stensgaard, I.; Nørskov, J. K.; Besenbacher, F., *Oxygen Vacancies as Active Sites for Water Dissociation on Rutile TiO_2 (110)*. Phys. Rev. Lett. **87** (2001) 266104. https://doi.org/10.1103/PhysRevLett.87.266104.

[10] Wendt, S.; Schaub, R.; Matthiesen, J.; Vestergaard, E. K.; Wahlström, E.; Rasmussen, M. D.; Thostrup, P.; Molina, L.; Lægsgaard, E.; Stensgaard, I., *Oxygen vacancies on TiO_2 (110) and their interaction with H_2O and O_2: A combined high-resolution STM and DFT study*. Surf. Sci. **598** (2005) 226-245. https://doi.org/10.1016/j.susc.2005.08.041.

[11] Rahimi, N.; Pax, R. A.; Gray, E. M., *Review of functional titanium oxides. I: TiO_2 and its modifications*. Prog. Solid State Chem. **44** (2016) 86-105. https://doi.org/10.1016/j.progsolidstchem.2016.07.002.

[12] Dharma, H. N. C.; Jaafar, J.; Widiastuti, N.; Matsuyama, H.; Rajabsadeh, S.; Othman, M. H. D.; Rahman, M. A.; Jafri, N. N. M.; Suhaimin, N. S.; Nasir, A. M.; Alias, N. H., *A Review of Titanium Dioxide (TiO_2)-Based Photocatalyst for Oilfield-Produced Water Treatment*. Membranes **12** (2022) 345. https://doi.org/10.3390/membranes12030345.

[13] Akakuru, O. U.; Iqbal, Z. M.; Wu, A., TiO_2 Nanoparticles. In *TiO_2 Nanoparticles: Application in Nanobiotechnology and Nanomedicine*, Wu, A.; Ren, W., Eds. 2020; pp 1-66.

[14] Zhang, H.; Banfield, J. F., *Understanding Polymorphic Phase Transformation Behavior during Growth of Nanocrystalline Aggregates: Insights from TiO_2*. J. Phys. Chem. B **104** (2000) 3481-3487. https://doi.org/10.1021/jp000499j.

[15] Ohtani, B.; Prieto-Mahaney, O. O.; Li, D.; Abe, R., *What is Degussa (Evonik) P25? Crystalline composition analysis, reconstruction from isolated pure particles and photocatalytic activity test*. J. Photochem. Photobiol. A **216** (2010) 179-182. https://doi.org/10.1016/j.jphotochem.2010.07.024.

[16] Katal, R.; Masudy-Panah, S.; Tanhaei, M.; Farahani, M. H. D. A.; Jiangyong, H., *A review on the synthesis of the various types of anatase TiO_2 facets and their applications for photocatalysis*. Chem. Eng. J. **384** (2020) 123384. https://doi.org/10.1016/j.cej.2019.123384.

[17] Pelaez, M.; Nolan, N. T.; Pillai, S. C.; Seery, M. K.; Falaras, P.; Kontos, A. G.; Dunlop, P. S. M.; Hamilton, J. W. J.; Byrne, J. A.; O'Shea, K.; Entezari, M. H.; Dionysiou, D. D., *A review on the visible light active titanium dioxide photocatalysts for environmental applications*. Appl. Catal. B **125** (2012) 331-349. https://doi.org/10.1016/j.apcatb.2012.05.036.

[18] Carp, O.; Huisman, C. L.; Reller, A., *Photoinduced reactivity of titanium dioxide*. Prog. Solid State Chem. **32** (2004) 33-177. https://doi.org/10.1016/j.progsolidstchem.2004.08.001.

[19] Hart, A. S.; Kc, C. B.; Gobeze, H. B.; Sequeira, L. R.; D'Souza, F., *Porphyrin-Sensitized Solar Cells: Effect of Carboxyl Anchor Group Orientation on the Cell Performance*. ACS Appl. Mater. Interfaces **5** (2013) 5314-5323. https://doi.org/10.1021/am401201q.

[20] Lun Pang, C.; Lindsay, R.; Thornton, G., *Chemical reactions on rutile TiO_2 (110)*. Chem. Soc. Rev. **37** (2008) 2328-2353. https://doi.org/10.1039/B719085A.

[21] Luschtinetz, R.; Frenzel, J.; Milek, T.; Seifert, G., *Adsorption of phosphonic acid at the TiO_2 anatase (101) and rutile (110) surfaces*. J. Phys. Chem. C **113** (2009) 5730-5740. https://doi.org/10.1021/jp8110343.

[22] O'Rourke, C.; Bowler, D. R., *DSSC anchoring groups: a surface dependent decision*. J. Phys. Condens. Matter **26** (2014) 195302. https://doi.org/10.1088/0953-8984/26/19/195302.

[23] Nilsing, M.; Persson, P.; Lunell, S.; Ojamäe, L., *Dye-sensitization of the TiO_2 rutile (110) surface by perylene dyes: quantum-chemical periodic B3LYP computations*. J. Phys. Chem. C **111** (2007) 12116-12123. https://doi.org/10.1021/jp072253l.

[24] Sokolović, I.; Reticcioli, M.; Čalkovský, M.; Wagner, M.; Schmid, M.; Franchini, C.; Diebold, U.; Setvín, M., *Resolving the adsorption of molecular O_2 on the rutile TiO_2 (110) surface by noncontact atomic force microscopy*. PNAS **117** (2020) 14827-14837. https://doi.org/10.1073/pnas.1922452117.

[25] Diebold, U., *The surface science of titanium dioxide*. Surf. Sci. Rep. **48** (2003) 53-229. https://doi.org/10.1016/S0167-5729(02)00100-0.

[26] Kappes, B. B.; Maddox, W. B.; Acharya, D. P.; Sutter, P.; Ciobanu, C. V., *Interactions of same-row oxygen vacancies on rutile TiO_2(110)*. Phys. Rev. B **84** (2011) 161402. https://doi.org/10.1103/PhysRevB.84.161402.

[27] Setvin, M.; Franchini, C.; Hao, X.; Schmid, M.; Janotti, A.; Kaltak, M.; Van de Walle, C. G.; Kresse, G.; Diebold, U., *Direct View at Excess Electrons in TiO_2 Rutile and Anatase*. Phys. Rev. Lett. **113** (2014) 086402. https://doi.org/10.1103/PhysRevLett.113.086402.

[28] Reticcioli, M.; Sokolović, I.; Schmid, M.; Diebold, U.; Setvin, M.; Franchini, C., *Interplay between Adsorbates and Polarons: CO on Rutile TiO2 (110)*. Phys. Rev. Lett. **122** (2019) 016805. https://doi.org/10.1103/PhysRevLett.122.016805.

[29] Yim, C. M.; Chen, J.; Zhang, Y.; Shaw, B.-J.; Pang, C. L.; Grinter, D. C.; Bluhm, H.; Salmeron, M.; Muryn, C. A.; Michaelides, A., *Visualization of water-induced surface segregation of polarons on rutile TiO_2 (110)*. J. Phys. Chem. Lett. **9** (2018) 4865-4871. https://doi.org/10.1021/acs.jpclett.8b01904.

[30] Tanner, A. J.; Wen, B.; Ontaneda, J.; Zhang, Y.; Grau-Crespo, R.; Fielding, H. H.; Selloni, A.; Thornton, G., *Polaron-adsorbate coupling at the TiO_2 (110)-carboxylate interface*. J. Phys. Chem. Lett. **12** (2021) 3571-3576. https://doi.org/10.1021/acs.jpclett.1c00678.

[31] Yin, W.-J.; Wen, B.; Zhou, C.; Selloni, A.; Liu, L.-M., *Excess electrons in reduced rutile and anatase TiO_2*. Surf. Sci. Rep. **73** (2018) 58-82. https://doi.org/10.1016/j.surfrep.2018.02.003.

[32] Perry, S. S.; Merrill, P. B., *Preparation and characterization of MgO(100) surfaces*. Surf. Sci. **383** (1997) 268-276. https://doi.org/10.1016/S0039-6028(97)00185-4.

[33] Ikemiya, N.; Kitamura, A.; Hara, S., *Surface structures of MgO(100) and $SrTiO_3$(100) as revealed by atomic force microscopy*. J. Cryst. Growth **160** (1996) 104-110. https://doi.org/10.1016/0022-0248(95)00567-6.

[34] Ochs, D.; Maus-Friedrichs, W.; Brause, M.; Günster, J.; Kempter, V.; Puchin, V.; Shluger, A.; Kantorovich, L., *Study of the surface electronic structure of MgO bulk crystals and thin films*. Surf. Sci. **365** (1996) 557-571. https://doi.org/10.1016/0039-6028(96)00706-6.

[35] Corneille, J. S.; He, J.-W.; Goodman, D. W., *XPS characterization of ultra-thin MgO films on a Mo(100) surface*. Surf. Sci. **306** (1994) 269-278. https://doi.org/10.1016/0039-6028(94)90071-X.

[36] Benedetti, S.; Benia, H. M.; Nilius, N.; Valeri, S.; Freund, H. J., *Morphology and optical properties of MgO thin films on Mo(001)*. Chem. Phys. Lett. **430** (2006) 330-335. https://doi.org/10.1016/j.cplett.2006.08.130.

[37] Dugerjav, O.; Kim, H.; Seo, J. M., *Growth of a crystalline and ultrathin MgO film on Fe(001)*. AIP Adv. **1** (2011) 032156. https://doi.org/10.1063/1.3642601.

[38] Pal, J.; Smerieri, M.; Celasco, E.; Savio, L.; Vattuone, L.; Rocca, M., *Morphology of Monolayer MgO Films on Ag(100): Switching from Corrugated Islands to Extended Flat Terraces*. Phys. Rev. Lett. **112** (2014) 126102. https://doi.org/10.1103/PhysRevLett.112.126102.

[39] Chambers, S. A., *Epitaxial growth and properties of thin film oxides*. Surf. Sci. Rep. **39** (2000) 105-180. https://doi.org/10.1016/S0167-5729(00)00005-4.

[40] Jette, E. R.; Foote, F., *Precision Determination of Lattice Constants*. J. Chem. Phys. **3** (1935) 605-616. https://doi.org/10.1063/1.1749562.

[41] Gerlach, W., *Die Gitterstruktur der Erdalkalioxyde*. Zeitschrift für Physik **9** (1922) 184-192. https://doi.org/10.1007/BF01326966.

[42] Starr, D. E.; Weis, C.; Yamamoto, S.; Nilsson, A.; Bluhm, H., *NO_2 Adsorption on Ag(100) Supported MgO(100) Thin Films: Controlling the Adsorption State with Film Thickness*. J. Phys. Chem. C **113** (2009) 7355-7363. https://doi.org/10.1021/jp900410v.

[43] Li, S.-C.; Wang, J.-g.; Jacobson, P.; Gong, X. Q.; Selloni, A.; Diebold, U., *Correlation between Bonding Geometry and Band Gap States at Organic−Inorganic Interfaces: Catechol on Rutile TiO_2(110)*. JACS **131** (2009) 980-984. https://doi.org/10.1021/ja803595u.

[44] Kirby, R. K., *Thermal expansion of rutile from 100 to 700 K*. J. Res. Natl. Inst. Stand. Sect. A Physics And Chemistry **71** (1967) 363. https://doi.org/10.6028%2Fjres.071A.041.

[45] Liu, G.; Yang, H. G.; Pan, J.; Yang, Y. Q.; Lu, G. Q.; Cheng, H.-M., *Titanium Dioxide Crystals with Tailored Facets*. Chem. Rev. **114** (2014) 9559-9612. https://doi.org/10.1021/cr400621z.

[46] Oliver, P. M.; Watson, G. W.; Toby Kelsey, E.; Parker, S. C., *Atomistic simulation of the surface structure of the TiO_2 polymorphs rutile and anatase*. J. Mater. Chem. **7** (1997) 563-568. https://doi.org/10.1039/A606353E.

[47] Kim, B.; Li, Z.; Kay, B. D.; Dohnálek, Z.; Kim, Y. K., *The effect of oxygen vacancies on the binding interactions of NH_3 with rutile TiO_2 (110)-1 × 1*. Phys. Chem. Chem. Phys. **14** (2012) 15060-15065. https://doi.org/10.1039/C2CP42754K.

[48] Köbl, J.; Wechsler, D.; Kataev, E. Y.; Williams, F. J.; Tsud, N.; Franchi, S.; Steinrück, H.-P.; Lytken, O., *Adsorption of phenylphosphonic acid on rutile TiO_2 (110)*. Surf. Sci. **698** (2020) 121612. https://doi.org/10.1016/j.susc.2020.121612.

[49] Seah, M. P.; Dench, W. A., *Quantitative electron spectroscopy of surfaces: A standard data base for electron inelastic mean free paths in solids*. Surf. Interface Anal. **1** (1979) 2-11. https://doi.org/10.1002/sia.740010103.

[50] Castle, J. E., *Practical surface analysis by Auger and X-ray photoelectron spectroscopy. D. Briggs and M. P. Seah (Editors). John Wiley and Sons Ltd, Chichester, 1983, 533 pp.* Surf. Interface Anal. **6** (1984) 302-302.

[51] Einstein, A., *Über einen die Erzeugung und Verwandlung des Lichtes betreffenden heuristischen Gesichtspunkt*. Annalen der Physik **322** (1905) 132-148. https://doi.org/10.1002/andp.19053220607.

[52] Tougaard, S., *Accuracy of the non-destructive surface nanostructure quantification technique based on analysis of the XPS or AES peak shape*. Surf. Interface Anal. **26** (1998) 249-269. https://doi.org/10.1002/(SICI)1096-9918(199804)26:4<249::AID-SIA368>3.0.CO;2-A.

[53] Tougaard, S., *Practical guide to the use of backgrounds in quantitative XPS*. J. Vac. Sci. Technol. A **39** (2020) 011201. https://doi.org/10.1116/6.0000661.

[54] Tougaard, S., *Improved XPS analysis by visual inspection of the survey spectrum*. Surf. Interface Anal. **50** (2018) 657-666. https://doi.org/10.1002/sia.6456.

[55] Hüfner, S., Photoelectron spectroscopy: principles and applications, Springer Science & Business Media, 2013.

[56] Ratner, B. D.; Castner, D. G., Electron Spectroscopy for Chemical Analysis. In *Surface Analysis – The Principal Techniques*, 2009; pp 47-112.

[57] Shirley, D. A., Many-electron and final-state effects: Beyond the one-electron picture. In *Photoemission in Solids I: General Principles*, Cardona, M.; Ley, L., Eds. Springer Berlin Heidelberg: Berlin, Heidelberg, 1978; pp 165-195.

[58] Papp, C.; Steinrück, H.-P., *In situ high-resolution X-ray photoelectron spectroscopy – Fundamental insights in surface reactions*. Surf. Sci. Rep. **68** (2013) 446-487. https://doi.org/10.1016/j.surfrep.2013.10.003.

[59] Chen, M.; Röckert, M.; Xiao, J.; Drescher, H.-J.; Steinrück, H.-P.; Lytken, O.; Gottfried, J. M., *Coordination Reactions and Layer Exchange Processes at a Buried Metal–Organic Interface*. J. Phys. Chem. C **118** (2014) 8501-8507. https://doi.org/10.1021/jp5019235.

[60] Franke, M.; Marchini, F.; Zhang, L.; Tariq, Q.; Tsud, N.; Vorokhta, M.; Vondráček, M.; Prince, K.; Röckert, M.; Williams, F. J.; Steinrück, H.-P.; Lytken, O., *Temperature-Dependent Reactions of Phthalic Acid on Ag(100)*. J. Phys. Chem. C **119** (2015) 23580-23585. https://doi.org/10.1021/acs.jpcc.5b07858.

[61] Muth, M.; Wolfram, A.; Kataev, E.; Köbl, J.; Steinrück, H.-P.; Lytken, O., *Accurate Determination of Adsorption-Energy Differences of Metalloporphyrins on Rutile TiO_2 (110) 1 × 1*. Langmuir **38** (2022) 8643-8650. https://doi.org/10.1021/acs.langmuir.2c01054.

[62] Massicot, S.; Gezmis, A.; Talwar, T.; Meusel, M.; Jaekel, S.; Adhikari, R.; Winter, L.; Fernández, C. C.; Bayer, A.; Maier, F.; Steinrück, H.-P., *Adsorption and thermal evolution of $[C_1C_1Im][Tf_2N]$ on Pt (111)*. Phys. Chem. Chem. Phys. **25** (2023) 27953-27966. https://doi.org/10.1039/D3CP02743K.

[63] Düll, F.; Steinhauer, J.; Späth, F.; Bauer, U.; Bachmann, P.; Steinrück, H.-P.; Wickert, S.; Denecke, R.; Papp, C., *Ethylene: Its adsorption, reaction, and coking on Pt/h-BN/Rh(111) nanocluster arrays*. J. Chem. Phys. **152** (2020) 224710. https://doi.org/10.1063/5.0011616.

[64] Freiberger, E. M.; Steffen, J.; Waleska-Wellnhofer, N. J.; Harrer, A.; Hemauer, F.; Schwaab, V.; Görling, A.; Steinrück, H.-P.; Papp, C., *Bromine Adsorption and Thermal Stability on Rh(111): A Combined XPS, LEED and DFT Study*. ChemPhysChem **24** (2023) e202300510. https://doi.org/10.1002/cphc.202300510.

[65] Hemauer, F.; Bauer, U.; Fromm, L.; Weiß, C.; Leng, A.; Bachmann, P.; Düll, F.; Steinhauer, J.; Schwaab, V.; Grzonka, R.; Hirsch, A.; Görling, A.; Steinrück, H.-P.; Papp, C., *Surface Chemistry of the Molecular Solar Thermal Energy Storage System 2,3-Dicyano-Norbornadiene/Quadricyclane on Ni(111)*. ChemPhysChem **23** (2022) e202200199. https://doi.org/10.1002/cphc.202200199.

[66] Zhdanov, V. P., *Arrhenius parameters for rate processes on solid surfaces*. Surf. Sci. Rep. **12** (1991) 185-242. https://doi.org/10.1016/0167-5729(91)90011-L.

[67] Kreuzer, H.; Payne, S., Theories of the adsorption-desorption kinetics on homogeneous surfaces. In *Studies in Surface Science and Catalysis*, Elsevier: 1997; Vol. 104, pp 153-200.

[68] Ehrlich, G., Activated Chemisorption. In *Chemistry and Physics of Solid Surfaces VII*, Vanselow, R.; Howe, R., Eds. Springer Berlin Heidelberg: Berlin, Heidelberg, 1988; pp 1-64.

[69] Rudzinski, W.; Borowiecki, T.; Panczyk, T.; Dominko, A., *On the applicability of Arrhenius plot methods to determine surface energetic heterogeneity of adsorbents and catalysts surfaces from experimental TPD spectra*. Adv. Colloid Interface Sci. **84** (2000) 1-26. https://doi.org/10.1016/S0001-8686(99)00022-6.

[70] Tait, S. L.; Dohnálek, Z.; Campbell, C. T.; Kay, B. D., *n-alkanes on MgO (100). II. Chain length dependence of kinetic desorption parameters for small n-alkanes*. J. Chem. Phys. **122** (2005) 164708. https://doi.org/10.1063/1.1883630.

[71] Tait, S. L.; Dohnálek, Z.; Campbell, C. T.; Kay, B. D., *n-alkanes on Pt (111) and on C (0001)/ Pt (111): Chain length dependence of kinetic desorption parameters*. J. Chem. Phys. **125** (2006) 234308. https://doi.org/10.1063/1.2400235.

[72] Redhead, P., *Thermal desorption of gases*. Vacuum **12** (1962) 203-211. https://doi.org/10.1016/0042-207X(62)90978-8.

[73] King, D. A., *Thermal desorption from metal surfaces: A review*. Surf. Sci. **47** (1975) 384-402. https://doi.org/10.1016/0039-6028(75)90302-7.

[74] Barrie, P. J., *The mathematical origins of the kinetic compensation effect: 1. The effect of random experimental errors*. Phys. Chem. Chem. Phys. **14** (2012) 318-326. https://doi.org/10.1039/C1CP22666E.

[75] Nieskens, D.; Van Bavel, A.; Niemantsverdriet, J., *The analysis of temperature programmed desorption experiments of systems with lateral interactions; implications of the compensation effect*. Surf. Sci. **546** (2003) 159-169. https://doi.org/10.1016/j.susc.2003.09.035.

[76] Barrie, P. J., *The mathematical origins of the kinetic compensation effect: 2. The effect of systematic errors*. Phys. Chem. Chem. Phys. **14** (2012) 327-336. https://doi.org/10.1039/C1CP22667C.

[77] Stöhr, J., NEXAFS spectroscopy, Springer Science & Business Media, 2013, Vol. 25.

[78] Bras, W.; Myles, D. A. A.; Felici, R., *When x-rays alter the course of your experiments*. J. Phys. Condens. Matter **33** (2021) 423002. https://doi.org/10.1088/1361-648X/ac1767.

[79] Deskins, N. A.; Rousseau, R.; Dupuis, M., *Distribution of Ti^{3+} Surface Sites in Reduced TiO_2*. J. Phys. Chem. C **115** (2011) 7562-7572. https://doi.org/10.1021/jp2001139.

[80] Fairley, N.; Bargiela, P.; Roberts, A.; Fernandez, V.; Baltrusaitis, J., *Practical guide to understanding goodness-of-fit metrics used in chemical state modeling of x-ray photoelectron spectroscopy data by synthetic line shapes using nylon as an example*. J. Vac. Sci. Technol. A **41** (2022) 013203. https://doi.org/10.1116/6.0002196.

[81] Harrison, K.; Hazell, L. B., *The determination of uncertainties in quantitative XPS/AES and its impact on data acquisition strategy*. Surf. Interface Anal. **18** (1992) 368-376. https://doi.org/10.1002/sia.740180510.

[82] Ninova, S.; Malcıoğlu, O. B.; Auburger, P.; Franke, M.; Lytken, O.; Steinrück, H.-P.; Bockstedte, M., *Morphology Dependent Interaction between Co (II)-tetraphenylporphyrin and the MgO (100) surface*. Phys. Chem. Chem. Phys. **23** (2021) 2105-2116. https://doi.org/10.1039/D0CP04859C.

[83] Gottfried, J. M., *Surface chemistry of porphyrins and phthalocyanines*. Surf. Sci. Rep. **70** (2015) 259-379. https://doi.org/10.1016/j.surfrep.2015.04.001.

[84] Adhikari, R.; Siglreithmaier, G.; Gurrath, M.; Meusel, M.; Kuliga, J.; Lepper, M.; Hölzel, H.; Jux, N.; Meyer, B.; Steinrück, H. P., *Formation of highly ordered molecular porous 2D networks from cyano-functionalized porphyrins on Cu (111)*. Chem. Eur. J. **26** (2020) 13408. https://doi.org/10.1002/chem.202001980.

[85] Röckert, M.; Franke, M.; Tariq, Q.; Ditze, S.; Stark, M.; Uffinger, P.; Wechsler, D.; Singh, U.; Xiao, J.; Marbach, H.; Lytken, O., *Coverage-and Temperature-Dependent Metalation and Dehydrogenation of*

Tetraphenylporphyrin on Cu (111). Chem. Eur. J. **20** (2014) 8948-8953. https://doi.org/10.1002/chem.201402420.

[86] Lexow, M.; Massicot, S.; Maier, F.; Steinrück, H.-P., *Stability and exchange processes in ionic liquid/porphyrin composite films on metal surfaces*. J. Phys. Chem. C **123** (2019) 29708-29721. https://doi.org/10.1021/acs.jpcc.9b08531.

[87] Schöniger, M.; Kachel, S. R.; Herritsch, J.; Schröder, P.; Hutter, M.; Gottfried, J. M., *Direct synthesis of dilithium tetraphenylporphyrin: facile reaction of a free-base porphyrin with vapor-deposited lithium*. ChemComm **55** (2019) 13665-13668. https://doi.org/10.1039/C9CC07170A.

[88] Buchner, F.; Kellner, I.; Hieringer, W.; Görling, A.; Steinrück, H.-P.; Marbach, H., *Ordering aspects and intramolecular conformation of tetraphenylporphyrins on Ag (111)*. Phys. Chem. Chem. Phys. **12** (2010) 13082-13090. https://doi.org/10.1039/C004551A.

[89] Klimeš, J.; Michaelides, A., *Perspective: Advances and challenges in treating van der Waals dispersion forces in density functional theory*. J. Chem. Phys. **137** (2012) 120901. https://doi.org/10.1063/1.4754130.

[90] Grimme, S.; Hansen, A.; Brandenburg, J. G.; Bannwarth, C., *Dispersion-Corrected Mean-Field Electronic Structure Methods*. Chem. Rev. **116** (2016) 5105-5154. https://doi.org/10.1021/acs.chemrev.5b00533.

[91] Liu, W.; Tkatchenko, A.; Scheffler, M., *Modeling Adsorption and Reactions of Organic Molecules at Metal Surfaces*. Acc. Chem. Res. **47** (2014) 3369-3377. https://doi.org/10.1021/ar500118y.

[92] Ehrlich, S.; Moellmann, J.; Reckien, W.; Bredow, T.; Grimme, S., *System-dependent dispersion coefficients for the DFT-D3 treatment of adsorption processes on ionic surfaces*. ChemPhysChem **12** (2011) 3414-3420. https://doi.org/10.1002/cphc.201100521.

[93] Bhattarai, A.; Marchbanks-Owens, K.; Mazur, U.; Hipps, K., *Influence of the central metal ion on the desorption kinetics of a porphyrin from the solution/HOPG interface*. J. Phys. Chem. C **120** (2016) 18140-18150. https://doi.org/10.1021/acs.jpcc.6b05964.

[94] Bhattarai, A.; Mazur, U.; Hipps, K., *Desorption Kinetics and Activation Energy for Cobalt Octaethylporphyrin from Graphite at the Phenyloctane Solution–Graphite Interface: An STM Study*. J. Phys. Chem. C **119** (2015) 9386-9394. https://doi.org/10.1021/acs.jpcc.5b01444.

[95] Lytken, O.; Lew, W.; Campbell, C. T., *Catalytic reaction energetics by single crystal adsorption calorimetry: hydrocarbons on Pt (111)*. Chem. Soc. Rev. **37** (2008) 2172-2179. https://doi.org/10.1039/B719543P.

[96] Schauermann, S.; Silbaugh, T. L.; Campbell, C. T., *Single-Crystal Adsorption Calorimetry on Well-Defined Surfaces: From Single Crystals to Supported Nanoparticles*. Chem. Rec. **14** (2014) 759-774. https://doi.org/10.1002/tcr.201402022.

[97] Arthur, J. R.; Cho, A. Y., *Adsorption and desorption kinetics of Cu and Au on (0001) graphite*. Surf. Sci. **36** (1973) 641-660. https://doi.org/10.1016/0039-6028(73)90409-3.

[98] Bertucci, M.; Le Lay, G.; Manneville, M.; Kern, R., *Desorption kinetics of condensed phases Two-dimensional phases of silver on Ge(111)*. Surf. Sci. **85** (1979) 471-492. https://doi.org/10.1016/0039-6028(79)90266-8.

[99] Opila, R.; Gomer, R., *Thermal desorption of Xe from the W (110) plane*. Surf. Sci. **112** (1981) 1-22. https://doi.org/10.1016/0039-6028(81)90330-7.

[100] Roos, M.; Breitruck, A.; Hoster, H. E.; Behm, R. J., *Entropic stabilization of large adsorbates on weakly binding substrates—a thermal desorption and scanning tunneling microscopy study*. Phys. Chem. Chem. Phys. **12** (2010) 818-822. https://doi.org/10.1039/B920481D.

[101] Kachel, S. R.; Klein, B. P.; Morbec, J. M.; Schöniger, M.; Hutter, M.; Schmid, M.; Kratzer, P.; Meyer, B.; Tonner, R.; Gottfried, J. M., *Chemisorption and Physisorption at the Metal/Organic Interface: Bond Energies of Naphthalene and Azulene on Coinage Metal Surfaces*. J. Phys. Chem. C **124** (2020) 8257-8268. https://doi.org/10.1021/acs.jpcc.0c00915.

[102] Gottfried, J. M.; Vestergaard, E. K.; Bera, P.; Campbell, C. T., *Heat of adsorption of naphthalene on Pt (111) measured by adsorption calorimetry*. J. Phys. Chem. B **110** (2006) 17539-17545. https://doi.org/10.1021/jp062659i.

[103] Joblin, C.; d'Hendecourt, L.; Léger, A.; Defourneau, D., *Infrared spectroscopy of gas-phase PAH molecules. 1: Role of the physical environment*. Astron. Astrophys. **281** (1994) 923-936.

[104] Witte, G., *Low frequency vibrational modes of adsorbates*. Surf. Sci. **502** (2002) 405-416. https://doi.org/10.1016/S0039-6028(01)01986-0.

[105] Klein, B. P.; Morbec, J. M.; Franke, M.; Greulich, K. K.; Sachs, M.; Parhizkar, S.; Bocquet, F. o. C.; Schmid, M.; Hall, S. J.; Maurer, R. J., *Molecule–Metal Bond of Alternant versus Nonalternant Aromatic*

Systems on Coinage Metal Surfaces: Naphthalene versus Azulene on Ag (111) and Cu (111). J. Phys. Chem. C **123** (2019) 29219-29230. https://doi.org/10.1021/acs.jpcc.9b08824.

[106] Olsson, S.; Dahlstrand, C.; Gogoll, A., *Design of oxophilic metalloporphyrins: an experimental and DFT study of methanol binding*. Dalton Trans. **47** (2018) 11572-11585. https://doi.org/https://doi.org/10.1039/C8DT02432D.

[107] Wölfle, T.; Görling, A.; Hieringer, W., *Conformational flexibility of metalloporphyrins studied by density-functional calculations*. Phys. Chem. Chem. Phys. **10** (2008) 5739-5742. https://doi.org/10.1039/B800566B.

[108] Speedy, R. J.; Debenedetti, P. G.; Smith, R. S.; Huang, C.; Kay, B. D., *The evaporation rate, free energy, and entropy of amorphous water at 150 K*. J. Chem. Phys. **105** (1996) 240-244. https://doi.org/10.1063/1.471869.

[109] Smith, R. S.; Huang, C.; Wong, E.; Kay, B. D., *Desorption and crystallization kinetics in nanoscale thin films of amorphous water ice*. Surf. Sci. **367** (1996) L13-L18. https://doi.org/10.1016/S0039-6028(96)00943-0.

[110] Jakob, P.; Menzel, D., *Initial stages of multilayer growth and structural phase transitions of physisorbed benzene on Ru (001)*. J. Chem. Phys. **105** (1996) 3838-3848. https://doi.org/10.1063/1.472204.

[111] Zhdanov, V.; Norton, P., *Simulations of desorption from amorphous films*. Surf. Sci. **459** (2000) 245-255. https://doi.org/10.1016/S0039-6028(00)00493-3.

[112] Doménech, A.; Doménech-Carbó, M. T.; Sánchez del Río, M.; Vázquez de Agredos Pascual, M. L.; Lima, E., *Maya Blue as a nanostructured polyfunctional hybrid organic–inorganic material: the need to change paradigms*. New J. Chem. **33** (2009) 2371-2379. https://doi.org/10.1039/B901942A.

[113] Singh, M.; Kaur, N.; Comini, E., *The role of self-assembled monolayers in electronic devices*. J. Mater. Chem. C **8** (2020) 3938-3955. https://doi.org/10.1039/D0TC00388C.

[114] Casalini, S.; Bortolotti, C. A.; Leonardi, F.; Biscarini, F., *Self-assembled monolayers in organic electronics*. Chem. Soc. Rev. **46** (2017) 40-71. https://doi.org/10.1039/C6CS00509H.

[115] Gong, J.; Liang, J.; Sumathy, K., *Review on dye-sensitized solar cells (DSSCs): Fundamental concepts and novel materials*. Renew. Sustain. Energy Rev. **16** (2012) 5848-5860. https://doi.org/10.1016/j.rser.2012.04.044.

[116] Telegdi, J., *Formation of Self-Assembled Anticorrosion Films on Different Metals*. Materials **13** (2020) 5089. https://doi.org/10.3390/ma13225089.

[117] Bhushan, B.; Liu, H., Self-Assembled Monolayers for Controlling Adhesion, Friction and Wear. In *Nanotribology and Nanomechanics: An Introduction*, Bhushan, B., Ed. Springer Berlin Heidelberg: Berlin, Heidelberg, 2005; pp 885-928.

[118] Choi, Y.; Tran, H.-V.; Lee, T. R., *Self-Assembled Monolayer Coatings on Gold and Silica Surfaces for Antifouling Applications: A Review*. Coatings **12** (2022) 1462. https://doi.org/10.3390/coatings12101462.

[119] Vericat, C.; Vela, M.; Benitez, G.; Carro, P.; Salvarezza, R., *Self-assembled monolayers of thiols and dithiols on gold: new challenges for a well-known system*. Chem. Soc. Rev. **39** (2010) 1805-1834. https://doi.org/10.1039/B907301A.

[120] Leary, E.; La Rosa, A.; González, M. T.; Rubio-Bollinger, G.; Agraït, N.; Martín, N., *Incorporating single molecules into electrical circuits. The role of the chemical anchoring group*. Chem. Soc. Rev. **44** (2015) 920-942. https://doi.org/10.1039/C4CS00264D.

[121] Grimm, O. C.; Somaratne, R. M. D. S.; Wang, Y.; Kim, S.; Whitten, J. E., *Thiol adsorption on metal oxide nanoparticles*. Phys. Chem. Chem. Phys. **23** (2021) 8309-8317. https://doi.org/10.1039/D1CP00506E.

[122] Materna, K. L.; Crabtree, R. H.; Brudvig, G. W., *Anchoring groups for photocatalytic water oxidation on metal oxide surfaces*. Chem. Soc. Rev. **46** (2017) 6099-6110. https://doi.org/10.1039/C7CS00314E.

[123] Ahangaran, F.; Navarchian, A. H., *Recent advances in chemical surface modification of metal oxide nanoparticles with silane coupling agents: A review*. Adv. Colloid Interface Sci. **286** (2020) 102298. https://doi.org/10.1016/j.cis.2020.102298.

[124] Zhang, L.; Cole, J. M., *Anchoring groups for dye-sensitized solar cells*. ACS Appl. Mater. Interfaces **7** (2015) 3427-3455. https://doi.org/10.1021/am507334m.

[125] Hagfeldt, A.; Boschloo, G.; Sun, L.; Kloo, L.; Pettersson, H., *Dye-Sensitized Solar Cells*. Chem. Rev. **110** (2010) 6595-6663. https://doi.org/10.1021/cr900356p.

[126] Brown, D. G.; Schauer, P. A.; Borau-Garcia, J.; Fancy, B. R.; Berlinguette, C. P., *Stabilization of Ruthenium Sensitizers to TiO_2 Surfaces through Cooperative Anchoring Groups*. JACS **135** (2013) 1692-1695. https://doi.org/10.1021/ja310965h.

[127] Abate, A.; Pérez-Tejada, R.; Wojciechowski, K.; Foster, J. M.; Sadhanala, A.; Steiner, U.; Snaith, H. J.; Franco, S.; Orduna, J., *Phosphonic anchoring groups in organic dyes for solid-state solar cells*. Phys. Chem. Chem. Phys. **17** (2015) 18780-18789. https://doi.org/10.1039/C5CP02671G.

[128] Guerrero, G.; Alauzun, J. G.; Granier, M.; Laurencin, D.; Mutin, P. H., *Phosphonate coupling molecules for the control of surface/interface properties and the synthesis of nanomaterials*. Dalton Trans. **42** (2013) 12569-12585. https://doi.org/10.1039/C3DT51193F.

[129] Brennan, B. J.; Llansola Portolés, M. J.; Liddell, P. A.; Moore, T. A.; Moore, A. L.; Gust, D., *Comparison of silatrane, phosphonic acid, and carboxylic acid functional groups for attachment of porphyrin sensitizers to TiO_2 in photoelectrochemical cells*. Phys. Chem. Chem. Phys. **15** (2013) 16605-16614. https://doi.org/10.1039/C3CP52156G.

[130] Hanson, K.; Brennaman, M. K.; Luo, H.; Glasson, C. R. K.; Concepcion, J. J.; Song, W.; Meyer, T. J., *Photostability of Phosphonate-Derivatized, Ru^{II} Polypyridyl Complexes on Metal Oxide Surfaces*. ACS Appl. Mater. Interfaces **4** (2012) 1462-1469. https://doi.org/10.1021/am201717x.

[131] Wagstaffe, M.; Thomas, A. G.; Jackman, M. J.; Torres-Molina, M.; Syres, K. L.; Handrup, K., *An experimental investigation of the adsorption of a phosphonic acid on the anatase TiO_2 (101) surface*. J. Phys. Chem. C **120** (2016) 1693-1700. https://doi.org/10.1021/acs.jpcc.5b11258.

[132] Gawalt, E. S.; Avaltroni, M. J.; Koch, N.; Schwartz, J., *Self-assembly and bonding of alkanephosphonic acids on the native oxide surface of titanium*. Langmuir **17** (2001) 5736-5738. https://doi.org/10.1021/la010649x.

[133] Pappin, B.; Kiefel, M. J.; Houston, T. A., Boron-Carbohydrate Interactions. In *Carbohydrates - Comprehensive Studies on Glycobiology and Glycotechnology*, Chuan-Fa, C., Ed. IntechOpen: Rijeka, 2012; pp 37-54.

[134] Wang, X.; Xia, N.; Liu, L., *Boronic Acid-Based Approach for Separation and Immobilization of Glycoproteins and Its Application in Sensing*. Int. J. Mol. Sci. **14** (2013) 20890-20912. https://doi.org/10.3390/ijms141020890.

[135] Akın Kara, D.; Kara, K.; Oylumluoglu, G.; Yigit, M. Z.; Can, M.; Kim, J. J.; Burnett, E. K.; Gonzalez Arellano, D. L.; Buyukcelebi, S.; Ozel, F.; Usluer, O.; Briseno, A. L.; Kus, M., *Enhanced Device Efficiency and Long-Term Stability via Boronic Acid-Based Self-Assembled Monolayer Modification of Indium Tin Oxide in a Planar Perovskite Solar Cell*. ACS Appl. Mater. Interfaces **10** (2018) 30000-30007. https://doi.org/10.1021/acsami.8b10445.

[136] Thompson, A., X-ray Data Booklet, 3rd Edition ed., 2009.

[137] Materials Science Beamline. https://www.elettra.eu/lightsources/elettra/elettra-beamlines/msb/specifications.html (accessed 19.01.2024).

[138] Chorkendorff, I.; Niemantsverdriet, J. W., Concepts of modern catalysis and kinetics, 3rd ed., John Wiley & Sons, Weinheim, 2017, p 124.

[139] Ontaneda, J.; Nicklin, R. E. J.; Cornish, A.; Roldan, A.; Grau-Crespo, R.; Held, G., *Adsorption of Methyl Acetoacetate at Ni {111}: Experiment and Theory*. J. Phys. Chem. C **120** (2016) 27490-27499. https://doi.org/10.1021/acs.jpcc.6b10023.

[140] Quevedo, W.; Ontaneda, J.; Large, A.; Seymour, J. M.; Bennett, R. A.; Grau-Crespo, R.; Held, G., *Adsorption of Aspartic Acid on Ni {100}: A Combined Experimental and Theoretical Study*. Langmuir **36** (2020) 9399-9411. https://doi.org/10.1021/acs.langmuir.0c01175.

[141] Tsaousis, P.; Ontaneda, J.; Bignardi, L.; Bennett, R. A.; Grau-Crespo, R.; Held, G., *Combined Experimental and Theoretical Study of Methyl Acetoacetate Adsorption on Ni{100}*. J. Phys. Chem. C **122** (2018) 6186-6194. https://doi.org/10.1021/acs.jpcc.8b00204.

[142] Gattinoni, C.; Tsaousis, P.; Euaruksakul, C.; Price, R.; Duncan, D. A.; Pascal, T.; Prendergast, D.; Held, G.; Michaelides, A., *Adsorption behavior of organic molecules: a study of benzotriazole on Cu (111) with spectroscopic and theoretical methods*. Langmuir **35** (2019) 882-893. https://doi.org/10.1021/acs.langmuir.8b03528.

[143] Tanuma, S.; Powell, C. J.; Penn, D. R., *Calculations of electron inelastic mean free paths. V. Data for 14 organic compounds over the 50–2000 eV range*. Surf. Interface Anal. **21** (1994) 165-176. https://doi.org/10.1002/sia.740210302.

[144] Wang, L.-Q.; Baer, D. R.; Engelhard, M. H.; Shultz, A. N., *The adsorption of liquid and vapor water on TiO_2 (110) surfaces: the role of defects*. Surf. Sci. **344** (1995) 237-250. https://doi.org/10.1016/0039-6028(95)00859-4.

[145] Perron, H.; Vandenborre, J.; Domain, C.; Drot, R.; Roques, J.; Simoni, E.; Ehrhardt, J. J.; Catalette, H., *Combined investigation of water sorption on TiO_2 rutile (110) single crystal face: XPS vs. periodic DFT*. Surf. Sci. **601** (2007) 518-527. https://doi.org/10.1016/j.susc.2006.10.015.

[146] Parkinson, G. S.; Muñoz-Márquez, M. A.; Quinn, P. D.; Gladys, M. J.; Tanner, R. E.; Woodruff, D. P.; Bailey, P.; Noakes, T. C. Q., *Medium-energy ion-scattering study of the structure of clean TiO_2 (110)*. Phys. Rev. B **73** (2006) 245409. https://doi.org/10.1103/PhysRevB.73.245409.

[147] Kröger, E. A.; Sayago, D. I.; Allegretti, F.; Knight, M. J.; Polcik, M.; Unterberger, W.; Lerotholi, T. J.; Hogan, K. A.; Lamont, C. L. A.; Woodruff, D. P., *Photoelectron diffraction investigation of the structure of the clean TiO_2 (110) surface*. Phys. Rev. B **75** (2007) 195413. https://doi.org/10.1103/PhysRevB.75.195413.

[148] Busayaporn, W.; Torrelles, X.; Wander, A.; Tomić, S.; Ernst, A.; Montanari, B.; Harrison, N. M.; Bikondoa, O.; Joumard, I.; Zegenhagen, J.; Cabailh, G.; Thornton, G.; Lindsay, R., *Geometric structure of TiO_2 (110): Confirming experimental conclusions*. Phys. Rev. B **81** (2010) 153404. https://doi.org/10.1103/PhysRevB.81.153404.

[149] Sayago, D. I.; Polcik, M.; Lindsay, R.; Toomes, R. L.; Hoeft, J. T.; Kittel, M.; Woodruff, D. P., *Structure Determination of Formic Acid Reaction Products on TiO_2 (110)*. J. Phys. Chem. B **108** (2004) 14316-14323. https://doi.org/10.1021/jp049833s.

[150] Lindsay, R.; Tomic, S.; Wander, A.; García-Méndez, M.; Thornton, G., *Low Energy Electron Diffraction Study of TiO_2 (110)(2×1)-$[HCOO]^-$*. J. Phys. Chem. C **112** (2008) 14154-14157. https://doi.org/10.1021/jp804016d.

[151] Cattani-Scholz, A., *Functional organophosphonate interfaces for nanotechnology: a review*. ACS Appl. Mater. Interfaces **9** (2017) 25643-25655. https://doi.org/10.1021/acsami.7b04382.

[152] Queffélec, C.; Petit, M.; Janvier, P.; Knight, D. A.; Bujoli, B., *Surface modification using phosphonic acids and esters*. Chem. Rev. **112** (2012) 3777-3807. https://doi.org/10.1021/cr2004212.

[153] Du, Y.; Petrik, N. G.; Deskins, N. A.; Wang, Z.; Henderson, M. A.; Kimmel, G. A.; Lyubinetsky, I., *Hydrogen reactivity on highly-hydroxylated TiO_2 (110) surfaces prepared via carboxylic acid adsorption and photolysis*. Phys. Chem. Chem. Phys. **14** (2012) 3066-3074. https://doi.org/10.1039/C1CP22515D.

[154] Hugenschmidt, M. B.; Gamble, L.; Campbell, C. T., *The interaction of H_2O with a TiO_2 (110) surface*. Surf. Sci. **302** (1994) 329-340. https://doi.org/10.1016/0039-6028(94)90837-0.

[155] Petrik, N. G.; Kimmel, G. A., *Reaction kinetics of water molecules with oxygen vacancies on rutile TiO_2 (110)*. J. Phys. Chem. C **119** (2015) 23059-23067. https://doi.org/10.1021/acs.jpcc.5b07526.

[156] White, J. M.; Szanyi, J.; Henderson, M. A., *The Photon-Driven Hydrophilicity of Titania: A Model Study Using TiO_2 (110) and Adsorbed Trimethyl Acetate*. J. Phys. Chem. B **107** (2003) 9029-9033. https://doi.org/10.1021/jp0345046.

[157] Henderson, M. A., *Complexity in the decomposition of formic acid on the TiO_2 (110) surface*. J. Phys. Chem. B **101** (1997) 221-229. https://doi.org/10.1021/jp961494i.

[158] Shibuya, T.; Yasuoka, K.; Mirbt, S.; Sanyal, B., *Subsurface Polaron Concentration As a Factor in the Chemistry of Reduced TiO_2 (110) Surfaces*. J. Phys. Chem. C **121** (2017) 11325-11334. https://doi.org/10.1021/acs.jpcc.7b00935.

[159] Reticcioli, M.; Setvin, M.; Schmid, M.; Diebold, U.; Franchini, C., *Formation and dynamics of small polarons on the rutile TiO_2 (110) surface*. Phys. Rev. B **98** (2018) 045306. https://doi.org/10.1103/PhysRevB.98.045306.

[160] Morita, K.; Shibuya, T.; Yasuoka, K., *Stability of Excess Electrons Introduced by Ti Interstitial in Rutile TiO_2 (110) Surface*. J. Phys. Chem. C **121** (2017) 1602-1607. https://doi.org/10.1021/acs.jpcc.6b09669.

[161] Fernández, C. C.; Wechsler, D.; Rocha, T. C.; Steinrück, H.-P.; Lytken, O.; Williams, F. J., *Adsorption of phosphonic-acid-functionalized porphyrin molecules on TiO_2 (110)*. J. Phys. Chem. C **123** (2019) 10974-10980. https://doi.org/10.1021/acs.jpcc.9b01019.

[162] Hall, D. G., Structure, Properties, and Preparation of Boronic Acid Derivatives. In *Boronic Acids*, 2011; pp 1-133.

[163] Dewar, M. J.; Jones, R., *New heteroaromatic compounds. XXV. Studies of salt formation in boron oxyacids by boron-11 nuclear magnetic resonance*. JACS **89** (1967) 2408-2410. https://doi.org/10.1021/ja00986a029.

[164] Hansen, J. Ø.; Huo, P.; Martinez, U.; Lira, E.; Wei, Y. Y.; Streber, R.; Lægsgaard, E.; Hammer, B.; Wendt, S.; Besenbacher, F., *Direct Evidence for Ethanol Dissociation on Rutile TiO_2(110)*. Phys. Rev. Lett. **107** (2011) 136102. https://doi.org/10.1103/PhysRevLett.107.136102.

[165] Duffin, A. M.; Schwartz, C. P.; England, A. H.; Uejio, J. S.; Prendergast, D.; Saykally, R. J., *pH-dependent x-ray absorption spectra of aqueous boron oxides*. J. Chem. Phys. **134** (2011) 154503. https://doi.org/10.1063/1.3574838.

[166] Xu, D.; Peak, D., *Adsorption of Boric Acid on Pure and Humic Acid Coated am-Al(OH)3: A Boron K-Edge XANES Study*. Environ. Sci. Technol. **41** (2007) 903-908. https://doi.org/10.1021/es0620383.
[167] Zhang, Z.; Yamaguchi, E. S.; Kasrai, M.; Bancroft, G. M., *Interaction of ZDDP with Borated Dispersant Using XANES and XPS*. Tribol. Trans. **47** (2004) 527-536. https://doi.org/10.1080/05698190490500725.
[168] Zhang, W.; Cao, L.; Wan, L.; Liu, L.; Xu, F., *A Photoelectron Spectroscopy Study on the Interfacial Chemistry and Electronic Structure of Terephthalic Acid Adsorption on TiO_2(110)-(1×1) Surface*. J. Phys. Chem. C **117** (2013) 21351-21358. https://doi.org/10.1021/jp406631x.
[169] Neese, F., *The ORCA program system*. Wiley Interdiscip. Rev. Comput. Mol. Sci. **2** (2012) 73-78. https://doi.org/10.1002/wcms.81.
[170] Toffoli, D.; Ponzi, A.; Bernes, E.; de Simone, M.; Grazioli, C.; Coreno, M.; Stredansky, M.; Cossaro, A.; Fronzoni, G., *Correlation effects in B1s core-excited states of boronic-acid derivatives: An experimental and computational study*. J. Chem. Phys. **151** (2019) 134306. https://doi.org/10.1063/1.5120175.
[171] Lytken, O.; Wechsler, D.; Steinrück, H.-P., *Removing photoemission features from Auger-yield NEXAFS spectra*. J. Electron Spectros. Relat. Phenomena **218** (2017) 35-39. https://doi.org/10.1016/j.elspec.2017.05.012.
[172] Quinn, F. M.; Teehan, D.; MacDonald, M.; Downes, S.; Bailey, P., *Higher-order suppression in diffraction-grating monochromators using thin films*. J. Synchrotron Radiat. **5** (1998) 783-785. https://doi.org/10.1107/S0909049597016440.
[173] Terminello, L. J.; McLean, A. B.; Santoni, A.; Spiller, E.; Himpsel, F. J., *Low pass filter for soft x-ray monochromators*. Rev. Sci. Instrum. **61** (1990) 1626-1628. https://doi.org/10.1063/1.1141124.
[174] Waki, I.; Hirai, Y.; Momose, A.; Hayakawa, K., *Higher-harmonics suppressor for soft x rays*. Rev. Sci. Instrum. **60** (1989) 2072-2075. https://doi.org/10.1063/1.1140829.
[175] Petersen, H. In *Plane grating monochromators: the working curve concept as implemented in the SX-700*, Soft X-Ray Optics and Technology, SPIE: 1986; pp 262-264.
[176] Davis, L. E., Handbook of auger electron spectroscopy : a reference book of standard data for identification and interpretation of Auger electron spectroscopy data, 2nd ed ed., Perkin-Emer Corp. Eden Prairie, Mn., Eden Prairie, Mn., 1979, p 190 pages : charts.

11. Appendix: Articles P1-P3

[P1] Adsorption energies of porphyrins on MgO(100): An experimental benchmark for dispersion-corrected density-functional theory

Alexander Wolfram, Quratulain Tariq, Cynthia C. Fernandez, Maximilian Muth, Martin Gurrath, Daniel Wechsler, Matthias Franke, Federico J. Williams, Hans-Peter Steinrück, Bernd Meyer, and Ole Lytken

Surf. Sci. 2022, 717, 121979

The author's contribution is sample preparation and measurement of multilayer TPDs, analysis and data interpretation of the experimental TPD data, and manuscript preparation.

[P2] Phenylphosphonic Acid on Rutile TiO_2(110): Using Theoretically Predicted O 1s Spectra to Identify the Adsorption Binding Modes

Alexander Wolfram, Maximilian Muth, Julia Köbl, Andreas Mölkner, Sascha Mehl, Nataliya Tsud, Hans-Peter Steinrück, Bernd Meyer, and Ole Lytken

J. Phys. Chem. C 2024, 128, 12735-12753

The author's contribution is sample preparation, measurement, data analysis, data interpretation, and manuscript preparation for the experimental data.

[P3] Adsorption of Phenylboronic Acid Derivatives on Rutile TiO_2(110)

Alexander Wolfram, Maximilian Muth, Federico J. Williams, Sascha Mehl, Nataliya Tsud, Hans-Peter, Steinrück, and Ole Lytken

J. Phys. Chem. C 2024, 128, 12450-12470

The author's contribution is sample preparation, measurement, data analysis, data interpretation, and manuscript preparation.